PROCESS DEVELOPMENT TO SOLVE CRITICAL CHALLENGES MOVING TOWARDS TWO INCH SINGLE CRYSTALLINE DIAMOND WAFERS

By

Matthias Muehle

A DISSERTATION

Submitted to
Michigan State University
in partial fulfillment of the requirements
for the degree of

Electrical Engineering - Doctor of Philosophy

2017

ABSTRACT

PROCESS DEVELOPMENT TO SOLVE CRITICAL CHALLENGES MOVING TOWARDS TWO INCH SINGLE CRYSTALLINE DIAMOND WAFERS

By

Matthias Muehle

Single crystalline diamond (SCD) has the potential to be widely used in high tech applications, i.e. optics, electro-optics and electronics. Currently, the limitation on commercialized diamond applications is the availability of large SCD wafers. SCD wafers of at least two inches in size will be necessary for a commercial adaptation of SCD applications. Today, the availability is limited to approximately 8.0 mm × 8.0 mm SCD wafers. Homoepitaxial growth of SCD material usually does not enlarge the top surface area. Thus, it is necessary to develop SCD engineering approaches to enlarge the wafer dimensions to two inches and above, and to develop key technologies that are required for low cost SCD wafer manufacturing.

The primary goal of this thesis is to address and solve some of the key challenges, which will enable technological advancement towards two inch SCD wafers and beyond. Three key diamond process, that have the potential to solve SCD wafer manufacturing issues are investigated in this thesis. These are: (i) laser cutting and shaping of SCD, (ii) ion implantation for SCD wafer manufacturing and (iii) increasing SCD growth rates.

Laser processing was investigated for the adaptation of SCD wafer processing and separation. It was found that SCD laser processing can be easily achieved using an infrared diamond cutting laser. A three stage procedure for separation of SCD wafers was established. However, the technology proved ineffective for large area SCD wafers due to material losses.

A Lift-Off technique using ion implantation weas introduced as alternative wafer separation technique was investigated. The procedure is virtually loss-free and scalable up to several

inches in size. Successful Lift-Off was demonstrated using protons, carbon and oxygen ions, and electrochemical etching. Alternative etching techniques were limited to small wafer dimensions due to diffusion limitations and partial etching of the SCD wafers.

Increasing the SCD growth rate and crystalline quality was achieved by increasing the operational pressure regime for microwave plasma assisted chemical vapor deposition from 280 Torr up to 400 Torr. The fundamental reactor behavior was studied by recording the absorbed power densities and the operational field map in this higher pressure regime. Absorbed power densities were increasing from 525 to 670 $\mathrm{W\,cm^{-3}}$. It was found, that the fixed geometry of the reactor limited the SCD growth, especially above 380 Torr. Thus, a readjustment of the cavity dimensions and substrate position inside the reactor will be necessary to increase the operating pressure even further.

SCD growth under high pressures was also explored. Individual deposition runs for different process pressures and methane concentrations were performed. Growth of freestanding high quality SCD plates was demonstrated for process pressures up to 400 Torr. The SCD growth rate increased from 9 to 28 $\mathrm{\mu m\,h^{-1}}$ as the process pressure increased from 180 to 380 Torr. The SCD top surface area increased by 40 %.

A stable pulsable microwave power supply was used to investigate the formation of pulsed microwave discharges. Video recording of the pulsed discharge formation was performed and the images were analyzed. Six different discharge ignition cases were identified within the parameter space (pulsing durations $\mathrm{T_{on}}$ and $\mathrm{T_{off}}$, and pulsing power levels $\mathrm{P_{on}}$ and $\mathrm{P_{off}}$).

Finally, preliminary results showed that optimizing the reactor geometry and the use of pulsed excitation has the potential to enhance SCD growth rates while retaining the high crystalline quality. In particular, the experiments indicate, that the growth rate can be increased by 70 to 100 %.

To my parents

TABLE OF CONTENTS

LIST OF TABLES

LIST OF FIGURES

Chapter 1

Introduction

1.1 Research motivation

Diamond possesses a unique set of physical properties, which makes it the ideal material for a variety of applications in thermal management, optics and electronics. For example, the thermal conductivity of diamond at room temperature can be as high $2000\,\mathrm{W\,m^{-1}\,K^{-1}}$ [1], which is the highest of all materials known. Hence, diamond would be the most suitable material for heat sink applications [2] and as high power IR windows for Gyrotrons [3] utilizing the low loss properties of diamond, such as having a low dielectric constant and high optical transparency.

Diamond shows high resistance to ionizing radiation. Thus all particle detectors installed at the Large Hadron Collider (LHC) are made out of SCD material [4]. Diamond is more transparent and much less absorbing to high energy photons compared to other elements making it the ideal material for all X-Ray optical components. Third generation synchrotrons are based on silicon optics. X-Ray free electron lasers (XFEL), the next generation of synchrotron sources, will reach energy densities, where the use of diamond optics is necessary [5]. Production and successful operation of diamond X-ray optics has already been shown [6, 7, 8].

Diamond has only one sharp Raman excitation at $1332\,\mathrm{cm}^{-1}$ [9]. A diamond Raman crystal can be used to alter the output wavelength of an incoming laser beam by increasing its wavelength due to Raman excitations. Mildren et al. [10] reported on a yellow output laser beam of 573 nm when using an input wavelength of 532 nm.

A particularly emerging field is the use of diamond in spintronics for quantum computing [11, 12, 13]. The main advantages of diamond over other spintronics materials, especially silicon, are that the $(NV)^-$ center emits in the visible range of the EM spectra (637 nm) [12] and that its decoherence time can be up to 1.8 ms [14].

By far the biggest interest of diamond is in its use as electronics material. Intrinsic diamond is a wide bandgap semidonductor with a bandgap of 5.47 eV [15]. Similar to silicon, diamond can be doped with boron [16, 17] or phosphorous [18, 19] to achieve p- and n-type conductivity. This has resulted in the successful realization of unipolar and bipolar diamond based electronic devices, i.e. Schottky diodes [20], bipolar junction transistors [21], field effect transistors [22] and high voltage switches [23] to name a few. The combination of doped and intrinsic layers have led to the design of deep UV light emitting diodes (235 nm) for sterilization [24]. Diamond electronics, when manufactured out of sufficiently high quality material, will outperform other wide bandgap semiconductors, i.e. silicon carbide and gallium nitride, due to its much more favorable Johnson's figure of merit [25], which defines the limit of various transistor parameters for devices made out of one particular material. Hence, diamond has the promise to become the ultimate material for realization of high-power, high-temperature and/or high-temperature electronics.

The main reason, why diamond based applications are not implemented by industry at the moment is the lack of availability of large scale and economic SCD wafers for device manufacturing. For example, 300 mm (12 inch) Si wafers are available at a high quality

and economic in cost [26], while 150 mm (6 inch) SiC wafers are commercially available and 200 mm (8 inch) wafers are currently under development [27]. In contrast, routinely available SCD wafers are limited to approximately 8.0 mm × 8.0 mm in size, while being significantly more expansive than Si and SiC, i.e. a 8.0 mm × 8.0 mm SCD wafer costs $3975 [28], while a 300 mm prime grade silicon wafer costs as little as $125 [29]. Hence, one carat (200 mg) of a SCD wafer costs currently $2959, while one carat of silicon costs as little as $0.15; a staggering 19 500 times difference.

Thus, in order to establish commercialization of diamond based devices it is crucial to: (i) increase the SCD growth rate and crystalline quality and (ii) increase the SCD wafer dimensions up to at least 2 inch and (iii) establish a loss-free and scalable SCD wafer separation technique, analogous to wire sawing for silicon wafers [26].

Increasing the SCD growth rate is of particular importance in order to reduce the deposition time and costs of SCD wafer manufacturing in an industrial environment, but will also be needed for the proposed SCD wafer enhancement engineering approach, which will ultimately yield 2 inch SCD wafers (see Section 2.6.3 for a detailed discussion). Similarly, it is necessary to develop a wafer separation technique, which is scalable in size and results in only minimal material loss, in order to further reduce the cost of SCD wafer manufacturing.

Ideally, SCD wafer dimensions must be as large as possible in order to benefit from scaling effects, i.e. more devices can be manufactured on a single wafer, bringing down the costs per device significantly. As of now, 2 inch SCD wafers have been identified as the minimum sized required for a commercial implementation of GaN on SCD serving as heat sink.

It can be seen, that moving towards 2 inch SCD wafers and manufacturing them possesses a whole set of technological challenges, some of which are addressed by this thesis. In particular, an engineered approach of enlarging SCD wafer dimensions without a loss in

crystalline quality needs to be identified and demonstrated. Such an engineered approach will require a significant amount of SCD shaping through laser machining. Additionally, a new separation technique has to be identified for SCD wafers as commonly used conventional cutting mechanism are inefficient due to the hardness of diamond. Finally, the previous tasks are linked with the growth rate, which is the key parameter to reduce the growth time necessary making the proposed engineering approach more feasible. The goal of this thesis is to study those tasks in order to set the framework for the engineering of 2 inch wafers.

1.2 Reseach objectives

The research pursued in this dissertation covers three areas: identify suitable SCD processing techniques, which will allow (i) to perform the suggested substrate engineering approach, (ii) to provide a loss-less separation method for 2 inch SCD wafers and (iii) optimize the SCD deposition process so that the growth rate is increased, while the crystalline quality remains at high quality. All three are required for the development of SCD wafer 2 inches and above in size. Additionally, those three areas are necessary for economic SCD wafer manufacturing of at least 2 inch in size in a commercialized matter.

The goal of the dissertation is to develop technologies to enable the development of two inch wafers and above and provide technologies for SCD manufacturing. The research presented in this dissertation is studying and identifying suitable techniques. The individual research tasks addressed in the dissertation are the following:

Task 1: Explore and establish wafer separation techniques. Specifically, investigate laser cutting and ion implantation based Lift-Off techniques, that enable the manufacturing of SCD wafers and evaluate the scalability of these techniques to large wafer area.

Task 2: Identify uses of a cutting laser for the SCD shaping required for diamond substrate engineering.

Task 3: Study SCD Lift-Off as alternative separation technique and evaluate the individual process steps, i.e. use of different ions for implantation and different separation techniques.

Task 4: Demonstrate successful diamond plate Lift-Off of grown SCD material as a loss-less and scalable separation technique.

Task 5: Extending the operational pressure for MPACVD SCD growth up to 400 Torr. Reactor B [30] and a stable microwave power supply are used to demonstrate operation at these high pressures.

Task6: Record the operational field map and absorbed power density in this new pressure regime up to 400 Torr and compare them to previous results at lower pressure [30, 31].

Task 7: Characterize the grown SCD and verify its crystalline quality.

Task 8: Introduce video imaging as a new analytical tool to investigate the temporal formation of pulsed microwave discharges.

Task9: Record the formation of microwave discharges and identify different ignition behaviors due to varying pulsing parameters.

Task 10: Verify, that existing models of pulsed microwave discharges do not accurately describe the ignition phase of the plasma discharge.

1.3 Dissertation outline

The dissertation consists of 9 chapters. Chapter 2 provides an overview of the necessary background knowledge and a literature review of recent publications from the global diamond community. The background covers the SCD growth chemistry and the microwave cavity

plasma reactor. Different approaches of achieving large area SCD wafers are analyzed, using homoepitaxy and heteroepitaxy. The literature reviewalso covers previous efforts on the measurement of operational field maps, SCD synthesis using continuous wave and pulsed excitation and on Lift-Off as SCD wafer separation technique utilizing ion implantation.

Chapter 3 contains a summary of the experimental details of the experimental systems used in this dissertation, i.e. it described details on the geometry of Reactor B, its subsystems and the pulsable microwave power supply. Additionally, it details analytical systems for diamond analysis, the cutting laser used for diamond processing and the Van de Graff accelerator. Etching setups for the Lift-Off technique are discussed as well.

SCD processing using a IR cutting laser is presented in chapter 4. It contains the introduction of a three stage recycling process for reuse of SCD wafers and an in-depth quality analysis of each individual step. Limitations of the procedure and the utilization of SCD processing for different purposes, i.e. SCD shaping and manufacturing of CVD grown SCD seeds, are discussed.

Chapter 5 introduces Lift-Off as an alternative SCD separation method utilizing ion implantation for local graphitization, followed by selective etching. Monte Carlo simulations have been performed. Different ions (H^+, C^+ and O^+) have been used and three different separation techniques have been studied (wetchemical and electrochemical etching, and thermal oxidation).

Chapter 6 contains a description of the fundamental reactor behavior in a newly explored pressure regime between 300 and 400 Torr. The methodologies of recording operational field maps and calculating absorbed power densities at these high pressures are discussed and performed. SCD growth is also demonstrated for pressures up to 400 Torr. The growth rate and the film quality as a function of pressure and methane concentration is presented.

Chapter 7 discusses the temporal formation of pulsed microwave discharges. First, the video recording setup is introduced. Discharge formation under various pulsing conditions are presented. Four different ignition patterns are identified.

Chapter 8 reports on preliminary experiments to further enhance the growth rate by (i) using a pulsed plasma discharge and (ii) retuning the reactor geometry to move the discharge closer to the SCD substrate. The chapter is finished with a table summarizing all SCD growth experiments performed in this dissertation.

Chapter 9 summarizes the dissertation by providing an overview of the research accomplishments and by providing an outlook on future research, including preliminary results based on the work in chapter 8 and a cost estimate for the fabrication of 1 inch SCD wafers comparing 2.45 GHz and 915 MHz growth technology and a brief overview of large area SCD HPHT processes.

Chapter 2

Theoretical background and literature review

2.1 Microwave plasma sources operating at high pressures

The efficient formation and maintenance of high power density microwave plasma sources has been demonstrated at pressures up to and above one atmosphere [32, 33]. In order to achieve the required efficient microwave coupling over a wide range of pressures and input powers, these plasma sources utilized internally tuned cavity applicator technologies [32, 33, 34], and were first demonstrated in free radical sources [35] and gas reforming applications [36]. These experiments clearly demonstrated that it was possible to efficiently create and maintain high power density and high charge density microwave discharges in the 100 Torr to one atmosphere regime. Thus, the use of microwave plasma sources at pressures that are greater than several hundred Torr is not new.

In fact, microwave discharges have been used in the demonstration of microwave electrothermal thruster spacecraft propulsion concepts using He and H_2 gases at pressures of up to

an atmosphere [37], and more recently plasma assisted combustion at atmospheric pressures [38]. These non-diamond microwave plasma source investigations support the intuitive idea that it should be possible to extend the MPACVD diamond growth processes to operating pressures that are as high as 400 Torr and even eventually to one atmosphere.

2.2 Diamond synthesis and reactor technology

2.2.1 SCD growth chemistry

The phase diagram of carbon is shown in Figure 2.1. Naturally occurring diamond is created by a phase change from graphite to diamond due to sufficiently high temperatures and pressures in the earths mantle. The same concept is mimicked when synthesizing diamond using the high-pressure high-temperature approach (HPHT), which was first realized by Erik Lundblad in February 1953 [39], but as the results were kept secret all fame was received by the GE diamond team, when they published their individual success [40]. Today, HPHT synthesis is commercialized by several companies such as Sumitomo or Element Six . The CVD approach differs significantly from HPHT synthesis. It should not be possible to produce diamond at sub atmospheric pressure in a purely thermal equilibrium process. Anyway, it is possible to deposit diamond using a non-equilibrium plasma process [41, 42]. Thus, additional reactions can occur during CVD SCD growth making the diamond phase preferable over the formation of graphite.

SCD growth is carried out in a using hydrogen H_2 and a hydrocarbon, usually methane CH_4. The discharge created by the microwave power input dissociates the molecular into atomic hydrogen and various hydrocarbon radicals. The underlying gas chemistry is complicated, containing 45 radicals and over 130 potential reactions [44]. Harris and Goodwin [45, 41]

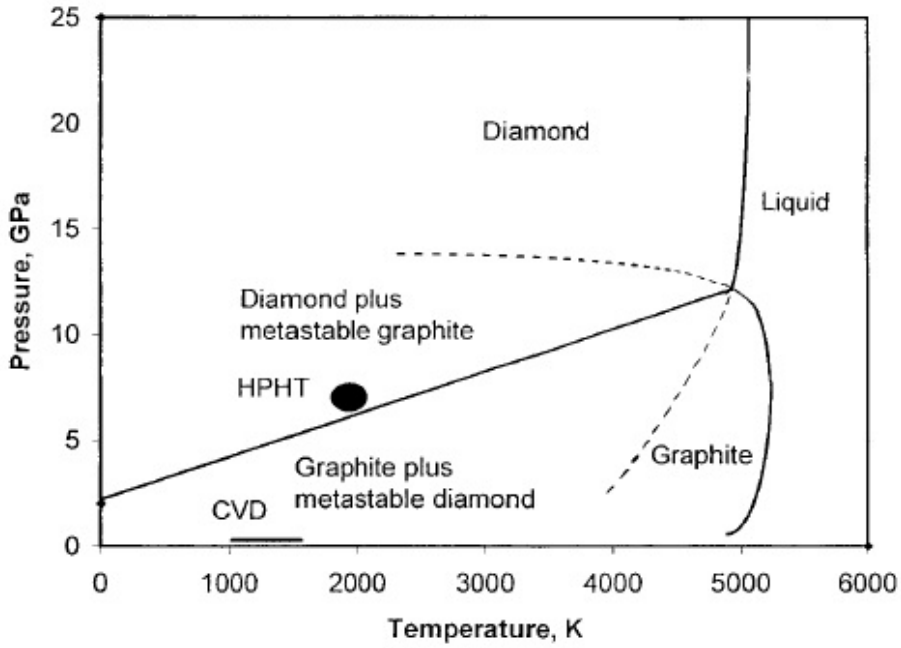

Figure 2.1 Sketch of carbon phase diagram. Regions of metastability of diamond and graphite are bounded by (dashed line) extensions of the melting curves of diamond and graphite, respectively. Approximate regions for high-pressure, high-temperature (HPHT) and chemical vapor deposition (CVD) synthesis of diamond are shown. [43].

proposed a simplified model utilizing only two gas species and five reactions to explain CVD synthesis. Atomic hydrogen plays an important role in stabilizing the diamond phase as well as etching any graphite formation [46]. Methyl radicals are widely accepted as carbon source. Simulations and plasma spectroscopy show [CH_3] as the main radical in vicinity to the seed substrate [47, 48]. The initial step needed for diamond synthesis is the creation of activated carbon sites on the diamond surface ${C_d}^*$. This is achieved by abstracting hydrogen from the carbon on the diamond surface. The atomic hydrogen atoms [H] combine to molecular hydrogen H_2:

$$C_d - H + H \xrightarrow{k_1} C_d^* + H_2$$

The corresponding reaction rate of is k_1. All reactions involved have their individual rates

k_x. It is possible that activated carbon sites are getting reoccupied by atomic hydrogen:

$$C_d^* + H \xrightarrow{k_2} C_d - H$$

This is the reversal of the abstraction reaction. This reaction effectively slows the growth process as activated sites are not getting occupied with additional carbon atoms . These two reactions are generating and closing active sites required for diamond deposition. The ratio of reactive sides is given by $\frac{k_1}{k_1+k_2}$. This ratio should be as high as possible to promote diamond growth. The ratio depends only on the seed substrate temperature according to Silva et al [49]. The abstraction reaction explains the important role of atomic hydrogen for diamond growth [44]. The first actual growth step is when a CH_3 radical bonds with an active carbon site:

$$C_d^* + CH_3 \xrightarrow{k_3} C_d - CH_3$$

The reaction can be reversed due to thermal desorption:

$$C_d - CH_3 \xrightarrow{k_4} C_d^* + CH_3$$

If a CH_3 radical is successfully bonded onto a carbon site eventually all 3 hydrogen atoms will be consecutively removed and the carbon site reactivated:

$$C_d - CH_3 + H \xrightarrow{k_5} C_d - CH_2^* + H_2$$
$$C_d - CH_2^* + H \xrightarrow{k_6} C_d - C_d - H + H_2$$

A schematic illustration of the microscopic growth process for the {110} and {111} crystallographic orientations is shown in Figure 2.2. These steps are repeated on a macroscopic scale resulting in the bulk deposition of SCD material.

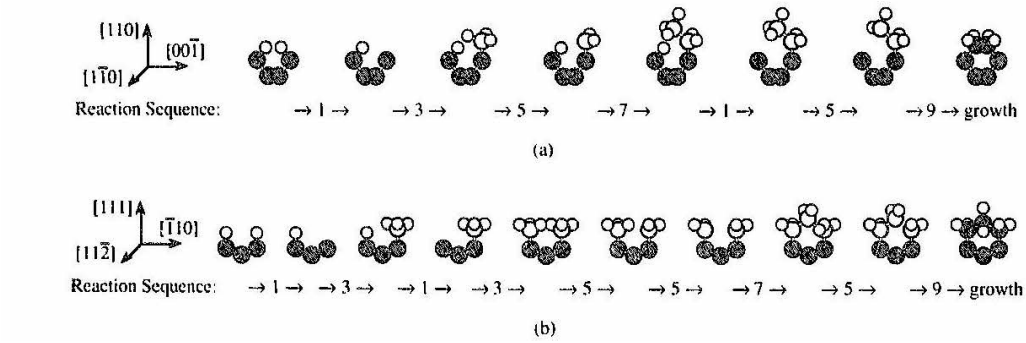

Figure 2.2 Examples of reaction sequences leading to the growth on the (a) {110} and (b) {111} faces of diamond. The images are schematics of the atomic processes involved in each reaction, and the text below them indicates the reactions (according to the labeling in Table 1 {of [50]} which occur between each atomic configuration. Dark grey circles are diamond, light grey circles are C atoms in chemisorbed hydrocarbons, and white circles are H atoms. [50]

The growth rate for the {100} crystalline orientation can be derived using the simiplified kinetic scheme as follows:

$$G_{\{100\}} = k_3 \frac{n_s}{n_d} \left(\frac{k_1}{k_2 + k_3} \right) \frac{[\mathrm{CH_3}]_\mathrm{s}[\mathrm{H}]_\mathrm{s}}{\frac{k_4}{k_5} + [\mathrm{H}]_\mathrm{s}} \tag{2.1}$$

where $[\mathrm{H}]_\mathrm{s}$ and $[\mathrm{CH_3}]_\mathrm{s}$ are the hydrogen and methyl concentrations at the surface [41]. n_s is the surface site density, which can be approximated with $2.61 \times 10^{-9}\,\mathrm{mol\,cm^{-1}}$ for {100} surfaces. n_d is the molar density, which is $0.2939\,\mathrm{mol\,cm^{-3}}$ [41]. Goodwin [41] determined the reaction rates based of experimental growth rates ranging from 0.1 to more than $7000\,\mu\mathrm{m\,h^{-1}}$. He determined the growth rate G as a function of the $[\mathrm{H}]_\mathrm{s}$ and $[\mathrm{CH_3}]_\mathrm{s}$ at the surface as following:

$$G_{\{100\}} = 1.8 \times 10^{11} \frac{[\mathrm{CH_3}]_\mathrm{s}[\mathrm{H}]_\mathrm{s}}{5 \times 10^{-9} + [\mathrm{H}]_\mathrm{s}} \tag{2.2}$$

Additionally, Goodwin [41] studied the rate of defect generation. He found, that at a constant temperature the defect fraction in the grown film X_{def} behaves as following:

$$X_{def} \propto \frac{G}{[\mathrm{H}]_\mathrm{s}^2} \tag{2.3}$$

When substituting Equation (2.2) into Equation (2.3) the dependence of the defect density becomes as follows:

$$X_{def} \propto \frac{[CH_3]}{[\mathrm{H}]} \tag{2.4}$$

Increasing the amount of $[\mathrm{CH_3}]$ will result in a higher growth rate, but also in a higher defect density. Nevertheless, this can be balanced if the amount of atomic hydrogen [H] is increased simultaneously. Optimizing the growth conditions is crucial for high quality SCD deposition with a reasonable growth rate. Goodwin [41] compiled the experimental data to plot the process map in the $[\mathrm{CH_3}]_\mathrm{s}$ and $[\mathrm{H}]_\mathrm{s}$ space. The solid lines represent equal growth rates, while the dotted lines mark equal defect densities. Figure 2.3 shows Goodwin's plot, where Silva et al. [49] updated the the map with computed data points using a 1D model of their LIMHP reactor. Their modeling results show that increasing the methane concentration results in a higher growth rate. Additionally, the $[\mathrm{CH_3}]_\mathrm{s}$ concentration increases while the [H] concentration remains almost unchanged. This results in an increase of the defect density. Increasing the pressure results in a higher growth rate as well due to an increased $[\mathrm{CH_3}]_\mathrm{s}$ concentration. At the same time, the atomic hydrogen concentration [H] increases more.

Thus the defect density is decreasing with pressure, while the growth rate increases. That illustrates why it is desirable to expand the existing growth window towards higher operating pressures.

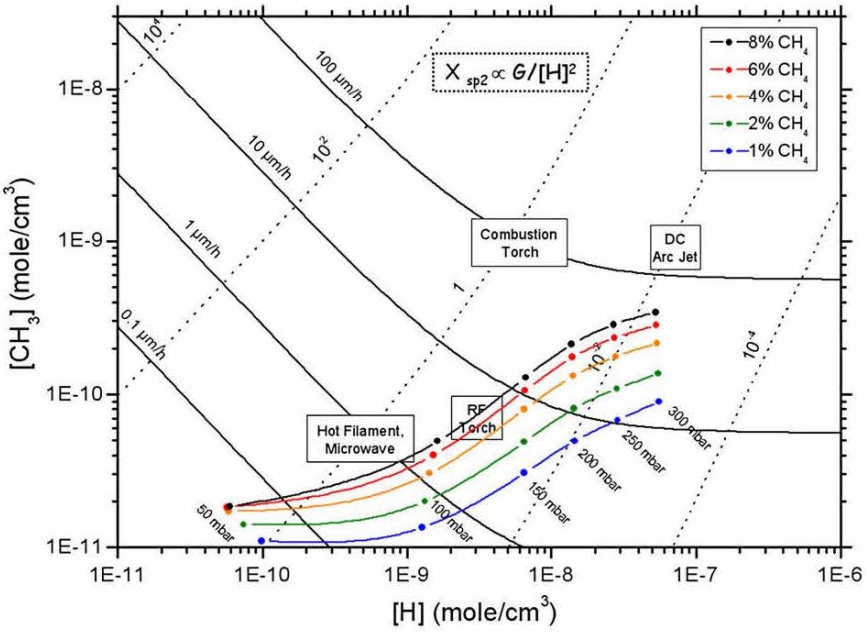

Figure 2.3 Process map in $[CH_3]_s$-$[H]_s$ space showing the operating ranges of the main CVD diamond growth process (from [41]). The evolution of the operating point of the LIMHP reactor as a function of the working pressure (from 50 to 300 mbar) and methane concentration (from 1 to 8 %) has been added. [49]

2.2.2 The microwave cavity plasma reactor design

Diamond synthesis was carried out using a later version of the microwave cavity plasma reactor (MCPR), which was initially developed at Michigan State University between 1975 and 1989 and commercialized by Wavemat/Norton for diamond growth between 1986 and 1995 [51]. After initial diamond growth was demonstrated at Norton/MSU, a new design was introduced by Zhang [52, 53] and then by Kuo et al. [51]. This reactor technology was used extensively by Norton in commercial applications from 1988 to 1999. The reactor

design was scaled in size up by designing a 915 MHz system in 1992. Recently, the original 2.45 GHz design received two upgrades, Reactor A [54] and B [30], using the same cavity configuration. The new design incorporated a variable length and reduced diameter cooling stages. A schematic cross-sectional view of a generic MCPR and some of its subsystems, which will be discussed in Section 3.1 can be seen in Figure 2.4.

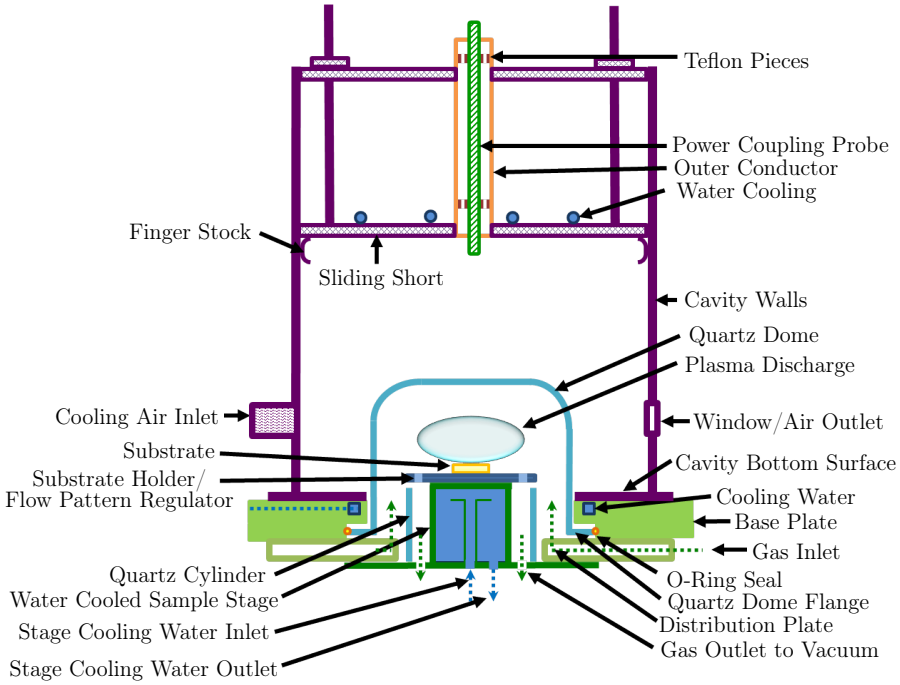

Figure 2.4 A cross-sectional view of a high pressure the MCPR including labeled details on the actual design. [55]

The overall working principle utilized the formation of a standing electromagnetic wave by tuning a 2.45 GHz microwave input inside a cylindrical resonance cavity. The microwaves are coupled into the cavity through an antenna (the excitation probe). The reactor chamber is separated from the cavity through a quartz bell jar. This dielectric window allows the transmission of microwaves into the discharge region and helps to stabilize the discharge. This region needs to be separated from the ambient enviornment and is part of the microwave gas handling system.

The position of the excitation probe inside the cavity L_p is variable. The cavity diameter is fixed, but the cavity length of the L_s can be adjusted. Additionally, the substrate position Z_s is variable as well. The applicator can be tuned and matched by adjusting L_p and L_s in a way that the electromagnetic excitation region is located above the substrate holder. The microwave power is coupled into the gas through electron inelastic collisions, ionizes the gas and creates a plasma discharge. The plasma discharge at typical process pressures (240 Torr) is weakly ionized with degrees of ionization as low as 1×10^{-6}. The neutral gas temperatures inside the plasma discharge are 2500 to 3500 K, depending on the process pressure [56]. The reactor can be matched efficiently and coupling efficiencies up to 100 % can be achieved [57].

The original design, as computationally described by Tan et al. [58] was first introduced by Zhang [53] and also used by Kuo et al. [51]. It utilized a 5 inch (127.0 mm) main holder and a 4 inch (101.6 mm) substrate holder. The cavity diameter was 7 inch (17.78 cm). The plasma discharge utilized a TM_{013} single mode excitation. Zhang [53] operated the reactor using a floating stage at pressures from 20 up to 95 Torr.

That design was consecutively upgraded by Zuo et al. [54] who reduced the diameter of the main holder to 4 inch (101.6 mm) and the substrate holder to 3 inch (76.2 mm). Plasma excitation was still achieved by a TM_{013} mode with proper retuning of the cavity variables L_p and L_s. The reduced holder dimensions led to a more confined plasma discharge and higher absorbed microwave power densities.

The traditional design of the MCPR received another upgrade, Reactor B, which was introduced by Hemawan et al. [30]. In this design, the main holder dimensions were reduced to 2.5 inch (63.5 mm) and the substrate holder was decreased to 1.5 inch (38.5 mm). Additionally, the cooling stage position was made length-adjustable. This new design incorporated four mechanically tunable geometrical varibles that allowed the internal reactor geometry to be

varied in situ enabling the reactor to be adaptable to a variety of process conditions while still achieving high microwave coupling efficiencies. This reactor utilized a hybrid TM_{013} + TEM_{001} mode for plasma excitation. Schematic cross-sections of Reactor A and B were shown in Figure 2.5.

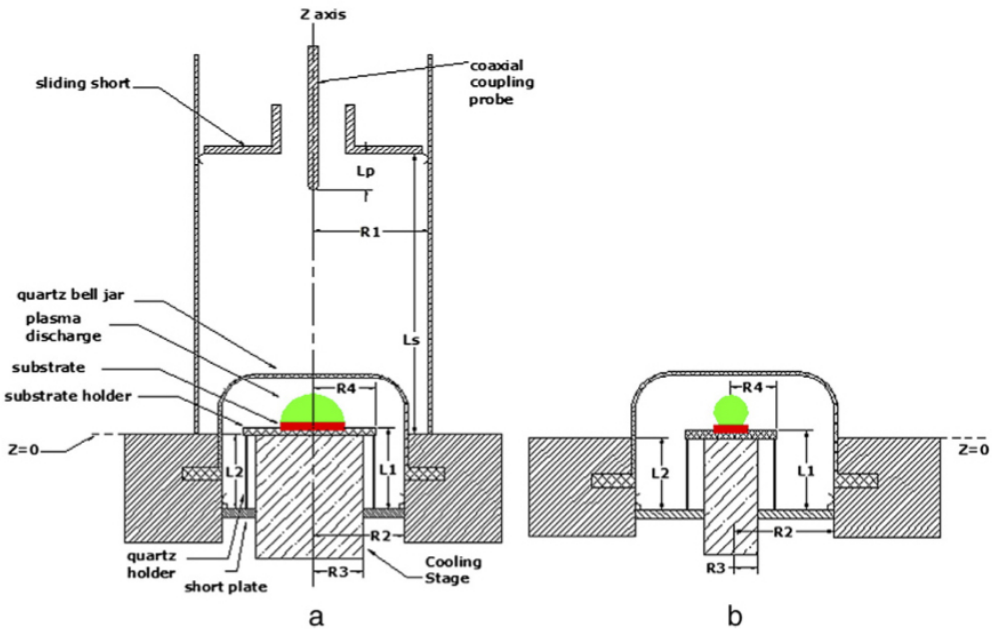

Figure 2.5 Schematic cross-sectional view of the discharge region in the chamber and the cavity for the (a) second generation (Type A) and (b) third generation (Type B) reactor technology. [30]

2.3 Previous operational field maps using the microwave cavity plasma reactor

The operational field map concept was first applied by Zhang and Asmussen [53].

Zuo et al. [54] recorded the operational field map for Reactor A between 60 and 160 Torr and results were shown in Figure 2.6 [54]. Significant absorbed power levels, as high as 3 kW were necessary due to low absorbed power densities [59].

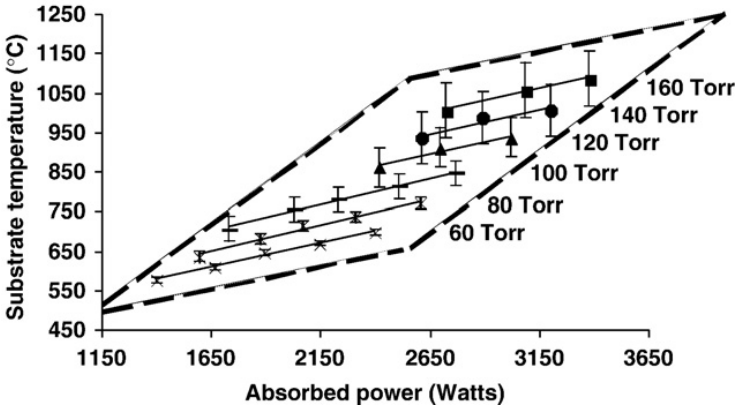

Figure 2.6 Substrate temperature vs. pressure and absorbed microwave power for the deposition plasma without argon. The vertical bars represent the minimum/maximum variation of temperature across a 75 mm diamond wafer. [54]

Hemawan et al. [30] recorded the operational field map for Reactor B and expanded the regime for diamond synthesis to 240 Torr. The results were shown in Figure 2.7 [30]. Efficient reactor operation was observed over the pressure regime and absorbed power densities as high as 450 $\mathrm{W\,cm^{-3}}$ were recorded. An absorbed power level of 2.3 kW was required to achieve a substrate temperature of around 1080 °C at 160 Torr, while around 3 kW were needed with Reactor A [54].

Lu et al. [31] expanded the pressure regime to 300 Torr and introduced SCD synthesis using reactor B. Additionally, an efficient and safe regime of operation was defined as shown in Figure 2.8 [31]. Operation outside of that regime towards lower substrate temperatures did not yield high quality SCD and operation at those low substrate temperatures was undesirable. Applying too much power did not further enhance the substrate temperature by much. Almost all of the excessive power was going into heating of the reactor walls and increased the likelihood of reactor failure. High pressure growth of SCD in reactor B was demonstrated.

Nad et al. [57] shifted the focus from redeveloping the reactor design into evaluating the

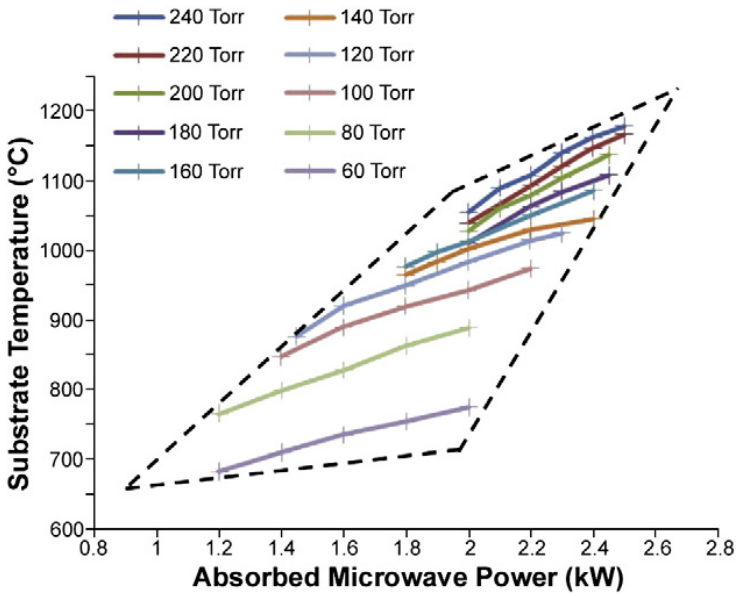

Figure 2.7 The operating roadmap of the improved plasma reactor showing the substrate temperature versus absorbed power at various operating pressures. $L_s = 20.5\,\text{cm}$, $L_p = 3.5\,\text{cm}$, $L_2 = 6.13\,\text{cm}$, $H_2 = 400$ sccm, $CH_4 = 3\,\%$ and $Z_2 = -0.31\,\text{cm}$. [30]

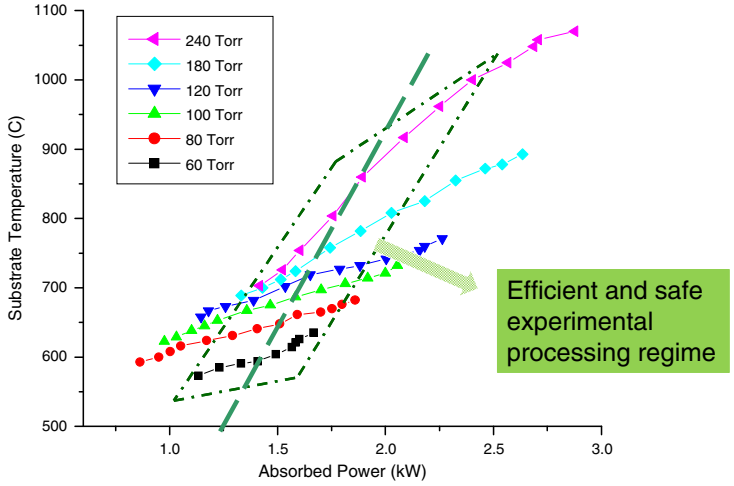

Figure 2.8 Operating field map curves and the identification of the efficient and safe experimental diamond synthesis regime for the Reactor B. Experimental conditions: $f_t = 412$ sccm, and $CH_4/H_2 = 3\,\%$, $Z_s = -5.7\,\text{mm}$. [31]

efficiency of the current operation of reactor B. Variations of the coupling efficiency, which is defined as the amount of power reflected, were studied by changing the reactor geometry. Figure 2.9 demonstrated two things: (1) The reactor had one well-matched position, where almost all input power was utilized in the discharge region. Variation of L_s changed the

length of the cylindrical resonance and hence detuned the configuration. Changes as little as 2 mm were sufficient so that 25 % of overall power was reflected. (2) The resonance body length L_s depended on the position of the sample holder z_s. Negative values of z_s meant, that the sample holder moved deeper into the reactor and pulled the discharge down to some extent as well. This was compensated by reducing L_s. Additionally, it was shown, that z_s around −8 mm was the optimal configuration eliminating virtually all reflected power.

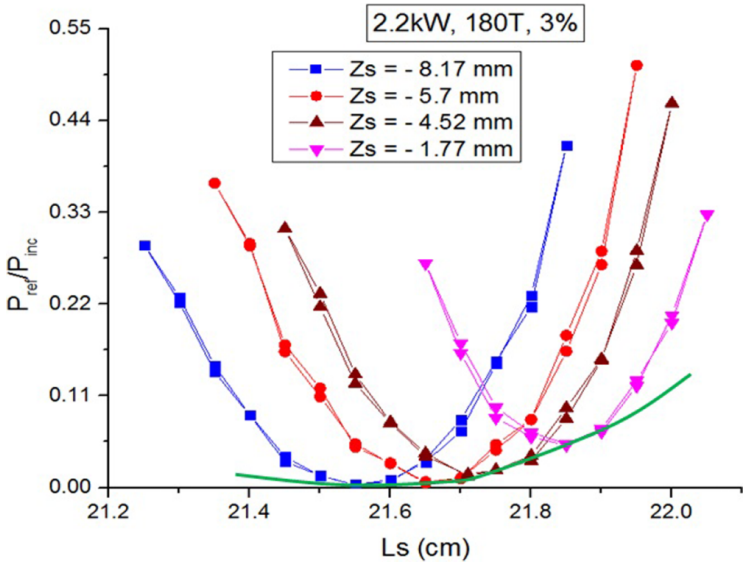

Figure 2.9 P_{ref}/P_{inc} vs. L_s for different z_s positions at a constant incident microwave power of 2.2 kW, operating pressure 180 Torr, and 3 % CH_4/H_2. [57]

Another interesting insight on the operational field map behavior was found by Nad et al. [57] when combining the substrate temperature with the coupling efficiency, as shown in Figure 2.10. It can be seen that the power regime for well-matched operation increased with pressure, i.e. higher levels were required to operate the reactor efficiently at higher pressures.

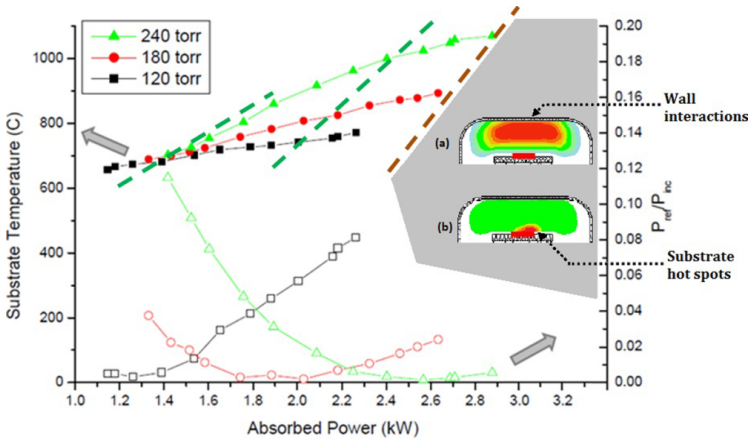

Figure 2.10 Operating field maps and matching, i.e. P_{ref}/P_{inc}, versus absorbed power for three constant pressure conditions: 120, 180 and 240 Torr. All other experimental variables are constant. [57]

2.4 SCD synthesis using continuous wave microwave discharges

Ongoing studies of SCD synthesis are carried out by numerous research groups. A summary of their recent advancements since 2012 can be found in the following subsections. For a detailed literature review of previous work, the reader is referred to the PhD thesis by Jing Lu [60].

2.4.1 Fraunhofer IAF, Germany

Widmann et al. [61] recently utilized an ellipsoidal reactor [62, 63], which operated in a TM_{036} mode, for SCD growth. The electromagnetic field distribution is shown in Figure 2.11. Figure 2.12 showed a schematic of the discharge region and Figure 2.13 shows a more detailed illustration of their heated substrate holder. Two different molybdenum holders with diameters of approximately 20 and 40 mm were used. The second one is slightly larger than for the type B MCPR (38.5 mm).

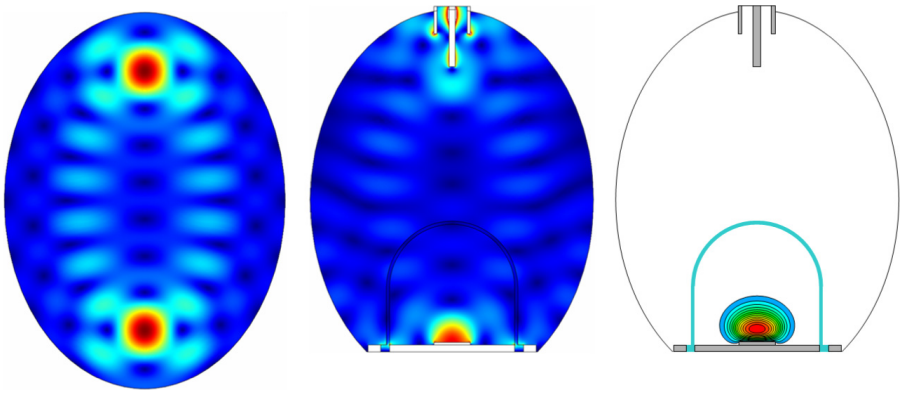

Figure 2.11 Illustration of the AIXTRON reactor design exploiting an ellipsoidal resonant cavity. The electric field structure in this cavity shows two very pronounced maxima at the two ellipsoid's foci, corresponding to the power coupling and plasma ignition locations, respectively. In the rightmost panel, we show modelling of a 200 mbar H_2 plasma. [63]

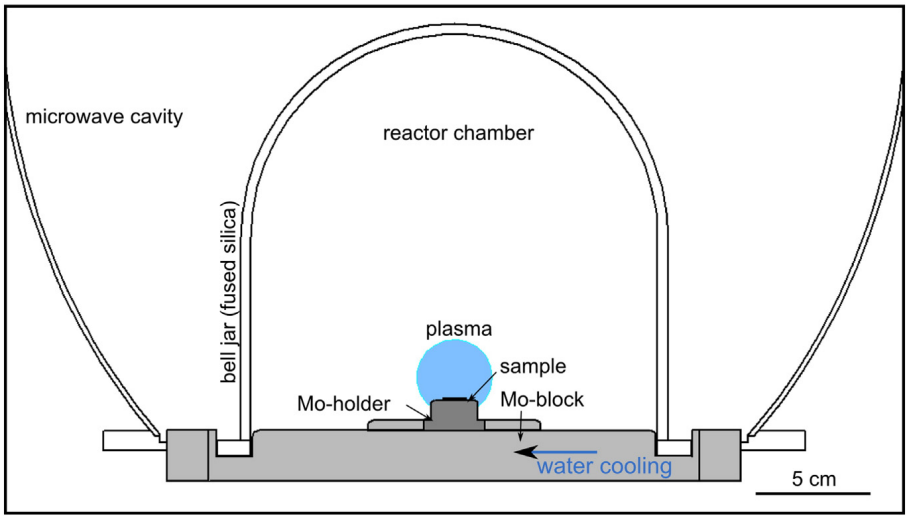

Figure 2.12 Sketch of the microwave plasma enhanced chemical vapor deposition chamber with low cooling set up underneath the molybdenum holder. [61]

SCD deposition was carried out for pressures between 262.5 and 300 Torr in a gas mixture containing 10 sccm CH_4 and 290 sccm H_2 and no nitrogen addition. This corresponds to 3.45 % CH_4 in H_2. The reactor was equipped with a 6 kW power supply and up to 3.0 kW of power was used for these deposition experiments. Each deposition run was carried out over 50 hours. Substrate temperatures were measured using a stationary one-color pyrometer Maurer KTR1075-2. It was not reported on how the substrate temperature was kept constant

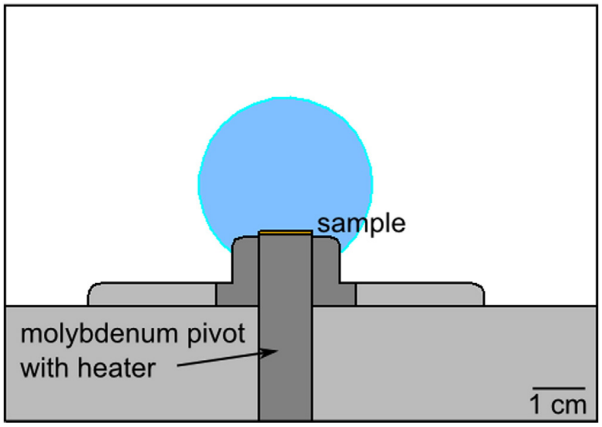

Figure 2.13 Schematic image of the new holder design. The sample is placed on a pivot in the middle of the high holder which can be additionally heated. [61]

versus time during an individual deposition run.

A linear increase of the SCD growth rate with increasing pressure was verified as shown in Figure 2.14. While this was consistent with previous reports using different reactor types [31] [46] it is worth noting that the growth rates reported by Widmann et al. [61] were significantly smaller than reported elsewhere, i.e. the reported growth rate for 262.5 Torr was around 2.3 µm h^{-1} and increased to around 6.7 µm h^{-1}, while Lu et al. [31] achieved growth rates between 26 and 28 µm h^{-1} at 240 Torr, but used a higher methane concentration of 5 %.

While SCD synthesis was demonstrated, it has to be mentioned that the process control was not described in detail and it seems that the process was not closely controlled versus time. A selection of their grown films is shown in Figure 2.15. The SCD surface area of S2 (b) was reduced, which can be contributed to excessive PCD formation on the substrate holder. Additionally, the entire top right corner of the film S3 (c) was missing and it broke off along the {111} direction indicating large amounts of internal film stress. Only sample S1(a) appeared to be of good quality, but it needs to be mentioned that the overall film thickness was only around 115 µm.

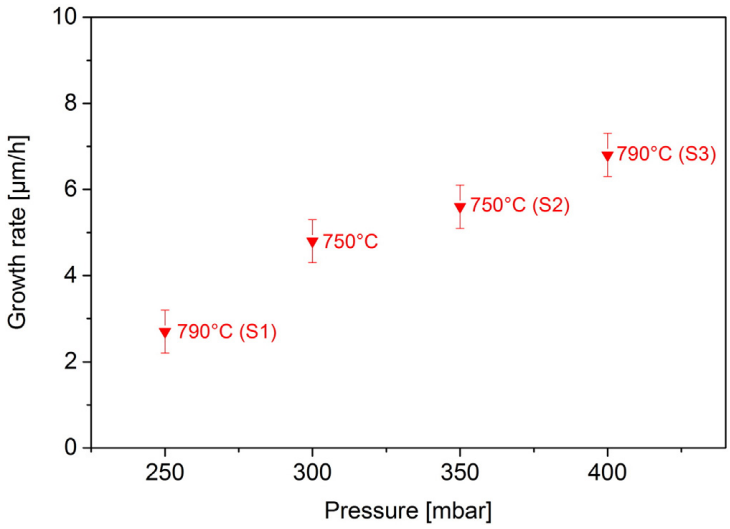

Figure 2.14 Dependence of growth rate on the pressure. For all experiments the microwave power is 3 kW and the methane concentration is 3 %. The average temperature of all experiments is 760 °C. [61]

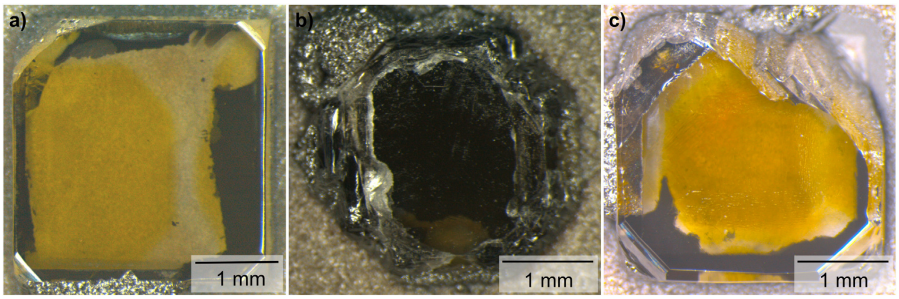

Figure 2.15 Microscopy images of samples S1 (a), S2 (b) and S3 (c). [61]

2.4.2 Carnegie Institute of Washington, Geophysical Laboratory, USA

The diamond efforts of Carnegie Institute of Washington was initially started by Liang, Vohra and Hemley [64, 65]. In more recent years, their research focus was to grow high quality bulk diamond in order to process them into larger brilliant cut anvils. Then, the brilliants were used as anvils for high pressure high temperature earth science experiments.

The last notable publication on SCD synthesis was published by Meng et al. [66]. They reported on the quality of a 13.5 carat SCD diamond block (8.5 mm × 8.5 mm × 5.2 mm in

dimensions), which was subsequently processed into a 2.3 carat brilliant cut diamond anvil. The reported diamond growth pressure range was between 100 and 200 Torr and the reported range of methane concentration was given as between 8 and 22 %, though it can be assumed that the actual deposition conditions were at the lower end of methane concentration. The reported growth rates were around $50\,\mu m\,h^{-1}$.

Figure 2.16 (A) shows the 13.5 carat dimond block and the consecutive processing steps (cleaving (B) and polishing (C). Figure 2.16 (A) shows, that substantial amount of PCD growth occured around the edge of the crystal. It is mentioned, that the crystal is of high quality and no growth steps for the individual deposition runs were visible. A fair amount of residual nitrogen was detectable based on UV/Vis absorption spectra spectroscopy.

Figure 2.16 The picture on the right shows a 2.4 carat single crystal diamond CVD diamond compared with 0.25 carat CVD diamond. Example of the evaluation of CVD diamond single crystal starting with crystal 13.5 carat block (A) to the 2.3 carat cut anvil (D). [66]

2.4.3 Michigan State University, USA

In addition to the recording of the operational field map (see Section 2.3) Lu et al. [31] also increased the SCD growth window to 300 Torr for reactor B and Gu et al. [59] established it for reactor C. An extensive study of the dependency of the SCD growth rate by various input parameters, i.e. pressure and nitrogen concentration, was performed.

Figure 2.17 showed the dependency of the growth rate as function of the pressure for reactor B and C. A clear linear dependency was found throughout the entire pressure range studied (180 to 300 Torr) and were in the range between 25 and 30 µm h^{-1} for a pressure of 240 Torr, a methane concentration of 5 % and without addition of external nitrogen besides residiual traces introduced by impurities in the process gases [67]. Individual deposition runs were limited to 10 to 12 h. SCD growth rates in reactor C were higher than in reactor B under otherwise similar deposition conditions, which was consistent with previous reports [59]. More recent reports on the growth rate in reactor B showed comparable results [68].

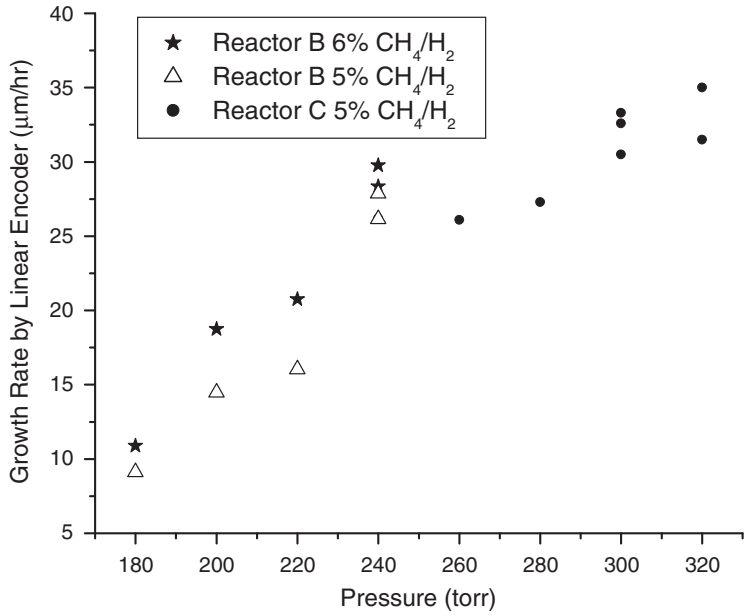

Figure 2.17 Growth rate vs. pressure for different methane concentration for Reactor B (Z_s = −4.5 mm, $T_s \approx$ 1050 - 1080 °C), and Reactor C (Z_s = −4.8 mm, $T_s \approx$ 1000 °C). [31]

Another common concept to increase the SCD growth rate was by adding small amounts of nitrogen into the process gas mixture [69, 70]. Figure 2.18 showed the dependency of the growth rate with the nitrogen content incorporated into the process gases (a) and the crystalline quality of the grown films using Raman spectroscopy (b). The growth rate was increasing linear with the amount of nitrogen available, see Figure 2.18 (a). The addition

of more nitrogen into the gas chemistry resulted in a higher level of nitrogen corporated into the SCD film as demonstrated using secondary ion mass spectroscopy (SIMS). The full-width-half-maximum (FWHM) of the diamond peak in Raman spectroscopy was used to evaluate the crystalline quality of the grown material. The FWHM did not increase significantly when adding moderate levels of nitrogen into the process gas mixture, as seen in Figure 2.18 (b). Nevertheless, the near bandgap optical absorption was increased, which gives nitrogen containing CVD diamonds its typical brown color [71].

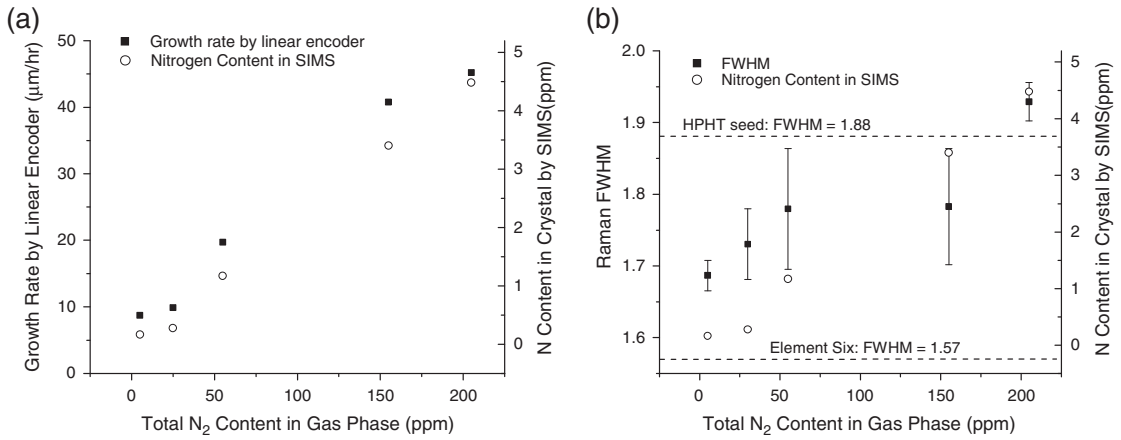

Figure 2.18 (a) Growth rate and nitrogen content in crystal vs. total nitrogen concentration in the gas phas (240 Torr, $CH_4/H_2 = 5\,\%$, $Z_s = -5.7\,\mathrm{mm}$), (b) FWHM and nitrogen content in crystal vs. nitrogen concentration in the gas phase for same samples. [31]

Gu et al. [59] showed how the plasma density is vastly increasing for each new generation of the MCPR. Only the microwave power density is altered when transitioning between reactor generations due to the adjusted holder geometries if the same operating pressure is used. Figure 5 in [59] showed how the growth rate increased when transitioning from reactor A to B and from reactor B to C due to the increased microwave power density.

Nad et al. [67] studied how reactor variables, i.e. variation of the holder layout, influenced the SCD growth and how the formation of PCD on the outer edges could be surpressed. A so called open holder was first used. In a open holder an SCD seed is placed on a flat

substrate holder without any recess. Hence, the diamonds' top surface was exposed to the plasma discharge. At these high growth pressures and discharge power densities, this caused an enhancement of the electric field above the substrate, as seen in Figure 2.19. Note the four edges of the SCD seed in Figure 2.19 (a) appeared brighter, which indicated a higher temperature. This enhancement was promoting PCD growth. This effect became more and more severe as diamond was deposited on the seed crystal. In Figure 2.19 (c) a seed crystal was pre-processed to be grown on its side, which reduced the growth surface area available while being located closer towards the plasma discharge. It can be seen that the plasma had separated from the substrate holder and was completely attached to the diamond seed. This caused the formation of hotspots. The seed crystal effectively shielded off the substrate holder. Figure 2.20 showed the growth of a diamond grown in the open holder geometry at 240 Torr and 5 % CH_4 over a total of 37.5 h. The deposition was carried out using five individual deposition runs. A large PCD rim had formed. The SCD quality in the center appears of high quality and without visible defects, but the smooth SCD surface area decreased by 25 %.

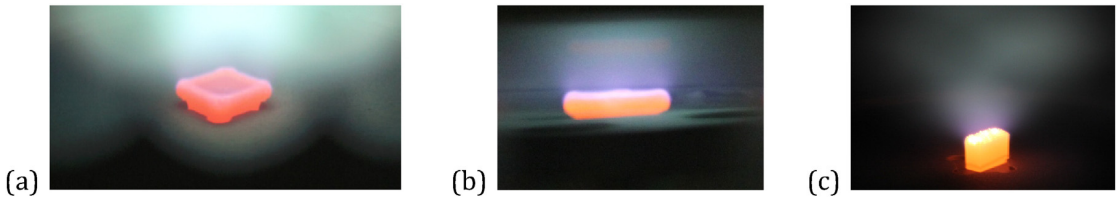

Figure 2.19 (a) An open holder during the growth process and (b) a side view of the discharge substrate boundary layer in the open holder configuration. (c) The discharge and seed substrate boundary layer just before discharge hot spot formation. The discharge clearly is separated from the holder and is concentrated on the top of the seed. [67]

A modified substrate holder (pocket holder) was used to shield the diamond seed from the electric fields and the intense discharge. This was achieved by utilizing a squared recess (pocket) in the center of the substrate holder of the holder with excess width w of 1 mm and depth d of 2.6 mm. The pocket is larger than the SCD dimensions. (Two such pocket designs

Figure 2.20 The seed substrate plus the synthesized diamond after 35.5 h of deposition time. [67]

used in this dissertation are shown in Section 3.1.4.) The substrate is situated completely inside the pocket. This allowed the active species to diffuse down and promote diamond growth on top of the seed substrates' top surface while shielding off the discharge. Figure 2.21 showed a side view of the interactions between the plasma and the substrate holder. The glowing orange was the recessed diamond seed. The plasma formed a uniform boundary layer between the core discharge and the holder providing active species for SCD growth. Figure 2.22 displayed a SCD film that was grown in a recessed pocket holder. The pocket had a depth d of 2.6 mm and the distance between the outer edge of the diamond and the walls of the pocket w was 1.0 mm. Not only was the PCD formation completely suppressed, the SCD top surface expanded and was more than doubled in area.

Figure 2.23 showed the dependency between the amount of SCD area gain (outgrowing) and the overall growth (thickness gain).

Figure 2.24 showed the lateral expansion of SCD material utilizing two growth steps in reactor C. The second growth step utilized a deeper pocket depth d in order to account for the larger thickness of the substrate and ensured that the relative position inside the pocket towards the plasma was the same. The SCD dimensions were expanded from 3.5 mm × 3.5 mm

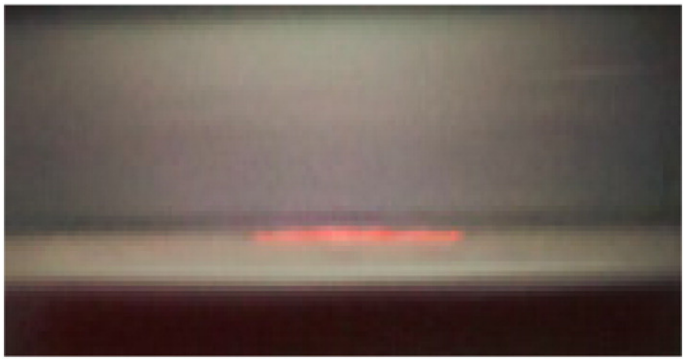

Figure 2.21 A uniform discharge–substrate boundary layer at a 240 Torr pocket holder SCD synthesis process. [67]

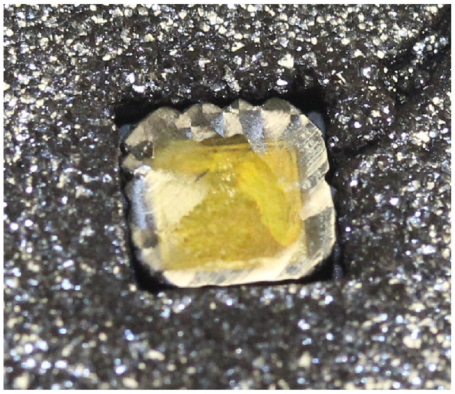

Figure 2.22 A close up view of the synthesized SCD grown in a pocket holder with d = 2.6 mm and w = 1.0 mm and with the adjacent PCD layer on the substrate holder. [67]

to 5.73 mm × 5.88 mm, an increase in SCD surface area by over 2.5 times.

Nad et al. [72] expanded on the study of rimless growth using an adjusted pocket design. The width remained the same with w = 1.0 mm, but the pocket depth was slightly reduced to d = 2.3 mm moving the top surface 300 µm closer to the plasma. Rimless growth was verified using this updated holder design. Figure 2.25 compared the reported SCD area increase with the updated holder design (the yellow, blue and red data point) with the previous results. While both data sets lined up quite well, it can be seen, that the area gain using the more shallow pocket was slightly shifted, i.e. more area gain within the same amount of vertical growth was achieved. Figure 2.26 showed a close-up SEM image of the outgrown SCD area.

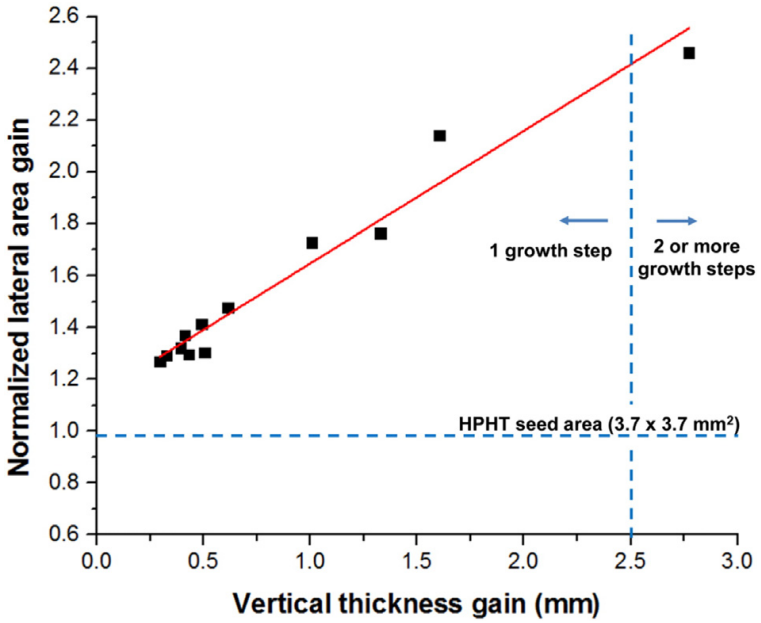

Figure 2.23 Plot of normalized lateral CVD area gain vs. vertical thickness gain for CVD substrates. The dotted line indicates the HPHT seed surface area. [67]

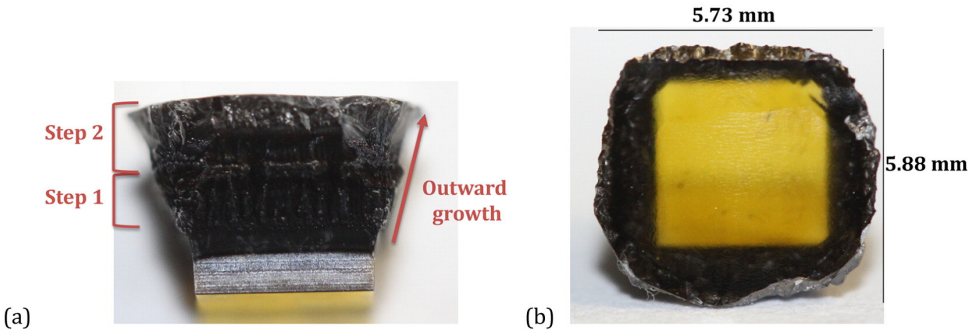

Figure 2.24 (a) Lateral expansion of the CVD growth for a 2 step as grown substrate (b) ≈ 2.5 times expansion of the final CVD substrate over the HPHT surface area. [67]

The outgrown material is truly SCD and of high quality, while different growth directions, i.e. {110} and {111}, were present. The top surface of the grown SCD was smooth, even on the outgrown area.

Nad et al. [68] studied the crystalline quality of the crystals grown using the optimized pocket holder design introduced in [67]. One of the observations was, that terrace growth occurred. The terraces were directed from the center towards the edges and corners. This was related to the spherical discharge being centered on top of the seed crystal resulting in a

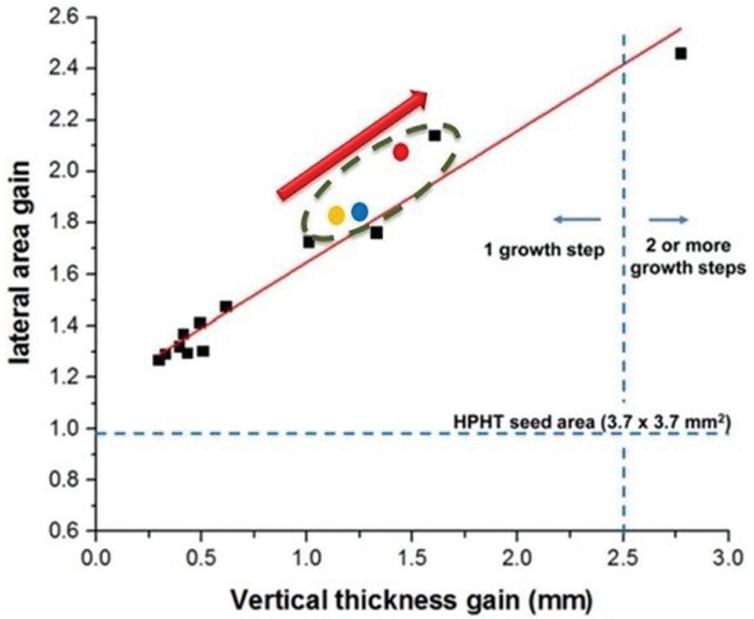

Figure 2.25 Outward growth of the CVD SCD substrates. [72]

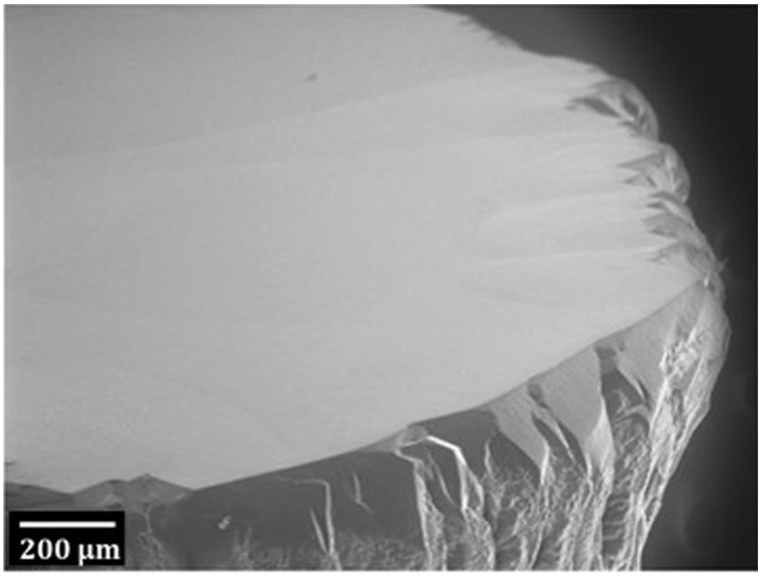

Figure 2.26 SEM image indicating PCD rim free CVD SCD substrate. [72]

slightly enhanced growth rate in the center. An AFM analysis of the terraces was shown in Figure 2.27. The individual terrace height was between 400 and 600 nm and had a width of $\approx 7\,\mu m$.

The nitrogen concentration was evaluated by SIMS and found to be between 88 and 97

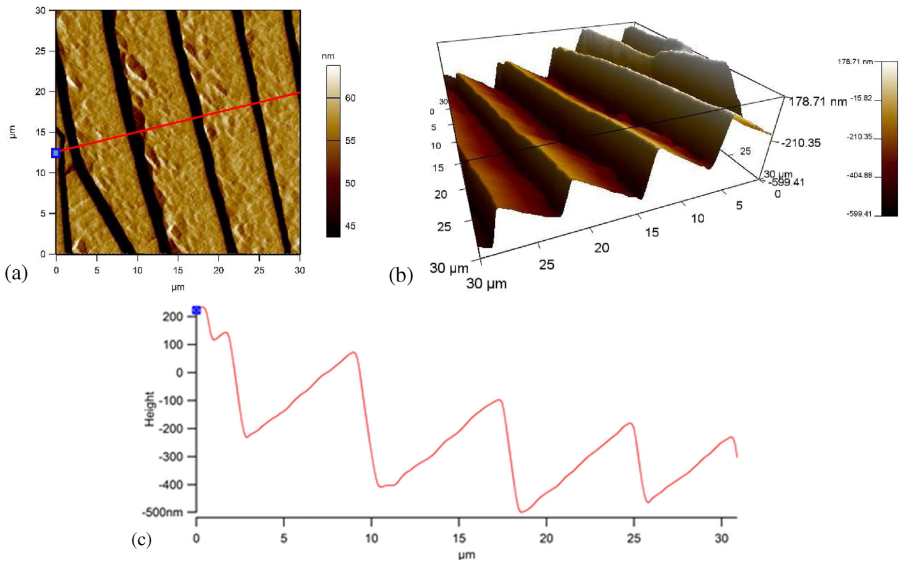

Figure 2.27 Atomic force microscopy analysis of an as-grown SCD substrate surface. (a) 2D AFM image, (b) 3D AFM image to display the growth steps, and (c) surface profile and roughness (R_a = 263.3 nm) of the red line shown in (a). [68]

parts per billion (ppb). This was verified by UV/Vis absorption spectroscopy, which showed a near bandgap absorption below 2 cm^{-1} [67].

Birefringence imaging was performed on a SCD film grown on a seed crystal, which had an angled top surface so that one side was forced to grow outside of the pocket to introduce a PCD rim. Birefringence images for increasing exposure times were shown in Figure 2.28. It can be seen, that the center of the substrate remained stress free, while the outer SCD areas showed moderate amounts of stress. The interesting fact was, that the left edge showed high amount of stress. The left edge was the side, where PCD was grown purposefully showing that PCD formation introduced crystalline stress,

Etch pits were created by exposing the film to a pure hydrogen plasma at 240 Torr for one hour. When a defect was present, the hydrogen plasma etched the surrounding area resulting in a pyramidal etch pit. Hence it was possible to determine the defect density through etch pits. Details on the etch pit formation mechanism were previously reported by Naamoun et

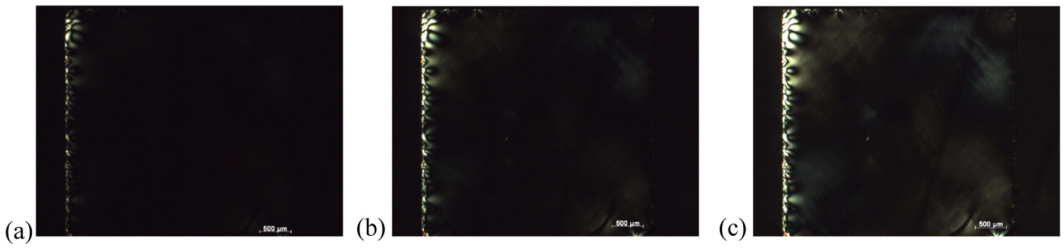

Figure 2.28 Birefringence images of a 221 µm thick CVD SCD plate with exposure times of (a) 500 ms (b) 2000 ms and (c) 5000 ms. [68]

al. [73].

Figure 2.29 shows the distribution of etch pits on a commercially available type Ib HPHT crystal without any further pre-treatment. It was shown that the etch pits had a non-uniform distribution. Some etch pits were distributed across the surface, but the majority of etch pits were aligned along polishing lines. It was assumed that polishing lines were introducing subsurface damage, which promoted the formation of etch pits and defects.

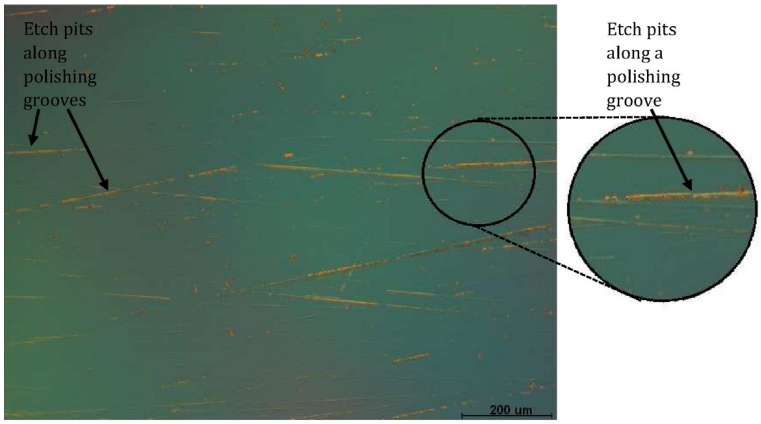

Figure 2.29 Etched surface of a representative type Ib HPHT seed. [68]

Etch pit densities were found to be in the region of $1.4 \times 10^5\,\mathrm{cm}^{-2}$ for HPHT crystals and were reduced to $3.7 \times 10^3\,\mathrm{cm}^{-2}$ for CVD grown films. Visualization of the distribution of etch pits on CVD grown films found that the etch pits appeared to be preferentially found near the edge of individual growth steps. Similar observations were made for films grown using heteroepitaxy [74, 75].

2.4.4 Recent results from LIMHP - CNRS, France

Recent work at LIMHP - CNRS was focused on substrate engineering to achieve a reduction in the defect density of the CVD grown diamond material. This has been achieved throughout three different approaches:

2.4.4.1 Pyramidal shaped substrates

Tallaire et al. [76] polished conventional {100}-oriented HPHT seed crystals into pyramidal shaped substrates with angles between 10 and 30°. The concept was inspired by the findings of Bauer et al. [77], who showed that it is more energetically favorable for dislocations to follow the <110> direction, if the off-axis angle is more than 10° towards the <100> direction. The schematic of two different realizations of pyramidal substrates were shown in Figure 2.30.

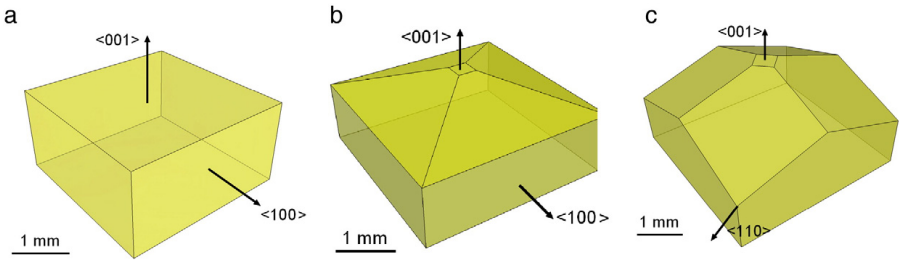

Figure 2.30 Schematics of the initial diamond substrate before polishing (a) and of substrates polished into a pyramidal-shape (b) type A, 20° {100}-misoriented, (c) type B, 20° {110}-misoriented. [76]

SCD growth was performed using 5 % methane and an absorbed power density of 100 W cm^{-3} (this corresponded to a process pressure of ≈ 180 Torr [70]). The overall concept is, that lateral growth in the <110>, <111> and <113> orientations were occurring simultaneously with the vertical growth in the <100> direction. The progress of the lateral overgrowth for increasing vertical film thickness was shown in Figure 2.31. Successful overgrowth was demonstrated, but in order to recover the entire surface area as much as 1.75 mm of vertical

growth was required for an misorientation angle of 30° along the <110> direction.

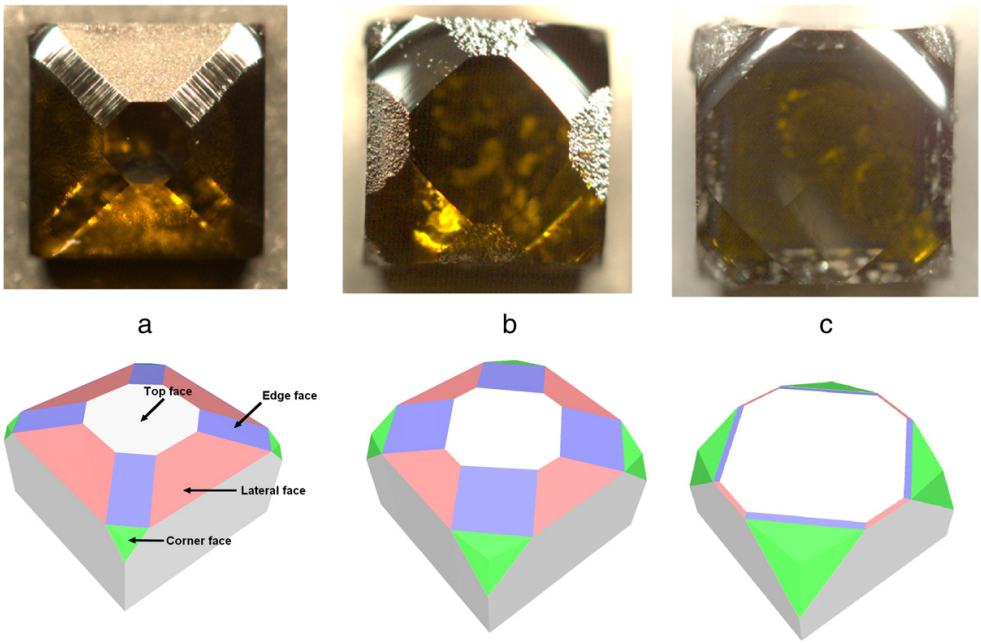

Figure 2.31 Optical images and 3D representation of the sample grown onto 20° {100}-misoriented pyramidal-shape substrates after several growth interruptions. The total thickness of the CVD layer is (a) 90 µm, (b) 270 µm, (c)500 µm. [76]

Etch pit analysis was performed to verify a reduction in defect density. Results were shown in Figure 2.32. It was shown, that the center part has the highest etch pit density. This corresponded to the area, which was unaffected by the off-axis engineering. Hence, the formation of dislocations was not suppressed. The successful reduction of dislocations everywhere else was clearly visible.

2.4.4.2 Self-assembling platinum masks

Naamoun et al. [78] used platinum nanoparticles to selectively mask of existing defects in order to prevent them from propagating. The schematic procedure was illustrated in Figure 2.33. First, defects were revealed by applying an H_2/O_2 plasma to open up etch pits. Afterwards, a 30 nm thick layer of platinum was deposited using MOCVD. Then, thermal

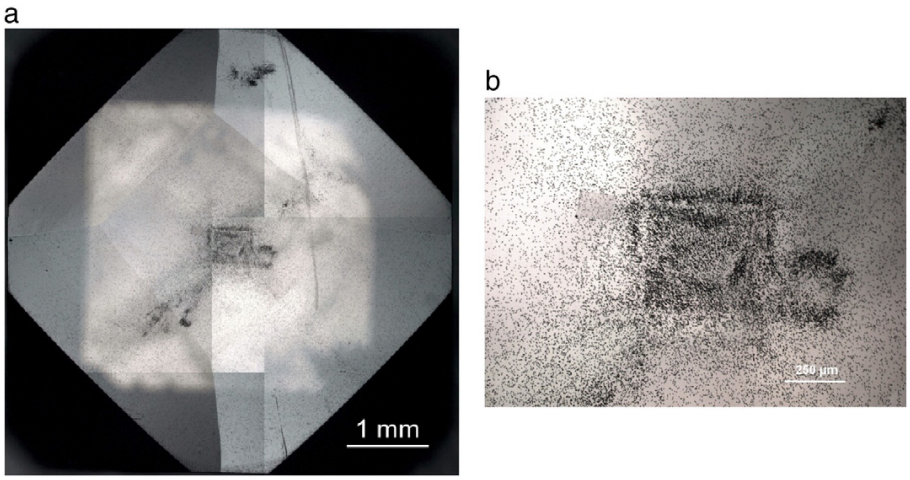

Figure 2.32 (a) Image of a 750 µm-thick CVD film grown onto 20° {100}-misoriented pyramidal-shape substrate after plasma etching to reveal dislocations. (b) Magnified area in the centre illustrating that there is a central square with a much higher etch-pit denisty. [76]

annealing in a H_2 plasma was carried out to form nanoparticles in the etch pits, hence selectively masking them. CVD growth on the masked material was carried out and another etch pit analysis was carried out to evaluate the impact of the platinum mask.

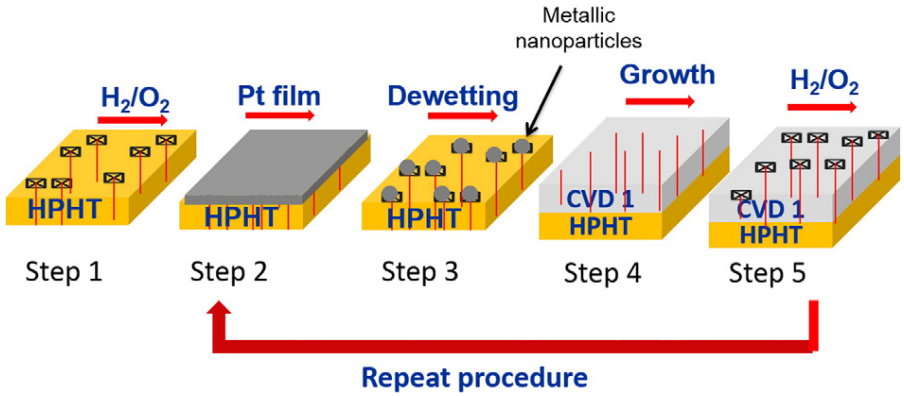

Figure 2.33 Procedure used to selectively mask substrate defects with metallic nanoparticles in an attempt to decrease dislocation densities. Step 1 aims at revealing extended defects at the crystal surface by an adapted etching treatment. Step 2 is the coating of the surface by a thin CVD platinum film. Step 3 is a thermal treatment so that nano-particles self-assemble to the etch-pits on the surface. Step 4 is the PACVD diamond overgrowth to embed Pt particles. Step 5 is a final etching treatment to reveal and count extended defects. The full process can be repeated several times to improve its efficiency as illustrated by the red arrow. [78]

Figure 2.34 showed the experimental procedure adapted by Naamoun et al. [78] to

evaluate the efficiency of the selective masking of defects using platinum nanoparticles. Three consecutive growth steps of 80 µm each were performed on a test sample, which was masked off in between steps and an unprocessed reference samples.

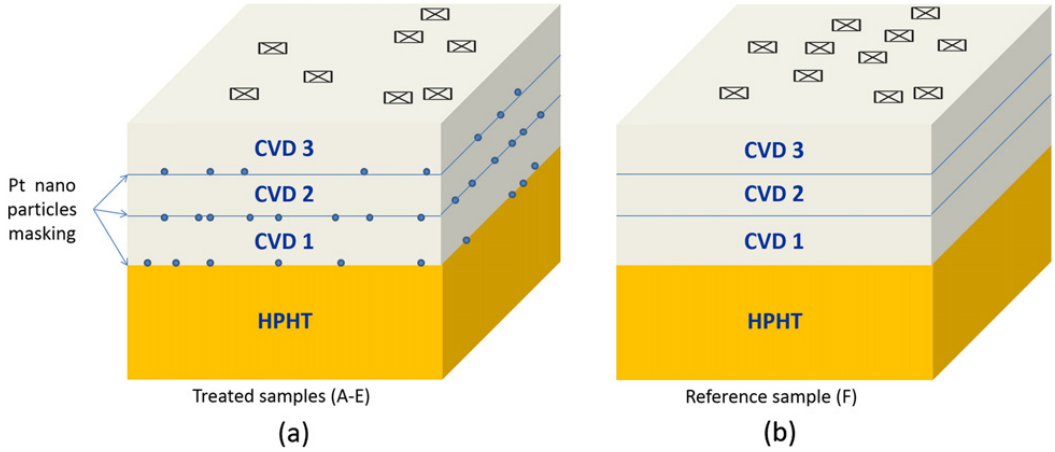

Figure 2.34 Schematic representation of the experiments carried out which consist of 3 successive growth runs with a thickness of about 80 µm. (a) Samples A to E were etched and masked with metallic nanoparticles at each step following the procedure described in Figure 2.33. (b) The reference sample F was etched but not masked coated with Pt. Finally a short etching run aiming at revealing dislocations was performed leading to the appearance of etch-pits at the surface. [78]

Results of the experiment were shown in Figure 2.35. It is well known, that already existing dislocations in the seed crystal will propagate further into the CVD grown material and that almost all of the new dislocations are formed in the interlayer between the seed and the newly grown material [79, 80]. This was verified in the behavior of the untreated reference sample, where the defect density was increasing for every consecutive growth step. The initial etch pit density was $\approx 1 \times 10^6\,\mathrm{cm}^{-2}$ and increased to $\approx 6.5 \times 10^6\,\mathrm{cm}^{-2}$. In contrast, the etch pit density for the masked CVD films decreased and consolidated at $\approx 5 \times 10^5\,\mathrm{cm}^{-2}$. The vastly reduced etch pit density for the film masked with platinum nanoparticles was visually verified in the optical images of Figure 2.35. The use of platinum nanoparticles seemed a good method to limit the propagation of defects, but its effectiveness seemed to be

limited due to the formation of some new dislocations during consecutive growth steps.

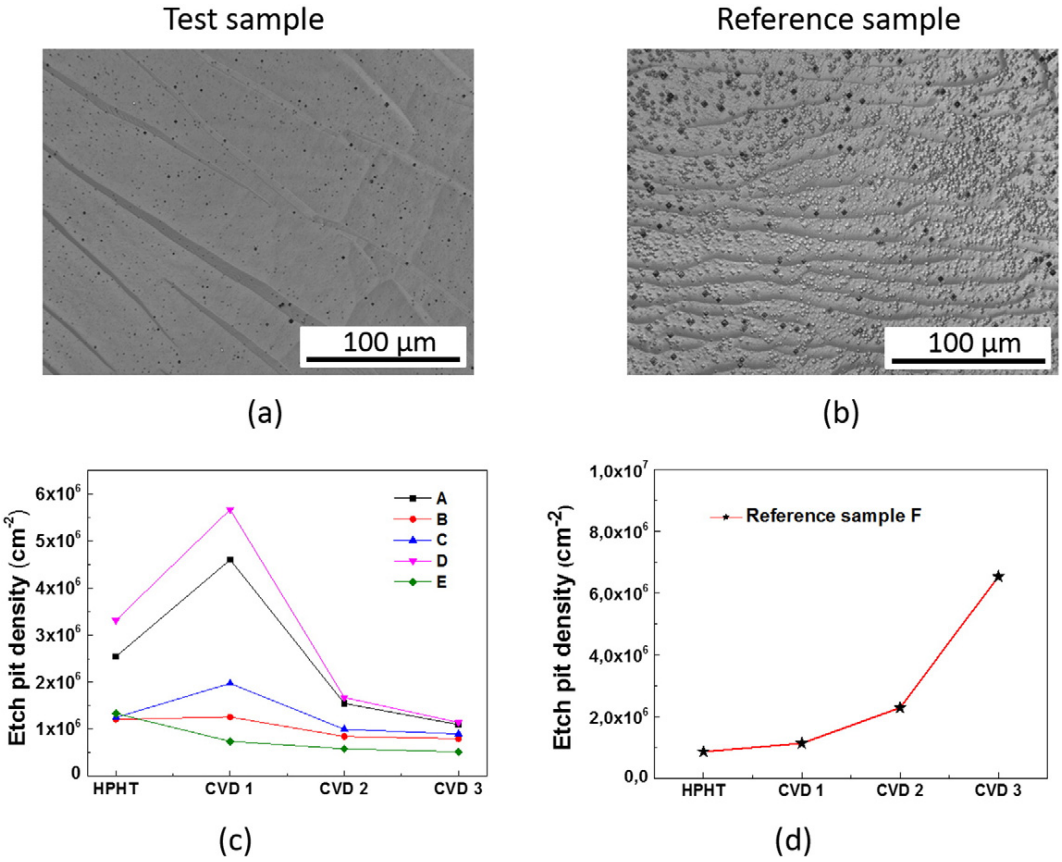

Figure 2.35 Laser microscope image of the surface of the CVD layers after 3 successive growth and etching to reveal dislocations for (a) one of the samples that underwent the masking procedure, (b) the reference sample with no masking. The evolution of etch-pit density averaged on the sample surface after each treatment is also reported for the test sample (c) and for the reference sample (d). [78]

2.4.4.3 Lateral growth over a macroscopic hole

Tallaire et al. [81] modified the concept of the pyramidal seed substrates and demonstrated SCD deposition and overgrow using a diamond seed with a macroscopic hole. The schematic concept of the hole and the lateral overgrowth were illustrated in Figure 2.36. Similar to the use of pyramidal substrates, the lateral overgrowth was deflecting defects. Defect propagation into the CVD grown film occurred only on top of the initial seed frame as illustrated in

Figure 2.37, where the black lines illustrated the propagation of defects.

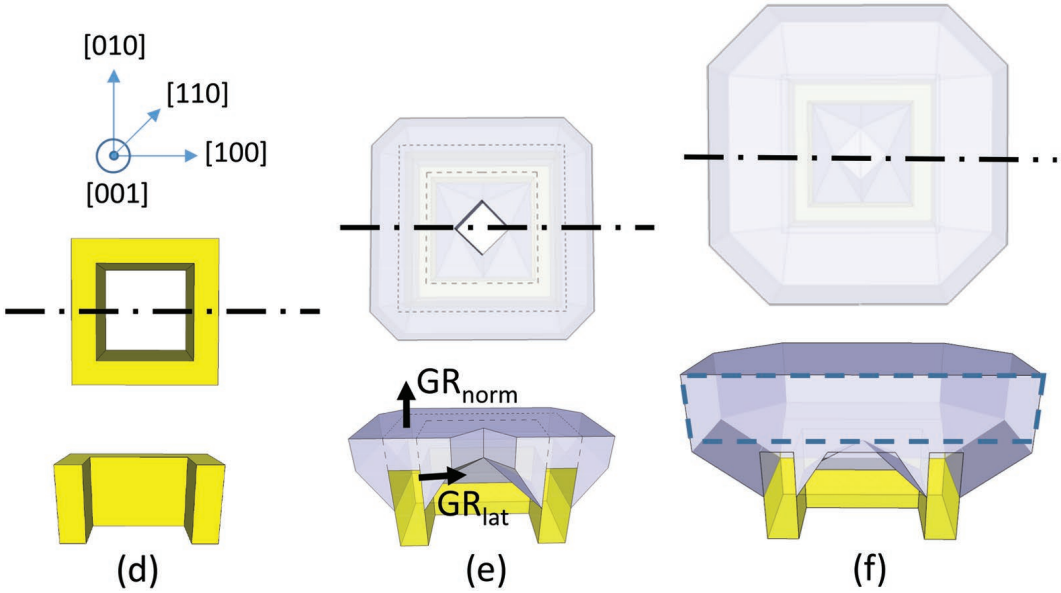

Figure 2.36 Thick CVD diamond layer grown on a HPHT diamond substrate hollowed out by a large hole. Top-view and cross-section schematics illustrating the growth of the CVD layer (blue) on the HPHT substrate (yellow) at the d) beginning, e) before, and f) after merging of the growth fronts and disappearance of the hole. The blue dotted square indicates the full CVD plate that can be retrieved from the sample. The crystalline directions are indicated for the top-view. [81]

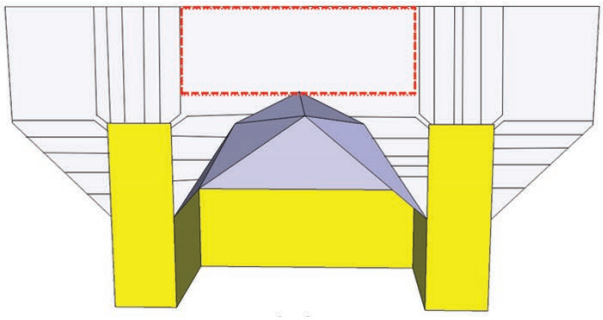

Figure 2.37 Schematics illustrating the observed propagation direction of dislocations (yellow: HPHT, blue: CVD, red square: dislocation-free area). [81]

The reduction of defects using a seed with a macroscopic hole were quantified with etch pit analysis. The SCD grown over the original frame area had a much higher etch pit density to a point where the frame dimensions were indentifiable by the etch pit distribution as shown in Figure 2.38. The defect density in the center (Figure 2.38 c) was found to be $2 \times 10^3\,\mathrm{cm}^{-2}$.

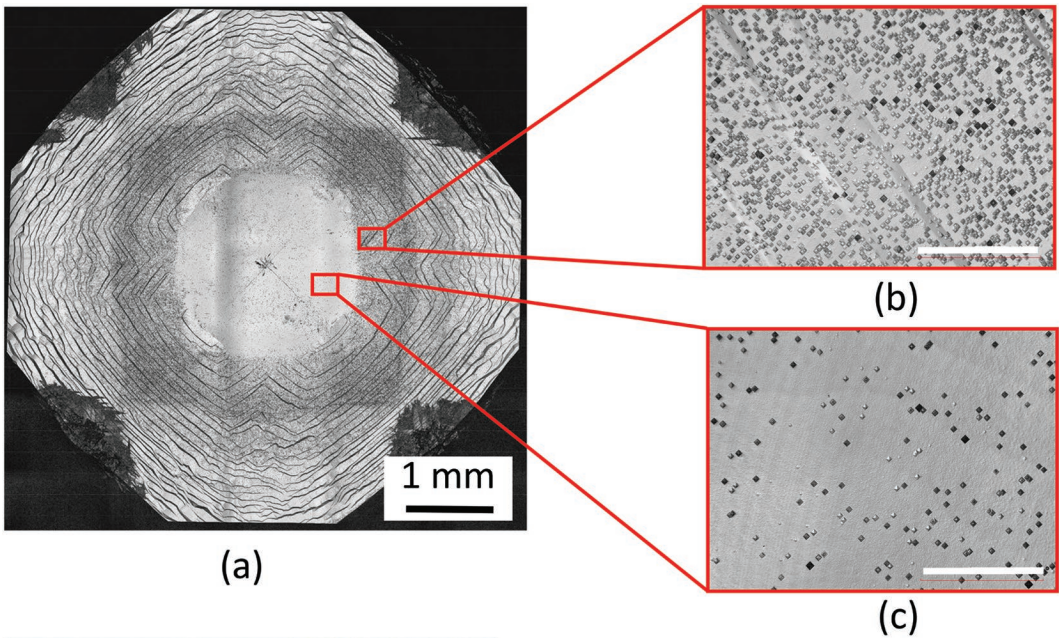

Figure 2.38 Laser microscope images of the CVD film grown on a HPHT substrate with a macrohole after plasma etching to reveal dislocations: a) full-size image showing the underlying square substrate, b,c) zoomed into the regions above the substrate and above the hole, respectively. Scale bars are 100 µm. [81]

The use of pyramidal shaped seed crystal resulted in a smaller area with high defect density due to vertical growth compared to the use of a seed with a macroscopic hole. Unfortunately, this small area was in the center of the grown film, while it was on the outside areas in the approach using a macroscopic hole. Additionally, the effort of making pyramidal shaped seeds using mechanical polishing required much more effort than making a seed with macroscopic hole, which only required laser cutting. It seems, that a combination of both approaches, i.e. first using the macroscopic hole, then using a pyramidal shape to eliminate the remaining defects from the initial frame, could result in a uniform reduction of defect density.

2.4.5 Prokhorov General Physics Institute Royal Academy of Science, Russia

The Prokhorov General Physics Institute, Royal Academy of Science is using a ARDIS-100 MPCVD reactor from Optosystems with a 5kW power supply [82]. The dielectric window in this reactor design is below the substrate holder in order to separate the quartz from the discharge region.

Bolshakov et al. [83] studied diamond deposition in gas mixtures with high methane concentrations resulting in soot formation. The operating pressure was 130 Torr without argon addition and 200 Torr when 20 % argon was added. Substrate temperatures were between 950 and 980 °C. Methane concentrations studied were between 2 and 18 %, both without and in the presence of 20 % argon. Overall flow rates were 500 sccm without, and 625 sccm, with argon addition. When increasing the methane concentration the formation of soot starts to form between 6 and 10 % methane. The optical image of such a sooty plasma was shown in Figure 2.39. The dominance of the orange soot corona was clearly detectable. The addition of argon was necessary as the formation of high amounts of soot caused the plasma to become unstable in a pure $CH_4/H/_2$ plasma.

The growth rate a function of the methane concentration without and with the presence of argon was studied and resulting growth rates for methane concentrations between 2 and 15 % were shown in Figure 2.40. Growth rates up to 105 µm h^{-1} were reported. The growth rate was increasing with increasing methane concentration as expected. Additionally, it was shown that the growth rates with argon addition were more than doubled. It was demonstrated before that the addition of 20 % and more of argon was an efficient way of increasing the growth rate [84]. The process pressure was simultaneously increased by 50 % when the argon

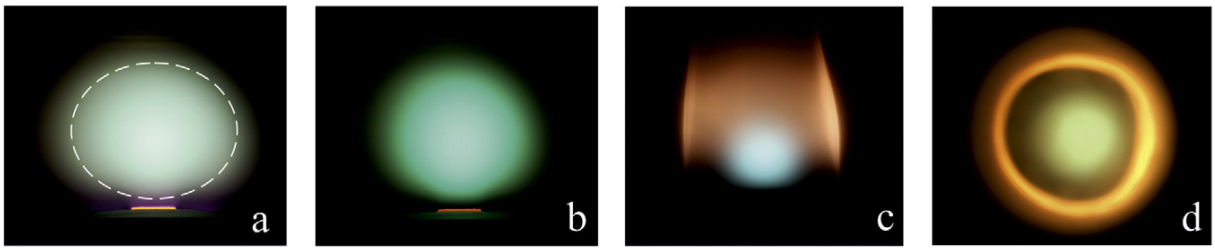

Figure 2.39 Photographs of plasma in CH_4/H_2 gas mixture (a) and in CH_4/H_2/20 %Ar mixture (b,c,d) with methane content of 4 % (a,b) and 15 % (c,d). The other process parameters are: microwave power P = 3.0 kW, pressure p = 130 Torr, total gas flow rate 500 sccm in CH_4/H_2 mixture (a), and 3.0 kW, 200 Torr, 625 sccm in CH_4/H_2/20 %Ar. The orange emission from soot is seen in side-view (c) and top-view (d) of the same plasma cloud. The white dashed elliptical contour in image (a) denotes half maximum brightness level used to measure the plasma volume and MW power density (300 W cm^{-3} for the particular regime). [83]

series was recorded by Bolshakov et al. [83]. Hence, the independent effects of the argon addition and the pressure increase are impossible to quantify.

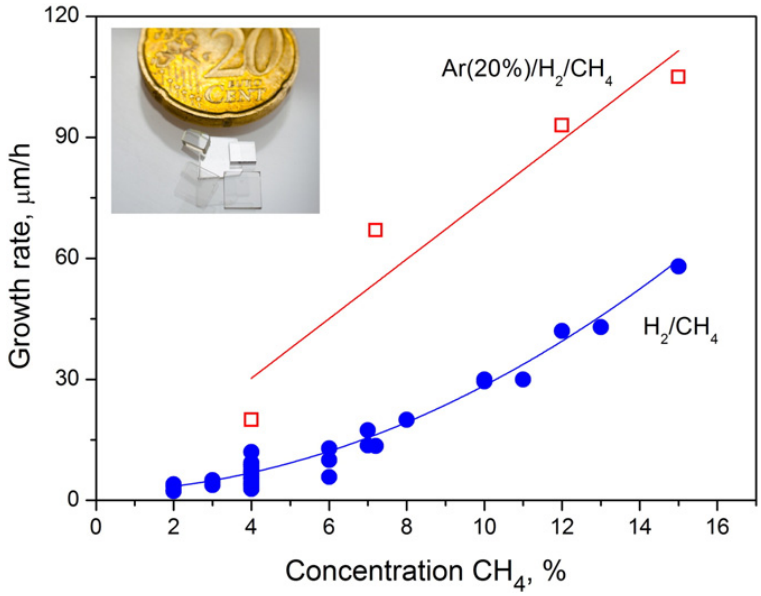

Figure 2.40 Dependence of the growth rate for SC diamond as function of the methane concentration in gas mixtures CH_4/H_2 at 130 Torr, 500 sccm (circles) and Ar (20 %/CH_4/H_2 at 200 Torr, 625 sccm (squares). Inset: a collection of SC CVD diamond plates separated from the substrate and polished. The lines are guides for eye. [83]

The growth of high quality SCD material was demonstrated. The inset of Figure 2.40 showed several free standing CVD plates with thickness up to 1 mm, which appeared optically

transparent and colorless. Raman spectroscopy showed FWHM values of the diamond peak of $1.8\,\mathrm{cm}^{-1}$ verifying high crystalline quality [31]. Anyway, it was reported that the crystalline quality decreases for increasing methane concentrations, particularly for 18 %.

One key limitation, which was not discussed in great detail by Bolshakov et al. [83], was the excessive formation of soot when operating the reactor in a sooty regime, i.e. they reported that over a deposition period of 1.5 h a total growth of 100 µm SCD material was achieved, but at the same time 250 µm of soot formed on the substrate holder and the chamber walls. The excessive amount of soot formation is a limiting factor of how long the reactor can be operated before soot is overgrowing onto the seed, as well as soot flakes falling off the walls and holder onto the seed. This limiting factor can been identified in their report of how the thick SCD plates were grown: They report on individual growth times of 100 h. This corresponds to much more modest growth rates of $10\,\mu\mathrm{m\,h}^{-1}$. Based on Figure 2.40 growth rates of $10\,\mu\mathrm{m\,h}^{-1}$ can already be achieved with methane concentrations of 5 % without the addition of argon. This means, that the reactor was operated in a non-sooty regime when bulk plates and high quality material was grown and the sooty regime does not seem suitable for long time deposition experiments.

Bushuev et al. [85] equipped the reactor used by Bolshakov et al. [83] with a Michelson interferometer, which allowed to monitor the diamond thickness in situ using laser interferometry. This allowed to get feedback on the growth rate while diamond deposition was carried out, but also on the reactor dynamic, i.e. how long is the time interval between an input parameter is changed and the growth rate was adjusted accordingly.

The SCD growth was performed at a process pressure of 130 Torr and a total flow rate of 500 sccm. Using an incident power level of 3.0 kW resulted in a substrate temperature of 930 °C. The methane concentration was varied between 8 and 17 %. Figure 2.41 showed

the development of the SCD thickness throughout their entire study, where a total of 82 µm of diamond was grown. When the methane concentration is increase the growth rate was stabilizing within a few minutes and remained constant afterwards as shown in Figure 2.41 (b).

Figure 2.42 replotted the growth rate determined in Figure 2.41 and illustrated it as a function of methane concentration. A linear increase of the growth rate with increasing methane concentration was measured. Additionally, the inset in Figure 2.42 showed an optical photograph of the interaction between the plasma discharge and the seed crystal. The formation of a boundary layer between the discharge core and the substrate was detectable.

Analogous to increasing the methane concentration Figure 2.43 studied the dynamic reactor behavior when the methane is turned off at the end of an ongoing growth experiment. Bushuev et al. [85] found that diamond growth at a much lower rate occurred for around 10 min before the overall diamond thickness started to decrease linearly indicating removal of diamond by H_2 plasma etching. Their anticipated etch rate was 432 nm h^{-1} based on an etching duration of 17 min.

Bushuev et al. [86] utilized the previously introduced in situ measurement of the growth rate using a Michelson interferometer [85] to perform an in situ field mapping of the multi variable input parameter space for SCD deposition. The process pressure was 130 Torr. Methane concentrations were varied between 1 and 13 %. Substrate temperatures were between 850 and 1100 °C. Input power levels were between 1.8 and 3.3 kW to regulate the substrate temperature.

Figure 2.44 showed the dependency of the growth rate from the methane concentration for a fixed substrate temperature. It was shown that the growth rate increased linear with the increase of methane. Figure 2.45 reversed the correlation of Figure 2.44 by analyzing

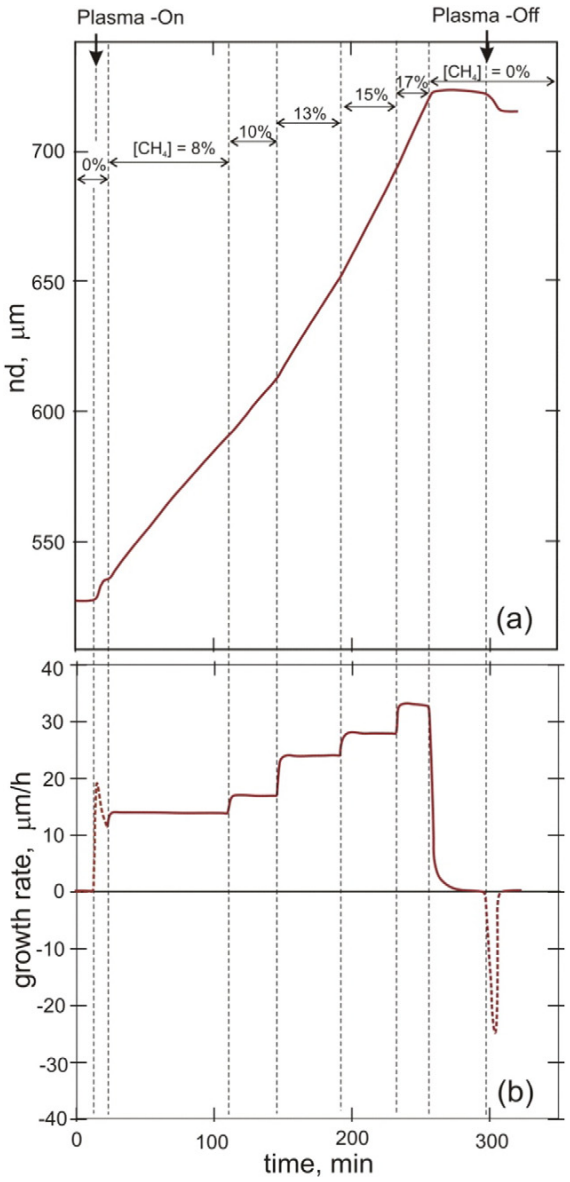

Figure 2.41 (a) Dynamics of optical thickness nd of diamond sample vs deposition time with stepped changes in CH_4 content. The moments of plasma On and Off are indicated by bold vertical arrows. The time intervals of the fixed methane flow are separated by vertical dashed lines, and the respective CH_4 percentage in H_2 is indicated by horizontal arrows. The sample is cooled down to R.T. after switching off the plasma. The signals before the CH_4 adding and after plasma switch off correspond to the temperature dependent nd changes only, without any diamond growth. (b) Growth rate vs deposition time calculated by differentiation and smoothing of the measured curve nd (t). The dashed lines at the start (end) of the kinetics reflect the heating (cooling) processes. [85]

the dependency of the growth rate from the substrate temperature for a fixed methane concentration. The maximum growth rate for a methane concentration of 1 % was found to

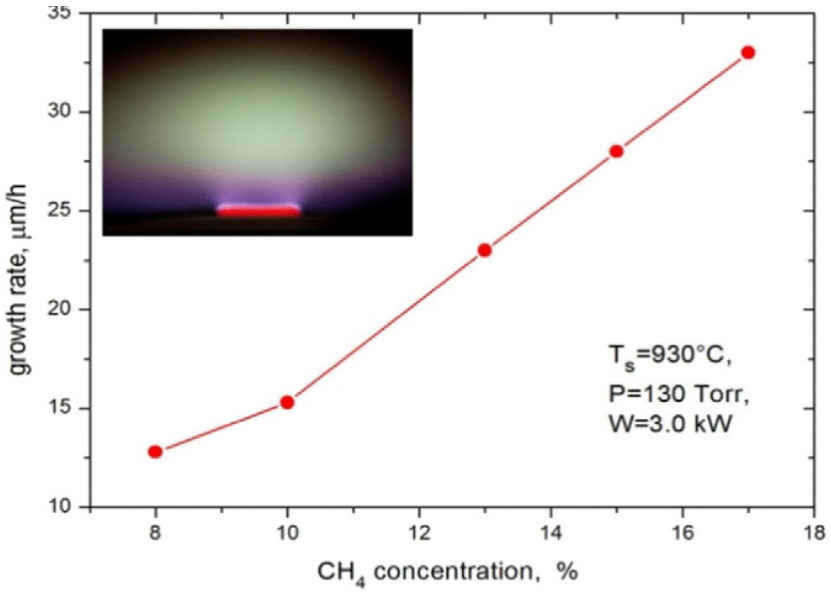

Figure 2.42 In situ measured diamond growth rate vs. CH_4 percentage in H_2-CH_4 mixture. Inset: a photograph of the substrate (red) and plasma cloud in the course of diamond growth. [85]

be below 800 °C and increased to 950 °C for 4 % CH_4. On the other hand, it was observed, that the growth rate kept increasing with increasing substrate temperatures were 7 % and higher. Additionally, the slope of the growth rate increase increased with CH_4 concentration. This is in accordance with Lu et al. [31] who found, that the optimum substrate temperature, which resulted in the highest growth rate, is a function of the methane concentration at a given pressure and increases with the methane concentration.

The dependence of the growth rate from the substrate temperature became especially critical for low methane concentrations, i.e. 1 %, where Bushuev at al. [86] reported that the diamond was actually etched.

Additionally, Bushuev et al. [86] introduced a different method of estimating the discharge volume and microwave power density. They took an optical image of the discharge using a H_α filter to only record the emission of atomic hydrogen as shown in Figure 2.46. Then, intensity analysis of the image was performed and 50 % of the maximum H_α was defined as

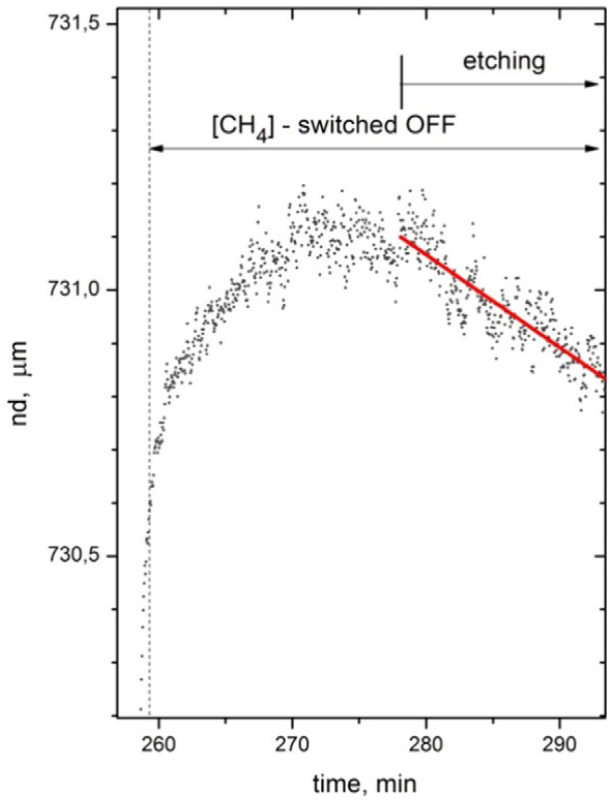

Figure 2.43 The diamond optical thickness nd vs time at the end of the growth process. The dashed vertical line at t = 259 min shows the moment of shut down of the CH_4 flow. The reduction in nd indicates diamond etching. The straight red line is the linear least square fit, determining the etch rate. [85]

the boundary of the plasma. Then, the plasma volume was calculated using an elliptical approximation.

Absorbed power densities were calculated by dividing the experimental absorbed power level with the discharge volume estimated using the image analysis as described in Figure 2.46. The results were plotted in Figure 2.47. Overall absorbed power densities were found to be between 250 and 450 $\mathrm{W\,cm^{-3}}$. The absorbed power density decreased with increasing overall absorbed power levels as well as with increased methane concentrations.

Overall the work of Bushuev et al. [85, 86] has a promising potential of optimizing the feedback loop with respect to growth conditions by monitoring the diamond growth in situ using a Michelson interferometer instead of determining the growth rate after a multiple

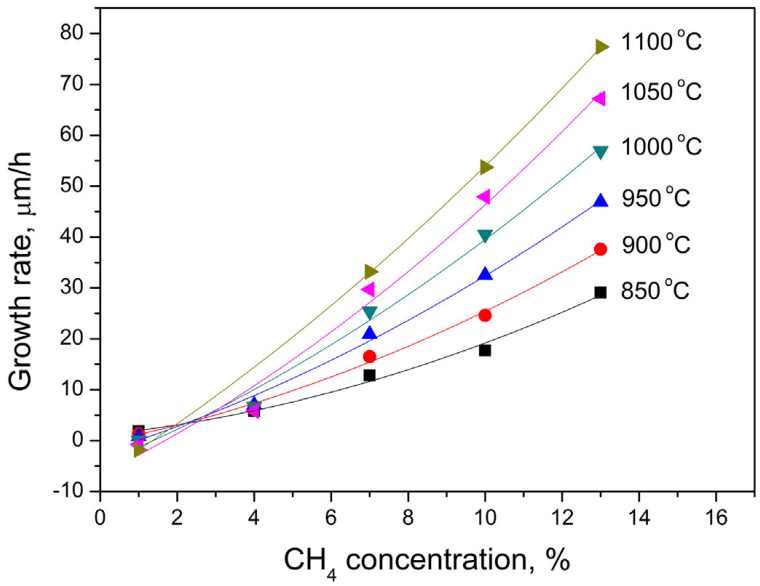

Figure 2.44 Dependence of the growth rate on methane concentration in gas at different substrate temperatures. [86]

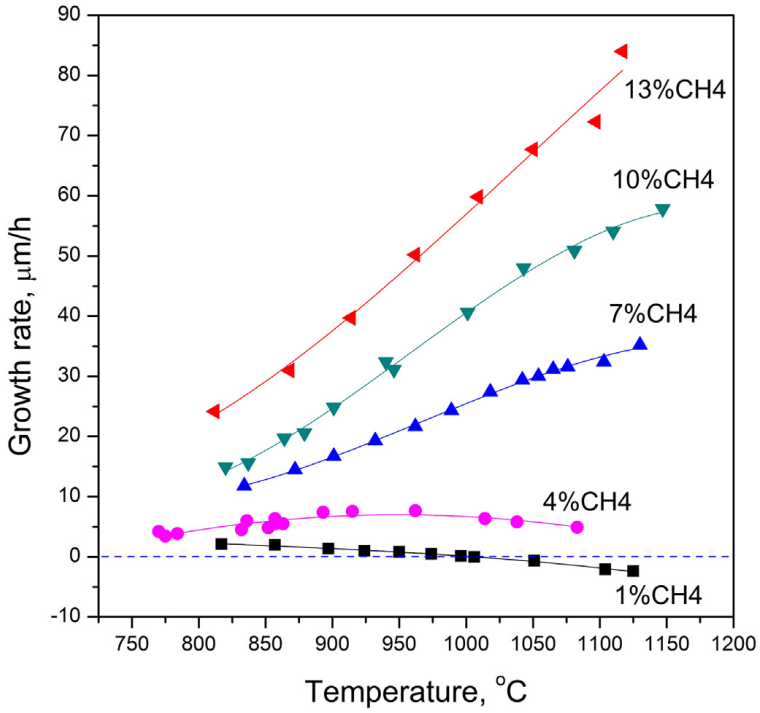

Figure 2.45 Dependence of growth rate on substrate temperature G(T) at different CH_4 contents in gas mixture. Note the net etching for 1 % CH_4 at T_s>1000 °C. [86]

hour deposition process. While it is of academic interest, to demonstrate and evaluate the diamond growth in a sooty regime [83] it remains questionable about how applicable those

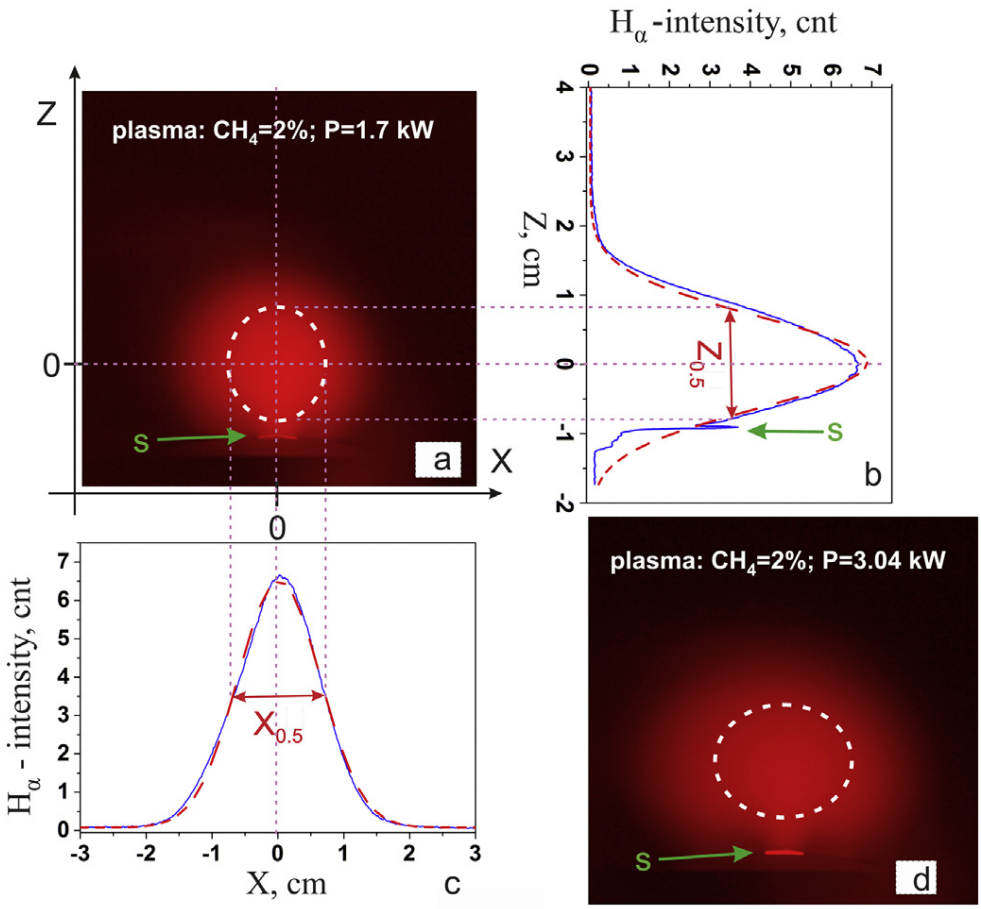

Figure 2.46 Photo of the plasma through H_α-filter (a) and (d) at different growth parameters (CH_4 = 2 %, P = 1.7 and 3.04 kW, respectively). Appropriate profiles of H_α-intensity for photo (a) i shown in X and Z direction shown by blue lines on (b) and (c); dashed red lines on the profiles denote Gaussian fits. While dashed ellipse on (a) and (d) shown area where H_α-intensity is equals to 0.5 x $I(H_\alpha)_{max}$. Green arrows on images and profile (d) indicate substrate position. [86]

conditions are in the deposition of bulk diamond films or if a non-sooty regime will be required, where an increase of the process pressure would be a more promising approach. Additionally, SCD growth at such high methane concentrations will need further in-depth analysis of the crystalline quality and defect density.

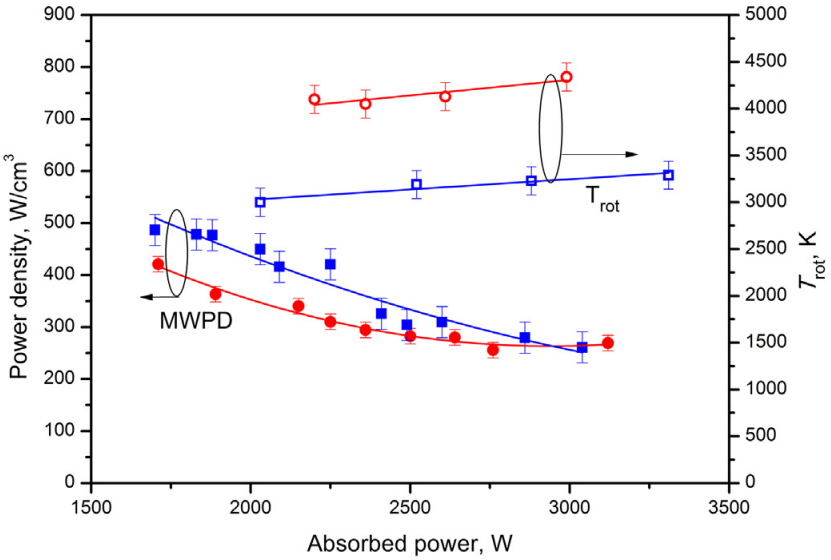

Figure 2.47 Left vertical axis: MW power density $\rho = P/V$ vs absorbed MW power P at concentrations 2 % CH_4 (full squares) and 10 % (full circles) in H_2. Right vertical axis: rotational temperature in the core of plasma cloud measured from C_2 emission spectrum at 2 % CH_4 (open squares) and 10 % CH_4 (open circles). Pressure p = 130 Torr. [86]

2.5 Lift-Off process for SCD plates

A three stage process utilizing ion beam bombardment has been demonstrated for separation of thin diamond films [87, 88, 89, 90, 91] and MEMS structures [92]. A schematic illustration of the process is shown in Figure 2.48. First, irradiation with high energy ions, such as carbon [88] or oxygen [87] ions, is used to locally destroy the lattice structure in a thin layer below the surface. Then, the damaged region is annealed at temperatures exceeding 900 °C [88] to transform the damaged layer below the diamonds' top surface into graphite. Finally, the graphite is removed through selectively etching the graphite.

Ion implantation is the highest-energy mode of possible ion-surface interactions and is occuring exclusively at ion energies exceeding 150 keV. Thereby, the ions are penetrating into the solid while interacting with the lattice atoms and electrons. Displacement of the lattice atoms and creation of vacancies by inelastic collisions reduces the kinetic energy of

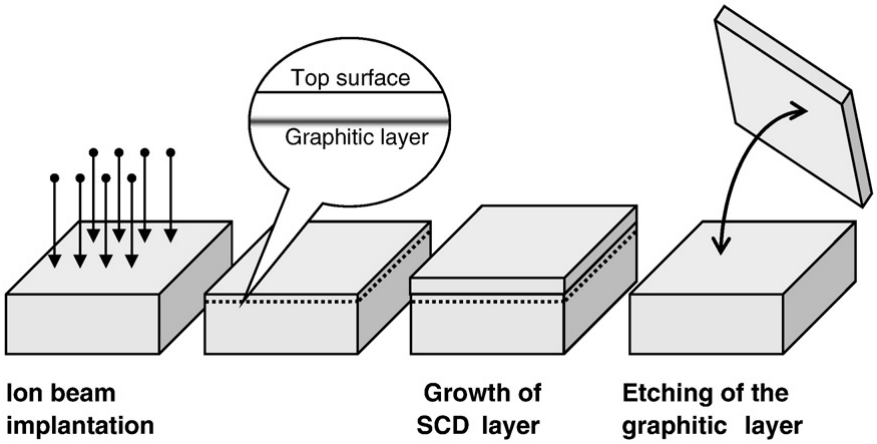

Figure 2.48 Schematic illustration of the individual steps of the lift-off procedure while including an additional CVD diamond growth step. [93]

the incoming ions until they are completely stopped. Figure 2.49 illustrates typical ion trajectories and the amount of damage by the interaction of ions with the crystal lattice. Ion implantation in diamond is usally performed using light ions, i.e. carbon or oxygen. Hence, most of the damage occurs at the end of the ion range within a thin layer at a controllable depth [87] while leaving the top surface almost entirely unchanged. A whole range of ion energies have been proven successful, i.e. Marchywka et al. [88] used 175 keV, Posthill et al. [90] used 190 keV and Mokuno et al. [94] used 3 MeV carbon ions with individual doses of $1 \times 10^{16}\,\mathrm{cm}^{-2}$. On the other hand, Hunn et al. [89] used 5 MeV of oxygen ions with individual doses of $1 \times 10^{16}\,\mathrm{cm}^{-2}$. Carbon and oxygen ions are the most commonly used ions for Lift-Off procedures. The use of carbon ions is obvious as diamond is sp^3 oriented carbon. The use of oxygen ions is inspired by the idea of embedding oxygen into the graphite, which could be converted into carbon oxides [87]. Nevertheless, other elements, such as boron, have been successfully used for graphitization as well [91, 95].

After ion implantation, the irradiated diamond is exposed to a high-temperature annealing step around 900 °C in inert atmosphere such as argon or vacuum [88]. If sufficient amounts

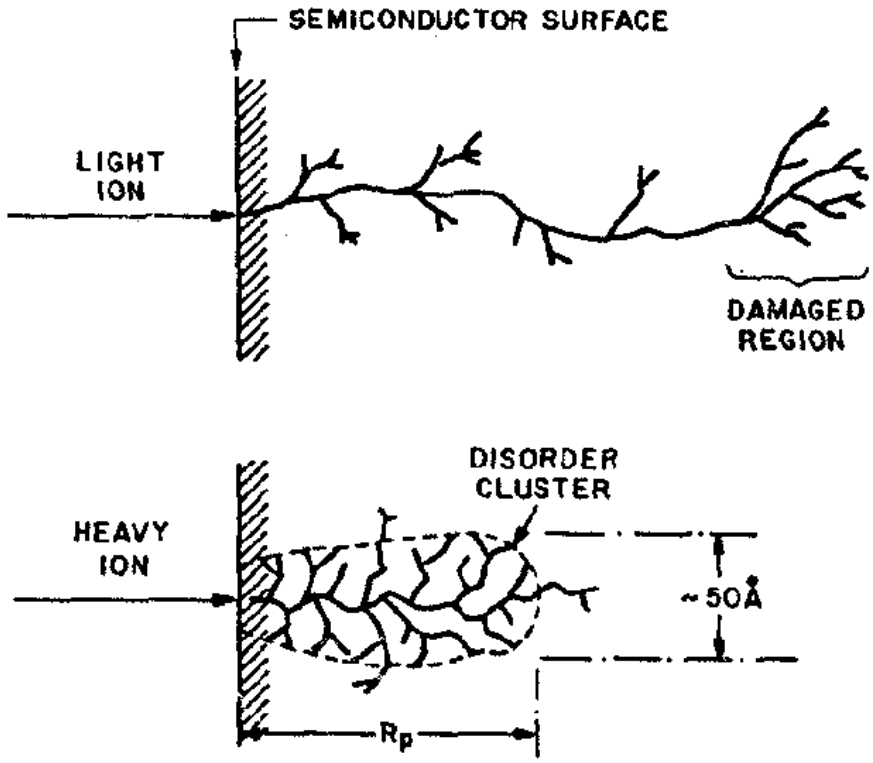

Figure 2.49 Trajectories and approximately damage created of light and heavy ions penetrating through a diamond crystal.

of damage to the crystal structure had been introduced, the dislocated carbon atoms will be recrystallized as graphite, the stable version of carbon under such conditions. The defect density for ion beam induced graphitization in diamond is about $1 \times 10^{22}\,\mathrm{cm}^{-3}$ [96]. This corresponds to approximately 10 % of the carbon atoms being displaced from the diamond lattice. If the threshold is not surpassed the local crystalline structure is intact enough to allow the crystal to heal itself once exposed to said temperatures.

Three different methods have been proven successful in selectively removing the graphite: (i) wet chemical etching of the diamond immersed in a hot acid solution, (ii) thermal oxidation in a hot oxygen rich environment and (iii) electrochemical etching.

Wetchemical etching using a boiling acid mixture of hot chromic-sulfuric acid (CrO_3/H_2SO_4) has been demonstrated to etch graphite much faster than diamond [90]. Unfortunately, the

slow etch rate limited by diffusion of the liquid in the narrow etch channel created and the carcinogenic nature of the acid solution pose serious concerns to this approach.

Thermal oxidation is a technique based on placing the diamond in a oxygen rich environment at elevated temperatures. Selective etching of the graphite is achieved as graphite is reacting into gaseous carbon oxides (CO, CO_2) at around 550 °C while diamond should not be oxidized below 600 °C [97]. Parikh et al. [87] demonstrated selective etching in a flowing oxygen environment at 550 °C. When increasing the temperature to 600 °C, they reported an increased etch rate of the graphite but etching of the diamond occurred. Additionally, they have demonstrated that using oxygen ions instead of carbon ions significantly increased the removal rate of the graphite. Posthill et al. [90] also demonstrated selective removal of the graphite using a oxygen environment at 550 °C without etching the diamond. They as well observed etching of the diamond when increasing the temperature to 600 °C. Tzeng et al. [98] demonstrated separation at 600 °C. They did not comment if the diamond had been etched throughout the procedure, but the optical micrograph provided in their figure 3 shows a rough surface morphology, which is an indicator, that the diamond got etched as well. Locher et al. [99] successfully demonstrated selective etching of graphite using thermal oxidation and flowing air rather than oxygen. They used 4.5 MeV oxygen ions, but reported on ten times higher doses needed (at least $10 \times 10^{16}\,\mathrm{cm}^{-2}$) for successful separation. This is certainly attributed to the significantly lower oxygen content in air (approximately 20.95 %).

Electrochemical etching has been first demonstrated and subsequently been patented by Marchywka [88]. The irradiated diamond is placed in an aqueous solution between two electrodes, made out of platinum [88, 91] or graphite [90]. Different aqueous solutions have been reported, such as chromic acid dissolved in distilled water [88] or pure deionized water [90]. A DC electric field between the electrodes of 200 V is applied creating a current flow

up to 100 mA [88]. The electric field causes a polarization of the graphite creating a virtual anode and cathode on the sample [89]. Anodic oxidation reactions occur at the edge of the conducting layer resulting in the selective removal of the graphite.

In the past, the Lift-Off procedure has been primarily used for separation of thin SCD films, which would be too thin for mechanical processing. More recently, using Lift-Off as separation method in the direct wafer technology [100] has been proven a key part in creating cloned tiles [93], which are essential for the mosaic wafer approach. The process flow of the direct wafer technology can be seen in Figure 2.50.

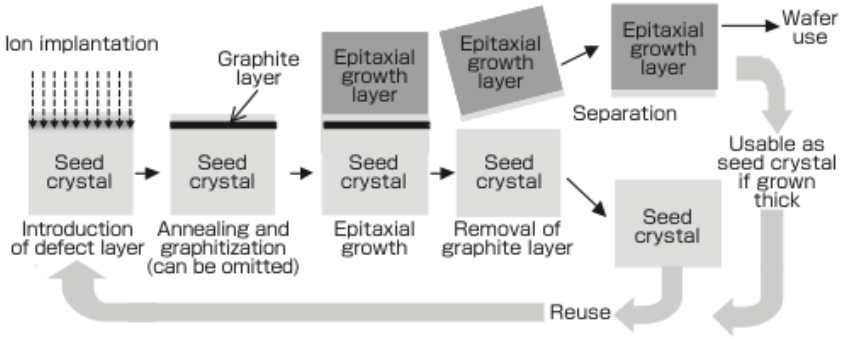

Figure 2.50 Process flow for the direct wafer technology. [100]

2.6 Homoepitaxial enhencement of SCD wafer dimensions

Silicon, currently the most used material in semiconductor manufacturing, is grown by the single crystal pulling method, known as Czochralski process. Thereby a seed crystal is immersed into a melt and pulled out while spinning around its axis [101]. More crystalline material is growing onto the starter crystal and the lateral dimensions are increasing inside the Czochralski furnace. A schematic of the process is shown in Figure 2.51. This method supported the development of new generations of silicon-based electronics from the first

transistor in 1947 [102] to devices with feature sizes close to 10 nm in 2015. Available wafer sizes are as large as 12 inch. This fostered technological advances in silicon based electronics so that integrated circuits can be made as cheap as for a few cents and as fast that physical limitations of silicon are approached limiting further scaling capabilities.

Silicon carbide (SiC) based electronics is the next logical step in advancing elctronic devices. One major concern with SiC is that it cannot be grown using the single crystal pulling method limiting available wafer sizes. This issue was overcome by using a modified Lely process [103], but the crystalline quality was not sufficient for electronics use. A suitable alternative was the use of CVD for crystal growth. Performing homoepitaxy on SiC resulted in the increase of lateral dimensions due to a mushroom type of growth [93]. SiC wafers of 6 inch are commercially available nowadays.

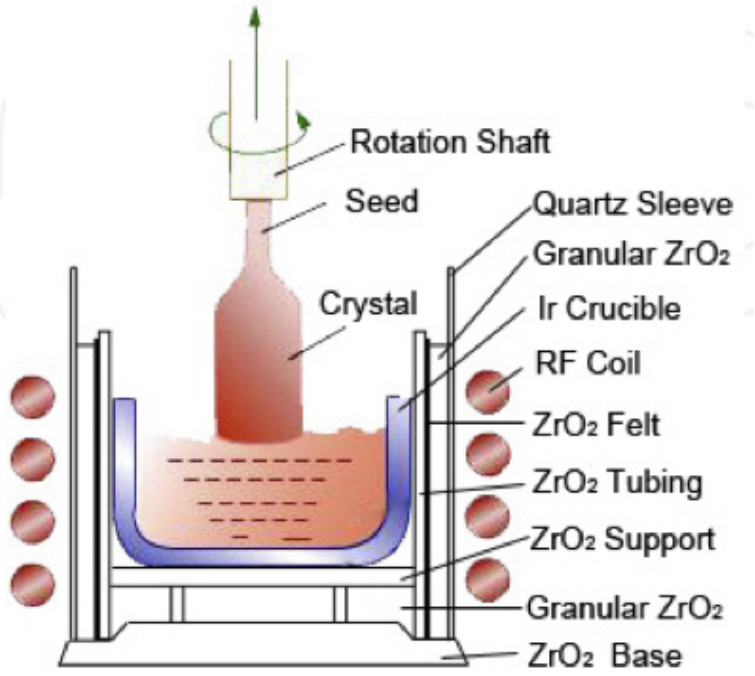

Figure 2.51 Schematic of a typical Czochralski furnace [104]

It would be desirable to utilize a similar mechanism to enhance the lateral dimensions

during diamond growth. Unfortunately, no technological approach has been identified yet for diamond, which ensures a significant improvement on the substrate dimensions while remaining the crystalline quality. Contrary to that, the available diamond surface tends to shrink during deposition [93]. The schematics illustrating the typical growth modes for Si/Sic and diamond are shown in Figure 2.52.

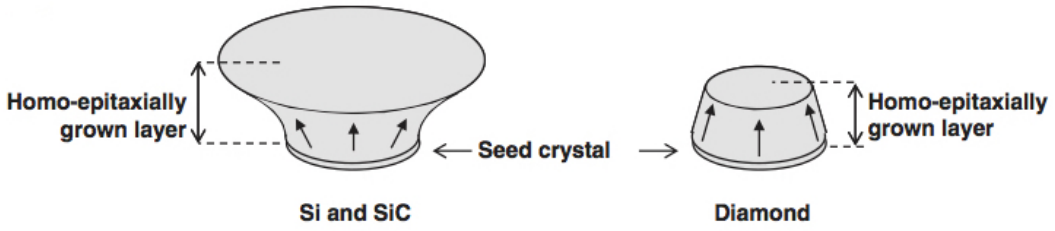

Figure 2.52 (left) Enlargement of the area during growth in the case of Si and SiC, (right) Shrinking of the area during crystal growth in case of single crystal diamond. [93]

Nevertheless, a few reports on enhancing the lateral dimensions during vertical growth were reported so far. Tallaire et al. [46] reported that a diamond film grown on a 3.5 mm × 3.5 mm substrate enhanced to 6.0 mm × 6.0 mm after undergoing a 45° rotation into the {110} orientation. Such twinning usually results in the formation of internal stress up to the introduction of cracks at the twinned edges [46]. Thus, utilizing twinning is not a useful approach of increasing the lateral dimensions. Nad et al. [67] reported that SCD deposition using a optimized pocket holder dimensions not only suppresses PCD formation, but enhance the SCD lateral dimensions. An area enhancement to more than 2.5 times from 3.7 mm × 3.7 mm to 5.7 mm × 5.8 mm was reported taking place over 2.9 mm of vertical SCD growth using two consecutive growth steps. While this is certainly a promising observation, more research needs to be done in order to identify whether or not this enhancement of lateral dimensions through vertical growth can be preserved. Enhancing the dimensions from 3.5 mm × 3.5 mm to 50.8 mm × 50.8 mm would require an lateral area enhancement by a factor of 210.6, which

will likely possess serious technological challenges on its own. Thus it is necessary to simultaneously investigate different substrate engineering approaches to enhance the SCD lateral dimensions. Three potential engineering solutions are currently known: (i) mosaic growth, (ii) flipped crystal, and (iii) flipped side approach.

2.6.1 Mosaic growth

The concept of mosaic growth is, that several identical SCD crystals (tiles) are aligned next to each other in a way that the top surfaces of the individual crystals are in good alignment. During SCD deposition the films grown on each individual crystal grows together and form one diamond film with lateral dimensions of all individual seeds. Mosaic growth was first studied by Janssen and Giling [105]. Initially, the alignment of the individual seeds was achieved by using high surface tension liquid [106]. An SEM picture of successful mosaic overgrowth of seven individual crystals, performed by Findeling-Dafour was shown in Figure 2.53. The individual tiles were still identifable and the boundary layer, where the individual tiles grew together appeared to be of low quality. Additionally, a major drawback of using high tension fluid was a poor thermal contact between the substrate and the holder, and there were difficulties in measuring the substrate temperature.

More recent research has used Lift-Off by ion implantation (see Section 2.5) to create several identical clones of one seed substrate. Afterwards, they are post-processed to have matched dimensions using laser processing. Then, the individual tiles can be aligned next to each other so that they form a seed crystal with enhanced dimensions without the need of a fluid [107]. The individual tiles are grown together during diamond deposition enhancing the lateral dimensions several times. A schematic illustration of the mosaic growth procedure using tiled clones created by Lift-Off processes is shown in Figure 2.54.

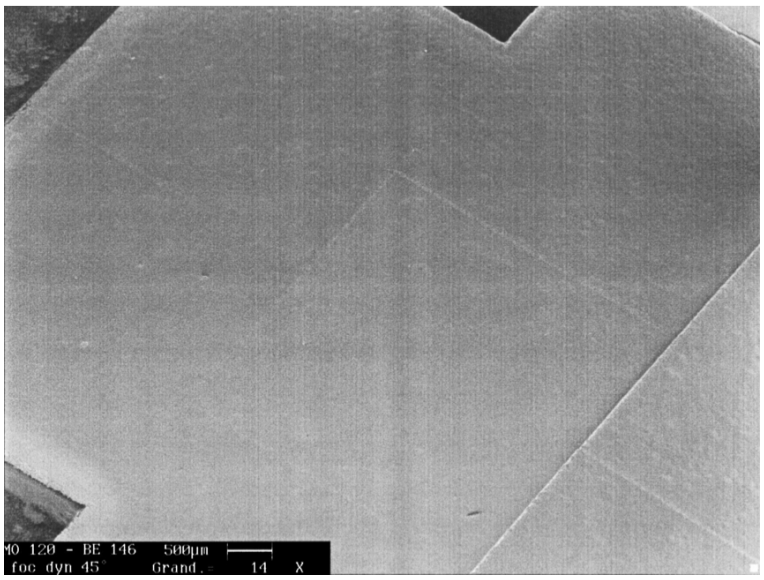

Figure 2.53 SEM overview of a seven-piece SCD mosaic. [106]

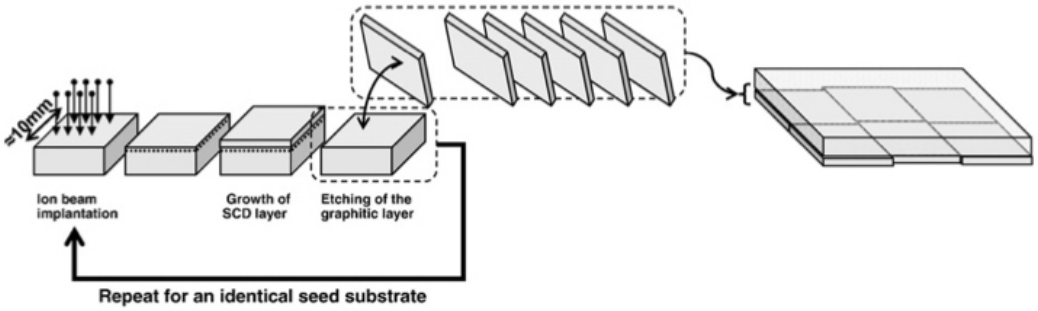

Figure 2.54 Mosaic growth by tiling together several clones, which are created from the same seed substrate. [93]

Initially, mosaic growth of tiled clones was used to demonstrate the fabrication of a 1 inch SCD wafer by Yamada et al. [107] and subsequentially improved the quality [108, 109]. Figure 2.55 showed a photograph of a 1 inch SCD wafer of relative good quality. To this date, tiled growth of a 2 inch wafer was demonstrated using this technique [110].

The same major set of problems problems on crystalline quality were reported on previous publicatiopns, i.e the high amounts of stress and formation of defects formation in the SCD boundary material between the individual tiles [105, 110], which even resulted in macroscopic cracks. The formation of defects and cracks throughout the SCD film was shown in Figure 2.56

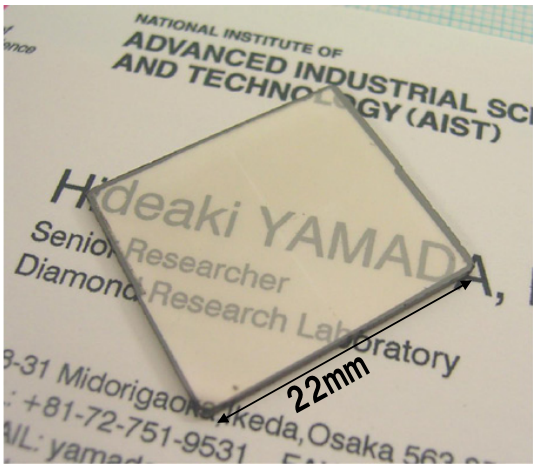

Figure 2.55 Photographs of the inch-sized wafer of tiled clones of a single-crystal diamond with an are of approximately 20 mm × 22 mm. Tranmission image [109]

[110].

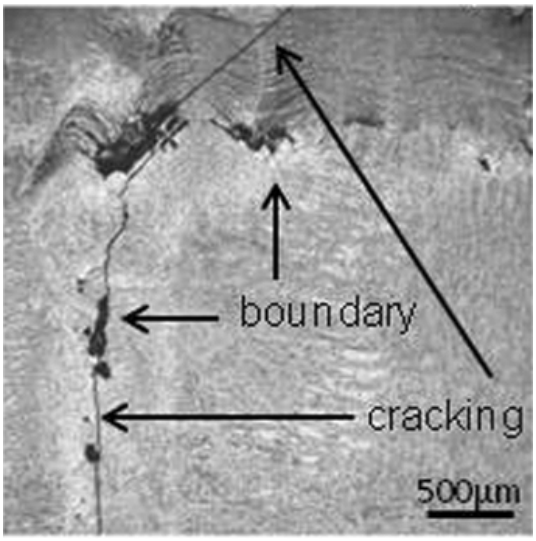

Figure 2.56 Formation of low quality SCD material in the interconnecting areas between individual tiles causing defect formation and crystal cracking. [110]

Yamada et al. [93] performed a cross-sectional stress analysis using birefringence imaging and found large amounts of internal stress in the boundary layer formed between individual stress and even more elevated levels right at the interface

Eliminating the denigration in crystalline quality in the boundary film, where the individual tiles are grown together is still an unsolved problem. While the mosaic approach can be

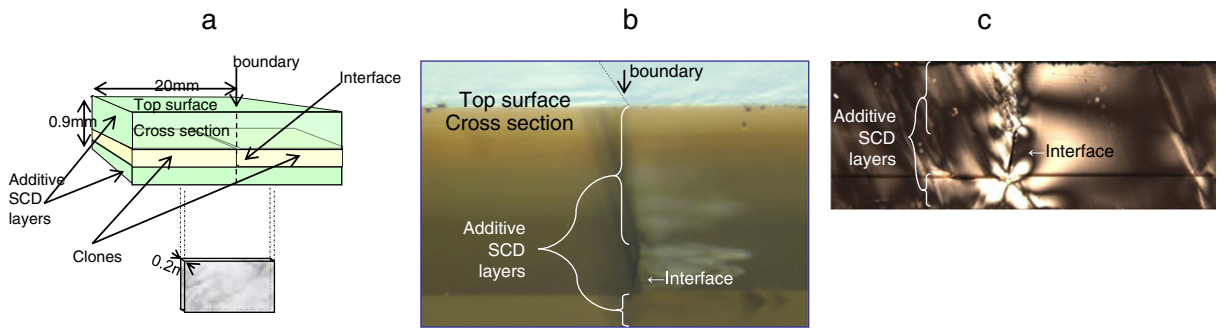

Figure 2.57 (a) A tiled clone, schmatically drawn with thickness of 0.9 mm, (b) An image of the cross section of a tiled clone, and (c) polarized microscope image of the cross section of a tiled clone. Image (c) was taken from the gray rectangle indicated in (a). [93]

used to growth SCD wafers of large dimensions suitable for industrial applications it clearly cannot deliver the quality needed. Future research is required and will show if it is possible to improve the quality so that mosaic diamond wafers become a viable option.

2.6.2 Flipped crystal approach

Another approach is the flipped crystal approach, sometimes also referred to side-surface growth as introduced by Mokuno et al. [111]. It relies the fact that all {100} crystal orientations in diamond are equivalent. Thus, growth can be equally carried out on the <100>, <010>, <001> orientations. The flipped crystal approach uses that in order to increase the lateral dimensions, such as shown in Figure 2.58. First, SCD deposition is carried out in the [100] direction. After growth, the crystal is post-processed by laser trimming and mechanical polishing to prepare a [010] direction as the top surface for a second growth step perpendicular to the initial growth.The growth area enhances as illustrated in Figure 2.58. Afterwards, the diamond is post processed again and prepared for another growth step in the initial <100> orientation as indicated in Figure 2.58. Finally, the diamond is processed again to be used as a seed crystal for deposition along the <001> direction (being orthogonal to the

two initial growth directions in Figure 2.58). The deposition area in the process schematic shown in Figure 2.58 is doubled during the first side-surface growth and doubled again for the second side-surface growth step. Thus, the overall crystal dimensions of the final seed crystals have been increased by a factor of four. Applying this technique resulted in creating half-inch sized wafers [111].

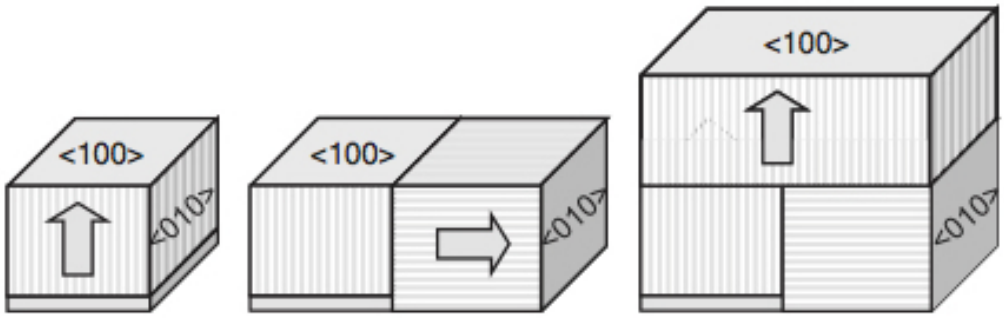

Figure 2.58 Schematic illustration of flipped crystal growth on three equivalent <100> orientations. [93]

It is possible to achieve the area enhancement with different combinations of side-surface growth steps due to the equivalance of the {100} sides. Figure 2.59 shows the schematical area enhancement by performing side-surface growth on three sides, instead of only two as shown in Figure 2.58.

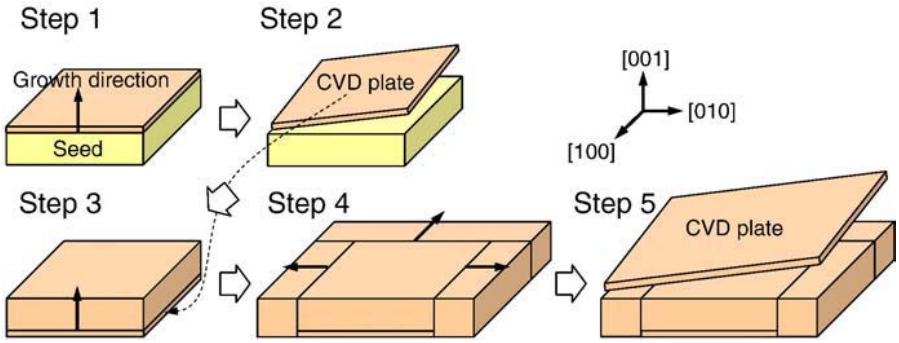

Figure 2.59 Schematic illustration of a crystal enlarging process by combination of lift-off process and side surface growth. [111]

Figure 2.60 shows a photograph of a seed crystal which was expended to 10 mm × 10 mm

using two side-surface growth steps, whereby each side-surface step contained several individual deposition steps in order to achieve the targeted thickness. The next process step for the substrate shown in Figure 2.60 would be to being processed into a 10 mm × 10 mm seed substrate for diamond deposition (in direction facing out of the picture).

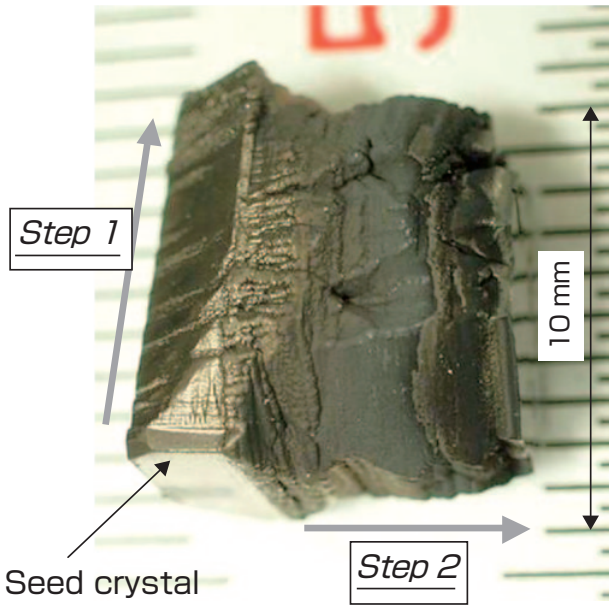

Figure 2.60 Lateral growth. [111]

The two biggest problems with the filpped crystal growth are the increased defect density and local strain at the interfaces, were the crystal flipping occurred. This was experimentally verified by Mokuno et al. [111]. Additionally, the growth of diamond is effected by the potential formation of PCD rim material. Thus, the final seed crystal will have an uneven shape, instead of being rectangular, as can be seen Figure 2.61. It would be necessary to trim off the outer areas to obtain a well-shaped SCD wafer, but that would reduce the wafer dimensions significantly.

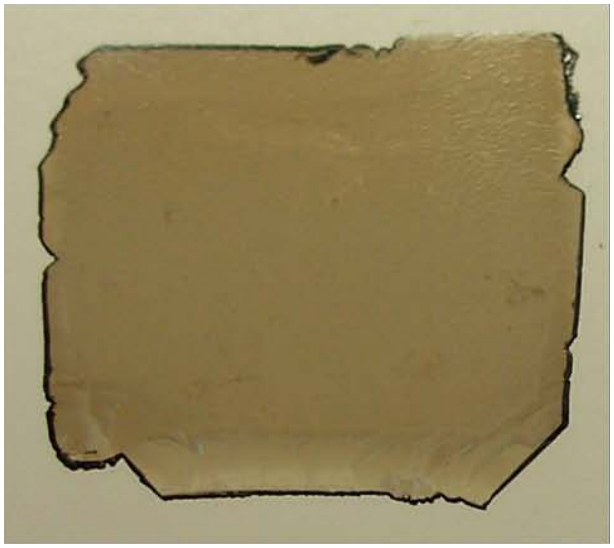

Figure 2.61 Photograph of a half-inch nitrogen-doped single-crystal CVD diamond plate produced under high growth rate ($32\,\mu m\,h^{-1}$) from the seed plate by lift-off using ion implantation. [111]

2.6.3 Flipped side approach

Another approach, which uses an altered version of the flipped crystal approach is the flipped side approach. A schematic of the entire procedure is shown in Figure 2.62, where a $3.5\,mm \times 3.5\,mm \times 1.0\,mm$ seed crystal is enlarged into an half inch SCD wafer.

First, SCD growth is carried out on a CVD seed crystal in the <100> direction. The dimensions of the initial seed crystal are $3.5\,mm \times 3.5\,mm \times 1.0\,mm$. After growing to a targeted thickness, i.e. 12.5 mm (half an inch) the growth is stopped (a). The resulting crystal has dimensions of $3.5\,mm \times 3.5\,mm \times 12.5\,mm$. Now, the diamond crystal is processed into several new seed crystals, which are cut perpendicular to the initial growth direction (b). The dimensions of those new seed crystals are $3.5\,mm \times 12.5\,mm \times 1\,mm$. Now, another set of SCD growth experiments is carried out. The growth direction is perpendiculary to the growth direction of the first growth step. It was demonstrated, that defects preferentially propagate along its initial growth direction [79, 80]. Friel et al. [80] demonstrated a vastly

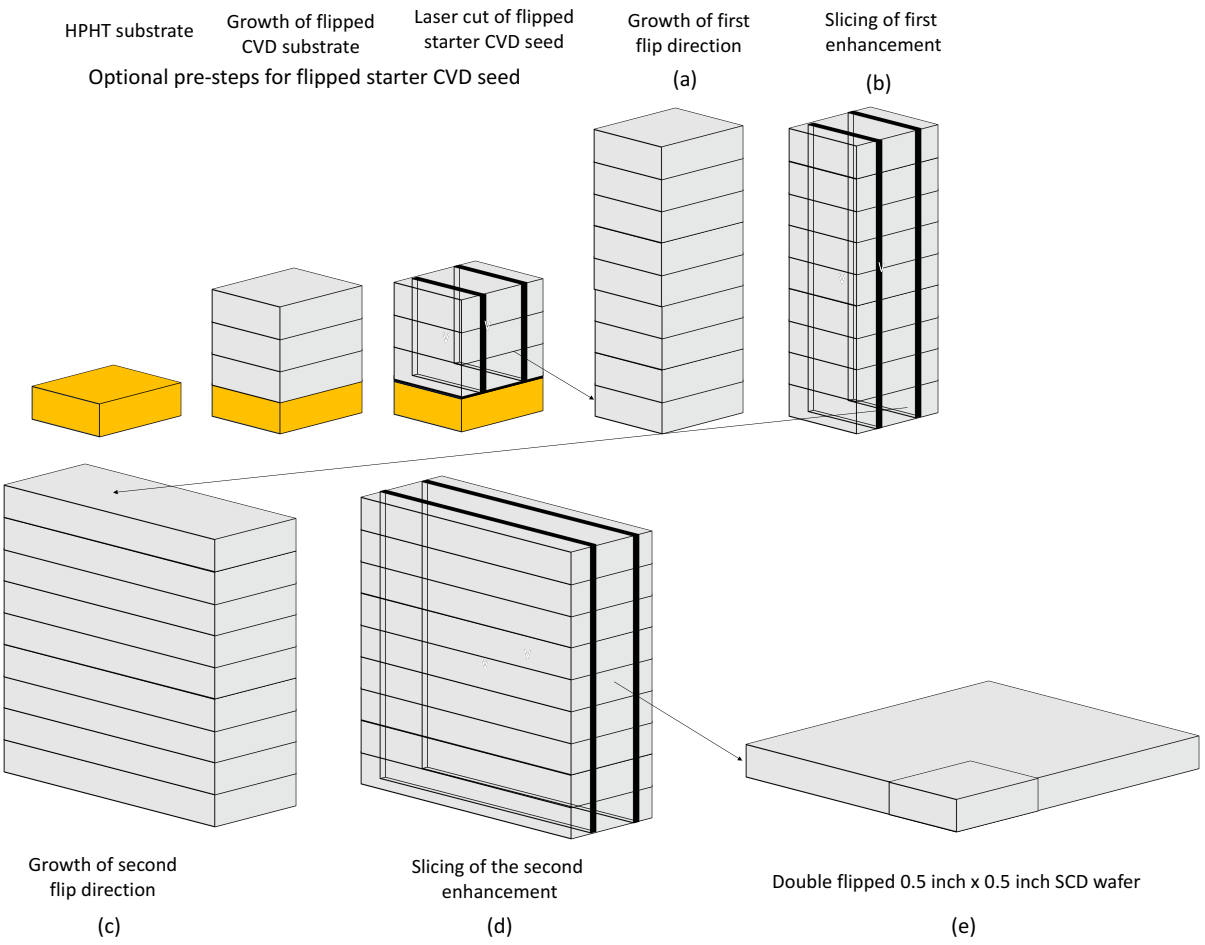

Figure 2.62 Schematic of the flipped side approach showing each individual step to increase a 3.5 mm × 3.5 mm SCD crystal into a 12.5 mm × 12.5 mm SCD wafer. The inset in the final wafer (e) illustrates the crystal dimensions of the initial diamond seed. The yellow block represents the initial HPHT seed crystal and the grey blocks represent CVD grown SCD.The bold black lines indicate, where the SCD is sliced.

reduced defect density by flipping the growth direction two times orthogonally. Friel et al. [80] recorded X-Ray topographs of a CVD-grown diamond, which was initially grown along the <001> direction, followed by growth along the <100> direction, see Figure 2.63. It can be seen, that the propagation of the defects along the <001> was stopped, once the growth direction was changed to the <100> direction. New defects formed in the interface when the second growth step was initialized, but overall the defect density in the [100] oriented diamond was reduced. This concept can be further utilized by start the flipped side approach

by creating a flipped CVD seed crystal, to have a reduced defect densityduring the first enlargement step already (see pre-steps in Figure 2.62).

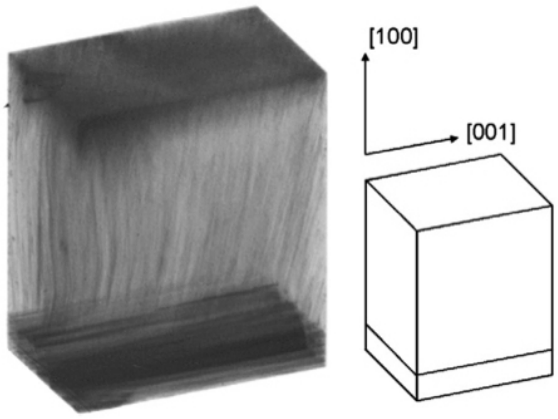

Figure 2.63 {111} projection topograph of a single crystal CVD diamond sample containing two generations of CVD growth along the [001] and [100] directions. [80]

In a second set of the growth steps, 12.5 mm (half an inch) of diamond are grown (c), while the defect density is reduced compared to the initial set of growth (a). The resulting diamond has dimensions of 3.5 mm × 12.5 mm × 12.5 mm. Again, new seed crystals will be processed out of the bulk material with crystal orientation perpendicular to the two previous growth directions (d). The resulting seed crystals are 12.5 mm × 12.5 mm in dimension and can be described as half inch SCD wafer (e). In order to approach two inch dimensions, the flipped side approach has to be repeated multiple times.

The main advantage of the flipped side approach is, that the final wafers only contain a single growth orientation, This is in contrast to the flipped crystal approach i.e. the CVD diamond shown in Figure 2.63 currently contains two growth directions. This can be easily achieved by growing each direction to thicker than the targeted thickness, followed by removing the initial seed crystal. This concept cannot be applied to the flipped side approach as the area enlargement is achieved by growing around the initial seed crystal in several directions. Hence, using the flipped side approach it is possible to increase the SCD

wafer dimensions while reducing the dislocation density at the same time making it the most promising approach for the production of two inch SCD wafers.

Nevertheless, there is one major drawback using the flipped side approach. The final dimensions of a tiled wafer manufactured using mosaic growth is assembled and the overgrown diamond instantly has the targeted dimensions. Only some effort has to be invested in the growth and processing of the individual tiles. The flipped crystal approach utilizes off the crystals initial dimensions. Thus the theoretically minimum growth necessary for extending a 6 mm × 6 mm SCD seed to a 12 mm × 12 mm, a case such as shown in Figure 2.58, would require two growth steps of 6 mm each. Hence, the total growth required would be 12 mm compared to at least 24 mm for the flipped side approach (2 growth steps of 12 mm each).

This problem intensifies when enhancing the SCD wafer dimensions even further, i.e. targeting 2 inch wafers. It seems unlikely that a 3.5 mm × 3.5 mm × 1.0 mm seed crystal could be grown for 50 mm into a single direction without any shrinking of the SCD surface area. Mokuno et al. [112] already observed a shrinking diamond top surface area when growing a total thickness of 10 mm SCD due to the formation of PCD material as shown in Figure 2.64. Thus, it seems necessary to increase SCD wafer dimensions in more modest steps, i.e. in half inch steps, which corresponds to a four fold increase of the wafer area each time. Unfortunately, this would result in an up-scaling of the growth required for each enlargement step as shown in Table 2.1. A total 250 mm of diamond growth would be necessary in order to enhance the SCD wafer dimensions to 2 inches.

The flipped side approach for enhancing SCD wafer dimensions seems superior compared to the flipped crystal approach and mosaic growth as the crystalline quality of the wafer would at least be maintained and potentially even increased. Unfortunately, the occurance of shrinking SCD surfaces throughout the growth steps could jeopardize the entire engineered

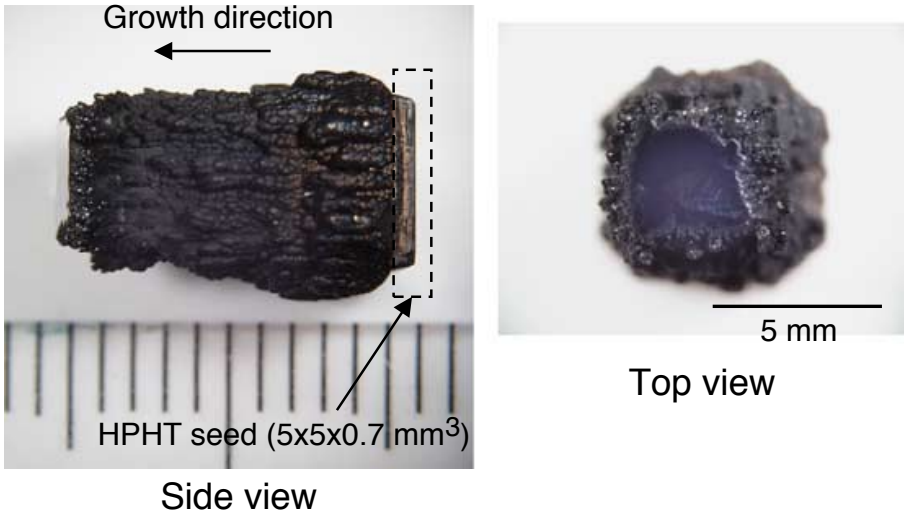

Figure 2.64 A 4.65 ct single-crystal diamond with the thickness of 10 mm grown by 24 times repetition of high growth with the growth rate of 68 µm h^{-1}. [112]

Wafer enlargement	**Growth required** [mm]
0.5 inch	25
1.0 inch	50
1.5 inch	75
2.0 inch	100
Total	250

Table 2.1 Total amount of growth required for each individual step for enhancing SCD wafer dimensions to 2 inches by half inch increments.

process. Hence, it is possible to establish procedures to prevent the formation of PCD in between individual deposition experiments or even achieve a slight expansion of the SCD surface area as reported by Nad et al. [67] [72]. The other big concern, which has to be overcome is the fact, that massive amounts of SCD growth are necessary, i.e. assuming a growth rate of 10 µm h^{-1} [81] would mean, that a total growth time of 1041.67 days would be required. This corresponds to 2 years and 10 months and does not include any additional time for analysis and processing in between individual experiments. Hence, it is critical to enhance the growth rate while remaining a high crystalline quality, i.e. increasing the process pressure [49], for the flipped side approach to succeed.

2.7 Heteroepitaxial SCD growth

Heteroepixial growth of diamond is another approach in order to achieve SCD wafers of large dimensions. The underlying concept is to grow diamond on a non-diamond substrate, which has the same crystalline structure. The most prominent materials were silicon and silicon carbide, where wafer sizes of 6 inches are easily available. Growth on unseeded silicon wafers is possible, but nucleation densities are as little as $1 \times 10^4\,\mathrm{cm}^{-1}$ [113] resulting in macrocrystalline diamond with individual grain sizes as big as 10 µm [114]. Nucleation densities have been significantly improved up to $1 \times 10^{11}\,\mathrm{cm}^{-1}$ [115] by applying various pre-treatment methods, i.e. scratch seeding with diamond nanoparticles [116], dip coating [117] or surface carburization [118] to name a few. The crystal sizes of a PCD film are increasing with film thickness as more and more individual crystals grow together. Hence, the idea of heteroepitaxy is to nucleate a very dense film of nanocrystalline diamond and grow a film thick enough so that all individual crystals merge into one. The seeding methods described above provide sufficiently high nucleation densities. Unfortunately, the nucleated crystals are randomly oriented. This results in a growth behavior as shown in Figure 2.65. It is clear, that the individual crystals are aligned with respect to each other. The misorientation towards each (tilt and twist) other limits how much the individual crystals can combine.

In order to grow together all individual crystals into one SCD, it is necessary that all of the individual nucleation sides and crystals are aligned perfectly. Bias-enhanced nucleation (BEN) has been proven to create highly oriented diamond nucleation sides, which subsequentially grow together as highly oriented diamond. The positive effect of BEN has been demonstrated on several substrate materials, such as silicon [120, 121, 122] and silicon carbide [120, 123]. Figure 2.66 shows a highly oriented diamond film [122]. The orientation

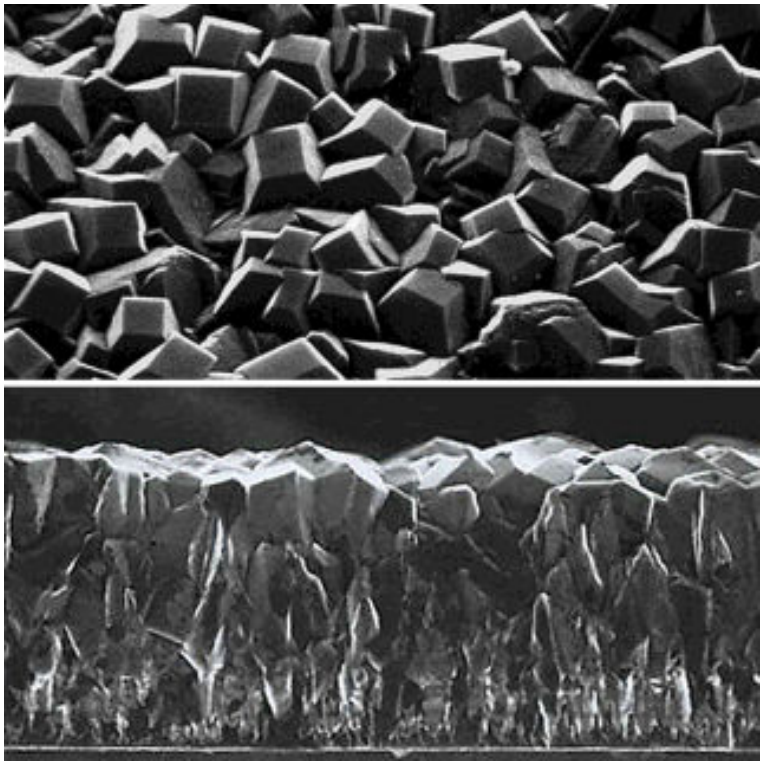

Figure 2.65 SEM images of the top and cross section of a microcrystalline diamond film. [119]

is much higher compared to unbiasedly nucleated PCD, which is shown in Figure 2.65. Nevertheless, substantial variations are still noticable limiting the use of Si and SiC as seed substrate to grown SCD.

Iridium is the only material, where successful heteroepitaxy of SCD has been demonstrated [124]. The lattice mismatch between diamond and silicon is 35 %, while it is only 7.1 % for iridium. A detailed mechanism for heteropitaxial diamond nucleation was introduced by Schreck et al. [125]. Figure 2.67 shows a high quality SCD film grown on iridium [126]. Deposition of iridium on silicon was demonstrated using yttra-stabilized zirconium (YSZ) [126] and strontium titanate [127]. YSZ turned out favorable as it reduced both, the in-plane rotation (twist) of the nucleation centers as well as the cross-sectional bent (tilt), while $SrTiO_3$ only reduced the twist. Experimental details for the deposition of YRZ and Ir can be found in [126]. A schematic of the multi layer system for heteroepitaxy of diamond can be

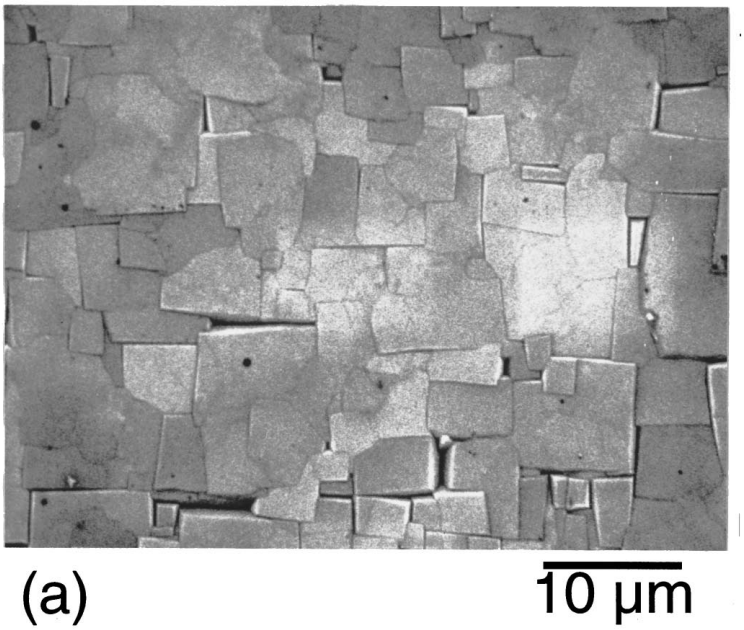

Figure 2.66 Scanning electron micrograph of a heteroepitaxially nucleated diamond film on Si(001). [122]

seen in Figure 2.68

Heteroepitaxy of SCD was demonstrated for up to 100 mm (4 inch) wafers. Figure 2.69 shows an optical photograph of successful diamond heteroepitaxy [128].

Despite all those promises, heteroepitaxy of SCD has several issues, such as the complexity of processes involved to deposit YSZ and Ir with sufficient quality, the cost associated with using such rare earth metals and the high temperature dependence of the stress formation [129, 130], which can lead to cracking of the wafer.

By far the most critical concern, is that the defect density of heteroepitaxially grown SCD is much higher compared to homoepitaxially grown SCD. Threading dislocations are the main concern limiting the adoption of diamond by generating birefringence [131], leak current [18, 132] or unwanted background luminesence [133]. Defect densities of a commercially available type Ib HPHT crystal, which is commonly used as a seed crystal, are in the order of 1×10^5 to $1 \times 10^6\,\mathrm{cm}^{-1}$. The defect density for a CVD film, grown on such a HPHT seed;

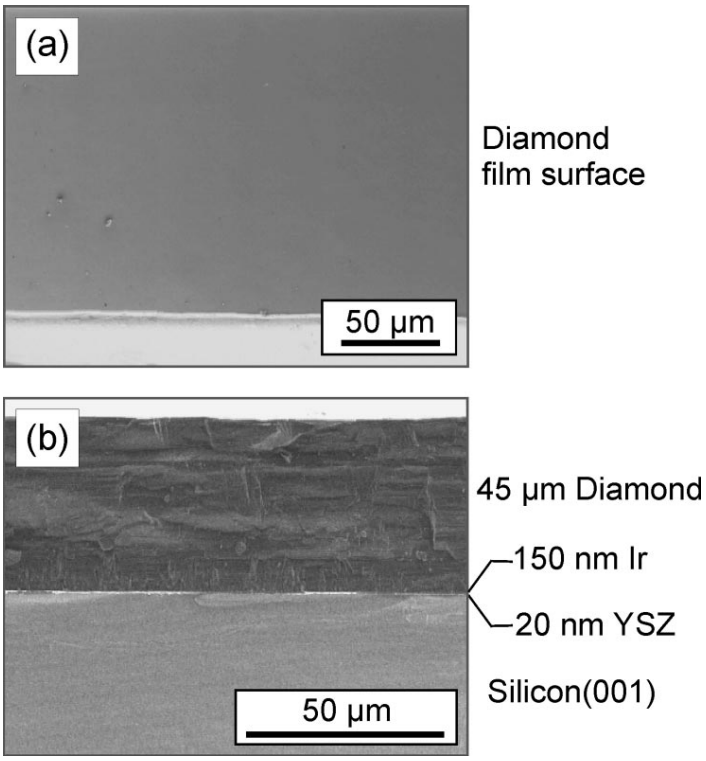

Figure 2.67 Scanning electron micrographs of a 45 µm thick heteroepitaxial diamond film deposited on Ir/YSZ/Si(001): (a) diamond film surface and the fracture edge near the lower border of the image; (b) cross section image. [126]

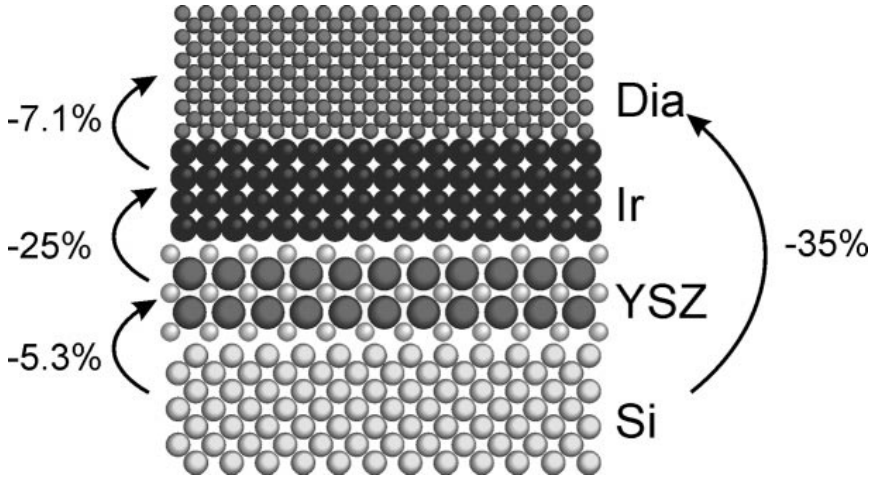

Figure 2.68 Schematic representation of the layer system diamond/Ir/YSZ/Si(001). In the YSZ crystal the large spheres correspond to the oxygen ions. Numbers indicate the lattice misfit between consecutive layers. [126]

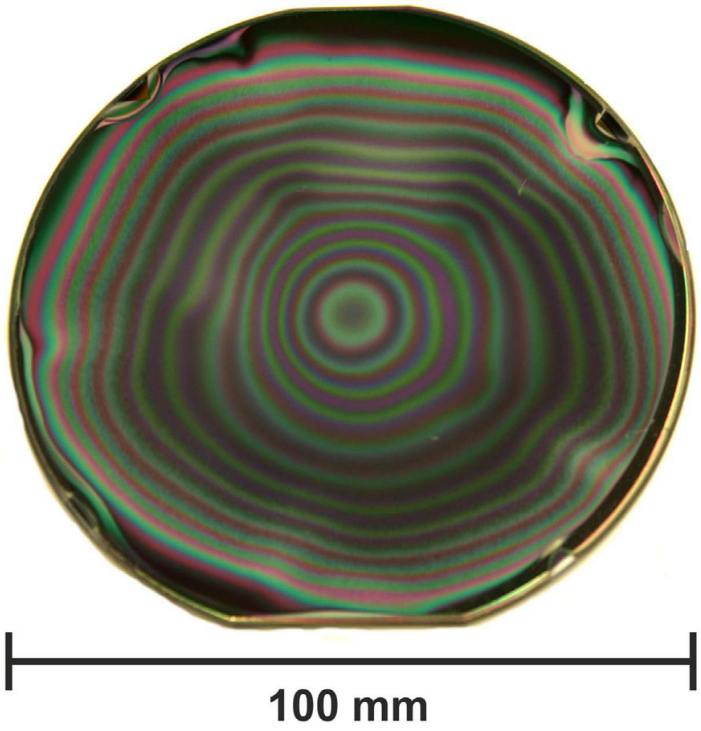

Figure 2.69 Optical photograph of an Ir/YSZ/Si(001)wafer after BEN and 2 µm growth by MWPCVD. Approximately 70 mm of the surface are covered by epitaxial diamond. The interference fringes result from a certain variation in diamond film thickness. [128]

is reduced by two orders of magnitude to $1 \times 10^4\,\mathrm{cm}^{-1}$ [67]. This value can be decreased even further by engineering the seed crystal, such as using a pyramidal-shaped seed in order to out-deflect dislocations [76] or using a macroscopic hole for lateral growth with fewer dislocations [81]. Additionally, the use of platinum nanoparticles has been demonstrated to stop the propagation of some dislocations [78]. Defect densities as low as $2 \times 10^3\,\mathrm{cm}^{-1}$ have been reported as described in detail in Section 2.4.4.3.

Figure 2.70 shows the development of the dislocation density along the growth of 1 mm of heteroepitaxially grown SCD. The defect density at a film thickness of 10 µm was $3 \times 10^9\,\mathrm{cm}^{-1}$ and reduced to $3 \times 10^7\,\mathrm{cm}^{-1}$. An inverse dependency between the defect density and the film thickness was identified. The average distance between defects increases with decreasing density. This reduces the probability for defect interactions and potential annihilation [128].

Thus, interpolating Figure 2.70 to $2 \times 10^3\,\mathrm{cm}^{-1}$, the state of the art for homoepitaxy, would require 50 km of heteroepitaxially grown SCD. Assuming a growth rate of $10.417\,\mu\mathrm{m\,h}^{-1}$ (this yields 250 µm per day) the total deposition time would be 547 570 years for a single substrate assuming that nothing goes wrong and also neglects any additional time for analysis and reconditioning of the substrate between growth steps. The absurdity of the is number is obvious. Research on alternative ways to reduce the defect density, and internal stress, in heteroepitaxially grown diamond are ongoing and summarized by Schreck et al. [128]. It remains questionable if heteroepitaxy will ever be a viable option for growing large area high quality SCD wafers.

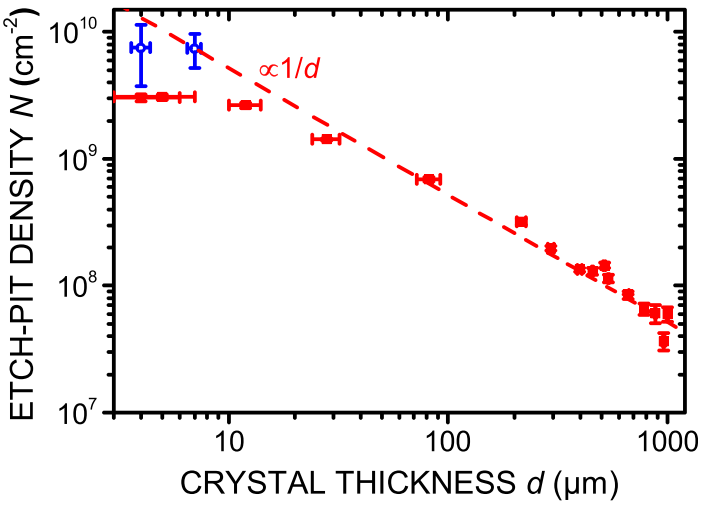

Figure 2.70 Dislocation density derived from the analysis of etch pits (red squares) and from TEM measurements (blue open circles) vs. the crystal thickness. The dashed red line shows a 1/d fit in the range 20–1000 µm. [134]

2.8 Computational description of the formation of pulsed microwave discharges

Lombardi et al. [135] provided a refined model based on previous computational work describing continuous [136] and pulsed [137] microwave discharges and compared the modeled data with experimental results. Both, the modeling and experimental conditions were a pressure up to 20 kPa (150 Torr). 6 kW of absorbed power resulted in an absorbed power density of 65 W cm^{-3}. The gas mixture contained 5 % CH_4 in H_2 and the total flow rate was 200 sccm. The experimental gas temperature was determined from the Doppler broadening of the H_α emission line [138].

The model used to describe the plasma discharge was a quasi-homogeneous model of a H_2/CH_4 mixture, which consisted of 28 neutral and ionized chemical species and 130 possible chemical reactions within three sets: The first set of reactions described the thermal hydrocracking in a hydrogen-methane gas mixture, the second involved the electron-impact dissociation and ionization processes of hydrocarbons and molecular and atomic hydrogen. The third set of reactions was related to the ion conversion and dissociative recombination of ions. A description of the time evolution of the discharge would in principle require the time integration of the species continuity equation and the total energy equation for a 2D geometry [135]. However, treating the problem in a 2D geometry was difficult due to the large number of species and the high pressure and high temperatures in the system. Thus, a quasi-homogeneous plasma model with two distinguished plasma regions was assumed: (i) a spatially homogeneous region which corresponded to the plasma bulk, and (ii) a boundary layer where all the plasma parameters, species, mole fractions, and gas temperature were assumed to vary linearly. Surface effects due to the substrate were assumed to be dominant

over those coming from the reactor walls, which were neglected, i.e. plasma wall interactions were excluded. The plasma ignition was assumed to be occurring under isobaric conditions. Details on the actual computational equations to carry out simulations based on those boundary conditions were reported by Lombardi et al. [135] using a substrate temperature of 1000 K and details of the time evolving parameters were presented.

Overall, it was found that the gas temperature obtained from the model was in agreement with the measured temperature, but a discrepancy was observed in the shape of the early time variation; see Figure 2.71.

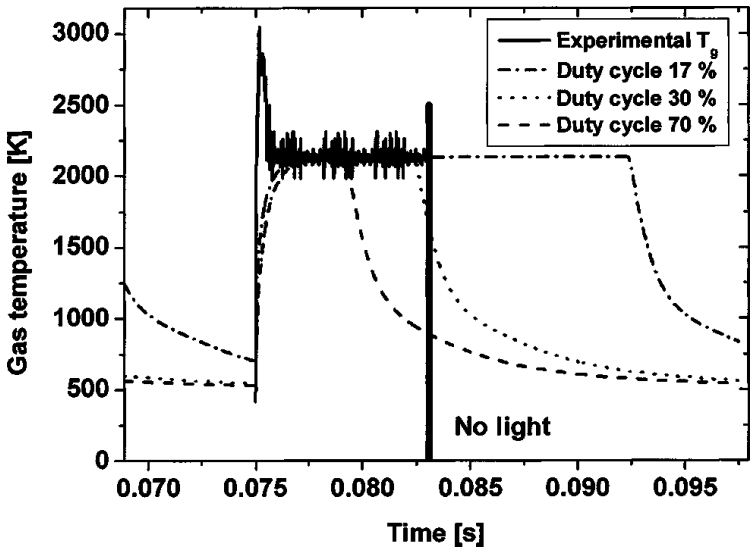

Figure 2.71 Comparison of the gas temperature obtained from the experiments (H_α temperature) and from modeling. Plasma conditions: peak power = 800 W, pressure = 3200 Pa, MWPD = 12 W cm^{-3}, duty cycle 17 %, T_s = 500 K. [135]

Additionally, the modeling results indicated that [H] and [CH_3 radical densities were substantially enhanced when small duty cycles below 50 % were used, i.e. see Figure 2.72. The enhanced species densities were caused by higher peak gas temperatures, which caused significantly higher levels of thermal dissociation of species.

Gicquel et al. [139] were providing further insight of the modeling process by comparing

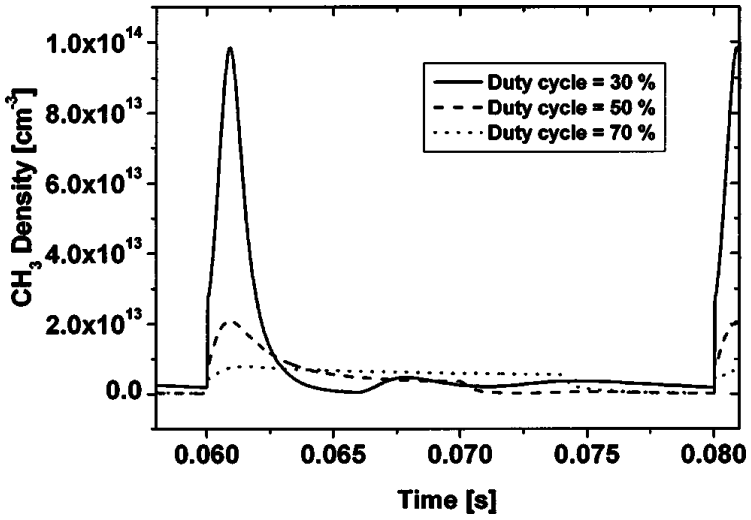

Figure 2.72 Calculated CH_3 radical density for different duty cycles, at a constant average microwave power = 600 W, T_s = 1000 K. [135]

the results of continuous and pulsed models. The same experimental settings used by Lombardi et al. [135] were used in their work. The time evolution of the plasma discharge was experimentally determined and the results were shown in Figure 2.73. It was observed, that the discharge density during the brief ignition period was significantly higher ($\approx 225\,\mathrm{W\,cm^{-3}}$) before stabilizing to it steady state value ($12\,\mathrm{W\,cm^{-3}}$). This in combination with the observed temperature overshoot of more than 800 K during discharge ignation and its discrepancy with the modeling results, as shown in Figure 2.71, led Gicquel et al. [139] to the assumption, that the quasi-homogeneous model did not properly describe the ignition phase. They concluded, that the discharge was initially forming just above the substrate in a small region with a strong electric field. Hence, all the microwave power would be confined in a small volume resulting in a significant amount of gas heating. Afterwards, the second stage of the discharge formation was following the quasi-homogeneous model. Gicquel et al. [139] recommended to use at least a 1D model that would properly describe the discharge expansion and the spatial non-homogeneity, but have not followed up on that as their overall model led to satisfactory

predictions of the steady state description.

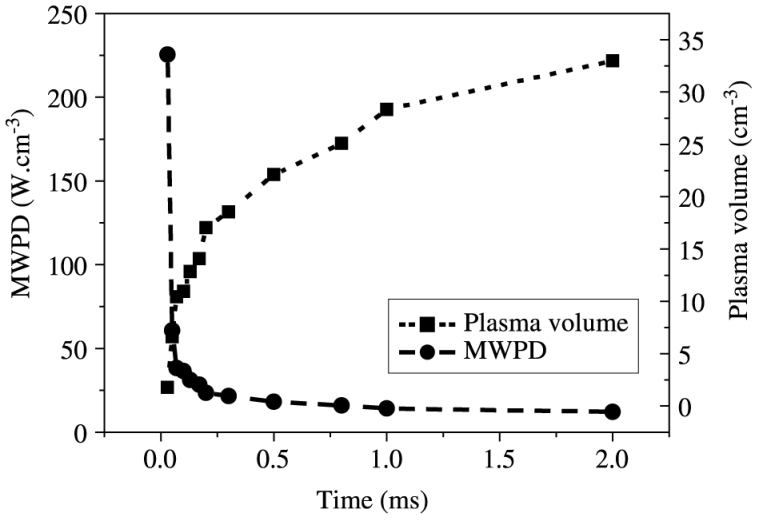

Figure 2.73 Evolution of plasma volume and MWPD as a function of the time. Plasma conditions: in-pulse 800 W, 3200 Pa, power density of 12 W cm^{-3}. [139]

Brinza et al. [140] re-evaluated the unstationary 1-D axial plasma model previously used [136, 137, 139] to identify which pulsing parameters would result in the highest average active species densities. The modeling efforts focused on [H] and [CH_3]. High [CH_3] densities were obtained under the presence of high atomic hydrogen densities, i.e. high gas temperature [141]. However, the ideal gas temperature for [CH_3] generation ranged between 1500 and 2000 K [142] as higher temperatures favored the conversion of CH_3 into other carbon species, i.e. CH_2 or CH. The importance of optimizing the pulsing parameters resulted out of the fact, that the gas temperature became a time-dependent variable under pulsing conditions. The gas temperature was decreasing during the shutdown of the plasma due to heat convection without providing power to offset the losses. The variation of the gas temperature and its impact on the [CH_3] density inside the plasma discharge region was plotted in Figure 2.74. In continuous operation the gas temperature remains constant at a fixed position in the reactor once steady state conditions were reached.

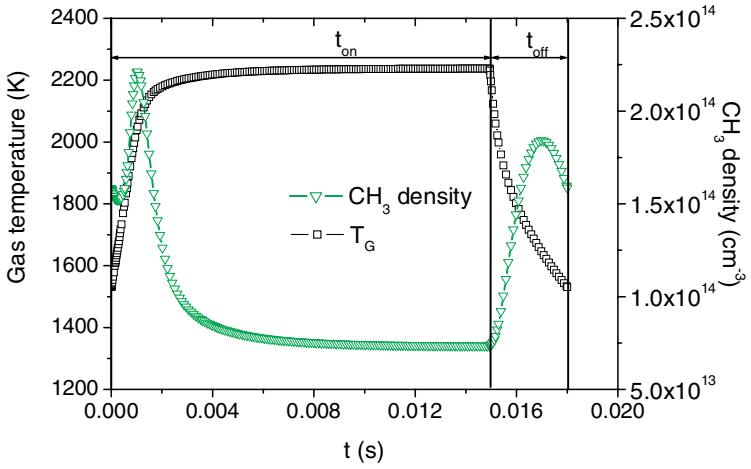

Figure 2.74 Temporal evolution of [H] and [CH_3] calculated in the plasma bulk for t_{on} = 15 ms and t_{off} = 3 ms. CH_3 species production is favoured at the ignition and at the shut down of the plasma when the gas temperature is in the range 1500 - 2000 K. [140]

The temporal development of the [H] and [CH_3] species for different off times t_{off} were evaluated in Figure 2.75. t_{off} of 2 ms was found to be the optimal values as only 50 % of hydrogen is lost during the off time of the plasma while enhancing the [CH_3] density. The enhancement of [CH_3] density for lower t_{off} is reduced, while the hydrogen concentration is greatly reduced when t_{off} increased from the optimal off time of 2 ms as significantly more recombination occurs.

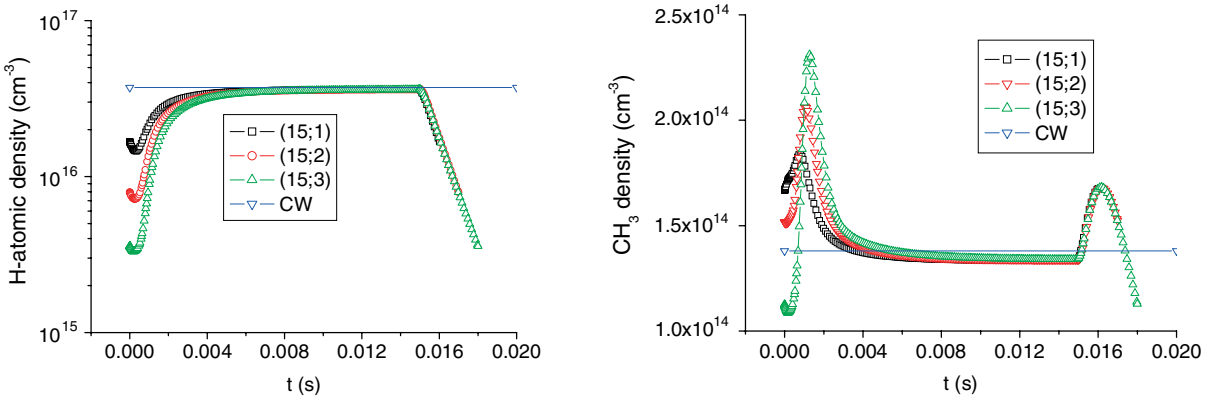

Figure 2.75 Temporal evolution of [H] (left) and [CH_3] (right) calculated iat a distance of 900 µm from the substrate during the pulse for a t_{on} of 15 ms and a t_{off} varying between 1 ms and 3 ms. [140]

The temporal development of the [H] and [CH_3] species for different off times t_{on} were evaluated in Figure 2.76. It was found, that [H] needed around 4 ms to reach 80 % of its steady state value, which is the minimum desired ensity. Hence, for t_{on} of 8 ms only 50 % of the on state were in the desired high hydrogen density range, while the fraction increased to 75 % when t_{on} was 15 ms. Thus, t_{on} of 15 ms was identified as the optimal on state duration.

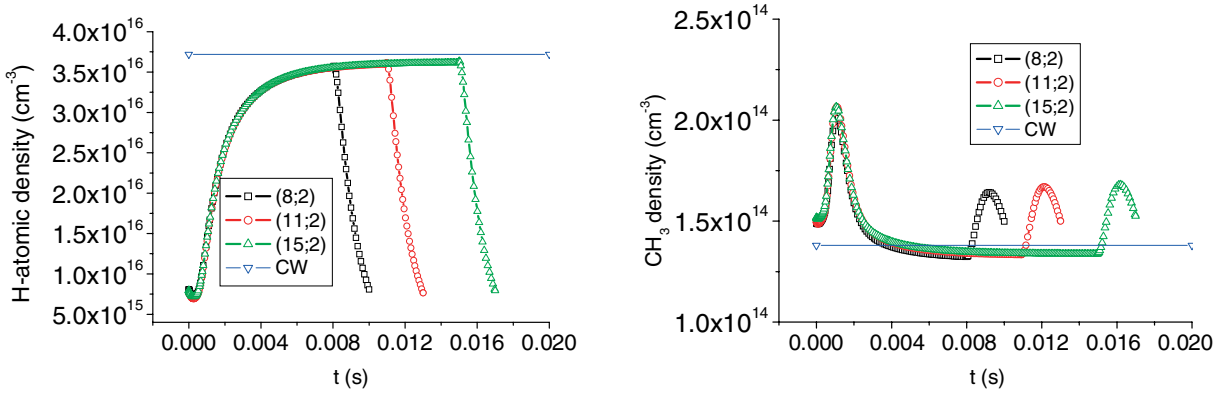

Figure 2.76 Temporal evolution of [H] (left) and [CH_3] (right) calculated iat a distance of 900 µm from the substrate during the pulse for different t_{on} and t_{off} of 2 ms. [140]

Overall, Brinza et al. [140] reported that t_{on} = 15 ms and t_{off} = 2 ms were the most efficient pulsing durations. This was experimentally verified, see Section 2.9. The frequency, corresponding to the pulsing durations, was 58.8 Hz and the duty cycle was 88.2 %. However, Brinza et al. [140] do not comment on why their recent findings are vastly different compared to previous results, i.e. Lombardi et al. [135] and Gicquel et al. [139] suggested low duty cycles, as low as 17 % to enhance the generation of [H] and [CH_3] species.

2.9 Diamond synthesis using pulsed microwave discharges

Diamond synthesis using pulsed microwave discharges was demonstrated by various research groups [140, 143, 144, 145, 146, 147, 148] and reported on an increased growth rate across the board.

Vikharev et al. [143] reported on PCD growth using a type A version of the MCPR between 50 and 70 Torr. The pulsing frequency was between 60 and 1000 Hz. They reported on pulsing as an efficient way to enlarge the discharge dimensions, which could be utilized in a larger growth area.

Tallaire et al. [144] were the first to report successful SCD deposition using pulsed discharges in the LIMHP reactor [70]. Process pressures were up to 202.5 Torr. No information on the pulsing frequency was reported, while duty cycles were selected as 50 %. Pulsing was found to increase the growth rate by 40 % when the same average power was applied. Additionally, they reported on less reactor heating in pulsed operation. Subsequently, the larger discharge dimensions under pulsed conditions due to the higher peak power levels were utilized by Tallaire et al. [145]. Three SCD samples were grown simultaneously. Based on the given power density of 95 W cm^{-3} the pressure was expected to be around 170 Torr [70]. The reported pulsing frequency was 750 Hz with a 50 % duty cycle. The growth rates for the three grown diamond films were 9, 12 and 19 µm h^{-1}. The sample, which grew much faster was located in the center of the deposition area. The sample was significantly (100 °C) warmer than the others and encountered a thermal run away in temperature, which increased the growth rate significantly.

Brinza et al. [140] supported their modeling efforts with some SCD deposition experiments. They found, that on times t_{on} of 15 ms and off times t_{off} of 2 ms increased the growth rate by 25 %. The on and off times corresponded to a frequency of 58.8 Hz and a duty cycle of 88.2 %. Surprisingly, they reported on reduced deposition rates for certain other combinations of t_{on} and t_{off} as shown in Figure 2.77.

Muchnikov et al. [146] reported on pulsed SCD deposition up to 250 Torr for 150 and 250 Hz at a 50 % duty cycle. They reported in an overall growth rate increase when pulsing

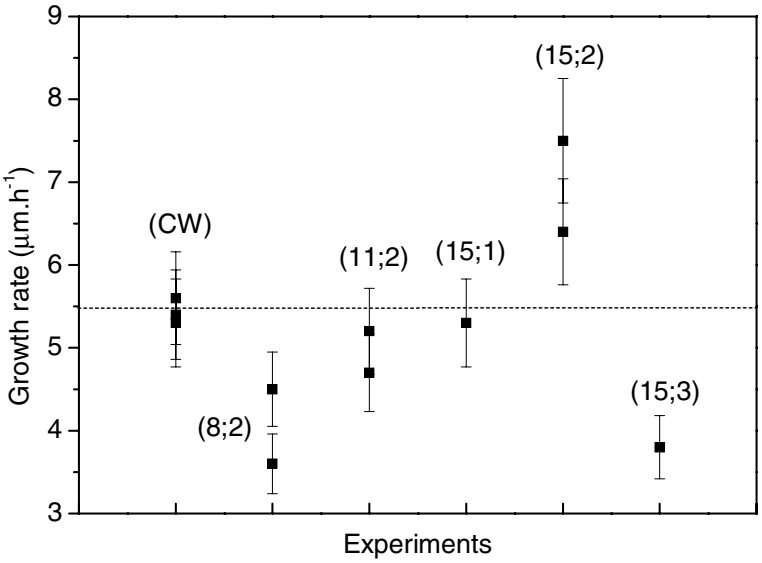

Figure 2.77 Growth rate of the different samples for different t_{on} and t_{off}. The dot line represents a guide for the eyes corresponding to the growth rate obtained in continuous mode. For specific conditions, an increase of the growth rate is obtained while injecting a low MWMP. [140]

compared to continuous excitation as shown in Figure 2.78. The exact effect is hard to quantify as the pressure was increased simultaneously with the pulsing. Additionally, it was found that pulsing at 150 Hz resulted in 30 % higher growth rates compared to 250 Hz.

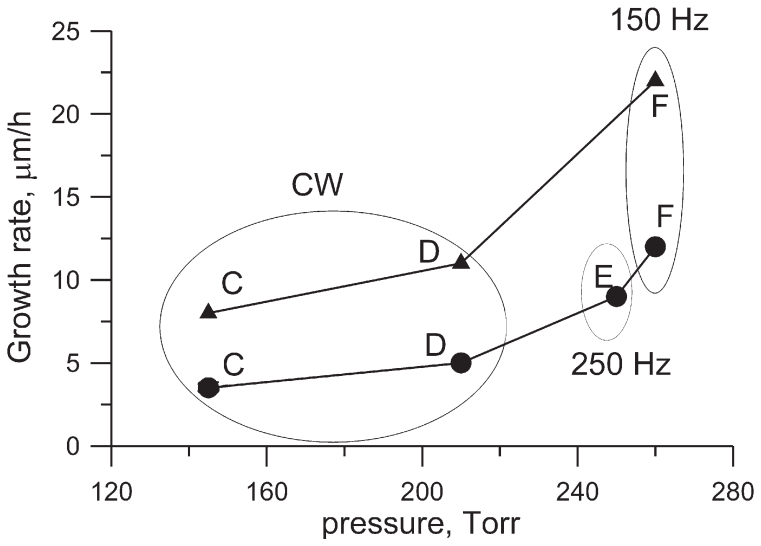

Figure 2.78 Dependence of the SCD growth rate on the gas pressure for CW and PW regimes at the same MWPD of 200 W cm^{-3} and the methane content of 4 percent (circle) and 8 % (triangle). [146]

Vikharev et al. [147] reported on PCD growth between 60 and 160 Torr for frequencies between 50 and 1000 Hz. They reported, that the growth rate was increased for the entire frequency range compared to continuous excitation. Additionally, 250 Hz was found as optimum frequency. This was in contrast to their previous reports on SCD deposition [146].

Yamada et al. [148] reported on a different pulsing approach. They investigated sub-ms pulses in the kHz range as 2 ms are sufficient for dissipation of radicals [140]. The studied frequency range was between 1 and 80 kHz and was supposed to promote inelastic collisions of electrons. SCD deposition was performed on 10 mm × 10 mm CVD-grown seeds and used 4.7 % CH_4 and 60 ppm N_2 in the gas phase. An enhancement of the growth rate by a factor of 4 was reported for on times of 10 µs. However, they reported, that the plasma became unstable at 120 Torr. The plasma was stabilized by increasing the on times to 50 µs, but the growth rate reduced significantly from 40 to 25 µm h^{-1} eliminating much of the enhancement previously achieved. Overall, it can be assumed, that the minimum on time required to provide a stable plasma, will increase even more when using pressures in the 300 to 400 Torr range probably reducing the beneficial effects even more. Hence, it remains questionable, if this different approach can be utilized efficiently at higher pressures.

Chapter 3

The reactor and experimental techniques

3.1 The reactor and associated systems

3.1.1 The microwave plasma cavity reactor

The experiments employ a specific plasma reactor geometry identified here as the microwave cavity plasma reactor (MCPR) [31]. The cross sectional schematic view of Reactor B is shown in Figure 3.1. Lu et al. [31] reported on the reactor specifications and dimensions in detail. The plasma discharge is achieved by utilizing a TM_{013}/TEM_{001} hybrid mode within the cylindrical applicator. The resonator length L_s and the probe position L_p were adjusted. The highest sensitivity of the reactor coupling efficiency is with respect to the resonator length [57]. Just small variations in Ls are enough to detune a well-matched reactor. Nad et al. [57] reported that a mismatch as little as 2 mm can result in a drop of reactor coupling efficiency ν by as much as 20 to 25 %. This illustrates how important a good understanding of the reactor operational performance is and how critical a proper tuning, i.e. matching, of the reactor is. All experiments reported here were carried out with a fixed reactor geometry. The following fixed cavity dimensions were employed: $L_s = 21.4$ cm; $L_p = 3.6$ cm and $Z_s = L_1 - L_2 = -4$ mm. The applicator and cooling stage dimensions were fixed for Reactor

B as follows: R_1= 8.9 cm, R_2 = 7.0 cm, R_3 = 1.9 cm and R_4 = 3.2 cm [31]. The reactor operated very efficiently, such as no reflected power was recorded, with this set of parameters over the range of the experimental conditions, i.e. pressures of 120 tor 400 Torr, used in this investigation.

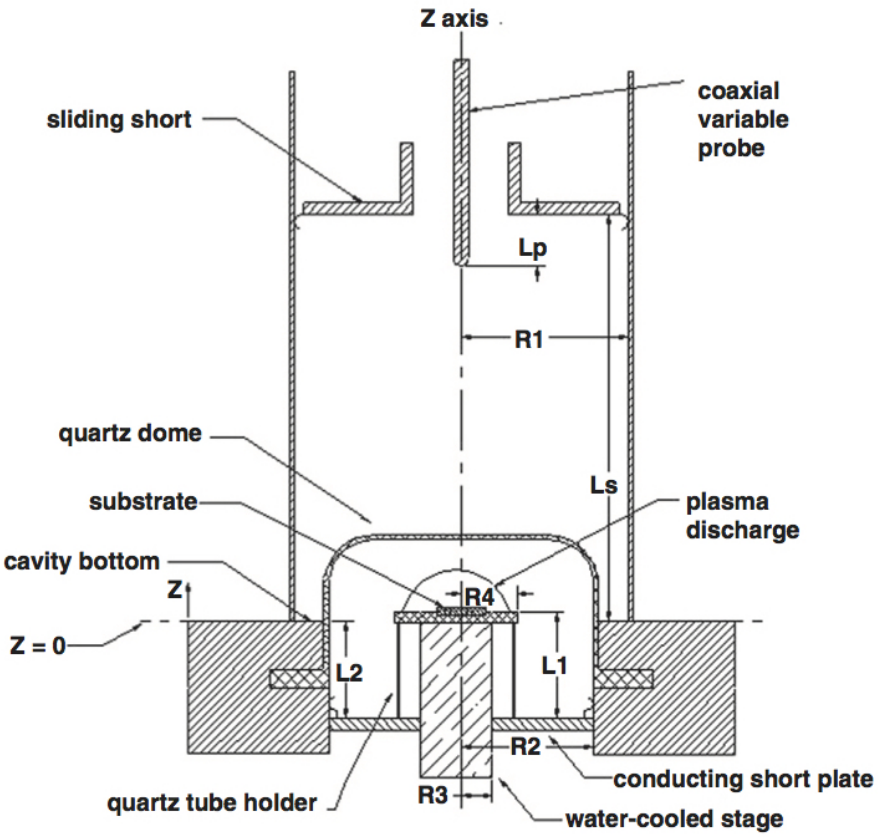

Figure 3.1 Cross sectional schematic view of Reactor B. [31]

3.1.2 Peripheral systems

The MCPR has a set of peripheral subsystems, which are required for operation. The schematic of a complete diamond deposition system, including its subsystems, is shown in Figure 3.2. It consists of five major subsystems: (1), the microwave power delivery and trasmission subsystem (2), the chamber subsystem (3) the gas flow control subsystem, (4) the

pressure control subsystem and (5) the cooling control subsystem and has been extensively described previously [43] [60] [149] [150].

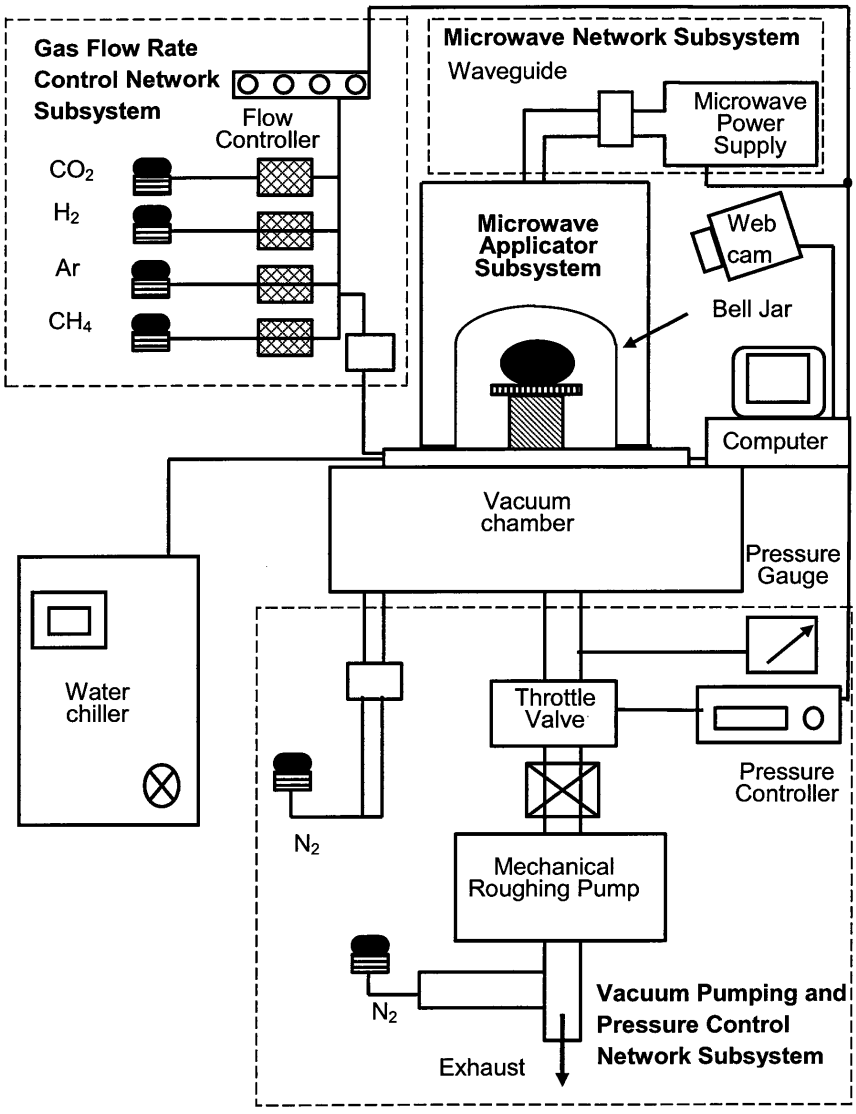

Figure 3.2 Schematic of the various peripheral system on a MPACVD reactor for diamond synthesis. [149]

The microwave power supply is discussed in detail in Section 3.1.3. The electromagnetic microwaves are transmitted to the cavity through rectangular waveguides and coupled into the reaction chamber through a coaxial coupling probe, which serves as antenna. Incident and reflected power levels are measured by the power supply unit.

The chamber subsystem consists of the vacuum chamber, the microwave plasma cavity applicator, the quartz bell jar and the substrate holder configuration, whose position inside the reactor is flexible with variables $Z_s = L_1 - L_2$. The cavity consists of a cylindrical wall and a movable sliding short at the top. A coaxial coupling probe is inserted into the cavity at the top center point. This cavity design allows the adjustment of the sliding short position in order to change the cavity resonator length L_s and coupling probe position inside the resonator L_p. Having freedom over these four parameters (L_1, L_2, L_s, L_p) allows to optimally match the resonator to achieve coupling efficiencies of almost 100 % [57]. The cavity is under ambient conditions and sits on top of the reactor chamber, which is filled with process gases (H_2, CH_4, ...). The reactor chamber is separated from the cavity through a quartz bell jar. This dielectric window allows the transmission of microwaves into the discharge region and helps to stabilize the discharge. This discharge region needs to be separated from the ambient environment and is part of the microwave gas handling system. The substrate holder configuration contains of a molybdenum substrate holder and a diamond seed crystal, which is placed on top of the actively cooled stage [67].

The gas flow control subsystem consists of a gas manifold, which feeds several input gases into the process chamber. Individual gas lines are opened and closed with pneumatic valves and individual flow rates are controlled by MKS mass flow controllers. Typical gases used for SCD synthesis are hydrogen (H_2) methane (CH_4) [44]. Additionally, argon (Ar) [84] or nitrogen (N_2) [69] can be added to enhance the SCD growth rate.

The pressure control system consists of a mechanical roughing pump (Alcatel 2020A), pressure gauges and a throttle valve. The pump is used to pump down the chamber to a base pressure of 1 mTorr. A 1000 Torr Baratron (MKS 626A13TBE) is used for monitoring the process pressure. A Pirani (KJL275863LL) is used for recording the base pressure and is

isolated from the chamber by a pneumatic valve during deposition runs. A throttle valve is located between the vacuum chamber and the roughing pump and its position is adjustable and can be varyied between fully closed and fully open. This regulates the chamber pressure as the throttle valve position is controlled by a throttle valve controller (MKS Type 152A).

The cooling subsystem consists of a recirculating chiller (Lytron RC045J03BG0C011), corresponding cooling lines and water flow meters to actively cool the microwave power supply, the microwave plasma cavity applicator, the vacuum chamber and the substrate holder configuration.

Several thermocouples are installed to the system in order to monitor the temperature of individual components of the reactor. Operation and control of the individual components is achieved by using a computer program, which was built using LabView 2016. The program includes interlocks, which will automatically shut down the reactor in case of an emergency. The shut down procedure consists of the following items: (1) setting the input power level to 0 W to turn off the plasma, (2) turn off the process gases and (3) pump down to base pressure.

A detailed discussion on the various variables and their influences on the performance of a MPACVD reactor can be found in Chapter 7, Figure 4 of the Diamond Film Handbook [43].

3.1.3 The stable and pulsable microwave power supply

The previous studies [30, 31, 57] used a Cober S6F microwave power supply with an excitation frequency of 2.45 GHz. This model was lowly filtered and had a significant ripple due to the AC to DC rectification. The resulting microwave excitation was pulsed with the superposition of two pulsing frequencies at 60 and 360 Hz. The 60 Hz is due to the input AC frequency and

360 Hz is caused by the three phases, which have been rectified. Thus, the microwave output fluctuated significantly versus time. These effects were optically visualized by a flickering plasma, which could even move around inside the reactor throughout a SCD deposition experiment. That behavior became especially problematic around 300 Torr, where those fluctuations frequently disturbed the discharge enough to die off for long enough that during operation sometimes reignition failed. This limited the operational pressure range of the reactor.

Thus, for the experiments presented in this dissertation the microwave power supply was upgraded with a stable well-filtered power supply. The reactor was equipped with a Muegge MX3000D-123KL switch mode microwave power generator and a MH3000S-210BB magnetron head. The ripple of the generator is less than 5 %. This microwave power supply can be operated in continuous or in pulsed excitation modes. Thus, it is possible to generate an almost ideal square wave when operating in pulsed mode. The pulsing schematic is shown in Figure 3.3. It is possible to set the high $\mathrm{P_{high}}$ and low power $\mathrm{P_{low}}$ values between 0 and 3000 W. Additionally, the high $\mathrm{T_{high}}$ and low durations $\mathrm{T_{low}}$ can be set to full digit numbers between 1 and 24 ms. Those four input variables are defining the pulsing frequency, duty cycle and average power consumption as follows:

$$f = \frac{1000}{T_{\mathrm{high}} + T_{\mathrm{low}}}\ [\mathrm{Hz}] \tag{3.1}$$

$$\text{duty cycle} = \frac{T_{\mathrm{high}}}{T_{\mathrm{high}} + T_{\mathrm{low}}}\ [\%] \tag{3.2}$$

$$P_{\mathrm{avg}} = \frac{T_{\mathrm{high}} \cdot P_{\mathrm{high}} + T_{\mathrm{low}} \cdot P_{\mathrm{low}}}{T_{\mathrm{high}} + T_{\mathrm{low}}}\ [\mathrm{W}] \tag{3.3}$$

The frequency can be set between 0 and 500 Hz by selecting the high and low durations, but values are limited to a discrete set of frequencies. The pulsing frequency and duty cycle are linked and different frequencies with the same duty cycle and vice versa can be selected.

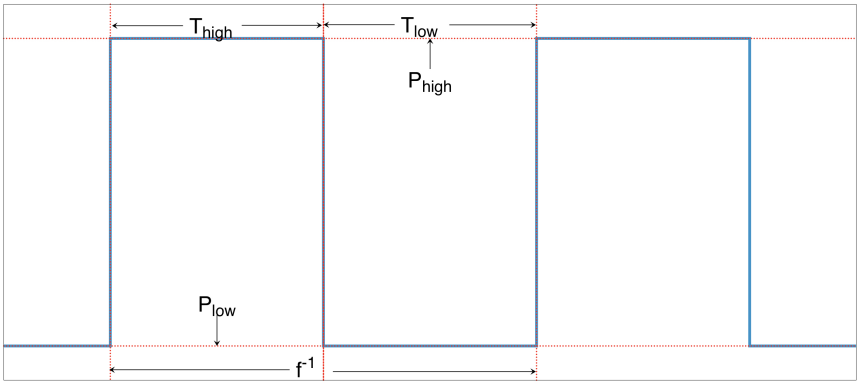

Figure 3.3 Shape of the pulsed microwave excitation generated by the switch mode microwave power generator and its variables.

3.1.4 The optimized pocket holder design for SCD growth

An optimized sample holder design was used to prevent PCD rim formation on the growing SCD [67]. The holder dimensions are given in Figure 3.4 for the use with 3.5 mm × 3.5 mm seed crystals. Figure 3.5 shows the dimensions of a holder optimized for rimless growth on 7.0 mm × 7.0 mm diamonds. The pocket is shallower compared to that used by Nad et al. [72].

3.2 The cutting laser

A Bettonville Ultra Shape 5xs-IR system is used for diamond shaping and laser cutting. It is operated with a continuous wave output Nd:YAG laser system from CSI Group. The output wavelength is 1064 nm. The laser beam is focused on the sample using a computer controlled

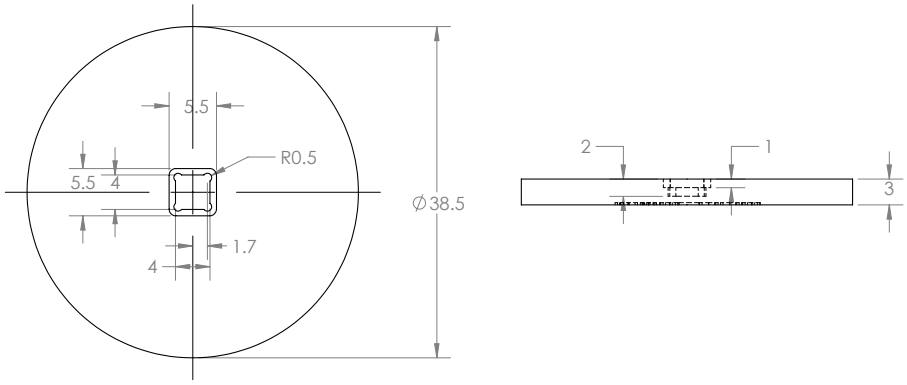

Figure 3.4 Schematic drawing of the pocketed sample holder optimized for rimless SCD growth on 3.5 mm × 3.5 mm substrates including dimensions in mm.

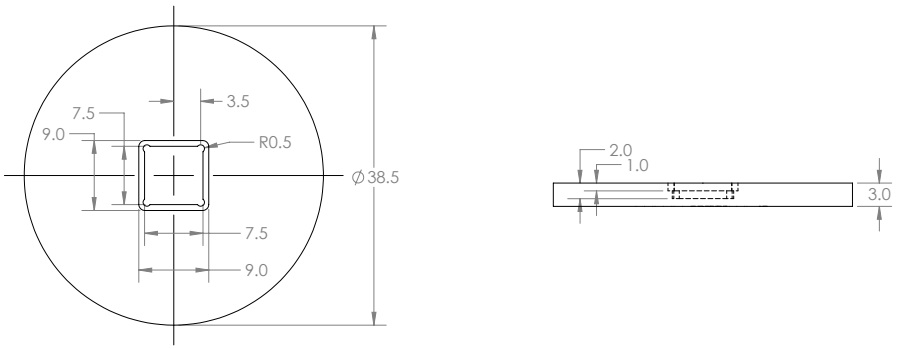

Figure 3.5 Schematic drawing of the pocketed sample holder optimized for rimless SCD growth on 7.0 mm × 7.0 mm substrates including dimensions in mm.

optics. The laser beam is focussed on the cutting surface and the resulting spot size is 20 µm in diameter. The laser power is 18 W and can is adjustable between 10 and 100 % of the maximum power. The diamonds are glued on a cutting holder using Loctite 352 light cure adhesive, which is exposed to a UV-A light emitting diode for hardening of the glue. The holder fits into a robotic cassette, which has five degrees of freedom: in plane (x, y) and vertical (z) movement, as well as in plane rotation and tilting of the sample in the vertical direction. This allows for a variety of different cutting procedures, i.e. in plane framing, slicing off of material and even SCD processing into more complex shapes such as brilliant or princess cut.

3.3 Van de Graaff Accelerator at Western Michigan University

Ion implantation was performed with a 6 MV tandem Van de Graaff accelerator at Western Michigan University [151]. The accelerator tank is filled with a gas mixture of 80 % N_2, 20 % CO_2 and traces of SF_6 at a pressure of 200 psi to avoid sparking by trapping electrons. A radio frequency (RF) ion source and a source of negative ions by Cs sputtering (SNICS) from National Electrostatics Corporation was used for ion generation.

Carbon and oxygen ions passed through a tungsten mesh of 80 % transmission before implanting into the substrates. The substrates were mounted on a holder stage with a two dimensional in-plane freedom of movement. The stage was computer controlled and can be used to irradiate SCD wafers of dimensions up to 3 inches by step-by-step exposure of the entire surface area to the $6 \times 6\,\mathrm{mm}^2$ ion beam to achieve irradiation on surfaces larger than the ion beam dimensions. The ion current on the substrates was measured to determine the irradiation doses.

Proton (hydrogen ion) implantation was carried out in a separate electrically floating scattering chamber. The proton beam was about 7.5 mm in diameter at the substrates. Size and uniformity of the beam on the sample were determined by taking an image on a gafchromic film prior to the actual exposure. After ion beam exposure the samples remained in the scattering chamber at a pressure of around 10^{-4} Torr for 24 hours.

3.4 Analytical Techniques

3.4.1 SCD dimensions

Growth rate and surface area of the grown SCD films have been measured by using a Solartron linear encoder. The thickness of the crystal during growth was determined by averaging five measurements; one in the center and four in the corners of the diamond. Weight gain of the grown SCD films was measured using a Mettler Toledo XS205DU scale.

3.4.2 FTIR spectroscopy

Fourier transform infrared spectroscopy (FTIR) was used to determine the infrared (IR) absorption of SCD plates using a Perkin Elmer 2000 spectrometer. The measurement range was between 2500 and 25 000 nm (4000 to 400 cm^{-1}). The transmitted intensity was recorded and averaged over 16 individual measurements. The absorption coefficient was calculated by applying a model of two parallel optical interfaces (air-diamond-air) [152].

3.4.3 Birefringence Imaging

Birefringence imaging was performed using a Nikon 3000D optical microscope in transmission mode. The diamonds were placed on a custom made sample holder. Two cross-polarizing polarization filters were in the optical path, one before and one after transmitting through the substrates. The ranodmly polarized emitted from the microscope was linear polarized by the first polarizer. Subequently, the polarization of the second polarizer is rotated by 90°. Hence, all the linear polarized light reaching the second polarizer would be absorbed and no transmitted intensity can be detected. The resulting image is black.

If a substrate containing internal crystalline stress is introduced into the optical path,

the presence of the internal crystal stress causes a rotation of the polarization vector of the traversing electromagnetic light wave. Thus, the exiting light beam is a superposition of both polarization orientations (s and p). Now, the second polarizer will only absorb one of the two polarizations and light, whose polarization was distorted due to the presence of internal crystal stress is recorded at the CCD detector. The recorded image shows a 2D projection of the distribution of the internal crystal stress.

The measurement setup offers a fairly good resolution in the range of 5 µm. Unfortunately, the measurements are only of qualitative nature. Using the same exposure time for each measurement reduces some of the uncertainty, but in order to truly perform quantitative measurements a different setup is required, where the individual light intensities are recorded and the amount of birefriengence is calculated in a 2D projection.

3.4.4 Raman spectroscopy

Raman spectroscopy was carried out using an Omnichrome argon gas laser with an excitation wavelength of 514 nm and an output power of a 200 mW. The laser is focussed on the sample using a 1482E MicraMate confocal Raman microscope resulting in a 10 µm spot size by using a 40x magnification lens. Wavelength separation is done using a Horiba Jobin Yvon SPEX 1250M spectrometer with a 1800 cm^{-1} grating and the intensity is measured using a nitrogen-cooled Spectrum One CCD with a spatial resolution of 0.2 cm^{-1}. Full-width-half-maximum (FWHM) of the Raman peak was determined using the software provided fitting routine for Lorentzian shaped peaks.

3.5 Setups for graphite removal

3.5.1 Thermal oxidation

A furnace from Thermo Systems, model Mini Brute 80, was used to perform thermal oxidation experiments. The systems contained a Thermo ANA-Lock Controller for temperature control. The furnace was heated up and and the chamber temperature stabilized for 90 min while being purged with nitrogen before before using the furnace for thermal oxidation experiments. For the thermal oxidation, the nitrogen flow was switched to an oxygen flow of 33 sccm prior to loading the samples into the furnace. ubstrates were placed on a inch silicon wafer, which was held horizontally by the supporting bars of a 4 inch wafer boat. This setup guaranteed fast and secure loading of unloading of the subtrate and ensured sufficient exposure to the oxygen.

3.5.2 Electrochemical etching

A setup similar to the one described by Marchywka [88] was established in order to etch graphite electrochemically. A substrate was immersed into a conductive aqueous solution and held in place between two electrodes. The electrodes were 15 mm × 15 mm of freestanding boron-doped PCD. Both, the substrate and the two electrodes were held in plase by a 3D-printed holder containing slots to vary the distance between the electrodes. The realization of the setup is shown in Figure 3.6. A magnetic stirrer was used to to ensure a constant circulation of the aqueous solution. A Fischer Scientific FB1000 DC power supply was operated in voltage control mode and was used for the generation of the electric potential and the current flow. The power supply was limited to maximum potentials of 1000 V and maximum currents of 1 A. Additionally, the power consumption is limited to 500 W.

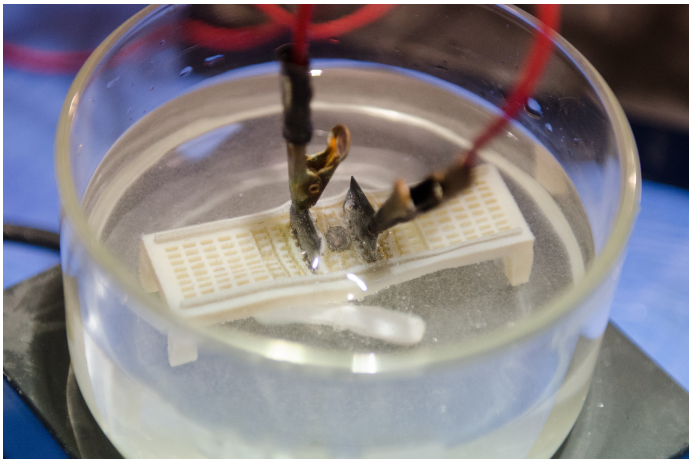

Figure 3.6 Realization of the electrochemical etching setup based on Marchywka [88].

Chapter 4

SCD processing

This chapter was previously published 2014 in volume 42 of Diamond and Related Materials, pages 8-14, under the title *Substrate crystal recovery for homoepitaxial diamond synthesis*. The authors were M. Muehle, M. F. Becker, T. Schuelke and J. Asmussen. Elsevier provided permission for reprint, both electronically and as hardcopy.

4.1 Introduction

The MPACVD synthesis of single crystalline diamond SCD is rapidly progressing with the potential to impact future diamond applications by making the material available at lower cost, higher quality and with wafer dimensions comparable to other semiconductor wafer substrate materials. Since the synthesis of SCD was first achieved [153], significant improvements were reported such as growth rates exceeding $100\,\mu m\,h^{-1}$ [65] and the synthesis of electronic grade diamond [154]. To date high-quality SCD is fabricated of sufficient size to implement sophisticated diamond applications. For example, advanced optical SCD applications such as Raman laser crystals [10, 155] and X-ray optical components [6, 7, 156, 157, 8, 158, 159, 160] are emerging. Successful wafer based ultraviolet (UV) emitting opto-electrical devices as well as electronic device fabrication were recently reported [161, 162, 163, 164, 165]. Many

advanced applications require large crystals to become economically feasible for diamond device manufacturing. Economic viability requires reuse of the diamond seed crystals. Furthermore, to achieve consistent reproducible high quality CVD grown diamond it is necessary to at least maintain a constant seed crystal quality. Thus it is desirable to develop a seed recovery process that does not introduce additional defects into the seed crystal surface. The need for a cheap and efficient seed recovery process becomes apparent, when multiple substrates, i.e. 80 or more [166], are used per process run.

There are different ways to separate the grown material from the seed crystal. Ion implantation creates a thin carbon defect layer in the seed crystal, which then separates the seed with low material loss [92, 94]. However, the method requires highly sophisticated machinery and processing time. Another approach used by researchers is laser cutting. Since modern diamond gem processing uses a laser for facet cutting that technology is already well developed. Insights of the diamond laser ablation process are discussed in [167]. However, there have been no publications on laser cutting with the purpose of seed separation or recovery. In this paper we describe a three-stage seed recovery procedure, which can be performed with commercially available laser cutting equipment. It is shown that the growth process and post-processing do not affect the seed crystal. This allows the recovery of the seed for multiple uses and opens the potential for seed crystal surface engineering via laser processing.

4.2 The three stage SCD material separation process using laser cutting

The seed crystal recovery is a three-stage process that has been performed on over several hundreds of samples. First, the grown CVD material is separated from the seed by laser cutting. The high power density output allows cutting a 3.5 mm × 3.5 mm sample within 5 minutes. The cut of a 7 mm × 7 mm seed takes approximately 20 minutes. Two different mounting setups are available: one with freedom of sample rotation and inclination towards the laser beam and one which can perform up to 12 cutting processes with fixed sample rotation. Usually the cut is performed in the interlayer between the seed and grown crystal material. Material loss occurs due to the nature of the process. As shown in Figure 4.1 a triangular cutting profile is performed resulting in one straight and one inclined cut with a height difference of the profile depth. The laser beam is scanned horizontally over the sample and ablating 90 µm deep and 25 µm broad layers without repetitions on each spot. Recent focus is set on a two-stage laser cutting procedure with reversed profiles to achieve two straight cuts. The profile is limited by the laser spot size and the chosen angle. Best results are achieved with an angle of 35 mrad resulting in approximately 175 µm material ablation for 3.5 mm × 3.5 mm samples. This increases to 350 µm for 7 mm × 7 mm substrates. This effect is almost linear and will reach 500 µm when separating CVD-grown material from 10 mm × 10 mm substrates. When out of focus the spot size will increase and the cutting profile is widened causing more material loss. When cutting in the HPHT/CVD interface the type Ib HPHT material loss is in the range of 30 to 50 µm and mainly determined by the operators skill to identify the bottom end of the seed crystal after mounting. The increased material loss with increased substrate size is a disadvantage of laser separation.

For a 10 mm × 10 mm sample and having a SCD growth rate of 20 µm h^{-1} this results in the loss of one day worth of growth time due to the cutting procedure. By using better optics the laser spot size and cutting angle can be reduced resulting in lower material loss due to a more narrow profile. With increasing growth rates, such as exceeding above 100 µm h^{-1} [65], the material loss due to the laser ablation becomes less of an issue.

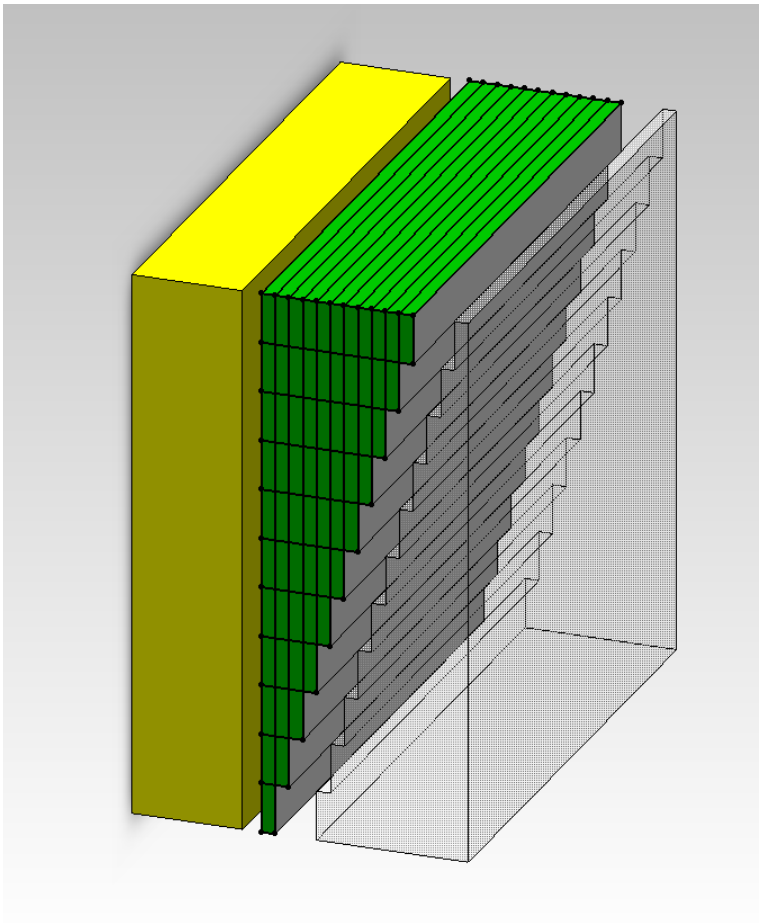

Figure 4.1 Cutting profile for seed substrate separation. The yellow crystal is the type Ib HPHT seed substrate, the grey part is the remaining CVD-grown material and the green part is the ablated diamond material. Each ablated segment is 25 µm wide and 90 µm deep.

Laser cutting introduces surface and subsurface damage. Therefore after laser cutting the seed crystal surface is polished using a Coborn PL3 planetary lapping bench. A solution of diamond powder in olive oil is brought on the rotating cast iron wheel and thermo-mechanical

polishing takes place. The rotation speed is 3000 rpm. The material ablation caused by polishing is in the range of 20 to 50 µm. Techniques used in polishing have been discussed in more detail in a recent publication [168].

The material loss of the seed substrate through the entire process amounts to 50 to 100 µm. The lower seed thickness limit for mechanical polishing is in the range of 200 to 250 µm. Polishing thinner plates often result in cracking the thin plate. Thus a seed can be reused up to 20 times before it becomes too thin to be reused.

The MPACVD growth process may also lead to the undesired formation of polycrystalline diamond material on the outer edges of the newly grown single crystal. Polycrystalline material may even begin to overgrow onto the sidewalls of the seed crystal and can subsequently negatively affect future growth processes. Such polycrystalline "rims" are therefore removed by laser cutting and the seed substrate is trimmed back to its dimensions before the growth process by laser cutting. If desired the trimmed sides of the crystals can also be polished to eliminate laser-introduced damage. Finally the recovered seeds are wet-chemically cleaned to prepare them for another homoepitaxial growth process.

4.3 SCD quality throughout the procedure

4.3.1 FTIR spectroscopy

FTIR absorption spectra such as shown in Figure 4.2 were measured on the HPHT seed plates throughout the processing steps. For all steps the absorption coefficient in the spectral range of 1500 to 4000 cm^{-1} is similar to published data [169]. The spectra show the typical two- and three-phonon absorption regions between 1900 to 2500 cm^{-1} and 3260 to 3560 cm^{-1}. Additional absorption bands can be identified for HPHT crystals between 1000 to 1400 cm^{-1}.

These are also shown in more detail in Figure 4.3. These can be attributed to nitrogen related crystallographic defects in the diamond lattice [71].

FTIR absorption is frequently used to detect and quantify the presence of nitrogen defect centers in natural and synthetic diamonds. Substitutional nitrogen atoms in the diamond lattice are referred to as C centers. C centers are the dominant defect in type Ib diamonds such as yellow colored HPHT crystals. A considerable yellow coloring occurs at about 10 ppm of substitutional nitrogen in the diamond lattice [71]. C centers have IR absorption peaks at $1130\,\mathrm{cm}^{-1}$ and $1344\,\mathrm{cm}^{-1}$, which can be used to quantify the defect concentration. For example, the amount of substitutional nitrogen atoms correlates linearly with the absorption coefficient at $1130\,\mathrm{cm}^{-1}$ where a value of $1\,\mathrm{cm}^{-1}$ equals (25±2) ppm of nitrogen [170].

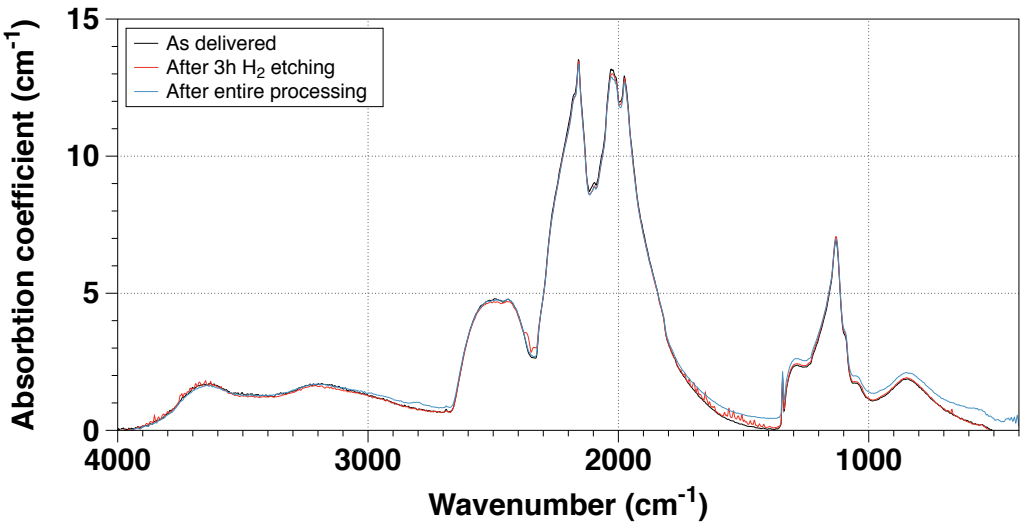

Figure 4.2 FTIR absorption spectra of HPHT crystals throughout their process steps showing the two-, three-phonon and C center absorption.

Figure 4.3 shows in greater detail the part of the spectra identifying the nitrogen impurities. These spectra have the shape typical for C center dominated type Ib diamonds. From the peak heights we determined that the nitrogen content in as-delivered HPHT crystals ranged from 110 to 180 ppm for various samples. Throughout the process steps the nitrogen concentration

detected in the seed crystal shown in Figure 4.3 is 173 ppm as received from the supplier, 176 ppm after 3 hours of etching in hydrogen plasma and 174 ppm after 143 hours of MPACVD growth and seed recovery processing. The variations throughout the processing steps are within the experimental error of the used spectrometer and sample mounting. This behavior was verified on multiple samples.

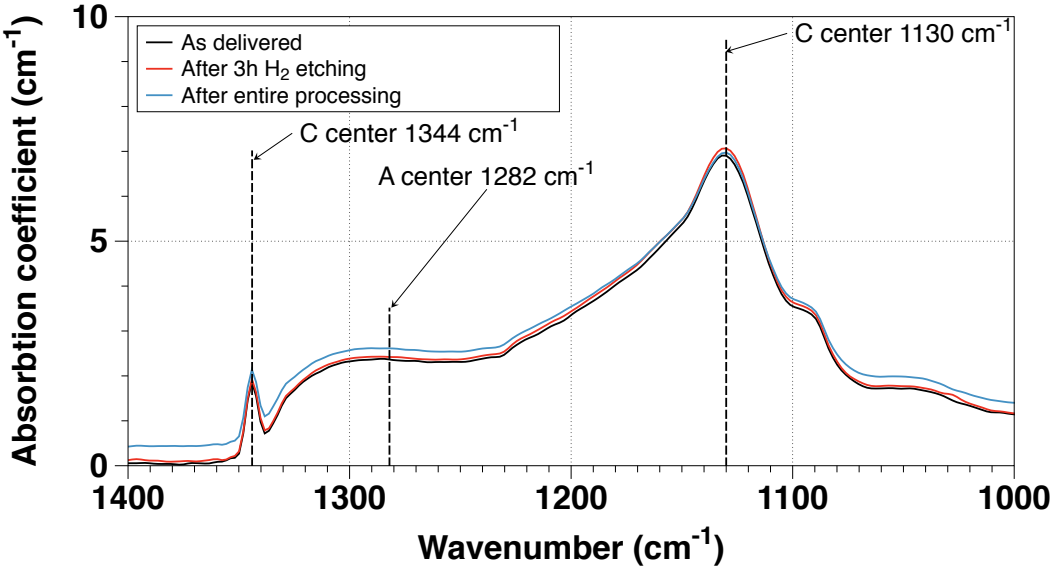

Figure 4.3 Detailed FTIR spectra in the region of nitrogen center absorption.

The transformation from C to A centers (A-aggregate) and a corresponding shape change of FTIR spectra are frequently observed when type Ib diamonds are annealed in a HPHT environment [170, 171, 172]. For example, Surovtsev et al. [171] report a complete conversion of all C centers to A centers when exposing C center dominated type Ib diamonds for 10 hours to 6.5 GPa pressure at 1800 °C. In the FTIR spectra the C center peak reduces and a clear A center peak emerges at wavenumber 1282 cm^{-1} (see examples in [170]). Such behavior was not observed in our spectra. Similarly, processing conditions with temperatures from 1400 to 2200 °C for up to 12 hours were discussed by Meng et al. and were described as a low pressure high temperature (LPHT) treatment [36]. The LPHT process did significantly

decrease the absorption across the UV, visible (Vis) and IR ranges in MPACVD grown crystals demonstrating a substantial effect of such conditions on optical properties and defects in diamond crystals. Our seed crystals on the other hand are exposed to a low pressure hydrogen dominated environment of up to 160 Torr (21.3 kPa) at lower temperatures of about 1200 °C. A typical exposure time is up to 145 hours, which includes an initial pure hydrogen plasma etching of several hours. The principle shape of the FTIR spectra measured for the HPHT crystals shown in Figure 4.3 did not change during MPACVD processing. Thus our growth process has no annealing effect on the seed crystals. As seen in Figure 4.3 the seed recovery procedure does not influence the nitrogen concentration in the crystal. Throughout the entire growth and post-processing process the HPHT crystal remains constant with respect to its nitrogen concentration and distribution of defect center agglomeration.

4.3.2 Surface profilometry

Line scans in different orientations were performed and the average roughness values were calculated. A new HPHT seed had an average R_a of 2.13 nm and $R_{z,din}$ of 17.16 nm. After laser cutting both roughness values significantly increased to an R_a of 179.84 nm and an $R_{z,din}$ of 1104.76 nm. The surface roughness increased approximately one hundred times. This shows the high amount of surface damage introduced by the laser cutting procedure. After polishing the roughness values reduced to 2.51 nm for R_a and 16.87 nm for $R_{z,din}$. Both values are in the same range as measured on new substrates (externally polished by the vendor). Thus the overall recovery process does not significantly increase the surface roughness and our in-house performed mechanical polishing process results in a similar surface roughness as new seed substrates.

4.3.3 Birefringence imaging

Birefringence imaging was performed to obtain information about the spatial distributions of internal stresses throughout the crystal. Some typical images are shown in Figure 4.4. The as-delivered HPHT (first row) crystals show a cloverleaf shaped birefringence intensity pattern. These patterns are associated with (110) growth directions during the HPHT growth process [173]. The average birefringence intensity remains constant after 3 hours of hydrogen etching (second row), SCD growth and seed recovery (third row) and after PCD trimming (fourth row). The hydrogen etching and the deposition processes do not have an annealing effect on the seed crystal. Additionally it is shown that the recovery process maintains the seed crystal's original properties, which improves the consistency when reusing these seeds for homoepitaxial CVD diamond growth. As is shown in Figure 4.4, third row the presence of polycrystalline material grown at the HPHT seed substrate can be seen after removing the CVD-grown layer. The middle picture and the birefringence image on the right are recorded in bright-field setup. Thus the polycrystalline material appears black. The change in crystalline quality from SCD to PCD in the transition region causes a high amount of stress, which can be identified in the birefringence image as bright thin dots/lines at the edges of the crystal. The effectiveness of PCD trimming can be seen in Figure 4.4, fourth row. No overgrown black areas indicating PCD material can be seen in the center picture.

4.3.4 Raman spectroscopy

Raman spectroscopy is often applied to investigate the crystalline quality of diamond by measuring the FWHM of the single phonon line at $1332\,\mathrm{cm}^{-1}$. Type Ib HPHT diamonds have typical FWHM values between 1.9 to $2.0\,\mathrm{cm}^{-1}$. The values recorded for the as received seed

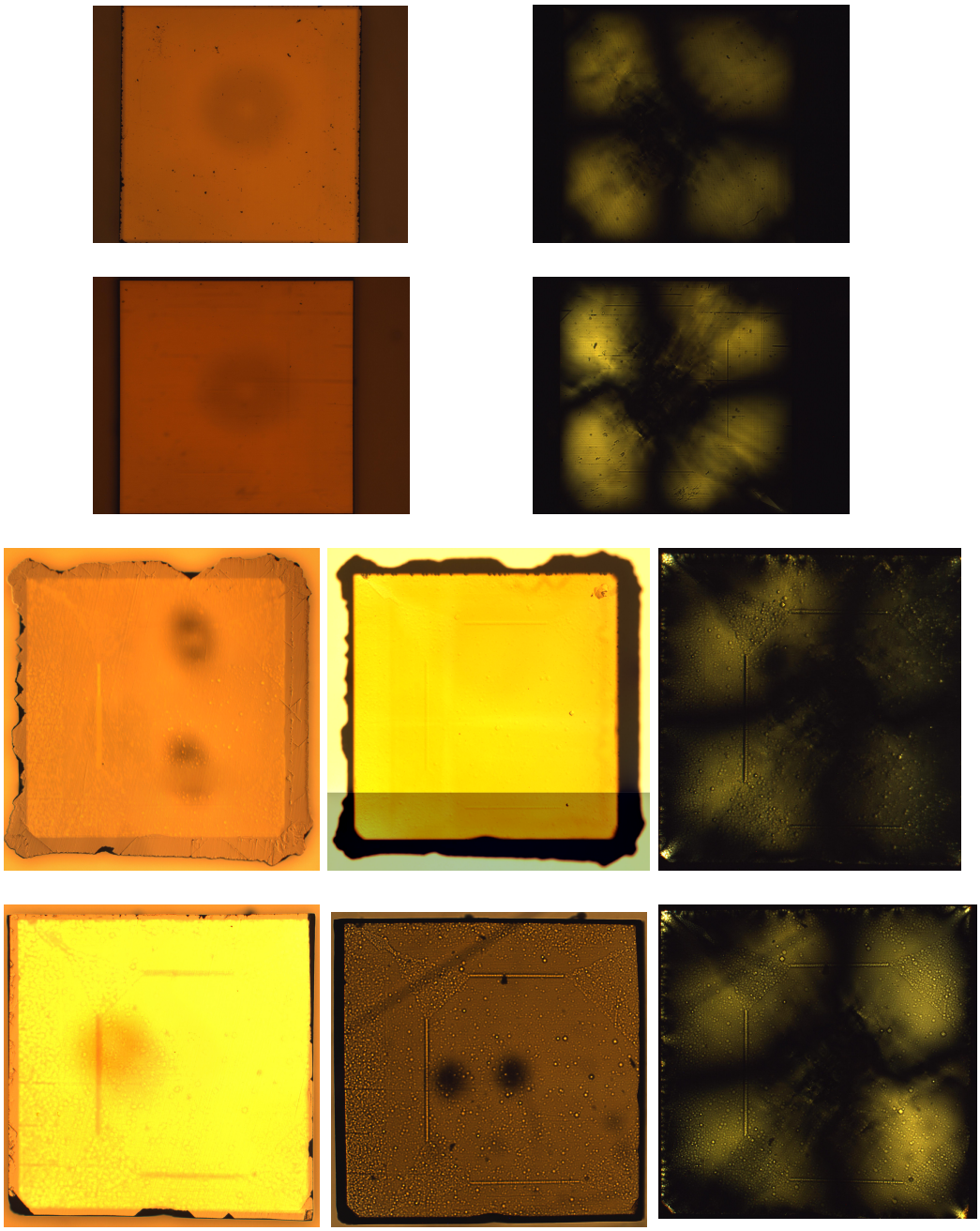

Figure 4.4 Microscope and birefringence pictures of the process steps; First row: top surface and birefringence picture of an unused type Ib HPHT seed crystal; Second row: top surface and birefringence after 3 hours of hydrogen plasma etching; Third row: top surface, bright-field and birefringence image of the type Ib HPHT crystal after laser separation and polishing; Fourth row: top surface, bright-field and birefringence image of the type Ib HPHT crystal after PCD trimming.

crystals ranged from 1.78 to 2.09 cm^{-1}. The FWHM's for recovered seeds ranged from 1.76 to 2.06 cm^{-1}. All individual values are within the same region. Surovtsev et al. [171] showed the dependency of the FWHM as a function of nitrogen concentration. Thus the Raman FWHM data also suggest that the nitrogen concentration in the seeds remains unchanged during the recovery process.

The first order Raman signal position shifts with mechanical stresses in the diamond crystal. The peak shift $\Delta\omega = \omega - \omega_0$ can be converted to stress values using a stress-shift relation [174]. In this case 0 is the absolute peak position of a truly unstressed diamond. Recorded Raman spectra from 15 to 25 locations per sample showed a range of peak positions indicative of a stress distribution present in the crystal. Due to the unavailability of an unstressed diamond sample the reference peak position 0 remained unknown and absolute stress values were not calculated. However, the maximum range of peak positions max can be obtained without knowing 0 and reflects the maximum stress variation within a sample. Such data are plotted for 3 as-delivered and 4 recovered HPHT samples in Figure 4.5. The samples are clearly stressed with absolute variations ranging from 20 to 60 MPa depending on the sample. On average such stress variations in as-delivered and recovered HPHT diamonds are very similar with 43.6 MPa and 41.7 MPa. This result indicates that the stress states in recovered samples did not significantly change during processing.

4.4 PCD rim removal by laser framing

The polycrystalline rim added during growth has much lower crystalline quality and contains grain boundaries. Even though the top surface area is increased after the growth process, trimming the area back to its original size is recommended before performing another

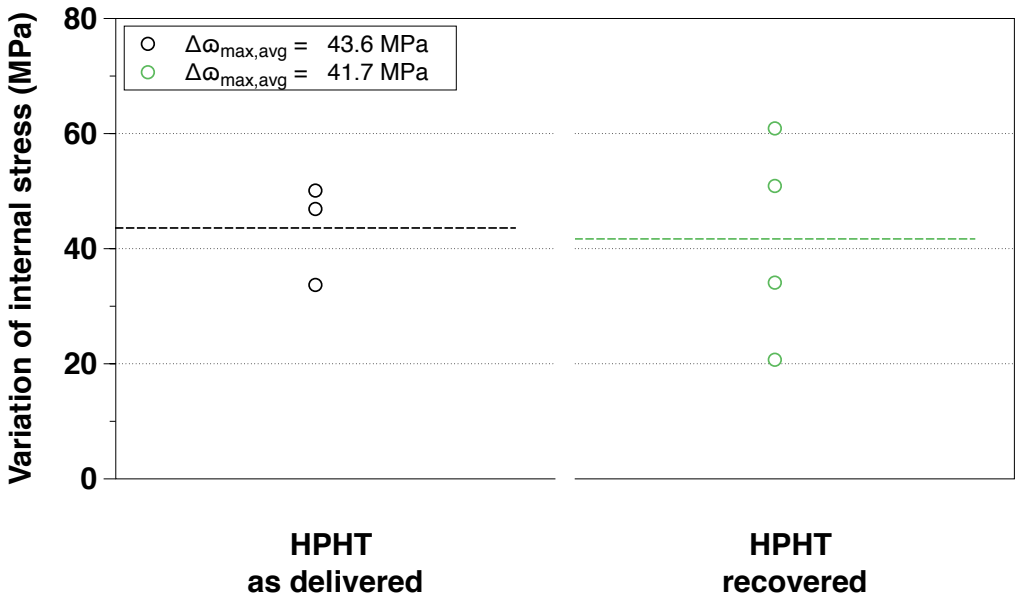

Figure 4.5 Maximal internal stresses for HPHT diamonds, calculated based on Raman peak shifts and sorted, $\Delta\omega_{\mathrm{max,avg}}$ is the average variation of internal stress for this sample group.

deposition experiment on the recovered seed crystal. PCD material will continue to grow if the PCD material at the edges of the recovered seed is not removed. The PCD rim expands with increasing growth time and slowly grows in towards the inner crystal area. The SCD diamond surface size slowly shrinks with increasing growth time. This can be seen in Figure 4.6, where 142 hours of deposition are added on a CVD-grown layer without removed PCD material. The increasing dimensions of the PCD and the decreasing SCD area can be clearly identified. The SCD area decreases from 7.1 mm × 7.0 mm (red rectangle) to 6.2 mm × 6.2 mm (green rectangle) during the MPACVD growth process with a thickness of 1.54 mm for the grown layer. Thus it is necessary to remove the PCD material at the seed substrate edges prior to the process to ensure high crystalline quality SCD growth over the entire seed crystal area. This applies to any seed recovery technique used.

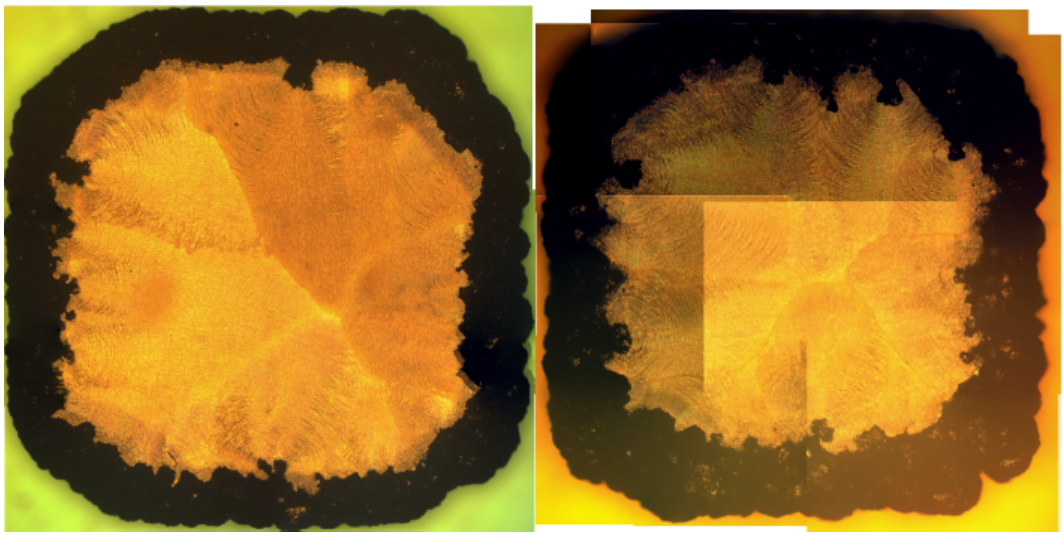

Figure 4.6 Merged microscope images of an untrimmed CVD-grown layer before (left) and after 142 hours of deposition (right).

4.5 CVD seed substrates

It has been shown using Raman spectroscopy that CVD grown SCD has superior crystalline quality over type Ib HPHT diamond [31]. Since the CVD growth process transfers the crystalline structure and the defects from the seed into the grown material, it is desirable to use the highest quality seed material. An increase of seed crystal quality can be achieved by using CVD-grown material instead of type Ib HPHT seed substrates. We have shown that the recovery procedure does not change the seed crystal and that no internal stress or subsurface damage is introduced. Thus it is possible to create free-standing CVD diamond plates, which can be used as a seed substrate. A typical CVD seed substrate can be seen in Figure 4.7. The self-standing CVD substrates are between 1.3 and 1.5 mm thick to ensure similar growth conditions compared to using type Ib HPHT seed substrates. After successful deposition the same three-stage recovery procedure can be applied for reusing the CVD seed substrate.

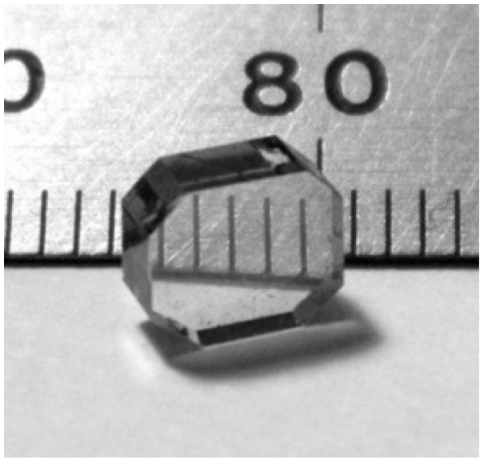

Figure 4.7 Picture of a self-standing 7.0 mm × 7.0 mm × 1.5 mm (1.25 carat) CVD diamond plate, which is usable as a seed substrate for MPACVD synthesis.

4.6 Summary

We have successfully developed a procedure for seed crystal recovery after homoepitaxial MPACVD growth. The three-stage process consists of (1) separation of the seed and grown material by laser cutting, (2) polishing of the seed's top surface and (3) edge trimming. The in-house performed mechanical polishing resulted in surface roughnesses comparable to commercially available products. Thus recovery and reuse of seed substrates is very useful for SCD synthesis. The reported procedure is a reasonable alternative to ion beam implantation for seed crystal separation prior to the growth step for small substrate sizes. The material loss caused by the laser cutting procedure increases from 175 to 350 µm as the seed substrate size is increased from 3.5 mm × 3.5 mm to 7 mm × 7 mm. With improvement of the cutting laser optics the material losses can be decreased further. Using higher growth rate MPACVD synthesis processes, i.e. 30 to 70 µm h^{-1}, reduces the significance of losses due to laser ablation.

The data obtained by FTIR spectroscopy, surface profilometry, birefringence imaging and Raman spectroscopy all showed that the growth process and the seed recovery procedure

do not affect the seed crystal's original properties. Various type Ib HPHT samples showed nitrogen concentrations of 110 to 180 ppm mainly in form of C center defects. Throughout all process steps the nitrogen concentration remained constant. Birefringence imaging identified stress patterns in the used seed crystals. The trimming of leftover PCD material left on the seed after laser cutting and polishing is crucial for repeatable growth of high-quality SCD's on the same seed crystal.

High temperature and/or high pressure annealing are commonly used to influence the optical properties of diamond. We have shown that the conditions for MPACVD synthesis of SCD material do not produce annealing effects that change the optical properties of the diamond seed. The growth times in our experiments exceeded 140 hours with substrate temperatures below 1200 °C. Other researchers [175] reported substrate annealing at 1400 to 2300 °C for only 13 hours. Thus the main source of substrate annealing is the substrate temperature rather than the exposure time of the sample.

The multiple growth sectors in HPHT seeds can be identified after being successfully used during MPACVD SCD deposition, where (110) sectors become apparent. The sector positions agree with modeled results [173]. A cloverleaf stress pattern can be recorded with birefringence imaging, which corresponds to (111) and (113) growth sectors within the (100) oriented crystal. The shape of the pattern remains unchanged throughout the entire engineering process.

Crystalline quality of HPHT seed crystals can be kept constant for multiple MPACVD growth processes. The recovery procedure allows the production of CVD seed substrates, which have a higher crystalline quality than type Ib HPHT crystals. The best cutting region at the HPHT/CVD diamond interface still requires further research and offers possibilities for surface engineering on the seed to be reused, such as to cut in the CVD material, the

interlayer or the seed substrate.

Chapter 5

SCD separation by ion implantation based Lift-Off technique

5.1 Introduction

Recent advances in SCD synthesis have led to renewed interest in diamond applications for optics [176, 155, 177] and electronics [154, 20]. Such devices are fabricated involving high quality homoepitaxial diamond layers that are grown on SCD substrates by chemical vapor deposition. The size of today's available substrates is limited to about 10 mm × 10 mm.

A critical factor for future commercial success of such diamond applications will be the fabrication of larger SCD substrate wafers with a diameter of at least 50 mm. Currently much effort is spent on enlarging the lateral size of SCD substrates. Conventional homoepitaxy does not increase the surface area compared to the original seed crystal. Thus, researchers have successfully fabricated larger plates by overgrowing several laterally tiled substrates [93]. Others pursue methods whereby a crystal is grown taller than its original width [178]. Vertical slicing then yields plates of larger dimensions and also reduces dislocation densities [79]. In addition, heteroepitaxial processes have been pursued [179]. Such promising technologies are all viable to eventually achieve wafer production. If by any method a large "master seed"

substrate of sufficient quality can be produced, it can be repetitively "cloned" by additional homoepitaxial growth and subsequent slicing off of the epitaxial material.

This paper addresses the challenge of slicing wafers from larger crystals along the desired crystal plane. Typical homoepitaxial CVD growth of high quality diamond material occurs on the (100) plane of the seed crystal. However, the crystal preferably cleaves along the (111) plane [168]. Sawing diamond along the (100) plane is very difficult, suffers from kerf losses and also damages the crystal surface. Surface damage is removable by polishing and plasma etching, but at much material loss. An alternative slicing method is laser cutting with substantial kerf material losses that increase with the lateral substrate dimension so that efficient laser cutting of diamond is limited to small crystals [180].

A solution to minimize material losses that is independent of substrate dimensions is offered by "Lift-Off" techniques based on ion implantation. At sufficiently high implantation doses the ions damage the crystal lattice within a thin subsurface region while keeping the crystal surface intact. Depending on the ion energy, the crystal damage occurs a few micrometers below the crystal surface [87, 181, 94]. Subsequent exposure of the implanted crystals to high temperatures at low pressures fully graphitizes the damaged region, while the surface remains intact and suitable for homoepitaxy. After homoepitaxial growth of new diamond material, the original seed crystal and the newly grown SCD are separated from each other by removing the graphitic region with processes that preferentially etch graphite over diamond. The separated seed crystal surface remains very smooth and can be reused for further homoepitaxial growth directly after separation without the need for additional polishing.

Previous reports of this method relied on a distinct annealing step between ion implantation and homoepitaxy. The samples were exposed to temperatures as high as 950 °C to completely

graphitize the implantation region. This step proved necessary to ensure that the final etch process could fully separate the crystals [87]. A process flow that does not require a distinct annealing step is demonstrated. Instead, the high substrate temperature during homoepitaxy is sufficient to fully transform the damage layer to nano-crystalline graphite. Typical process substrate temperatures during MPACVD are about 900 to 1100 °C [31]. At such temperatures, the graphitization of the subsurface damage layer occurs simultaneously with new diamond growth on the crystal surface. Furthermore, to separate the new material from the seed crystal by removing the graphite, we explored several etching techniques including wet-chemical etching, electrochemical etching and thermal oxidation.

5.2 SRIM Monte Carlo simulations

SRIM (Stopping and Range of Ions in Matter) software was used to predict the energy dependent ion transport in diamond crystals [182]. To set up diamond as a target material in the software a displacement energy per carbon atom of 45 eV [183], a lattice binding energy of 5 eV [184] and a surface binding energy of 7.5 eV [185] has been selected. The damage threshold defect density for ion beam induced graphitization in diamond is about $1 \times 10^{22}\,\mathrm{cm}^{-3}$ [96]. The Monte Carlo simulation does not accumulate the damage with each implanted ion. Instead, the penetration of each incoming ion is simulated as if it interacts with a perfect diamond crystal. Therefore, the simulated crystal damage and implantation depths may be slightly underestimated. Simulations for protons, carbon and oxygen ions in the energy range from 100 keV to 6 MeV have been performed. Simulated ion penetration depths as a function of kinetic energies are plotted in Figure 5.1.

The light protons cause less damage and penetrate much deeper into the diamond crystal

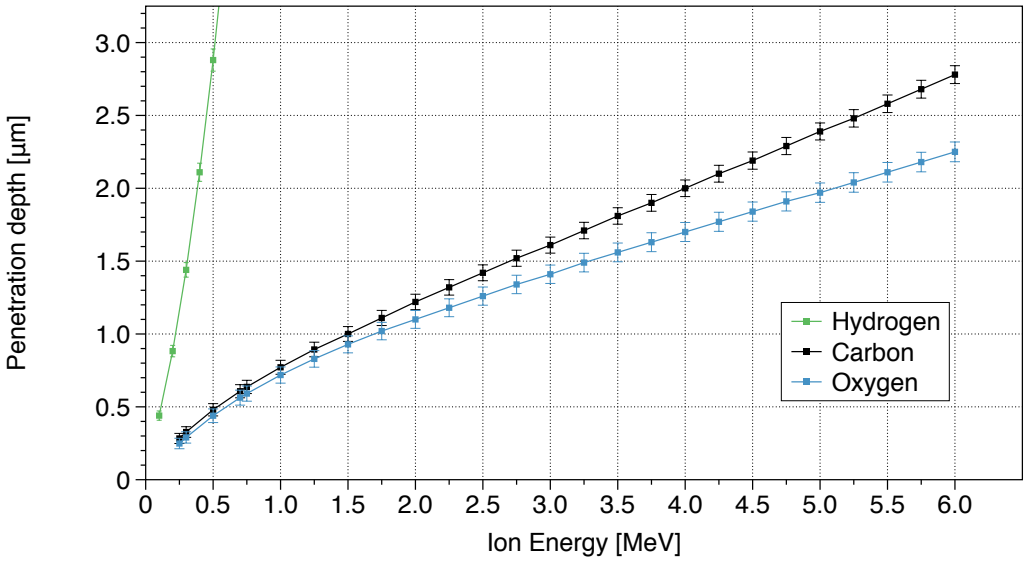

Figure 5.1 SRIM simulations for different ion types and energies.

at a given energy than the heavier carbon and oxygen ions. At 1.5 MeV carbon and oxygen ions penetrate the crystals about 1 µm deep. This is sufficient to create the damage layer at a depth suitable for homoepitaxy and subsequent crystal separation. The total length of the vertical error bars for each data point in Figure 5.1 is equal to 2 or twice the standard deviation ("straggle") of the simulated ion penetration depth distribution. The value remains between 70 and 130 nm for the heavier ions. In the case of protons, 2 increases substantially from 60 nm for low energies to 5.4 µm for 6 MeV ions (not shown in plot). Selected numerical results are compiled in Table 5.1.

The rows in bold font in Table 5.1 mark those conditions that were selected for actual implantation experiments. The minimum irradiation dose required to reach the damage threshold for graphitization is calculated based on the damage caused per ion. Protons cause the least amount of lattice damage and therefore require much higher doses and thus longer exposure times. The required minimum doses for carbon and oxygen ions are 50 to 100 times lower than those for protons. Consequently, the required irradiation times increase by

Ion	**E_{kin}** (MeV)	**Depth** (µm)	**2σ** (µm)	**Damage per ion vacancies / Å x 10^{-4}**	**Minimum required dose x $10^{16}\,cm^{-2}$**
H^+	0.3	1.43	0.10	28	3.6
H^+	**0.7**	**4.67**	**0.23**	**1.6**	**6.3**
H^+	3.0	48.1	1.72	2.8	36.0
C^{2+}	0.7	0.61	0.09	1200	0.08
C^{2+}	**3.0**	**1.62**	**0.11**	**950**	**0.11**
O^{2+}	**3.75**	**1.63**	**0.11**	**1600**	**0.06**

Table 5.1 SRIM simulation results of depths and minimum doses required for different ion types and energies. The data rows marked in bold font were conditions selected for actual implantation experiments.

similar factors when using protons instead of carbon and oxygen ions. With increasing lateral dimensions of the diamond substrate the processing time will increase further if the ion beam needs to be scanned to cover the full sample area. This makes it more challenging to achieve cost-efficient Lift-Off processes using protons. If the introduction of oxygen into the diamond crystal can be tolerated, the advantage over carbon is a 40 % reduction in exposure time to create the same damage.

5.3 Implantation experiments followed by SCD synthesis

5.3.1 Protons

Proton implantation was performed with doses ranging from 0.5 to $75 \times 10^{16}\,cm^{-2}$ at 700 keV. Irradiation times varied between 24 minutes and more than 55 hours. Only those crystals exposed to proton doses higher than $10 \times 10^{16}\,cm^{-2}$ turned dark (opaque) after irradiation. This color change indicates substantial damage to the diamond lattice. Lower proton doses did not change the appearance of the crystal. That is, the crystals remained optically transparent. The surfaces of the irradiated crystals did not show visible damage due to ion bombardment at any dose.

Epitaxial diamond growth was performed on proton implanted samples for 8 to 24 hours using the MPACVD process at temperatures of 950 to 1000 °C. The growth rates were between 17 and 22 µm h^{-1}. The film morphologies and growth rates on implanted seeds were comparable to those obtained from MPACVD experiments on seeds that were not exposed to ion implantation [186]. Polycrystalline diamond, which formed around the edges and on the sidewalls of the crystal was removed by laser cutting and the sidewalls were polished. The CVD grown SCD on the top surface of the crystals was of high quality similar to the example shown in Figure 5.2.

Figure 5.2 Top view microscope image (reflected light) of a CVD-grown layer on a HPHT 3.5 mm × 3.5 mm seed irradiated with 3.75 MeV oxygen ions with a dose of 5×10^{16} cm^{-1}

Originally transparent crystals turned opaque after implanting with doses exceeding 10×10^{16} cm^{-2} but became again transparent after the diamond deposition process if the dose was less than 30×10^{16} cm^{-2}. Only crystals irradiated with proton doses exceeding 30×10^{16} cm^{-2} remained opaque after the MPACVD process. The opaqueness corresponds with a visible black line between the HPHT seed and the CVD-grown SCD in transmission optical microscopy of the cross section, see Figure 5.3. This result suggests that the diamond lattice was repaired during the exposure to high temperatures for those samples that were

dark after implantation but were not exposed to a sufficient ion dose to fully graphitize the implantation region during the CVD process. Based on these sample coloration results it appears that the simulations underestimated the minimum dose required to cause sufficient damage by a factor of about five.

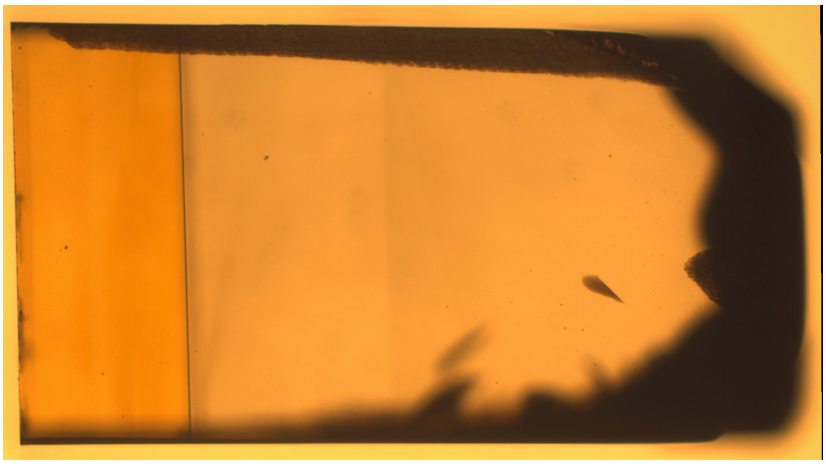

Figure 5.3 Cross-sectional microscope image (transmitted light) of a CVD-grown layer on a HPHT 3.5 mm × 3.5 mm seed irradiated with 700 keV protons with a dose of $30 \times 10^{16}\,\mathrm{cm}^{-1}$.

5.3.2 Carbon and oxygen ions

Carbon and oxygen ion implantations were performed with doses of 1 to $5 \times 10^{16}\,\mathrm{cm}^{-2}$. These ion doses were about 10 to 80 times higher than the simulated minimum to compensate for underestimations. After irradiation, all samples were opaque and remained dark after MPACVD as shown in Figure 5.4. The damaged regions in the samples were completely converted to graphite and the crystal lattice did not heal during the 24-hour growth process.

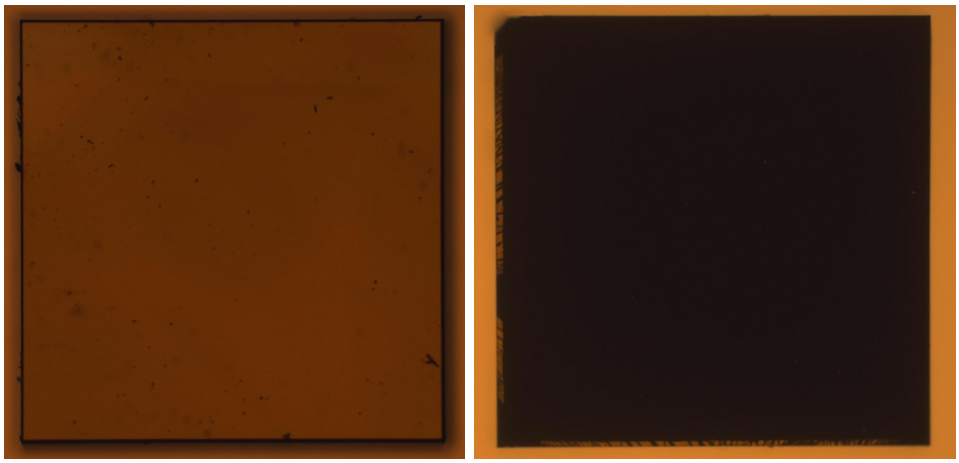

Figure 5.4 Top view microscope images (transmitted light) of a 3.5 mm × 3.5 mm samples before 3 MeV carbon irradiation with a dose of $1 \times 10^{16}\,\mathrm{cm}^{-1}$ (left) and after SCD deposition and post-processing (right).

5.4 Feasibility of different separation techniques

5.4.1 Wetchemical etching

Wetchemical etching is a well established method for removing non-diamond carbon selectively, which forms during SCD deposition on the backside of the seed crystal. The diamond is placed in a boiling solution of nitric (15.9M) and sulfuric (18.0M) acid mixed together in a 1:1 ratio. The carbon is removed within an hour while the SCD remains untouched by the acid etch.

5.4.2 Thermal oxidation

Another concept to selectively remove graphite is to use thermal oxidation. Thereby, the sample is placed inside a furnace with a floating oxygen environment and the entire chamber is heated as described in Section 3.5.1. Once the oxidation temperature is surpassed, the carbon is oxidized into CO and CO_2. The oxidation temperature for graphite (sp^2 carbon) is around 550 °C and 600 °C for diamond (sp^3 carbon) [97]. Thus, it should be possible

to selectively etch the graphite by set the furnace temperature high enough to oxidize the graphite while leaving the diamond untouched.

A bulk piece of graphite (2 mm × 2 mm × 2 mm) and two HPHT diamonds with similar volumes and surface areas have been placed simultaneously into a furnace for an hour each for various furnace temperatures. The oxygen flow was kept constant at 33 sccm. The relative weight loss is used as an indicator of how much carbon has been oxidized and the results are illustrated in Figure 5.5. It can be seen that the overall prediction, that graphite has a much strong oxidation behavior compared to diamond. Diamond does not show signs of oxidation until temperatures around 600 °C are reached, which is is in agreement with the theoretical prediction [97]. Once diamond etching occurs, it is relatively modest with a relative weight loss of less than $0.1\,\%\,\mathrm{h}^{-1}$. The etching behavior for graphite shows a different behavior. First, the oxidation starts at temperatures lower than predicted. Even temperatures as low as 400 °C are enough to cause modest oxidation of $0.1\,\%\,\mathrm{h}^{-1}$. That etching for such low temperature is in fact happening can be seen when expanding the weight loss into higher temperature. The increase is almost linear on a logarithmic y-scale over the entire temperature range up to 600 °C. Thus, the oxidation effects are increasing exponentially with increasing temperature, which is the same observation as Figure 2 (b) in [97]. The weight loss becomes especially noticeable for furnace temperatures exceeding 580 °C were as much as 58 % of graphite are oxidized within one hour.

It has been demonstrated, that using a furnace to selectively etch graphite by thermal oxidation is a viable option. Graphite oxidized over a broad temperature range while the diamond remained unetched. One particular issue is the exponential dependency of the oxidation rate with the temperature. Thus, it is desirable to use furnace temperatures as high as possible (in the region around 580 °C) to maximize the graphite removal. Unfortunately,

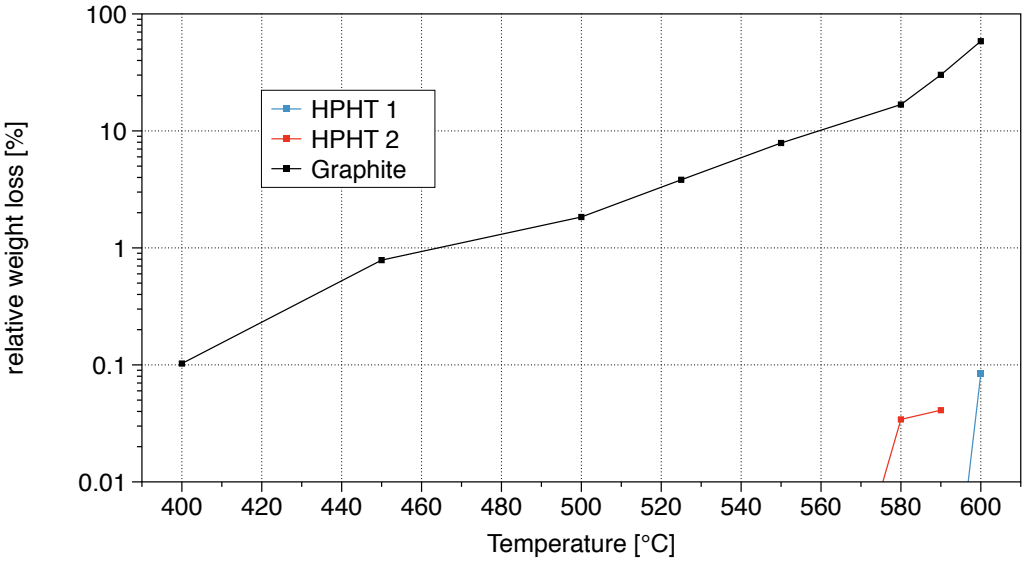

Figure 5.5 Relative removed graphite and diamond as a function of the furnace temperature.

this is the same temperature regime, where diamond starts being etched (580 to 600 °C). The different low temperature thresholds for diamond etching could be caused by different crystalline quality of the material. Crystalline defects are regions of weaker bonds where oxidation can occur at lower temperatures than for the rest of the crystal. Thus for a greater density of defects, the etch rate will increase. The etch selectivity between graphite and diamond at 600 °C is as high as 725, but diamond etching is occurring and visibly noticeable.

5.4.3 Electrochemical etching

The setup described in Section 3.5.2 has been used for performing electrochemical etching experiments. The key variables for optimization of the etching setup are the type of solution, the voltage and current applied. The distance between the two electrodes has an effect of the performance as well. The distance between the two electrodes should be minimized to achieve maximum current flow. The spacing between the two electrodes has been chosen to

be 1 cm. When the distance has been increased a sharp drop in current flow has been noticed. The effectiveness of etching has been evaluated by measuring the relative weight loss of bulk graphite after exposure to the etching conditions for one hour.

First, the influence of the solution on the etching has been evaluated. Initially, an acidic, a neutral and a basic solution with the same conductivity have been used. The acidic solutions contain nitric acid in water. The basic solution is a dilution of NuKlean in water. NuKlean is a commercially available soap. Two different neutral solutions have been used by either dilution NaCl or KCl in water. The resulting etch behavior for the four different solutions can be seen in Figure 5.6. It can be clearly seen, that the etch behavior of the acidic and basic solution is approximately the same. The etch rate of the neutral salt solution is roughly twice that of acidic and basic solutions.

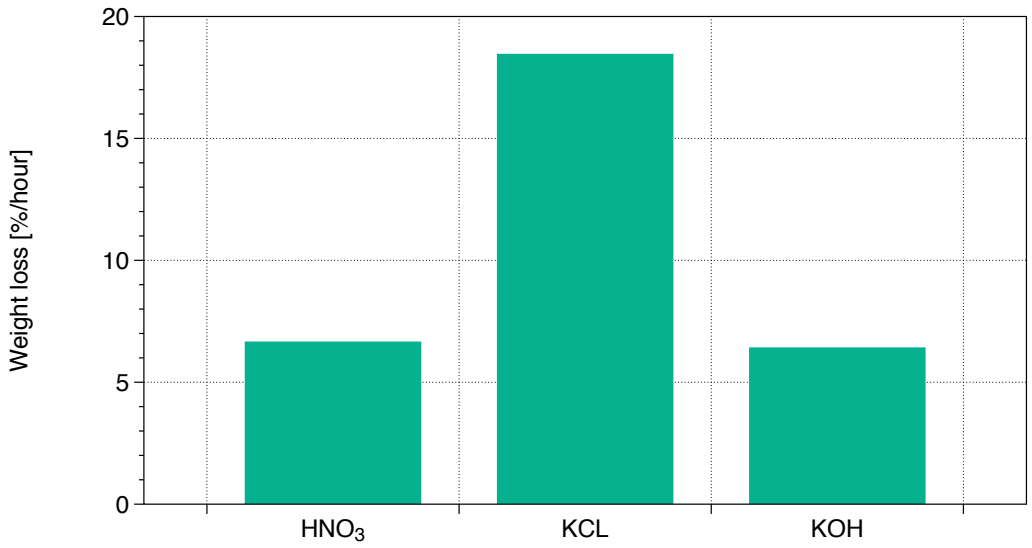

Figure 5.6 Relative etching of graphite for different aquaeous solutions having the same conductivity.

The etch rate behavior can be explained by the nature of the different ions created, once the acid, base and salt are dissolved into the water. The following reactions are occurring for each of the cases:

$$HNO_3 + H_2O \rightarrow H_20 - H^+ + NO_3^-$$

$$KCl \rightarrow K^+ + Cl^-$$

$$NaOH \rightarrow OH^- + Na^+$$

It is obvious, that dissolving the salt results in two solid ions for each dissolution reaction. For th acidic and basic dissolution on the other hand, one ion is a hydronium or hydroxide ion and one is a solid ion cluster. It is plausible to assume that the etching is in fact a physical ablation of the graphite, rather than based on chemical reactions. That way, only solid ions contribute to the removal, which leads to having double the etch rate for the salt solution over the acidic and basic solution. The fact, that the pH does not have an effect on the etch rates is another indicator, that the weight loss is in fact a physical ablation by ion impact.

The second step of evaluating the solution is by using a set of salts (NaCl, KCl, KBr, KI) having the same conductivity. Doing so will alter the weight of the anion while remaining everything else unchanged, except of NaCl vs. KCl were the weight of the cation is changed. The resulting etch rates can be seen in Figure 5.7. It can be seen, that the weight loss for all different salts is within the expected fluctuation of this rather simple testing setup. It can be concluded that the kinetic energy of the individual anions are not high enough to remove several carbon atoms out of the graphite lattice. Thus, the ion weight is not a contributing factor to the etch performance. Dissolved KCl in water has been selected as solution for all future experiments as it showed the best etching performance and KCl is cheap and readily

available.

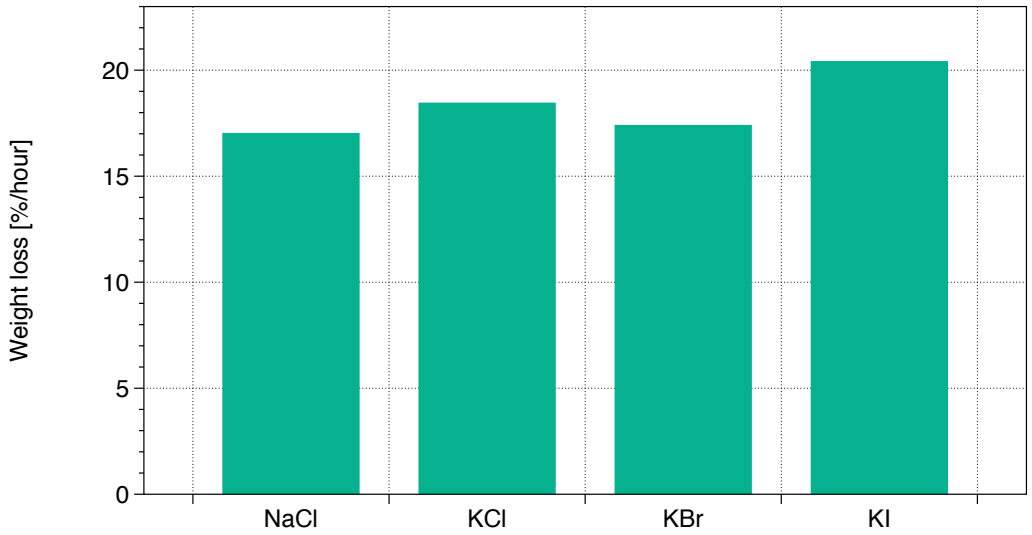

Figure 5.7 Relative etching of graphite for different aquaeous potassium-based salt solutions having the same conductivity.

For evaluating the influence of the current on the removal of graphite a different power supply is used. This power supply provides currents up to 1 A and is much more stable in current control operation, but only allows operation up to 100 V. Increasing the current results with a linear increase of the removed graphite as illustrated in Figure 5.8. This observation supports the conclusion, that the graphite removal is solely a physical ablation. More ions are moved within the electric field if the current between the two electrodes is increased. As the sample is located in this increased ion flux it is bombarded by a larger number of ions, which lead to a higher removal rate. Especially the linear increase is another validation point, that the removal is physical ablation rather than based on chemical reactions.

Finally, the influence of the voltage on the graphite removal under a constant current is evaluated. Doing so increases the kinetic energy of the ions impacting the graphite while keeping the total amount of impacts constant. The results are displayed in Figure 5.9. One surprising finding is, that the removal rate increases and becomes constant for applied voltages

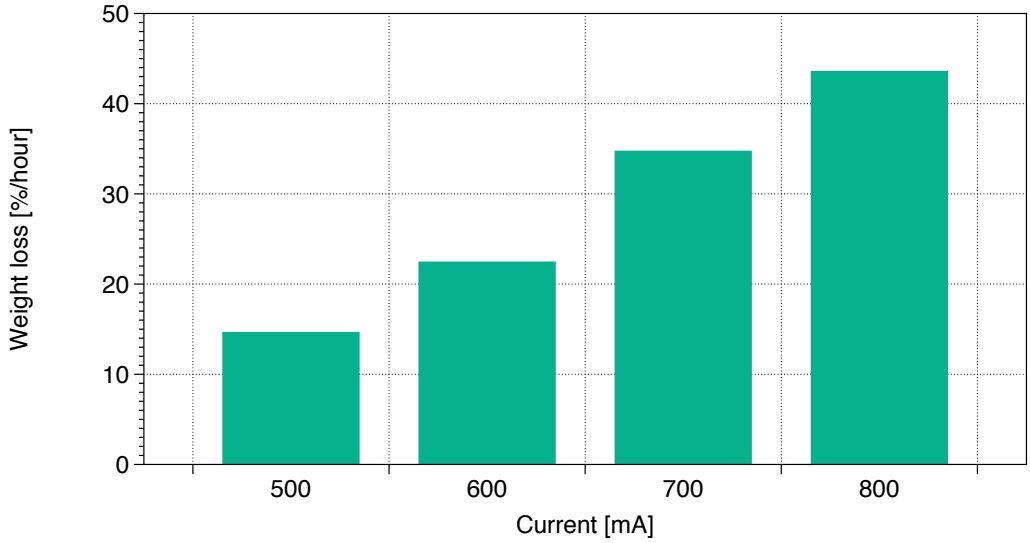

Figure 5.8 Relative etching of graphite as function of the applied current.

around 290 V. This can be explained by the binding energy of carbon ions inside a graphite lattice, which is 285 eV [187]. All ions in the solution are single charged. If the applied voltage is below 285 V the resulting kinetic energy of the ion is lower than the binding energy of the graphite. Thus, not every ion impact is removing a carbon ion from the graphite lattice. Once that energy level is surpassed (by applying a sufficient electric potential) each ion is removing a carbon ion, but does not have enough excess energy left to remove a second one causing the removal rate to plateau. Another increase would be achievable once the applied electric field would surpass 600 V, which would provide sufficient energy to remove two carbon ions per impacting ion. Unfortunately, the used power supply is limited to 500 V. Thus, it is sufficient to use 300 V for the SCD etching experiments. Applying a higher electric field would just introduce excess energy, which is then distributed as thermal energy into the aqueous solution.

Overall, it has been shown that the electrochemical etching process is in fact a physical ablation process and no chemical oxidation reactions are involved. If chemical processes

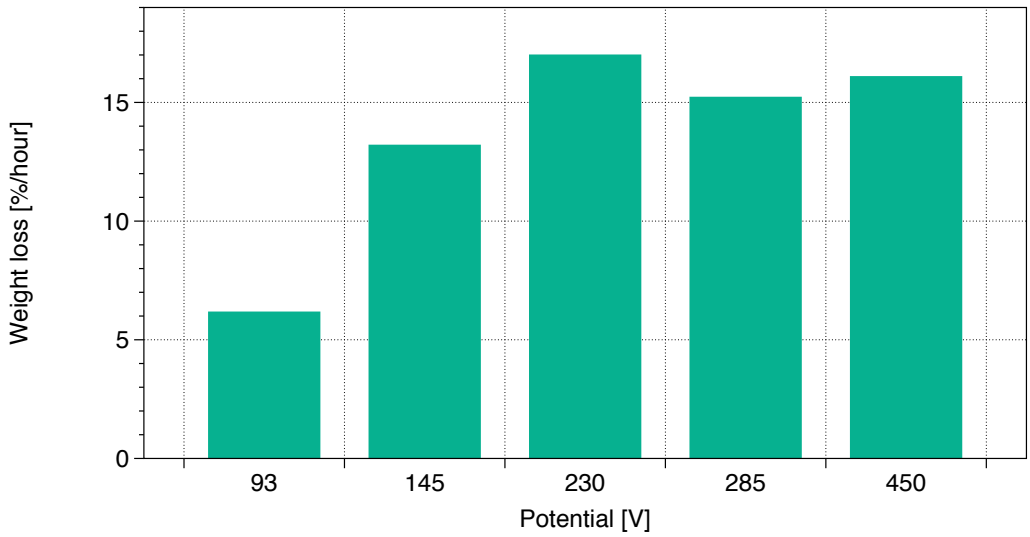

Figure 5.9 Relative etching of graphite as function of the applied potential.

would start to contribute a strong increase of the removal rate would have been expected and no increase of ablation rate with increasing current would be seen. Using the setup currently available, it has been found, that using a salt solution (KCl), applying an external electric field of 300 V and having a current flow as high as possible (500 mA) results in the fastest removal of graphite.

5.5 Separation experiments of SCD

5.5.1 Wetchemical etching

Wet-chemical etching in a boiling acid solution was performed to remove the graphitic layer and thereby separate the MPACVD grown diamond from the seed crystal. Figure 5.10 shows the progress after 2 (left) and 8 (right) hours of etching a crystal that was irradiated with protons. The opaque damage region recedes with increasing etching time as the damaged layer is removed and the light can pass through the crystal in the area of the lower right

corner. After 8 hours of wet-chemical etching time about half of the graphite was removed. Characterization of the composition of the damaged layer is performed in section Section 5.7.

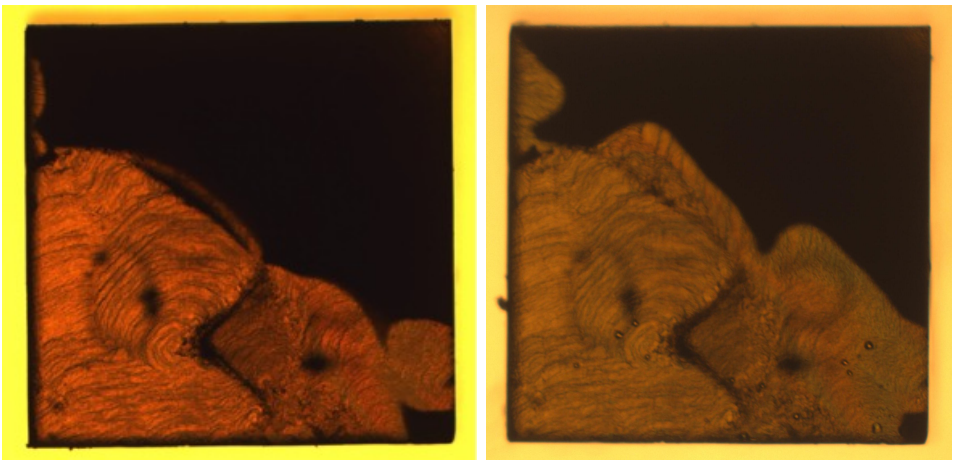

Figure 5.10 Top view microscope image (transmitted light) of a 3.5 mm × 3.5 mm substrate after SCD deposition that was irradiated with $50 \times 10^{16}\,\mathrm{cm}^{-2}$ dose of 700 keV protons, post-processing and 2 hours of wet-chemical etching (left) and after 6 additional hours of etching (right).

The successful removal of the graphitic layer was confirmed with scanning electron microscopy of a sample cross-section. A 4 µm wide and well-defined channel inside the proton implanted crystal had formed after 8 hours of etching as shown in Figure 5.11. This gap width corresponds to about 14 times the simulated 2σ of the ion penetration depth distribution. Thus most protons are stopped within the narrow straggle region but the actual damage region is substantially broader. Only substrates that remained opaque after MPACVD formed etch channels. Samples that turned transparent again during MPACVD did not form any etch channels in boiling acid solution.

The wet-chemical etching results were substantially different for substrates that were implanted with carbon and oxygen. Even though these samples remained opaque after MPACVD, wet-chemical etching did not have any removal effect at any implantation dose. Even after many hours in boiling acid solution there was no evidence of any apparent etching

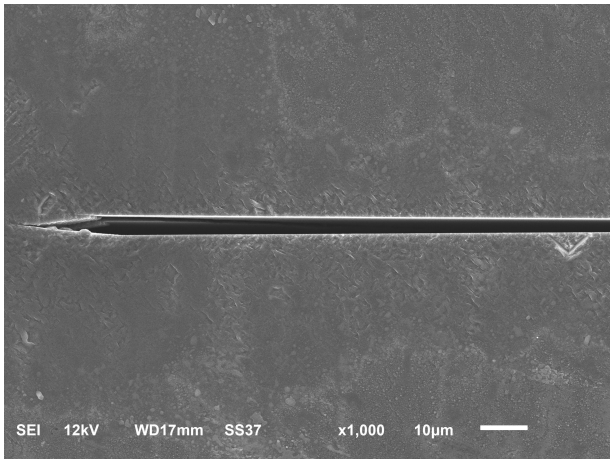

Figure 5.11 SEM image of the channel etched by removal of the graphitic layer using wet-chemical etching of a substrate irradiated with a $50 \times 10^{16}\,\mathrm{cm}^{-2}$ dose of 700 keV protons.

progress.

5.5.2 Thermal oxidation

After proving in Section 5.4.2, that thermal oxidation is a viable option to selectively etch graphite in diamond, this concept is used to separate the grown SCD from the seed crystal. Furnace temperatures were set between 570 and 590 °C and the oxygen flow was kept constant at 33 sccm.

Applying this process to proton implanted samples with doses of 20 to $75 \times 10^{16}\,\mathrm{cm}^{-2}$ formed 4 to 10 µm wide etch gaps within 2 hours. All substrates irradiated with doses of $10 \times 10^{16}\,\mathrm{cm}^{-2}$ and lower did not etch. Interestingly, a substrate exposed to a $20 \times 10^{16}\,\mathrm{cm}^{-2}$ proton dose turned transparent after MPACVD but it still developed a 10 µm wide etch gap during thermal oxidation. This indicated that the diamond crystal did not fully anneal the diamond lattice despite being transparent again. On the other hand, such samples did not wet etch in boiling acid even though the damage region is wide. This effect was only observed with proton implantation. Further investigations are required to determine the

carbon structure that causes this behavior.

Carbon and oxygen irradiated substrates were placed consecutively in the furnace with individual dwell times between 5 and22 hours. Transmitted light microscope images were recorded between oxidation steps to monitor the etching progress. The etched percentage of the sample area was determined after each step using open source image analysis software [188]. Figure 5.12 shows how far the removal of the damaged layer had progressed after a total dwell time of 54 hours. The black center part is not etched, which corresponds to 56 % of the total area. The etching advances relatively uniformly from all 4 sides toward the center of the sample. Uniform 1 µm wide etch channels formed on all four sides.

The etching progress over time for different ion doses and types are plotted in Figure 5.13. When the process begins etching advanced quite rapidly but the area removal rate reduces quickly once 85 to 90 % of the area are etched. This corresponds to a remaining center area of roughly 1 mm × 1 mm and an inwards etching of 1 mm into the sample from each side. Apparently the process is transport limited. The further the etching advances the more difficult it becomes for the gaseous etchants to reach the graphite. Similarly, the volatile byproducts of the oxidation reaction (e.g. CO_x) have increasing difficulties to diffuse out of the growing etch channel.

The gas diffusion limitation increases with the length of the etch channel. This is directly evident from the red plot in Figure 5.13. The etching process for this sample was started similar to the other samples. However, after 31.5 hours (marked as (A)) of etching the already etched parts of the sample were cut off. As a result, the length of the etch gap was significantly reduced and the etch rate (etched diamond area per time) increased again for a while until the etch rate slows down once more with increasing etching depth. The points B1 and B2 in Figure 5.13 also show changes in etching rates, however, these were

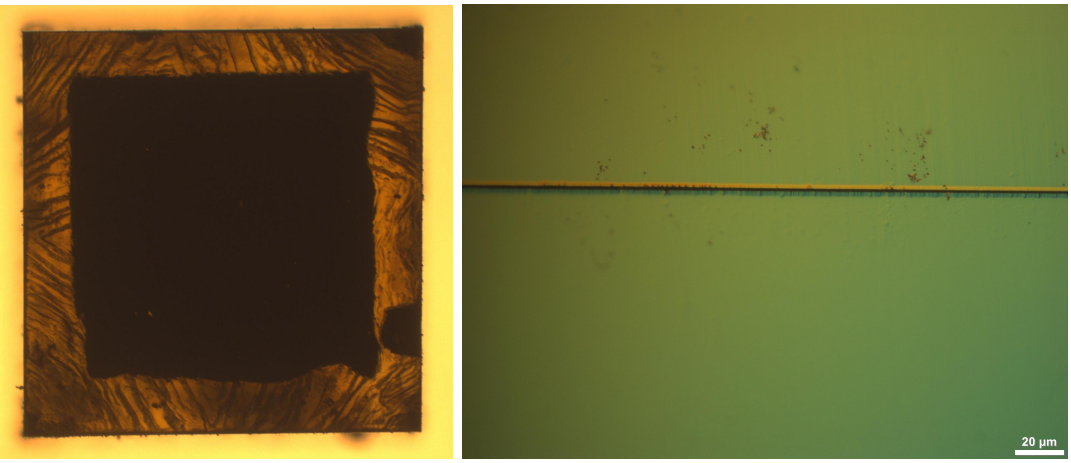

Figure 5.12 Transmitted light (left) and cross-sectional reflected light (right) microscope image of the substrate from Figure 5.4 after thermal oxidation for 54 hours.

not obtained on purpose and may be the result of different conditions in the furnace when changing samples. Overall we conclude that this gas diffusion driven process depends on the gas flow conditions in the furnace and ultimately is limited by the narrow transport channel that gets ever deeper with etching. Once SCD dimensions are exceeding 2 mm × 2 mm the process becomes severely slow due to these diffusion limitation effect, where oxygen has to diffuse towards the graphite while carbon oxides have to diffuse outward.

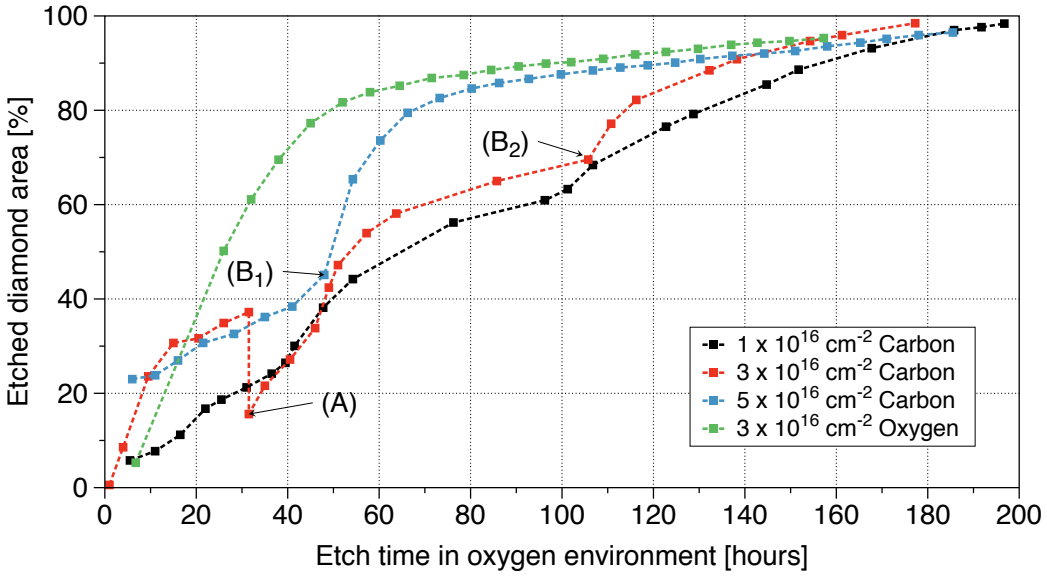

Figure 5.13 Relative removed graphite as a function of the overall dwell time in the furnace.

Figure 5.13 also shows that the process benefits from oxygen implantation (green plot). The implanted oxygen ions enhance the initial etch rate, which was also reported by Parikh et al. [87]. However, ultimately this process is also diffusion limited. While the overall etch time was the lowest with implanted oxygen ions, a total etch time of 157 hours is still not desirable from a process standpoint.

5.5.3 Electrochemical etching

Electrochemical etching to selectively remove the graphite has been performed based on the optimization obtained from the initial feasability study in Section 5.4.3. The diamond substrates were placed having the damaged layer parallel to the current flow. Figure 5.14 shows the progress of removing the graphitic layer that was created by carbon ion implantation. Comparing the two left images in the bottom row shows the sample after diamond deposition and framing and then after 28.5 hours of etching. While the graphite layer was partially removed from all four sides of the sample, there is a clear directional (horizontal) preference visible. This is due to the electrodes, which were, in this orientation, placed to the left and the right of the sample. A sharp etch channel is formed throughout the process. Through consecutive etch steps the CVD-grown layer was removed after 39 hours. The etching time was further reduced to 12 hours and even 37 minutes for one particular sample by tailoring the aqueous etching solution to a conductivity of $324.6\,\mu S\,cm^{-1}$. This illustrates how important the properties of the aqueous solutionare in maximizing the etch rate and should be further investigated in the future.

This process does not suffer from transport limitations that were observed for the gaseous thermal oxidation process. The electric field introduces a directional force to drive the etchants. The importance of the forced directional etching becomes obvious when comparing

etch rates. These are the highest for electrochemical etching in spite of the formed etch gap being the thinnest. Thus the even deeper aspect ratio of the etch gap in this process causes significantly less transport limitations if compared to boiling acid wet etching and thermal oxidation processes.

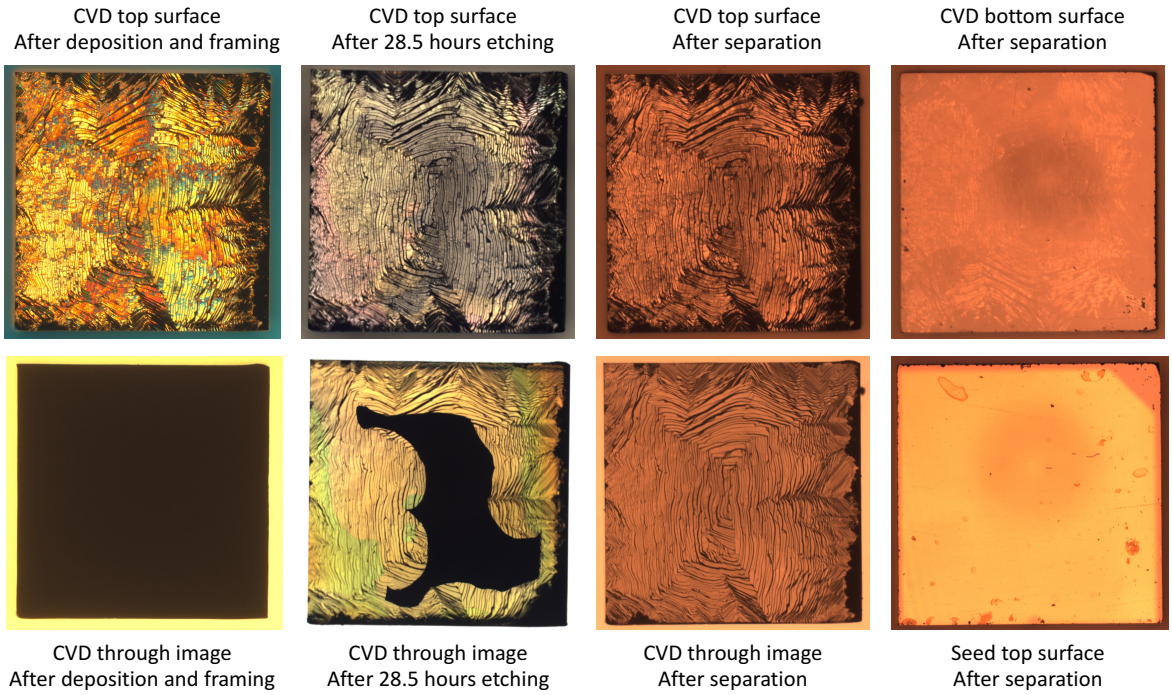

Figure 5.14 Progress of the electrochemical etching of a SCD diamond film grown on a HPHT seed irradiated with 3 MeV carbon ions with a dose of $3 \times 10^{16}\,\mathrm{cm}^{-2}$. The remaining graphite can be identified by the black areas within the diamond. The progress can be identified as more and more of the area becomes transparent.

As shown in Figure 5.15 the observed etch gap is about 480 nm wide. This is only half the gap width compared to thermal oxidation when using comparable substrate configurations. Additionally, Figure 5.15 confirms the simulation results in terms of penetration depth. The ions penetrated to a depth of about 1.6 µm and converted the diamond lattice into a roughly 480 nm thin sheet of graphite inside the crystal, which then was removed by etching. The simulation predicted a penetration depth of 1.62 µm for 3 MeV carbon ions (Table 5.1). The gap extends symmetrically by less than twice the simulated 2σ of the ion penetration depth

distribution in each direction.

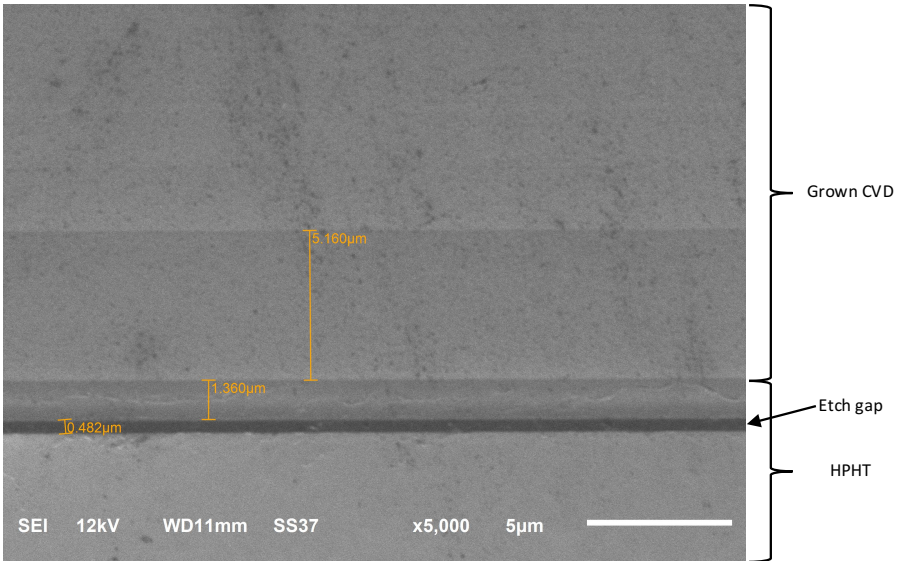

Figure 5.15 SEM image of the etch channel created by removal of the graphitic layer using electrochemical etching of a substrate irradiated with 3 MeV carbon ions with a dose of $3 \times 10^{16}\,\mathrm{cm}^{-2}$.

5.6 Analysis of the separated plates

A photograph of the freestanding CVD film and HPHT seed substrate without additional cleaning or processing after the Lift-Off is shown in Figure 5.16 (left). The CVD layer was separated using electrochemical etching. The surface roughness was measured after separation at 8 and 50 nm for R_a and R_z. These values are comparable to those obtained by mechanical polishing [180].

The right picture in Figure 5.16 shows different sizes and shapes of separated CVD diamond plates. These pieces originated from a single seed substrate that was laser cut during the oxidation experiments. The surface roughness caused by thermal oxidation etching is visible on all pieces. As shown in the left picture of Figure 5.17, there appeared several visible defects across the top surface after CVD diamond deposition. Holes in the SCD films became

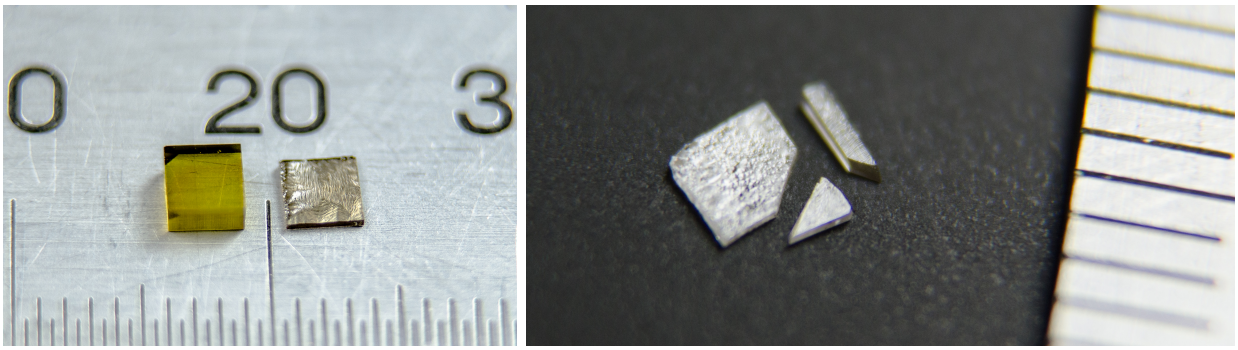

Figure 5.16 Photograph of a HPHT seed substrate and free-standing CVD film after successful Lift-Off using electrochemical etching (left), various free-standing CVD films obtained from Lift-Off using thermal oxidation (right).

apparent after performing thermal oxidation three times for 5.5 hours (middle picture of Figure 5.17). The position of those holes matched the locations of visible defects prior to etching as indicated by the blue arrows. After successful separation, it was clear that the defect etching occurred throughout the entire CVD layer. This proves that those defects initially formed at the seed-film interface and continued to build throughout the CVD layer all the way to the top surface. Additionally, the entire top surface was slightly etched by the thermal oxidation process. A close up view (right picture) shows the etched morphology. The surface etching does not follow a particular pattern. Sometimes it occurred already after a few hours and for other diamond films it only happened for long individual dwell times of around 18 hours. Once the diamond crystal was slightly etched the effect worsened even for short thermal oxidation times. Thus thermal oxidation did not only etch the damage layer but also attacked other defects that may occur for various reasons on the crystal surface.

Overall, electrochemical etching appears to be the favorable separation technique. It can be used with all ion types that were studied for implantation. The process does not damage the seed substrate. The grown CVD layer separates significantly faster compared to wet-chemical etching and thermal oxidation. No mechanical polishing is required to reuse

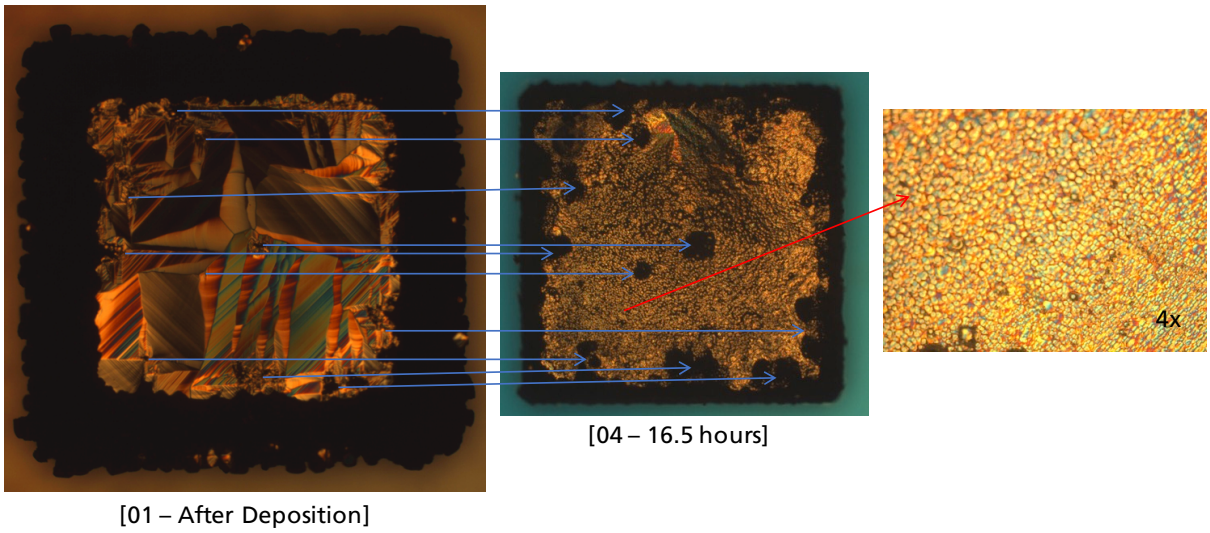

Figure 5.17 Reflected light microscope image of a CVD-grown layer on a HPHT seed irradiated with 3.75 MeV oxygen ions with a dose of $3 \times 10^{16}\,\mathrm{cm}^{-2}$ (left), Damage created by thermal oxidation for three times 5.5 hours (middle), four times enhanced close up microscope image of the overall etched SCD top surface (right).

the seed. This has been confirmed by growing high quality SCD on a lifted off seed without additional surface treatment after successful separation.

5.7 Analysis of the damaged layer

Another question is whether the damage layer is actually graphite after ion implantation and high temperature CVD. To analyze this, the CVD film of a partially etched sample was sheared off the seed, which left some remaining black material from the damage layer region. This material, created after implantation using carbon ions, was analyzed by Raman spectroscopy. Raman measurements of the already etched areas on the seed and grown material showed a sharp diamond peak at $1332\,\mathrm{cm}^{-1}$. The Raman spectra of the black material is shown in Figure 5.18. No diamond peak is present there. Instead the spectrum is made up of the D and the G peaks. The peak positions of the two bands are $1352\,\mathrm{cm}^{-1}$ for

the D and 1607 cm^{-1} for the G mode. The G mode is the stretching vibration of sp^2 sites in crystalline graphite. The D mode originates from "breathing" aromatic rings indicating that long-range crystallinity is broken [189]. The G mode is present, but shifted upwards from 1580 cm^{-1} for pure graphite. The peak ratio of the D to G mode is 1.28. Taken all this information into account it can be concluded that ion implantation and high temperature exposure during MPACVD forms nano-crystalline graphite in the implanted damage region [189]. Thus the use of the term "graphitization" to describe the damage layer after high temperature exposure seems justified. Nevertheless, it is still necessary to explore the situation after implantation and prior to MPACVD to understand the carbon atom arrangement as a direct result of implantation.

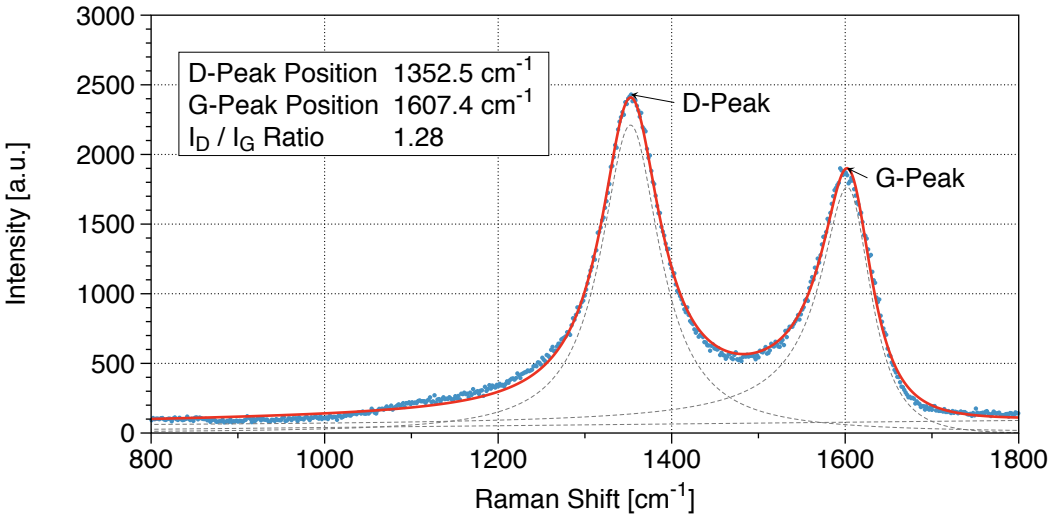

Figure 5.18 Peak fit of the Raman spectrum of the graphitic layer remaining after successful Lift-Off.

5.8 Summary

The commercial success of single-crystalline diamond applications will require ever larger substrates. In addition to enlarging crystal sizes, an important technology will be the efficient

separation of epitaxial layers from the seed crystals with minimized material loss and high throughput. It will be commercially important to reuse the seed crystals many times. A Lift-Off technique that is scalable to wafers of any size was studied. This technique uses ion implantation to create a subsurface damage layer in the seed crystal at a defined depth. The subsequent MPACVD grows epitaxial diamond and graphitizes the damaged region. A final thermal oxidation or electrochemical etching process removes the graphitic layer to separate the epitaxial plate from the seed crystal.

The SRIM software proved a very useful tool to determine implantation conditions with respect to identifying the required ion energies for different ion types to achieve a targeted implantation depth. The simulations also provide a reasonable estimate for the required minimum dose to reach the necessary damage threshold. However, due to the nature of the simulation code these estimates tend to be on the lower side. As the experiments with proton irradiation have shown one should use about 3 times higher doses than simulated to ensure full graphitization of the damaged layer. Throughout all etching processes sharp channels formed indicating the thickness of the graphitic layer. The channels created for proton-irradiated substrates were larger than for carbon- and oxygen-implanted samples, which is in agreement with the higher straggle observed by SRIM simulations.

Protons, carbon and oxygen ions were explored to create the subsurface damage layer. All ion types were able to achieve the goal if implanted with a sufficient dose. For protons a working dose is about $30 \times 10^{16}\,\mathrm{cm}^{-2}$ and carbon and oxygen ions will require $0.1 \times 10^{16}\,\mathrm{cm}^{-2}$. The use of oxygen instead of carbon ions reduces the required doses by 40 % based on SRIM simulations. Proton energies of 300 to 700 keV, carbon energies of 3 MeV and oxygen energies of 3.75 MeV are required to achieve a useful penetration depth of a few micrometers. If samples changed their appearance from transparent to opaque during the implantation

process and remained opaque after MPACVD, epitaxial material could be separated from the seed crystals by various methods. Under these conditions the damage layer created after carbon ion bombardment turned out to be nano-crystalline graphite based on analyzing some remaining material with Raman spectroscopy.

To separate the epitaxial diamond plates from the seed crystal the damage layer has to be removed. This can be accomplished by thermal oxidation and chemical etching techniques. Wet-chemical etching, thermal oxidation and electrochemical etching were investigated. Boiling acid solutions showed no effect on graphitized layers created by carbon and oxygen ions, but worked for protons due to the greater width of the damage layer. Thermal oxidation at temperatures of 590 °C were effective to selectively etch the graphitic layer for all substrates that were irradiated with ion doses exceeding the damage threshold. It was observed that etching progress by thermal oxidation is ultimately limited due to diffusion effects of the gases used. Overall, electrochemical etching is the favorable separation technique. It can be used with all the studied elements. The process does not damage the seed substrate surface. The grown epitaxial CVD diamond layer separates within a few hours for a 3.5 mm × 3.5 mm sample, which is significantly faster compared to wet-chemical etching and thermal oxidation. Further optimization may be possible by modifying the etching solution. No mechanical polishing is required to reuse the seed.

Open research questions remain as to the annealing effect on proton irradiated samples with doses of about $20 \times 10^{16}\,\mathrm{cm}^{-2}$. These samples turned opaque after implantation indicating graphitization but became again transparent during high temperature CVD. The effect is certainly some form of annealing, however, the diamond lattice was not completely repaired as those samples etched in thermal oxidation conditions forming a gap of 10 µm corresponding to a thick damaged region.

Chapter 6

Continuous wave reactor operational field mapping and SCD synthesis for pressures up to 400 Torr

6.1 Introduction

During the last 20 years, microwave plasma assisted chemical vapor deposition (MPACVD) technologies have become the most established method to grow single crystalline diamond (SCD) [30, 59, 31, 67, 72, 190, 56, 49, 46, 66, 191, 192, 61, 100, 193]. Several different reactor designs have been proven successful in diamond growth. Recently, Mallik [194] compiled a detailed MPACVD technology review and presented the schematics of the important different reactor designs currently in use. Despite the recent improvement in MPACVD diamond growth technologies, there is a continuous need to further increase high quality diamond growth rates.

Using the diamond deposition theory as provided by Harris and Goodman [45, 41], i.e. referred to here as the Harris-Goodman CVD diamond deposition theory, Silva et al. [49]

showed that increasing the process pressure is a key parameter to simultaneously increase the SCD growth rate and crystal quality. Silva's computed model indicated that an increase in pressure results in a higher concentration of [CH_3] radicals in the discharge, which in turn directly corresponds to a higher SCD growth rate. The Harris-Goodwin theory also indicates, as illustrated in Figure 4 of [49], as pressure increases the concentration of atomic hydrogen [H] increases ten to a hundred times faster thanthe increase in [CH_3] radicals.

According to the Harris-Goodwin theory, as introduced in Section 2.2.1, the defect density X_{sp^2} is, inversely proportional to the atomic hydrogen radical density as follows [41]:

$$X_{sp^2} \propto \frac{G}{[H]_s^2}$$

where G is the growth rate. Silva et al. [49] showed that [H] radicals increase much faster with pressure than the [CH_3] radicals. According to Equation (2.2), the defect density decreases as pressure increases. Thus, non-diamond carbon and defects are greatly reduced as pressure increases during deposition while the growth rate also increases. and as a non-diamond carbon and defects are greatly reduced during deposition as pressure increases. Thus, as pressure increases the growth rate increases while the defect density decreases. This behavior has been verified for a broad pressure range [190, 31] of experimental conditions.

Another common approach to increase the growth rate is by increasing the methane concentration in the gas phase. Doing so results in a linear increase of the [CH_3] radical density [49] resulting in a linear increase of the SCD growth rate [56] [85]. Unfortunately, if operating at a constant pressure, the [H] concentration remains virtually unchanged as [CH_3] increases. Thus, under constant pressure operation, the defect concentration will increase as CH_4 increases [70]. However, at high methane concentrations, i.e. greater than

6 %, soot formation occurs. This illustrates the specific desire during process development to increase the process pressure as much as possible and to concentrate on growth conditions with moderate methane concentrations.

Most current reactor designs have reported operating results at a pressure range of 100 to 240 Torr [194]. More recent research efforts have resulted in increasing the operational range to 300 Torr and have successfully demonstrated SCD deposition [59, 31, 61]. Additionally, the stable operation of the microwave cavity plasma reactor (MCPR) up to 350 Torr has been reported [195], but there has been no extensive systematic experimental MPACVD diamond growth results reported yet at pressures between 300 and 400 Torr.

When increasing the pressure a particular set of problems and uncertainties arise: (1) It is well known that the absorbed discharge power density increases super linear with increasing pressure [59] up to 300 Torr and this behavior is likely to continue for higher pressures. Thus, high pressure operation will result in an even more compressed discharge and an associated higher power density discharge. (2) The discharge gas temperature further increases with increasing pressure [195] and can easily surpass 3500 °C. This makes it even more important to ensure that no interactions between the plasma and reactor walls are occurring [57] or else there is a possibility for a critical failure. (3) The discharge becomes much more buoyant with increasing pressure. Slight detuning of the cavity or fluctuations of the output microwave power frequency can actually result in an unsteady flickering discharge or a discharge that moves around inside the reactor [31]. Finally, (4) there is the possibility of hotspot formation, where the discharge attaches to the seed [196, 57] or some other available surface, i.e. the substrate holder. Hence it is more difficult to control the discharge and to ensure a safe and efficient operation with increasing pressure, especially at pressures above 300 Torr.

The objective of this chapter is to advance MPACVD deposition knowledge into the

pressure regime between 300 and 400 Torr and to explore the fundamental MPACVD behavior of SCD growth in this pressure regime. Stable and repeatable operational conditions in this new pressure regime have been found, and high quality SCD growth up to 400 Torr under safe and efficient operating conditions, as has been described earlier for lower pressures [31], has been demonstrated. First, the description of a specific reactor configuration that is used to operate efficiently and safely at pressures between 300 and 400 Torr is presented and then the general experimental methods and procedures are reviewed. Then, the reactor performance in the 300 to 400 Torr pressure regime is experimentally explored. The reactor operating field map and the absorbed power density versus pressure are experimentally measured. These results are then compared to the previously published results from the reactor operation at lower pressure and lower power densities [30, 31, 59]. Finally, SCD is grown under high pressure operating conditions and the growth rate, morphology and crystalline quality of SCD is investigated versus pressure and methane concentration. All experiments use a pocket holder, that has been optimized for rimless SCD growth [72].

6.2 The fundamental reactor behavior at pressures above 300 Torr

6.2.1 Recording of the operating field map and measuring the discharge power density

Previous experiments determining the operating field maps up to 300 Torr employed a 1 inch silicon wafer as substrate for field mapping reference measurements [30, 31]. Lu et al. [31] described the procedure of recording operational field maps in detail. When attempting to

utilize 1 inch silicon wafers above 300 Torr frequent hot spots occurred and melted the wafer. Thus, a 3.5 mm × 3.5 mm × 1.4 mm Type Ib HPHT SCD seed was used as the substrate for this operating field map study and was placed in the optimized pocket holder that is shown in Figure 3.4. In all of the experiments described here the reactor geometry was held fixed as mentioned in Section 3.1.1 and only the input pressure and power were varied. The hydrogen flow rate was held constant at 400 sccm. A constant methane flow of 12 sccm was added for a methane concentration of 3 % and a total gas flow of 412 sccm. The substrate temperature was measured using a IRCON Ultimax one-color infrared pyrometer. The emissivity was set to 0.6.

Optical photographs of the plasma discharge have been recorded during the operating field mapping using a Canon EOS 20D. The camera was placed on a tripod outside the reactor to ensure a fixed position. The plasma was displayed through a screened window machined into the cavity. The exposure time was kept constant to compare the different images. The pocketed substrate holder had a diameter of 38.5 mm and which was found to be 2337 pixels in the photo images of the discharge. The plasma discharge volume V_d was calculated analyzing the photographs using image analysis software Fji [188]. The discharge diameter d was determined by intensity analysis of a line scan across the center of the spherical discharge. The threshold intensity was identified as 66 %, as 50 % overestimated the plasma volumes significantly due to the corona of the bright discharge. The discharge volume was calculated by assuming a spherical discharge and using:

$$V_{\mathrm{d}} = \frac{\pi}{6} d^3 \tag{6.1}$$

The discharge power density was calculated by:

$$< P_{\mathrm{abs}} >= \frac{P_{\mathrm{abs}}}{V_{\mathrm{d}}} \tag{6.2}$$

This approach is similar to the method used by Bushuev et al. [86]. They recorded two adjunct images of the plasma discharge using a H_α filter. They defined 50 % intensity as the boundary of the discharge core and determined the two individual ellipsoid plasma projections to calculate the discharge volume. Their reported absorbed microwave power density at 130 Torr was between 200 and 500 $\mathrm{W\,cm^{-3}}$ using a different reactor than the one used in this study.

6.2.2 Discharge behavior and absorbed power density

It is well known that an increasing pressure results in decreasing discharge dimensions under constant absorbed input power [30]. This means that increasing the pressure results in an increased discharge power density [30, 190]. Thus, increasing the pressure and absorbed power simultaneously is a good way to enhance the discharge power density while keeping the discharge dimensions constant. Another benefit of increasing the pressure is that as the growth rate increases the defect density decreases [49]. It is possible to increase the discharge power density independently from the pressure by altering the reactor dimensions, i.e. by reducing the substrate holder diameter as discussed in [30, 59]. For example, when redesigning Reactor A to Reactor B the cooling stage/holder diameter was reduced by a factor of 2 and the discharge power density for the same pressure was increased by a factor of 4 to 5 [59]. The effect of the increased discharge power density resulted in a factor of three increase in grow rate [54, 30].

Previous reports did show a super linear increase of the discharge power denisty with

increasing pressure for Reactor B up to 240 Torr [59]. In this investigation, which utilizes the highly filtered continous microwave power supply, the power density was determined up to 400 Torr. The discharge volume was approximated as described in Section 6.2.1. Figure 6.1 shows the photographs of the discharges between 120 and 400 Torr. The estimated plasma volumes and the calculated absorbed discharge power densities are plotted versus pressure in Figure 6.2. The graph shows that the plasma volume is descreasing for increasing process pressure while the absorbed input power level is held constant. This results in an increase of the absorbed discharge power density with increasing pressure. As shown in Figure 6.2 the discharge has a volume of 7.6 cm^3 for a process pressure of 120 Torr and an absorbed power level of 2100 W, and decreased to 4.0 cm^3 and 3.1 cm^3 for 300 and 400 Torr, respectively.

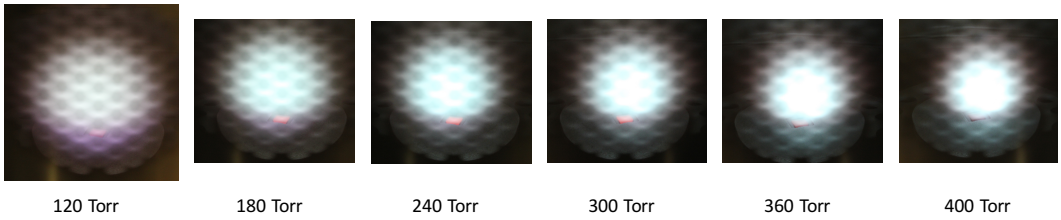

Figure 6.1 Photographs of the discharge above a 3.5 mm × 3.5 mm SCD substrate in a 1.5 inch molybdenum holder as the pressure is increased from 120 to 400 Torr. The absorbed power is kept constant at 2100 W.

The development of the absorbed discharge power density can be broken down into two regimes. A linear increase from 275.4 to 526.4 $W\,cm^{-3}$ is observed for moderate pressures from 120 to 300 Torr. Then, in the second regime when increasing the pressure up to 400 Torr the absorbed power denisty increases super linear to 671.3 $W\,cm^{-3}$.

The changes in absorbed power densities when increasing the overall absorbed input power for certain pressures are shown in Figure 6.3. It can be seen, that the power densities for moderate pressures remain relatively constant over power ranges between 1.2 and 2.7 kW. This is in contrast to previous reports, where an increase of overall power resulted in a

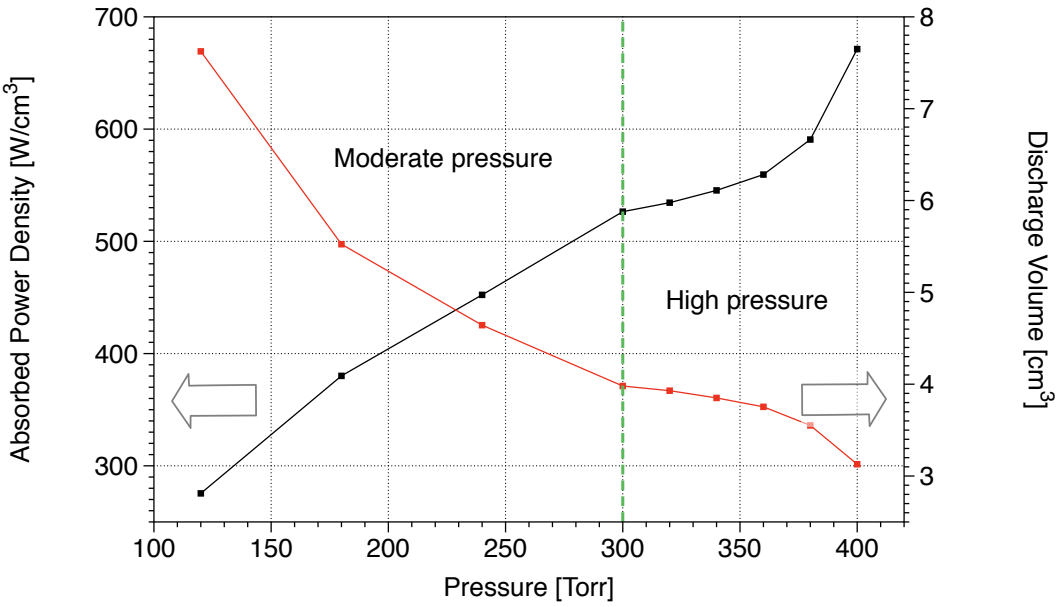

Figure 6.2 Discharge power density and volume as a function of the pressure for the discharges utilizing $P_{abs} = 2100\,W$ and 3 % CH_4 as shown in Figure 6.1. The differentiation between the previously investigated moderate pressure regime and the high pressure regime is indicated by the green dashed line.

reduced absorbed power density [31] as much as 30 % [86] at more moderate pressures in the 100 Torr pressure regime. However, the behavior is different in the high pressure regime, where a parabolic upper trend can be seen, i.e. as the input power increases the absorbed power density first decreases and then at the higher input levels the absorbed power density increases with increasing input power levels. This increase in power density may imply that the discharge at these higher power levels is becoming more of an arc-like and thermal-like discharge. Understanding of this requires further investigation.

6.2.3 High pressure experimental field map

The substrate temperature and pressure as a function of the absorbed power, i.e. the reactors' operational field map, was recorded from 120 Torr to 400 Torr. This set of curves defines the non-linear behavior between the three major input variables pressure, absorbed power and

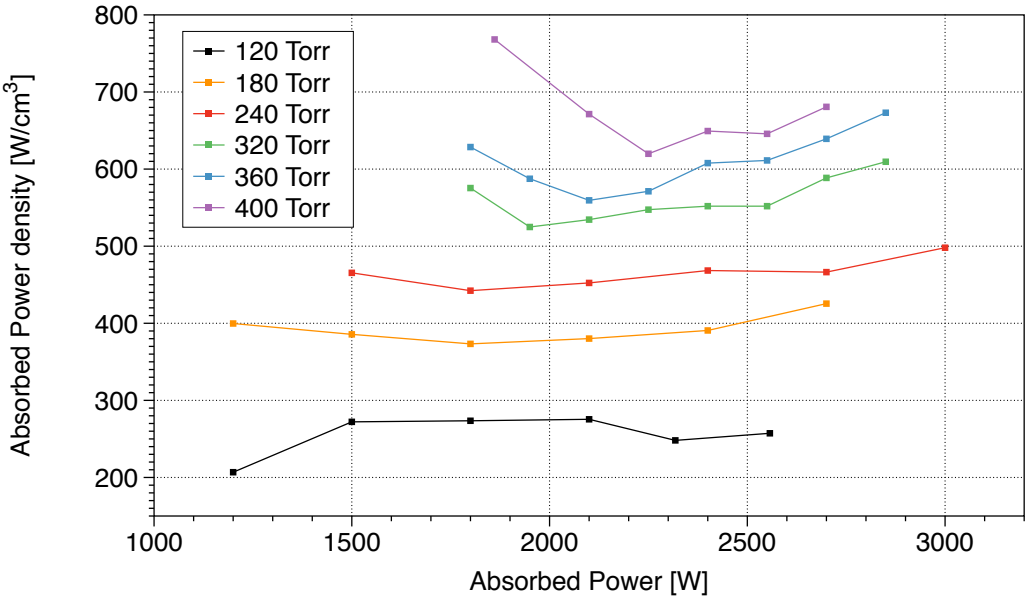

Figure 6.3 Absorbed power densities as a function of the overall absorbed power in the discharge for pressures ranging between 120 and 400 Torr at 3 % CH_4.

substrate temperature. The results for the entire 120 to 400 Torr pressure region are plotted in Figure 6.4. It can be seen that all curves can be described with a linear approximation of the substrate temperature T_s as follows:

$$T_s\left(p, P_{abs}\right) = m\left(p\right) \times P_{abs} + T_{off}\left(p\right) \tag{6.3}$$

where m(p) represents the pressure dependence of the temperature slope $\Delta W/\Delta T$ for increasing absorbed power levels P_{abs}. $T_{off}(p)$ represents a mathematical term which is used to describe a theoretical temperature the substrate would have without input power based on the linear fit. Obviously, this is just a theoretical term as no plasma discharge would be present at 0 W, hence leaving the substrate temperature at room temperature.

Overall, two different pressure regimes have been identified, i.e. one for moderate pressures, 120 to 300 Torr, illustrated in Figure 6.6, and a high pressure regime, 300 to 400 Torr, which is illustrated in Figure 6.7. These two different pressure regimes display different behavior.

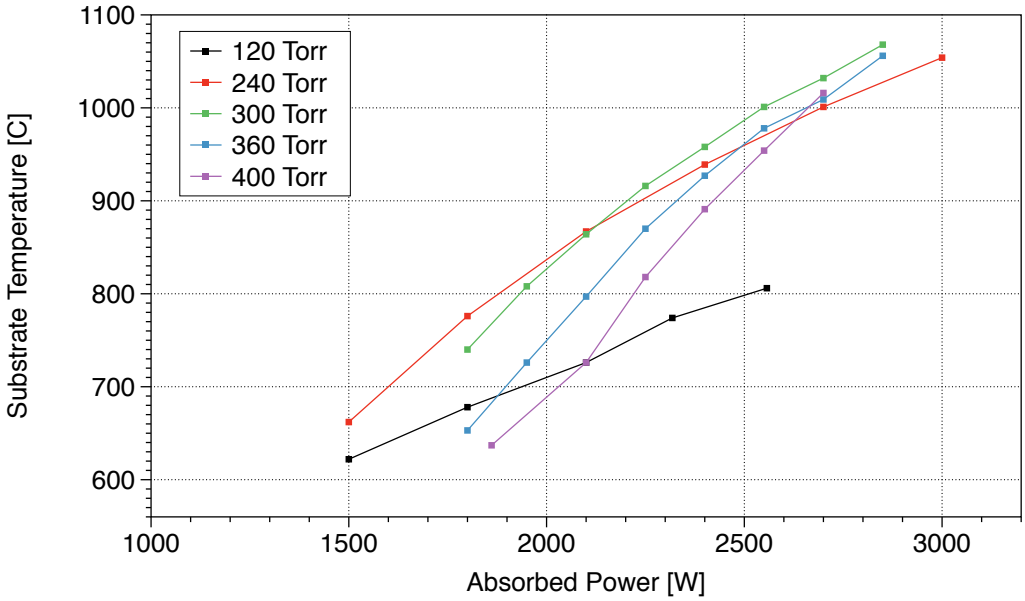

Figure 6.4 Operational field map for Reactor B using a SCD substrate over the entire pressure regime. Experimental conditions: flow = 412 sccm, $CH_4/H_2 = 3\,\%$, $Z_s = -4\,\mathrm{mm}$, $\epsilon = 0.6$

Additionally, the development of the individual curves of the operational field maps was quantified by plotting the parameters of the linear approximation, m(p) and $T_{off}(p)$, as a function of the pressure. The results are shown in Figure 6.5. The separation between the moderate (120 to 300 Torr) and high pressure regime (300 to 400 Torr) and the different behaviors between those two regimes can be clearly well.

The substrate temperature behavior for moderate pressures (120 to 300 Torr) is comparable to previous reports using an unfiltered discharge [30, 31]. Increasing the absorbed power at a given pressure results in an almost linear increase of the substrate temperature across all absorbed power levels as shown in Figure 6.6. This behavior can be verified with the behavior of the fitting parameters of the temperature curves, as shown in Figure 6.5. The slope m(p) is increasing with pressure. Hence, T_s is increasing with the absorbed power at a given pressure. At the same time Ts is also increasing with increasing pressure. This can be explained by the fact, that $T_{off}(p)$ is decreasing with pressure, but the increase of m(p) with pressure is

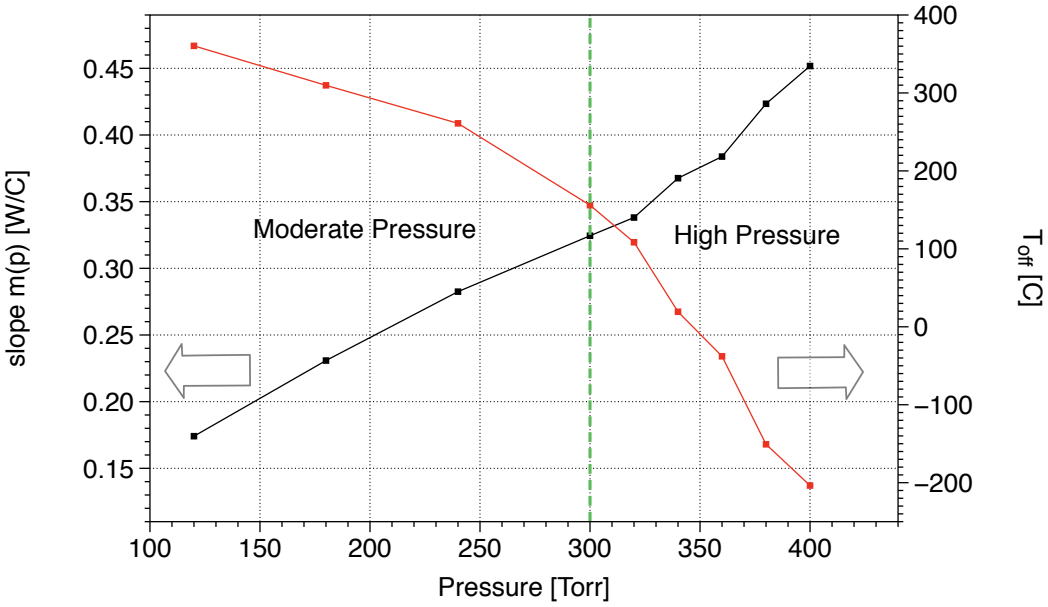

Figure 6.5 Dependency of the fitting parameters used for the linear approximation of the individual temperature curves of the operational field maps as a function of pressure. Data points from additional road map curves in the high pressure regime are shown in Figure 6.7. The differentiation between the previously investigated moderate pressure regime and the high pressure regime is indicated by the green dashed line.

high enough to counter the behavior of $T_{off}(p)$. This results in the increased overall SCD substrate temperature. The same trend can actually be seen in Figure 7 of Lu et al. [31] when evaluating the temperature curves for m(p) and $T_{off}(p)$. It can be seen, that $T_{off}(p)$ is decreasing, especially for 180 and 240 Torr. The observation of the decrease in $T_{off}(p)$ is an indicator, that higher absorbed power levels will be necessary in order to operate the reactor at a regime with substrate temperatures suitable for SCD diamond growth.

Figure 6.7 displays a more detailed view of the field map over the high pressure regime. As shown in the figure, once the pressure is increased into a high-pressure regime (300 to 400 Torr) a different behavior is noticeable. This behavior is more easily detectable when evaluating the fitting parameters of the temperature curves, as shown in Figure 6.5. The temperature slope m(p) is still increasing linear with pressure, but at a higher slope compared to the moderate pressure regime. At the same time, the temperature offset $T_{off}(p)$ decreases

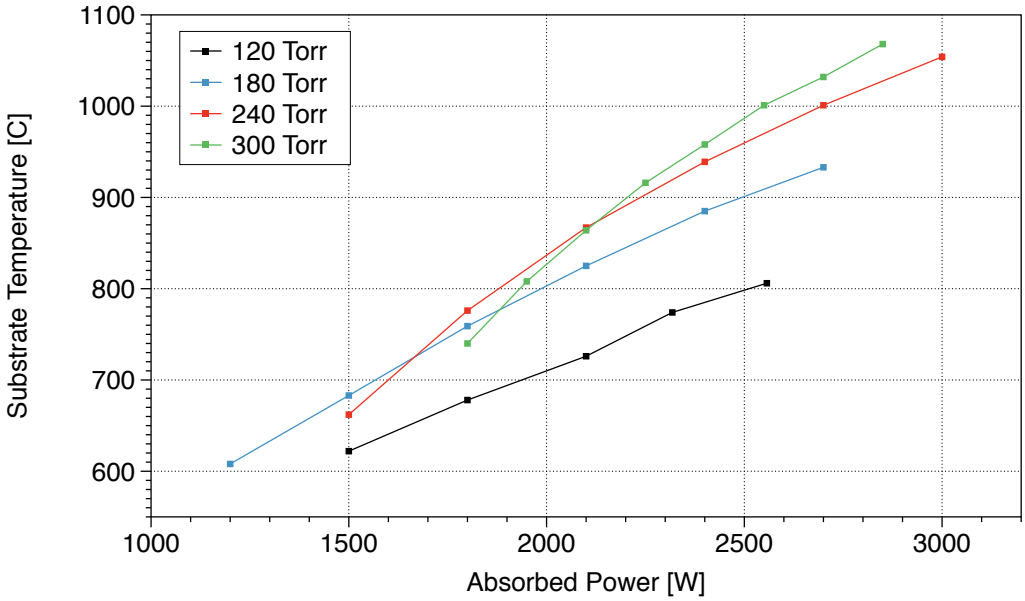

Figure 6.6 Operational field map for Reactor B using a SCD substrate over the previously explored moderate pressure regime (120 to 300 Torr). Experimental conditions: flow = 412 sccm, $CH_4/H_2 = 3\,\%$, $Z_s = -4\,\text{mm}$, $\epsilon = 0.6$

at a much higher rate. Hence, the substrate temperature is decreasing unless significant power levels are used. This is a clear indication, that the interaction between the discharge and the substrate becomes different in this high pressure regime. This increase in the slope of m(p) while $T_{off}(p)$ is decreasing may indicate the beginning of a thermal runaway of the plasma, which becomes disjointed from the substrate, where the pulling away from the substrate results in an insufficient flux of species and energy onto the SCD substrate. The runaway becomes especially noticeable for high pressures of 380 and 400 Torr. The pulling of the plasma from the discharge can be explained as follows: the reactor geometry is fixed as the pressure is increased. It is observed plasma dimensions continue to shrink when the pressure is increased. This was shown in Figure 6.1. It was also observed that the center point of the discharge remains the same throughout the entire pressure regime. Therefore, the plasma discharge pulls away from the substrate as the pressure is increased. This results in an increasing distance between the substrate and the boundary of the spherical plasma discharge

with increasing pressure. This further results in a lower species flux onto the substrate. Thus, the plasma-substrate layer, which forms in the space between the substrate and the discharge increases as the pressure increases [67]. Overall, this results in a lower substrate temperature.

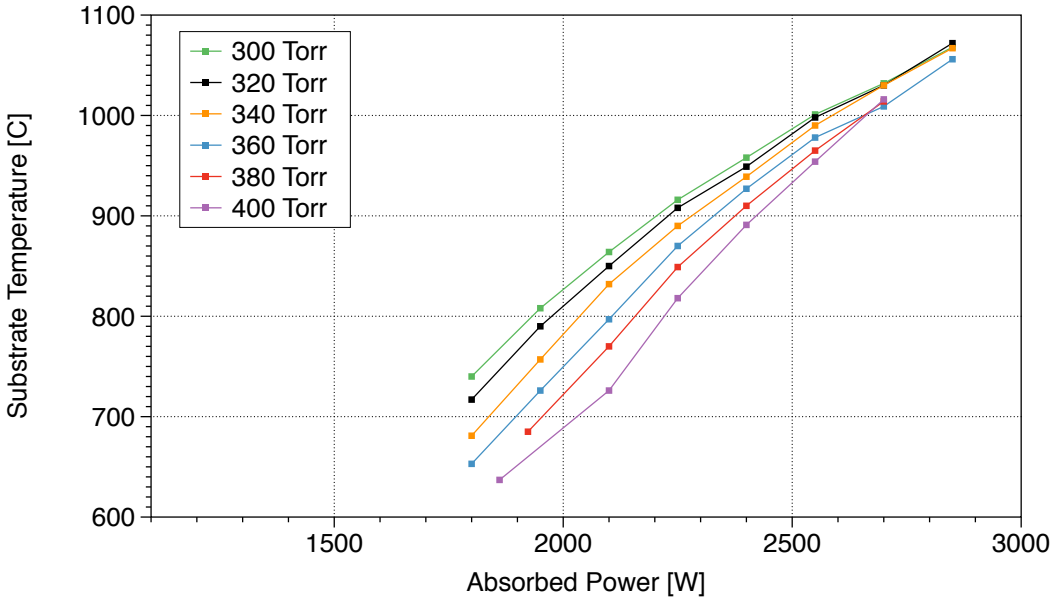

Figure 6.7 Operational field map for Reactor B using a SCD substrate over the previously unexplored moderate pressure regime (300 to 400 Torr). Experimental conditions: flow = 412 sccm, $CH_4/H_2 = 3\,\%$, $Z_s = -4\,mm$, $\epsilon = 0.6$

There are two different possibilities two overcome this effect and to increase the substrate temperature to levels suitable for SCD deposition. One option, as demonstrated Figure 6.4 in and Figure 6.7, is by increasing the absorbed power level of the plasma discharge, i.e. it is necessary to increase the absorbed power from 2400 to 2550 W to maintain similar substrate temperatures when going from 300 to 400 Torr. The center location of the plasma discharge remains the same, but the overall plasma diameter and volume increases as more power is available. This moves the discharge boundary closer to the substrate. The plasma boundary is then moved back closer to the substrate. The boundary layer is reduced and the substrate temperature and growth rate increases.

Alternatively, the reactor configuration can be retuned by adjusting the cavity lengths L_s

and L_p and the position of the substrate within the reactor L_1 and L_2. A proper retuning would allow the movement of the center of the plasma discharge closer to the substrate. This will reduce the boundary layer between the discharge and substrate effectively increasing the substrate temperature and the growth rate, consecutively.

Overall, the discharge dimensions are smaller, when using the approach of retuning the reactor over simply adding more power. Hence, retuning of the reactor seems the most efficient approach when increasing the operating pressure even further. More and more additional power will be required to increase the discharge dimensions in order to offset the increasing distance between the discharge and the substrate. This means, that the reactor is no longer operated efficiently and instead a retuning for efficient operation in this new high pressure regime is preferable.

6.3 Single crystalline diamond synthesis and analysis

6.3.1 SCD deposition

Each experimental SCD deposition lasted 20 hours. The growth processes employed the same cooling stage setup and reactor geometry as shown in Figure 3.1. Process pressures were between 180 and 400 Torr at 5 % methane for the experimental runs in the pressure series. Methane concentrations were varied between 5 and 9 % at 300 Torr for the methane series. During experimental startup, the reactor was ramped up to operating pressure only using hydrogen. Methane was added as soon as process pressure was reached. Unwanted nitrogen incorporation into the reaction chamber caused by the purity of the feed gases is below 6 ppm [68]. Substrate temperatures have been kept constant around 900 °C (this corresponds to 1050 – 1100 °C when measuring with an emissivity of 0.1) by adjusting the absorbed power.

Absorbed power levels were in the range of 2.1 to 2.4 kW. In order to maintain a constant substrate temperature, the absorbed power was decreased throughout the deposition run to compensate for the growing SCD [60]. After deposition, the CVD-grown layer was separated from the seed crystal by laser cutting and mechanical polishing [180]. PCD, which has formed on the substrate holder during deposition was removed after each SCD deposition experiment [67].

6.3.2 Pressure series: the experimental demonstration of SCD growth at 300 to 400 Torr

6.3.2.1 Growth rate versus pressure

Based on the Harris-Goodwin theory an increase in process pressure results in an almost linear increase of growth rate, while reducing the defect density significantly due to the presence of much higher amounts of atomic hydrogen [49]. This behavior has been verified in various reactor geometries for lower pressures, including up to 280 Torr [31] using an unfiltered microwave discharge. In this investigation SCD growth was performed for pressures between 180 and 400 Torr.

The experimental growth rate and weight gain as a function of the process pressure were measured and are plotted in Figure 6.8. An almost linear increase of the growth rate can be seen up to 380 Torr. Overall, the growth rate tripled from 9.3 to 28.1 $\mu m\,h^{-1}$ when the pressure increased from 180 to 380 Torr. The growth rates reported here were smaller compared to previously reported growth rates using a Reactor B from 180 up to 280 Torr, which was equipped with an unfiltered microwave power supply [30, 31, 67]. For example Lu et al. [31] reported growth rates between 26 and 28 $\mu m\,h^{-1}$ for a process pressure of

240 Torr, while only 16.2 µm h^{-1} have been achieved in this investigation. Examples of Lu's experimental results are plotted in Figure 6.8 as the five red individual data points. This is in accordance with the recognition that the discharge by Lu et al. [31] was fluctuating which leads to increased growth rates due to the increased creation of [CH_3] species [140, 146, 147].

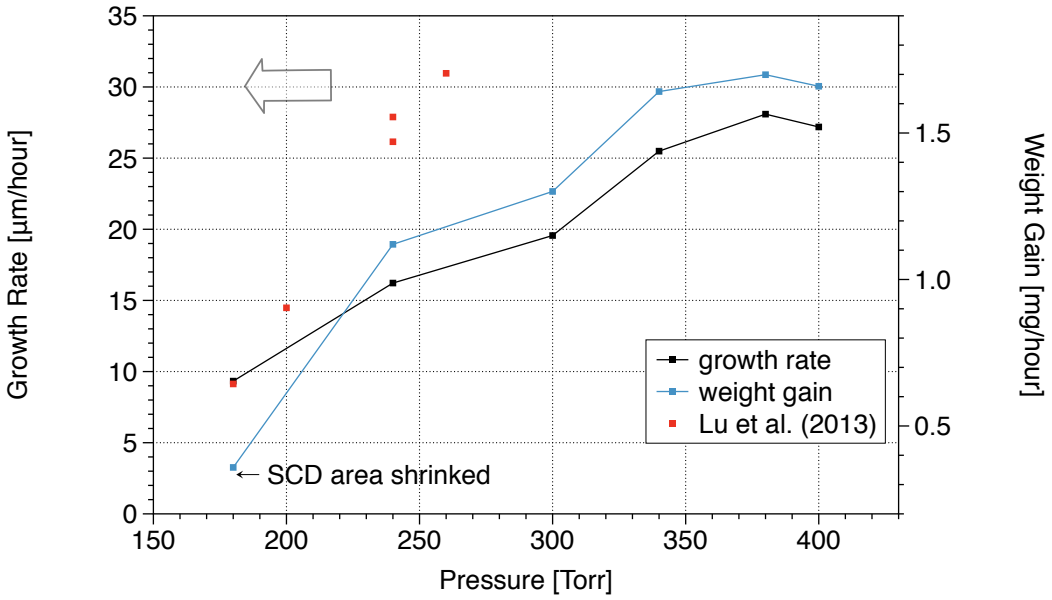

Figure 6.8 Linear growth rate and weight gain as a function of the process pressure and comparing the growth rates to previously reported results by Lu et al. [31]. Experimental parameters: flow = 420 sccm, CH_4/H_2 = 5 %, Z_s = −4 mm, T_s = 900 °C , ϵ = 0.6, t = 20 h

When the pressure is increased further from 380 Torr to 400 Torr, the growth rate flattens out. The most likely explanation of this phenomenon is to associate it with the observations, which were made and analyzed in Section 6.2.2. In other words, as the pressure increases the distance between the discharge and the substrate also increases. It is plausible to assume that the region of high density [CH_3] creation is being pulled away from the surface of the substrate.

The increase of the weight gain as function of the pressure follows the growth rate behavior. This is reasonable as no PCD has been formed throughout deposition, as seen Figure 6.9.

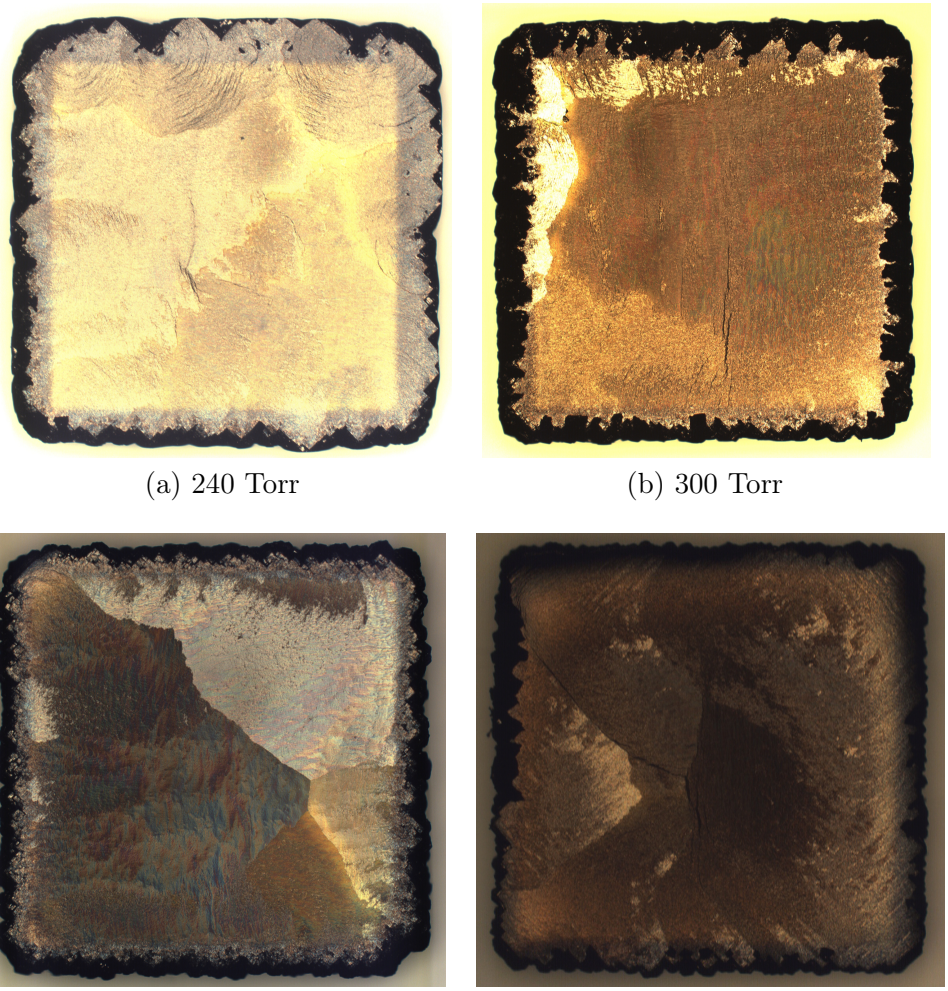

(a) 240 Torr (b) 300 Torr

(c) 380 Torr (d) 400 Torr

Figure 6.9 Top surface of SCD films grown in the pressure range between 240 and 400Torr.

6.3.2.2 Morphology versus pressure

The morphology of the grown SCD films after deposition without additional processing can be seen in Figure 6.9. No PCD formation occurred throughout the entire pressure regime by using a pocket holder design similar to the design that was optimized for rimless growth [72]. Additionally, the SCD surface area enlarged from 3.6 mm × 3.6 mm to approximately 4.3 mm × 4.3 mm, which is an overall increase of around 40 %. The outgrowing occurs in a rather similar way for the entire pressure regime. Only a few experiments occurred, where

the outgrowing was not as dominant, such as the example shown in (b) of Figure 6.9, where nevertheless the SCD area still increased by more than 25 %. The formation of a few local defects in the outgrown SCD material occurred, see (a) in Figure 6.9, where the middle of the top edge features a few defects. Other than that, it can be noted, that the morphology of the center SCD area looks almost perfect. No growth defects are visible and the SCD grew in layer-by-layer mode resulting in a smooth surface.

6.3.2.3 Birefringence versus pressure

Figure 6.10 shows the birefringence images of the freestanding CVD-grown SCD films from Figure 6.9 after they were laser cut and mechanically polished [180]. Unfortunately, the plates in (a) (240 Torr) and (b) (300 Torr) cracked during mechanical polishing due to their rather thin film thickness. The only detectable amount of birefringence is located at the edges of the SCD in the outgrown areas. The stress is distributed around all four sides and can be attributed to the (110) and (111) oriented lateral growth directions [46]. For examples, (d) of Figure 6.10 features the highest amount of birefringence in its four corners being attributed to the (111) oriented growth [46]. The center of each grown SCD film is virtually stress free and covers the entire area of the original HPHT seed crystal. All HPHT seeds showed a high amount of birefringence in the typical clover like stress pattern [180]. This indicates that internal stress, as shown in Figure 6.10, is not propagating from the seed crystal itself into the grown CVD film.

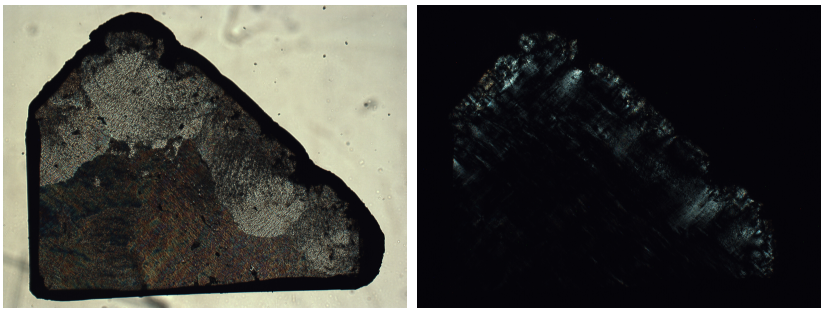

(a) 240 Torr

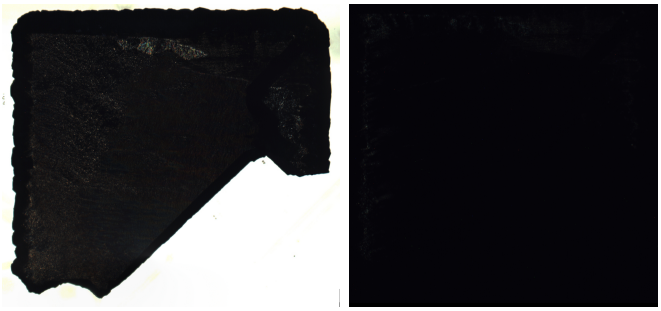

(b) 300 Torr

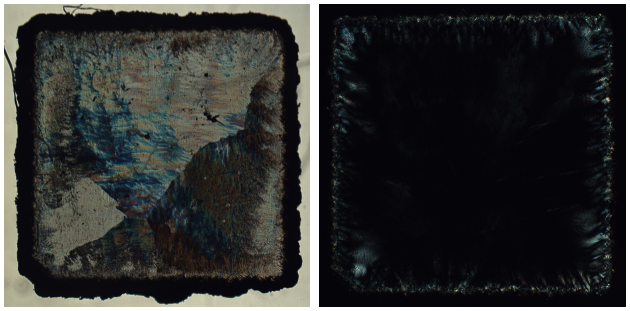

(c) 380 Torr

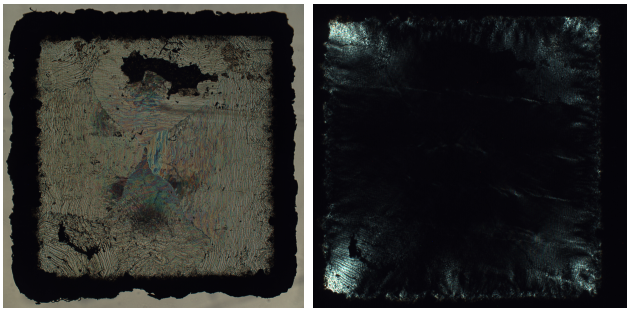

(d) 400 Torr

Figure 6.10 Through (left) and birefringence (right) images of grown SCD films for pressures between 240 and 400 Torr.

6.3.3 Methane series: the exploration of SCD growth at high methane concentrations at 300 Torr

6.3.3.1 Growth rate versus methane concentration

Another way to increase the growth rate of SCD films is by increasing the methane concentration [49, 70]. A linear increase of the growth rate with increasing methane concentration has been reported [186]. Increasing the methane concentration has two intrinsic problems, which have to be balanced: (1) Increasing the methane concentration in the reactor past a certain value frequently causes soot formation and an overall coating of the internal reactor walls, i.e. the quartz dome and the metal walls with carbon containing films [46, 197], and (2) increasing the methane concentration increases the amount of methyl radicals, but does not change the amount of atomic hydrogen [49]. This will result in a higher defect density based on Equation (2.3).

The growth rate and weight gain as function of the methane concentration from 5 to 9 % are plotted in Figure 6.11. The addition of more methane into the reactor results in a moderate increase of the growth rate. When increasing the methane concentration from 5 to 9 % the growth rate increases from 19.6 to 27.1 $\mu m\,h^{-1}$. This is an increase in the growth rate by almost 40 %.

An interesting observation can be made when comparing the increase in growth rate and in weight gain as a function of the methane concentration. While both curves were basically identical for increasing pressure, they show different dependency on methane as shown in Figure 6.11. The graph for the growth rate can be broken down into a region of below 7 % and above that. Contrary to that, the graph for the weight gain is one straight line. This difference can be easily explained by the fact, that the rimless growth disappears at a methane

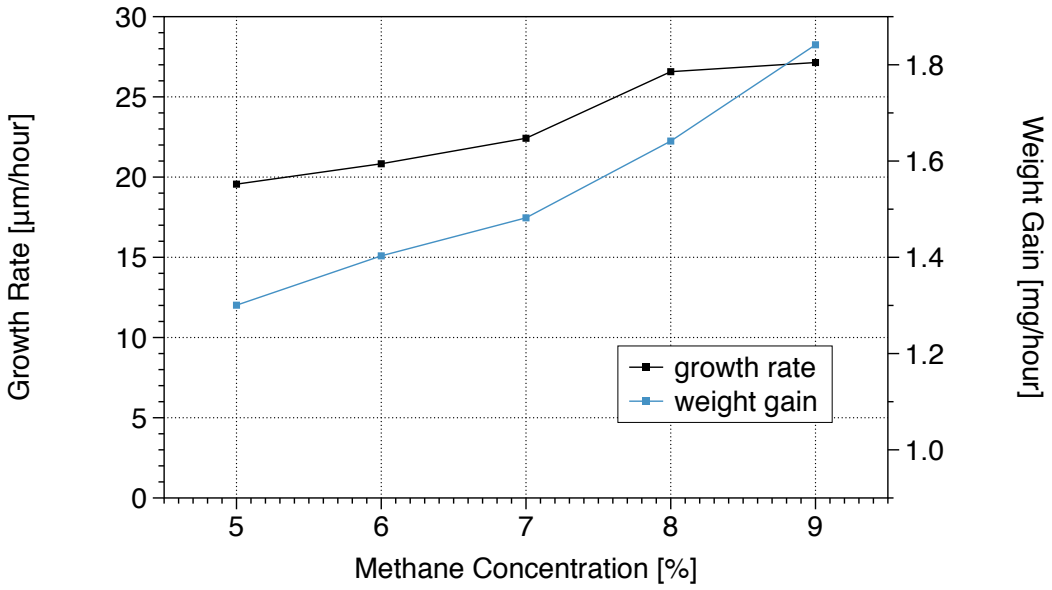

Figure 6.11 Linear growth rate and weight gain as a function of the methane concentration. Experimental parameters: p = 300 Torr, $Z_s = -4$ mm, $T_s = 900\,^{\circ}$C , $\epsilon = 0.6$, t = 20 h

concentration greater than 6 % and a PCD rim forms for 7 % methane and above as shown in Figure 6.12. The total amount of carbon grown onto the seed crystal is increasing linearly as expected, which reflects in the graph of the weight gain. Once the formation of PCD sets in, the growth mode changes, which impacts the linear SCD growth rate in the center of the sample.

6.3.3.2 Morphology versus methane concentration

Another interesting observation in addition to the PCD formation for methane concentrations for 7 % and above is a visible change in morphology of the grown SCD material. As shown in Figure 6.12 the SCD films grown with 5 and 6 % methane are smooth. This clearly changes for higher methane concentrations. The growth mode transfers first into an oriented terrace growth. This trend has been observed by others as well [186]. The growth at 9 % methane can almost be classified as island growth [198]. This somewhat uncontrolled growth results

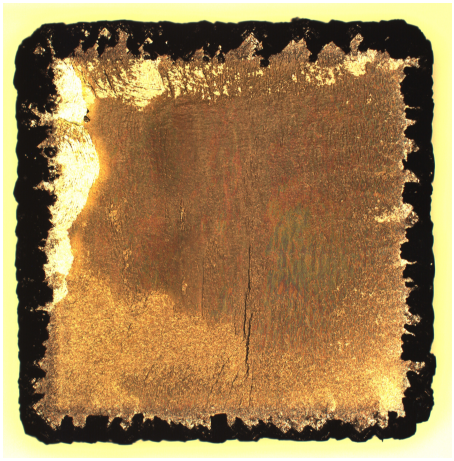

(a) 5 %

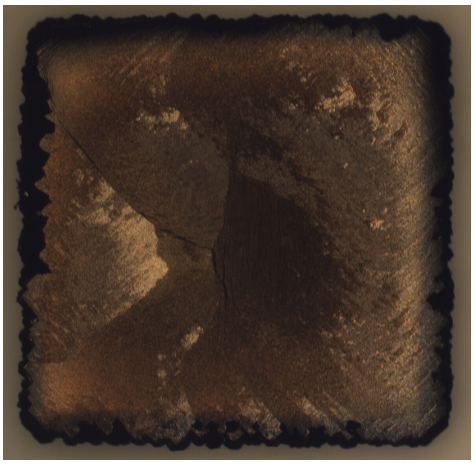

(b) 6 %

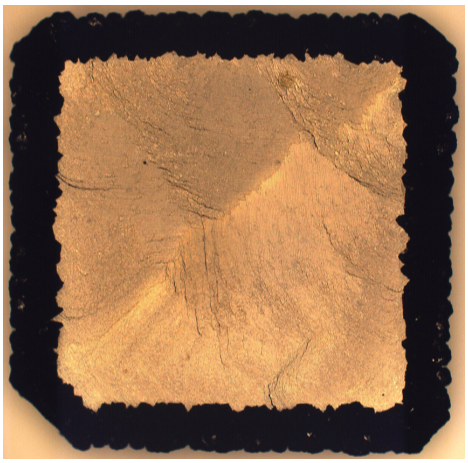

(c) 7 %

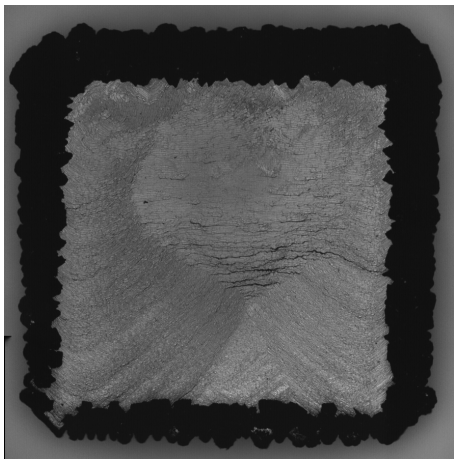

(d) 8 %

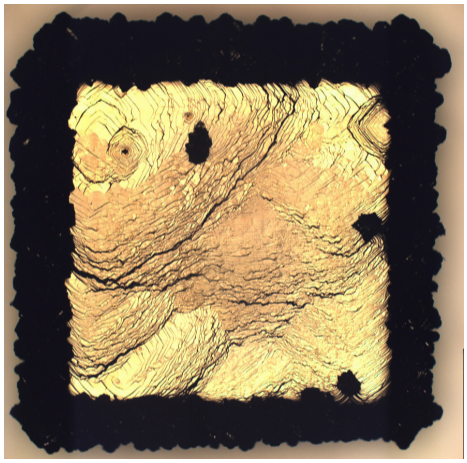

(e) 9 %

Figure 6.12 Top surface of grown SCD films for methane concentrations between 5 and 9 %.

in the formation of several visible defects.

6.3.3.3 Birefringence versus methane concentration

Birefringence images of the freestanding films are shown in Figure 6.13. Additionally, (a) in Figure 6.10 is the corresponding image for 5 % methane concentration. The stress behavior follows the same trend as the growth mode. Five and 6 % methane concentration contain only small amounts of internal stress on the outgrown part of the SCD being attributed to the (110) oriented lateral growth while the center is stress free. This changes for higher methane concentrations. SCD films grown with at least 7 % methane all show various degrees of internal stress, distributed across the entire film. One could speculate, that the transformation in growth mode does not only cause the formation of PCD material, but also introduces stress into the film. The stress pattern of the underlying HPHT seeds had the typical clover like appearance. Contrary to that, the stress pattern found in the CVD-grown films do not follow the clover like stress pattern observed in the HPHT seed, indicating that the occurrence and type of internal crystal stress in the CVD-grown materials is created independently from the seed crystal.

6.4 Summary

The growth window for SCD was increased into the 300 to 400 Torr pressure regime and the deposition of high quality stress free SCD was demonstrated by utilizing a stable continuous microwave power supply. Individual deposition runs were carried out over 20 hours each using a fixed reactor geometry. Substrates were placed in a shallow pocket holder (d = 2.0 mm) and the substrate temperature was kept constant at 900 °C by adjusting the absorbed power

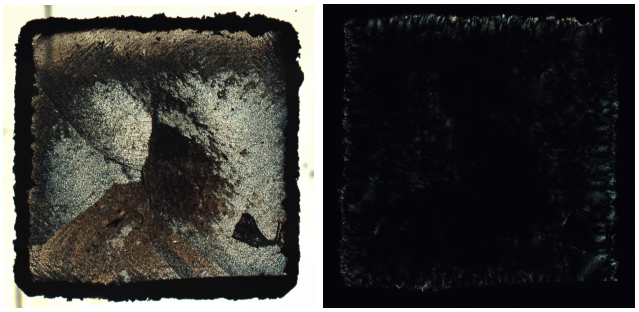

(a) 6 %

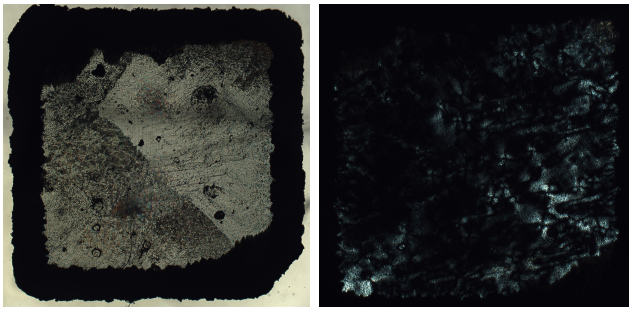

(b) 7 %

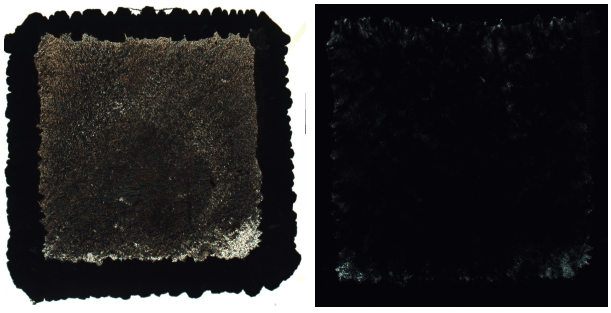

(c) 8 %

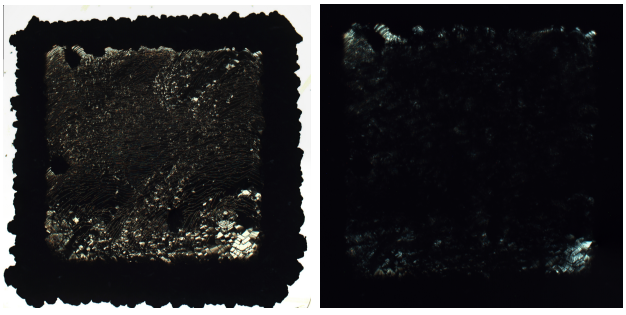

(d) 9 %

Figure 6.13 Through (left) and birefringence (right) images of grown SCD films for methane concentrations between 5 and 9 %.

between 2.1 and 2.4 kW. Growth rates increased with pressure and were as high as 28.1 µm h^{-1} for 380 Torr. The freestanding SCD plates were grown without a PCD rim and did not show birefringence. The reactor demonstrated repeatable deposition performance throughout the 300 to 400 Torr pressure range during more than 50 growth experiments. For example, the plasma discharge remained stable in size and position without any presence of flickering and almost identical absorbed power levels were used in individual growth experiments to achieve the same growth conditions.

The reactor was experimentally characterized by measuring the operational field map and the associated absorbed power densities between 300 and 400 Torr. Refined methods for recording the operational field map and absorbed power densities were established. Absorbed discharge power densities in the 300 to 400 Torr pressure regime increased from 525 to 670 W cm^{-3} as pressure was increased.

The current understanding of diamond growth versus pressure, i.e. the Harris-Goodwin theory, was verified over the 300 to 400 Torr pressure regime. The discharge volume keeps decreasing and the absorbed power density increases with pressure. The growth rate increases with pressure and the quality of the grown diamond films remains high.

Rimless SCD was grown at 5 and 6 % methane and the SCD surface area expanded by 40 %. Higher methane concentrations resulted in a change of surface morphology and the formation of a PCD rim and the likelihood of soot formation. The current understanding of diamond growth versus methane concentration was verified in the high pressure regime of 300 Torr, i.e. the growth rate increased by 40 %, but the formation of defects during deposition increased as well as predicted by the Harris-Goodwin theory [41].

The plasma discharge decreased in size and pulled away from the diamond seed and substrate holder for very high pressure experiments (above 380 Torr), both when recording

the operational field map and during SCD growth and the growth rate slightly decreased. This indicates, that the reactor configuration, i.e. the substrate holder design and position z_s, has to be readjusted and tuned to further enhance the SCD growth performance. This process optimization remains to be investigated in future work when the operational regime will be enhanced even further by operating in even higher pressures. Hence, further experiments are expected to result in optimized results on the SCD growth rate and crystalline quality. Additionally, further investigation of the plasma, i.e. optical emission spectroscopy and determination of the gas temperature, in this high pressure regime is still necessary.

Chapter 7

Time resolved formation of pulsed microwave discharges

7.1 Introduction

Pulsing of the discharge, which is inside of a microwave plasma assisted chemical vapor deposition (MPACVD) diamond deposition reactor, has attracted great interest in recent years [199, 200, 201, 139, 135, 144, 140, 146, 147, 148]. One of the major benefits of pulsing a microwave discharge is that it efficiently increases the amount of atomic hydrogen [H] in the discharge [199, 143], which in turn plays a crucial role in the growth of single crystalline diamond (SCD) by enhancing the crystalline quality [41, 49]. Additionally, in each duty cycle, the discharge gas cools down when not supplying power. The reduced average gas temperature [140] moves the process into a regime that is better suited for optimal net balance of [CH_3] [202, 203], which enables high growth rate [49].

The efficiencies of using pulsed discharges to enhance diamond growth rates due to the higher number of radicals have been independently verified by several research groups [144, 146, 147, 148]. For example, Tallaire et al. [144] achieved 40 % higher growth rates and Yamada et al. [148] reported up to four times the growth rates. Tallaire et al. [144] also

reported on a significantly improved film quality of the SCD wafers grown with a discharge pulsed with a 50 % duty cycle. Another advantage of pulsing a microwave discharge is that the peak power instead is utilized instead of the average power. This allows the operation of the reactor with a lower overall power consumption [139], while still covering a larger deposition area [145]. In summary, the use of pulsed microwave discharges is a promising approach to increase the MPACVD SCD growth rate and growth area.

Unfortunately, the pulsing process itself is not yet fully understood, leaving room for further improvement. The big shortcomings in fully understanding the underlying processes are: (1) there is no unified theory describing the nature of pulsed microwave discharges, i.e. various studies investigated different pulsing frequencies leaving the field disjoint rather than trying to construct a theory valid for a large experimental variable space. For example, the modeling efforts by Brinza et al. [140] indicated, that pulsing frequencies around 80 Hz would yield the most promising results, while Vikharev et al. [147] identified 250 Hz as the most efficient and Yamada et al. [148] claimed that pulsing in the kHz range outperformed lower frequencies, but introduced plasma instabilities by the pulsing when operating above 120 Torr. It will be necessary to unify those approaches in order to get a solid understanding of the detailed processes involved in the pulsing routine. (2) The pulsing behavior is dependent of the reactor geometry, i.e. absorbed power density, gas flows, diffusion and volume recombination, but this fact is never addressed in the past published work. (3) Most modeling efforts rely on simplistic 1D axial plasma models, which do not account properly for all dynamic processes during expansion and vanishing of the discharge, i.e. Gicquel et al. [139] suggested, that a pulsed discharge may be ignited in a small volume near the SCD surface and hence the ignition phase of the pulsed microwave discharge would not be properly reflected by their developed model. (4) All of the past work has been carried out at lower operating pressures.

Modeling has not been performed for pressures above 150 Torr [148, 136, 139]. Most deposition experiments were in the same pressure region (150 to 202 Torr), only Muchnikov et al. [146] reported on pulsed SCD deposition up to 260 Torr. (5) Most previous studies focused on pulsing frequency and duty cycle as parameters. Even though these two are the easiest to access and visualize, they depend on the high and low times (T_{high} and T_{low}) of the pulsing cycle. Additionally, the pulsing times and the microwave power provided for the pulsing cycles (P_{high} and P_{low}) have an impact of the average power. The individual variables are inter-dependent. Therefore, the average power, the frequency and the duty cycle should be specified and then similar experiments can be compared to each other. For example, it is easy to construct vastly different pulsing behaviors, i.e. $T_{high} = 2\,ms$ and $T_{low} = 4\,ms$ will have a different pulsing dynamic than $T_{high} = 12\,ms$ and $T_{low} = 24\,ms$, even though both sets of pulsing parameters have a 33 % duty cycle and the same average power P_{avg} if P_{high} and P_{low} are kept constant.

A need of using previously unexplored analytical tools in order to gain a deeper insight was identified in order to establish a different view on the dynamic nature of pulsed microwave discharges. It appeared that the biggest discrepancy is that the plasma simulations created in the past have not included the ignition and transient behavior of the actual plasma. Instead, they were usually compared to steady state analytical techniques, i.e. optical emission spectroscopy, or diamond growth rates. Thus, in this dissertation a new recording technique, video recording was identified as a direct assessment tool for the dynamic formation of the discharge. Recording the dynamic formation of the discharge inside the reactor under actual deposition conditions will finally allow the review and comparison of the simulations with what is actually experimentally happening and to identify potential improvements of the previously used models. Lastly, it is expected that recording the discharge formation for

pulsed discharges at pressures of 300 to 400 Torr will motivate new simulation efforts that are more realistic for SCD deposition [195].

7.2 The video recording setup and procedure

High speed videos of the pulsed discharges were recorded using a Photron FASTCAM APX-RS camera and a Nikon FX AF MICRO-NIKKOR lens with a focal length of 105 mm and a f/2.8 aperture. No external filters were used in the setup. The camera and objective were mounted on a tripod and were focused on the discharge region though a screened window in the cavity. The experimental setup is shown in Figure 7.1. The recording was focused onto the SCD substrate. Control and recording of the camera was performed using an external computer, which was independent of the computer control system of the reactor. The camera setup was focused in live view mode of the software once the reactor reached process pressure. The videos were recorded with a frame rate of 5000 frames per second (fps). This corresponds to an interval of 200 µs between individual frames. The frames have been recorded in color mode and contain 512 by 512 pixel.

The camera recording software saved each individual frame and also created a video of all individual frames in correct order. The video recording sequence was recorded without external triggering of either the high or low shoulder of the square wave of the pulsed discharge (see Figure 3.3). Instead, the recording was started manually and 20 pulsing cycles were recorded for each individual measurement. The recording of multiple cycles was done to ensure a repeatability of the individual pulsing cycle. The number of frames per cycle matched with the anticipated time for the on and off duration of the pulses for all recording illustrating the high stability and repeatability of the pulsed microwave power supply. The first frame of

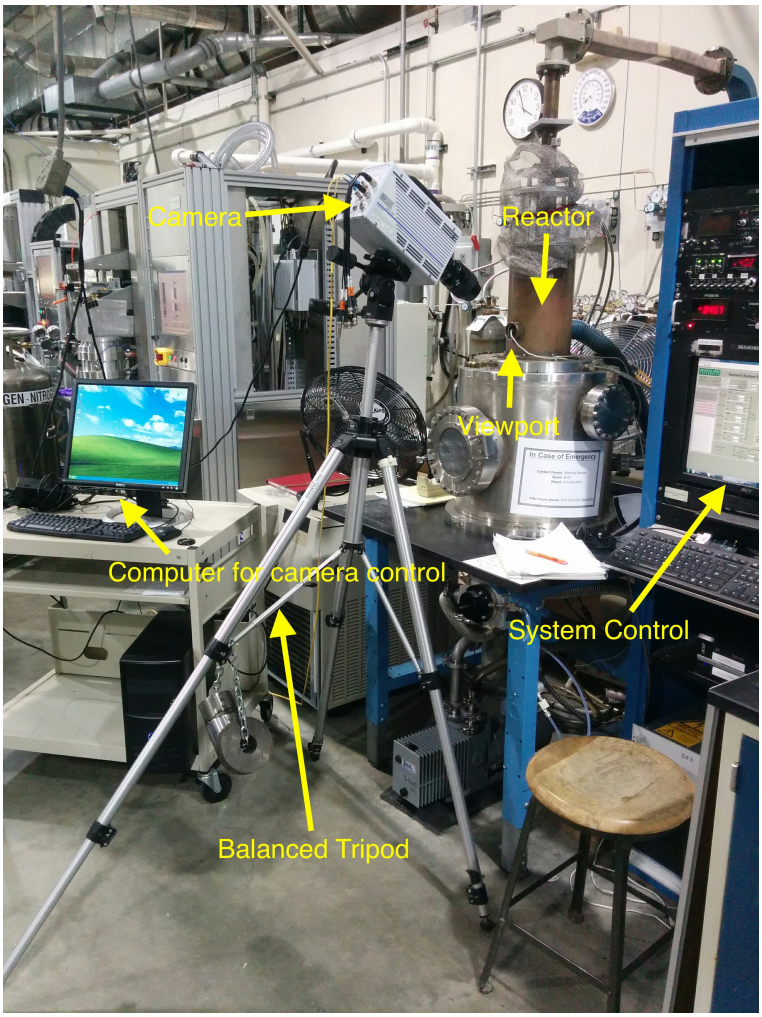

Figure 7.1 Experimental setup for the video recording of the formation of pulsed microwave discharges.

the pulsing cycle was manually identified for data processing (hence the different image IDs for the different cases discussed). The images were individually inspected and the individual time duration within the pulsing cycle were determined based on the image ID and the given frame rate of 5000 fps.

All videos were recorded at a process pressure of 300 Torr. The hydrogen flow rate was held constant at 400 sccm. A constant methane flow of 20 sccm was added for a methane concentration of 5 % and a total gas flow of 420 sccm. A 3.5 mm × 3.5 mm × 1.4 mm Type Ib HPHT single crystal diamond was placed in a water cooled pocket holder to represent

actual SCD deposition conditions. The diamond top surface was recessed compared to the holder's top surface.

All studied pulsed behaviors were done using P_{high} of 3000 W and P_{low} of 0 W as fixed variables. Hence, the pulsing can be described as a true on-off pulsing. Thus, T_{high} is the time of the on period within the pulsing cycle and T_{low} corresponds to the off period of the pulsing cycle. Subsequently, T_{on} and T_{off} are used in the rest of the discussion to emphasize that the studied pulsing behaviors are one special case in the four-dimensional pulsing parameter space. The equations to calculate the dependent pulsing variables can be simplified as follows:

$$f = \frac{1000}{T_{\text{on}} + T_{\text{off}}} \,[\text{Hz}] \tag{7.1}$$

$$\text{duty cycle} = \frac{T_{\text{on}}}{T_{\text{on}} + T_{\text{off}}} \,[\%] \tag{7.2}$$

$$P_{\text{avg}} = \frac{T_{\text{on}} \cdot 3000}{T_{\text{on}} + T_{\text{off}}} = 3000 \cdot \text{duty cycle} \,[\text{W}] \tag{7.3}$$

The reactor operated for five minutes each between changing pulsing parameters and video recording to ensure that the reactor is in a steady state. This ensures that the recorded dynamical discharge was caused by the pulsing itself and was not a transient response to changing the external reactor conditions.

7.3 The pulsing cycle of pulsed microwave discharges

Throughout all recorded videos it was found, that the discharge is following a periodic cycle when applying an on-off switched pulsing between 0 and 3000 W. First, the discharge is

igniting. After the brief ignition period, the discharge expands to dimensions, which match those of a discharge created by 3000 W of continuous wave excitation. The phenomena observed in the ignition phase are discussed in the following sections. The images provided cover both, the ignition and expansion phase. If the pulsing duration is long enough to allow the discharge to fully expand, then the discharge will remain in a state corresponding that of a 3000 W continuous wave excitation discharge until the off part of the cycle is reached. This state of the discharge is referred to as steady state operating point.

Moving into the off part of the cycle causes the input power to go to zero. This means, that no additional power is provided to offset losses, i.e. light emission, heat conduction and convection. Thus, the discharge decays as more and more of the energy remaining in the discharge is removed up to the point where the visible discharge disappears and then remains without optical emission for the entire off duration. Once the next on state is reached the discharge is reignited and the cycle repeats.

7.4 The steady state discharge decay

An example for the plasma decay is shown in Figure 7.2. The orange cube shown in each figure is the SCD substrate, which glows due to its sufficiently high temperature. It can be seen that the center of the plasma with the highest emission intensity is collapsing first within 600 µs while the overall plasma dimensions remain rather constant. The plasma at this time is comparable to images made for an absorbed power level of 2400 W with continuous excitation. The frame afterwards (800 µs) corresponds to a continuous absorbed power level of 2250 W. Overall, the visible discharge is completely vanished within 1.6 ms and no more optical emission can be seen. This is comparable to the numerical description by Brinza et

al. [140], who determined, that diffusion and recombination of ionized species would take approximately 2 ms. It can be seen that the SCD substrate is still glowing, but at a dark red, which indicated that the substrate temperature has already dropped. This can be attributed to the active and constant substrate cooling, while the energy transfer to the substrate is reduced when the discharge collapses.

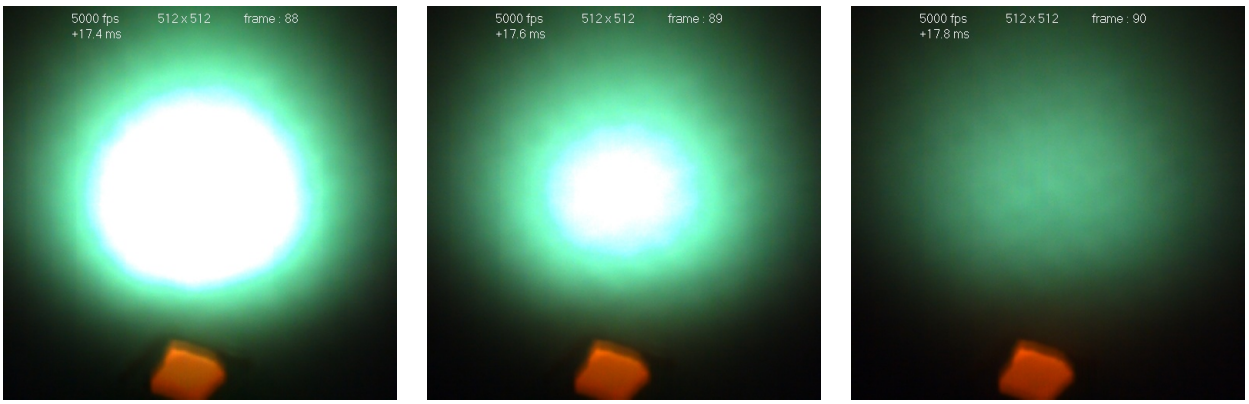

(a) 0.0 ms (b) 0.2 ms (c) 0.4 ms

(d) 0.6 ms (e) 0.8 ms (f) 1.6 ms

Figure 7.2 Example of the decay of a pulsed discharge with an on duration long enough to ensure, that the discharge expended completely to its 3000 W steady state equivalent. The input power goes to 0 W in the first image at 0.0 ms.

7.5 Influence of the duty cycle: identification of five different discharge regimes

Variation of the duty cycle and its effect on the gas temperature and species spatial and temporal distribution were simulated in the past [135, 139]. Unfortunately, those studies were performed at significantly lower pressures than what is commonly used for SCD deposition nowadays. All experiments presented here were performed with $T_{on} + T_{off} = 20\,\text{ms}$, which corresponds to 50 Hz. The pulsing occurred between 3000 and 0 W. Using 50 Hz results in duty cycle increments of 5 %. Records were started at the highest duty cycle of 95 % and successively reduced until a point was reached, where the discharge became instable and died off.

Increasing the duty cycle simultaneously increases the time period when the discharge is active and reduces the time period, when the discharge is off. Thus, the average gas temperature should be increased with a higher duty cycle. Additionally, the number of ionized species is expected to be higher at the beginning of the next pulse due to the shorter off time of the pulsing cycle. A summary of the recorded settings including the pulsing parameters, the resulting dependent variables and classification of the observed discharge formation is summarized in Table 7.1. Overall, five regimes are identified as (1) to (5). Each regime has a different spatially and time varying discharge pattern. Selective videos for each of the four cases, where a discharge is actually created, can be found in the supplemental files.

Pulsing parameters		Dependent parameters			
T_{on} ms	T_{off} ms	duty cycle %	P_{avg} W	f Hz	Spatially different discharge parameters
6	14	30	900	50	(1): no discharge
7	13	35	1050	50	(2): formation of one inhomogenous arc
8	12	40	1200	50	(2): formation of one inhomogenous arc
9	11	45	1350	50	(2): formation of one inhomogenous arc
10	10	50	1500	50	(2): formation of one inhomogenous arc
11	9	55	1650	50	(2): formation of one inhomogenous arc
12	8	60	1800	50	(3): formation of one homogenous arc
13	7	65	1950	50	(3): formation of one homogenous arc
14	6	70	2100	50	(3): formation of one homogenous arc
15	5	75	2250	50	(4): single ignition detached from SCD
16	4	80	2400	50	(4): single ignition detached from SCD
17	3	85	2550	50	(4): single ignition detached from SCD
18	2	85	2700	50	(4): single ignition detached from SCD
19	1	95	2850	50	(5): never goes off

Table 7.1 Different pulsing parameter settings used to study discharge formation for duty cycles between 30 % and 95 %.

7.5.1 Case 5

In the regime labeled (5), it was observed that the discharge never disappears. This was the case for a duty cycle of 95 %. T_{off} is only 1 ms, which is lower than the observed decay time of 1.6 ms. Hence the discharge can be better described by being seen as periodically disturbed continuous discharge, where the short off period of the pulsing cycle introduces that disturbance.

7.5.2 Case 4

Another discharge pattern, described as (4), was observed for duty cycles between 75 and 90 %. Selective images of the temporal discharge development in case of an 80 % duty cycle are shown in Figure 7.3. The discharge ignites half way between the SCD substrate and the steady state position. It is worth noting, that the location of the discharge ignition and

where the discharge decayed and died off are not the same. The discharge ignites below the center of the image (see Figure 7.3, (a)), while it decays within centered to the top third of the image (see Figure 7.2 (e)). After ignition, the discharge expands and moves towards the steady state position. The duration to reach the steady state position and plasma dimensions is between 10 and 12 ms depending on the specific duty cycle.

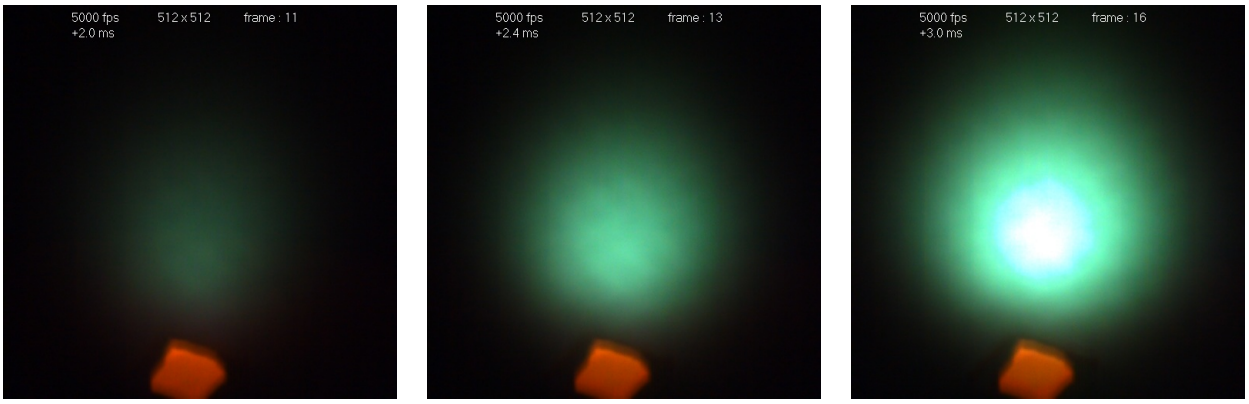

(a) 0.4 ms (b) 0.8 ms (c) 1.4 ms

(d) 2.0 ms (e) 4.0 ms (f) 12.0 ms

Figure 7.3 Temporal development of a discharge with T_{on} of 16 ms and T_{off} of 4 ms corresponding to a 80 % duty cycle with a pulsing frequency of 50 Hz.

7.5.3 Case 3

A third pattern of discharge development, described as (3), was observed for duty cycles between 60 and 70 %. The temporal development is shown in Figure 7.4 for a duty cycle

of 60 %. It can be seen, that the discharge is actually igniting on the SCD substrate or in close proximity. Initially, the discharge is not spherical. Instead it has a stretched-out shape pointing from the SCD substrate to the steady state position. The light intensity is the highest close to the SCD substrate and becomes dimmer moving towards the steady state position. At the same time the discharge is spreading out with reduction of the light intensity giving it fan-like shape. Overall, the ignition behavior appears like a microwave breakdown forming right above the SCD substrate and reaching towards steady state discharge region. This can be seen more profoundly in the images given for an experiment discussed later in Section 7.6 (Figure 7.10). The shape of the ignition of the discharge matches the distribution of the electric field in the coaxial section of the cavity without discharge as shown in Figure 7.5 [149]. Hence, the discharge ignition occurs under MPCR conditions, which match with the electric field of the standing wave forming inside the cavity without a plasma load. The discharge remains attached to the SCD for around 1 ms while mainly expanding towards the sides first changing in an elliptical shape (see Figure 7.4 (c)) and finally being close to spherical when the discharge detaches from the substrate (see Figure 7.4 (d)). After detaching from the substrate, the discharge is floating towards and into the steady state position while expanding in size. The steady state position is reached around 12 ms into the specific cycle. Hence, the steady state is reached for all duty cycles with the third pattern of discharge development.

7.5.4 Case 2

A fourth pattern of the discharge development of the pulsed discharges, described as (2), was found for duty cycles between 35 and 55 %. The temporal development is shown in Figure 7.6 and is much more complicated in nature. On first sight, it appears that two discharges are

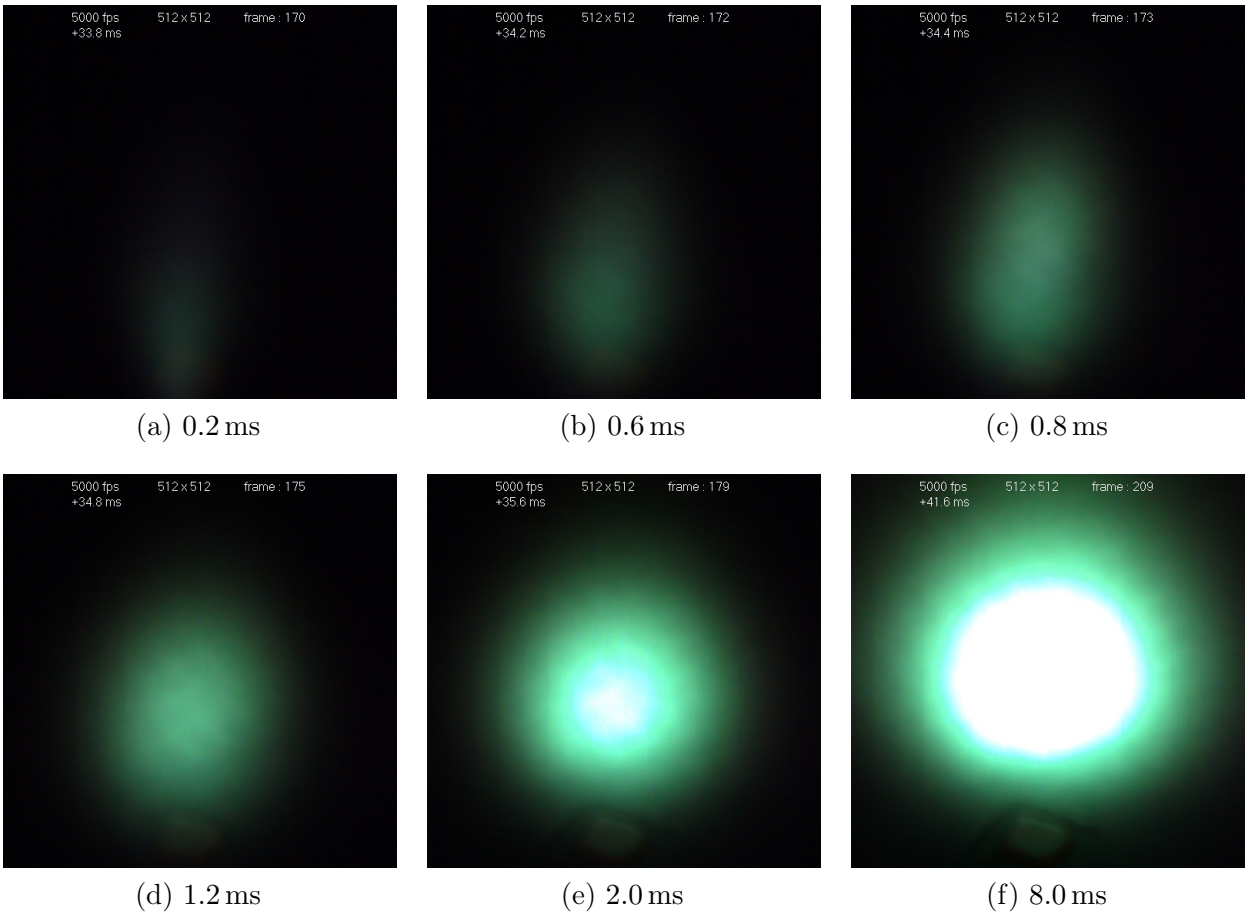

(a) 0.2 ms (b) 0.6 ms (c) 0.8 ms

(d) 1.2 ms (e) 2.0 ms (f) 8.0 ms

Figure 7.4 Temporal development of a discharge with T_{on} of 12 ms and T_{off} of 8 ms corresponding to a 60 % duty cycle with a pulsing frequency of 50 Hz.

formed. Alternatively, it can be argued, that one arc-like discharge is formed. This arc consists of three individual discharge regions from the substrate towards the steady state position: (i) a green discharge region forming on the SCD substrate and having a slight fan-like opening, which develops into (ii) a thin and narrow purple region and finally (iii) a white-purple narrow arc-region reaching into the steady state position. The coloration of the second region (ii) indicates an excitation of hydrogen rather than methane as the purple coloration comes from the overlap of the H_α and H_β atomic lines. Interestingly, the location of that region corresponds roughly to being the center of the spherical discharge ignition observed in case (4), see Figure 7.3. The coloration of the third region on the other hand

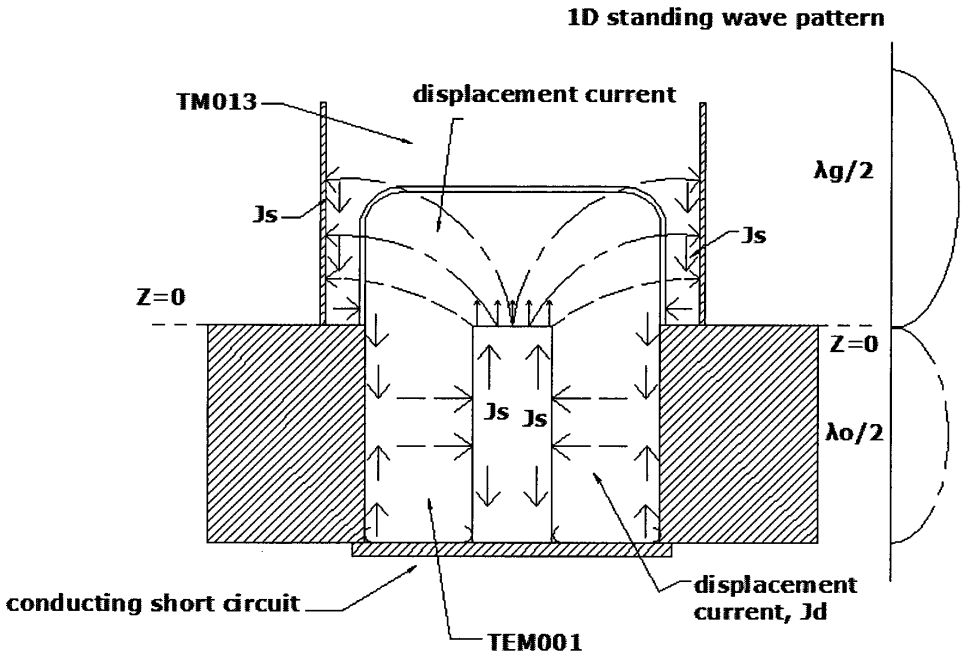

Figure 7.5 Electromagnetic standing wave and surface current in the coaxial section of the applicator. [149]

corresponds to the typical coloration of a low-pressure methane discharge. This is contrary to the arc formation in Figure 7.4, where a uniform green color was recorded and only the intensity fluctuated. The same fluctuation in intensity can be seen in region (i) of Figure 7.6. Overall, the arc formed in the fourth pattern is narrower and reaches up much further towards the steady position. Additionally, the width of the arc is an overlap of a fan-like shaped and a straight part across discharge length, while it spread out like a fan across the entire discharge region in the third pattern. Afterwards, the regions (i) and (iii) of the arc-like discharge are contracting towards the purple region (ii) while the coloration of region (iii) changes from the initially observed white-purple to the typical green of a methane discharge. The initially straight arc is turning into a dumbbell shape (see Figure 7.6 (c)). The narrow center of that dumbbell shaped discharge is still given by the narrow and thin purple discharge region (ii). The discharge becomes ellipsoidal and visibly detaches from the SCD substrate 1.8 ms after

ignition and the purple region within the plasma discharge disappears simultaneously. The discharge starts floating up towards the steady state position and quickly becomes spherical. However, the time of the pulsing cycle where power is provided is not sufficiently long to reach the steady state of the discharge.

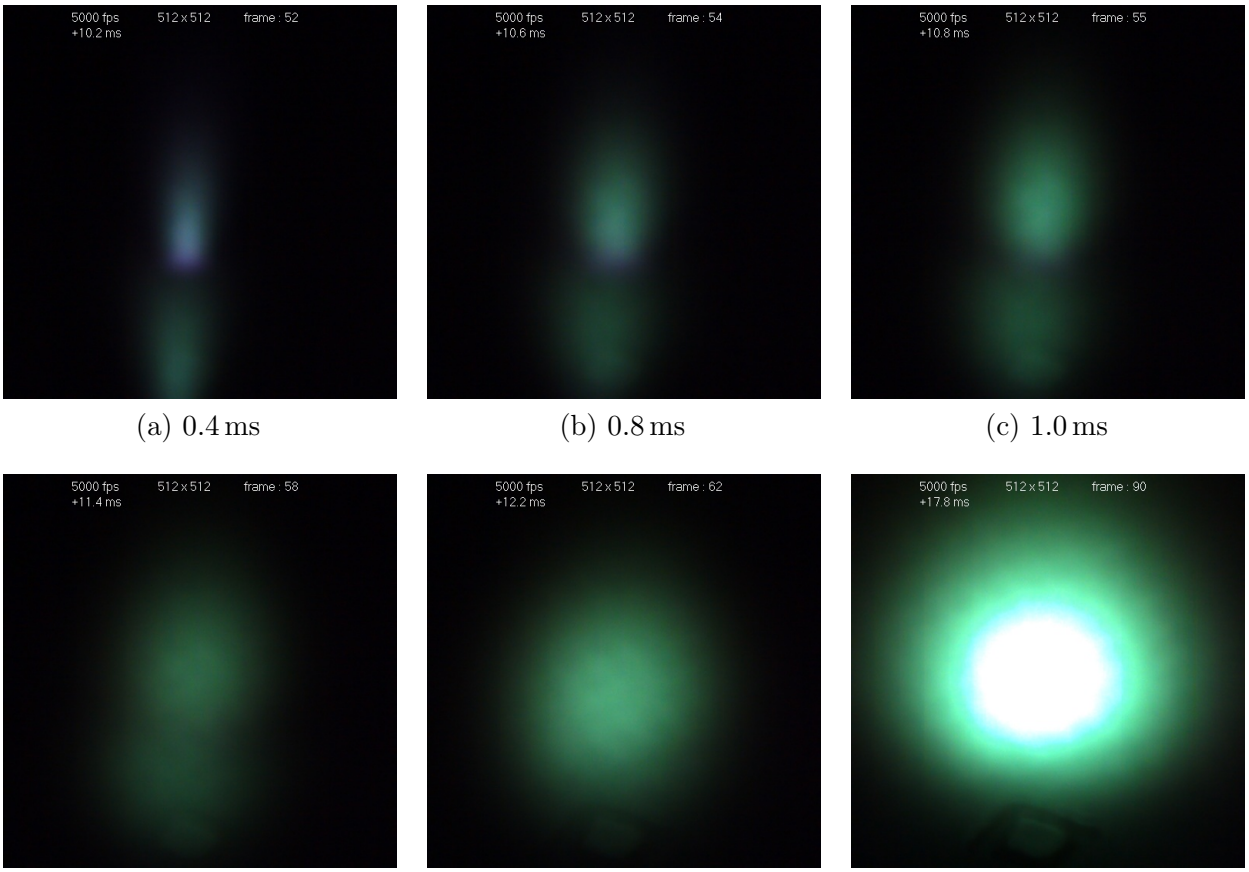

(a) 0.4 ms (b) 0.8 ms (c) 1.0 ms

(d) 1.6 ms (e) 2.4 ms (f) 8.0 ms

Figure 7.6 Temporal development of a discharge with T_{on} of 10 ms and T_{off} of 10 ms corresponding to a 50 % duty cycle with a pulsing frequency of 50 Hz.

7.5.5 Case 1

The discharge became instable, eventually collapsed and died off when the duty cycle was reduced to 30 % (T_{on} = 6 ms, T_{off} = 14 ms). It was not possible to sustain or reestablish the discharge making it the fifth discharge pattern observed. It is described as case (1).

7.5.6 The T_{on}-T_{off} space diagram

The T_{on}-T_{off} space diagram is introduced in order to map the occurrence of the individual discharge patterns and to evaluate their existence. The x-axis contains increasing on times. Simultaneously, the y-axis contains increasing off times. Thus, the x-axis represents c.w. microwave discharge with an absorbed power level of 3000 W ($T_{off} = 0$) and the y-axis represents no excitation ($T_{on} = 0$, $P = 0$ W). The use of T_{on} and T_{off} is in order to reflect, that those are the two fundamental parameters within the analyzed parameter space. Nevertheless, the dependent pulsing variables frequency, duty cycle and average power are represented in the Ton-Toff space diagram as well. The dependencies of those variables within the T_{on}-T_{off} space is shown in Figure 7.7. It can be clearly seen, that all three dependent variables are changing within the T_{on}-T_{off} space. The average power and duty cycle follow the same lines and are increasing rotational from the y- to the x-axis. This corresponds to the fact, that the y-axisrepresents the case of no excitation and the x-axis describes the case of c.w. excitation. At the same time, lines of equal frequency are aligned normally on the 1500 W, 50 % duty cycle line. The frequency decreases when moving away from the point of origin. It can be clearly seen, how complex the description of pulsed discharges is as the variation of T_{on} and/or T_{off} has an impact on other variables, such as the average power, as well. The T_{on}-T_{off} space diagrams containing the data points of the individual video recordings do not include the dependent variables. Instead, those can be retrieved from Figure 7.7 if necessary.

Overall, a total of five different discharge patterns were identified when simultaneously changing the T_{on} and T_{off} space. They are plotted in a T_{on}-T_{off} space diagram as shown in Figure 7.8 based on the experimental settings given in Table 7.1. The five different discharge

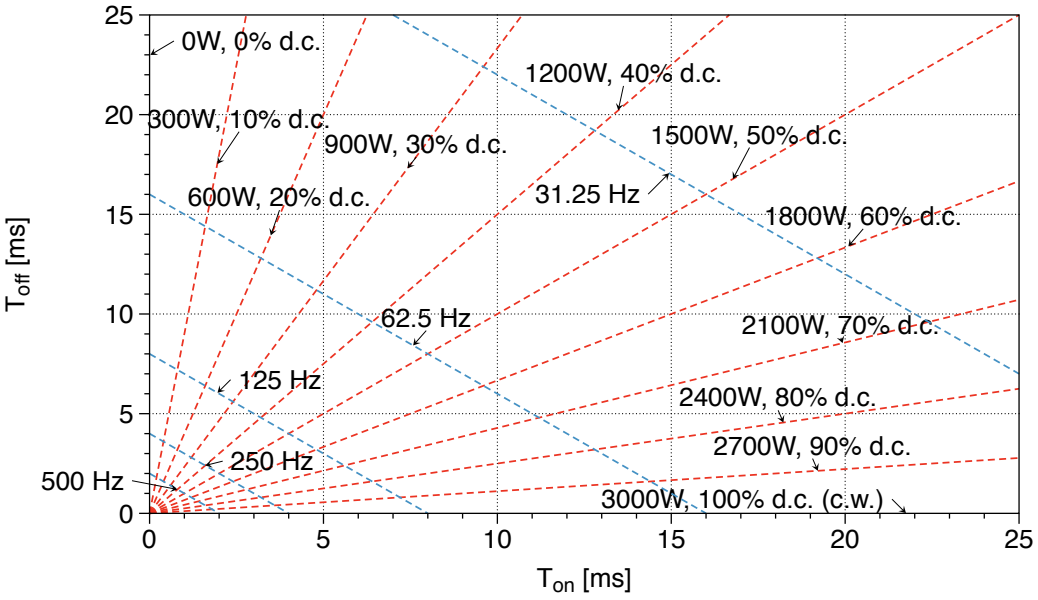

Figure 7.7 The red dashed lines are illustrations of sets of (T_{on}, T_{off}) which result in the same average power and duty cycle in increments of 300 W, 10 % duty cycle. The blue dashed lines are representing sets of (T_{on}, T_{off}) which result in the same pulsing frequency. The frequency is decreasing with both, T_{on}, and T_{off}.

patterns are illustrated as follows: The disturbed variation of a continuous discharge, case (5) in black, the unsustainable discharge, case (1) in violet. Additionally, three different patterns of pulsing cycles of periodic reignition of the discharge were found. Case (2) is illustrated in green, case (3) in blue and case (4) in red. The regimes for the appearance of the individual cases was estimated based on the intersection of the individual cases in the duty cycle series. The dashed lines are representing the lower limits for the appearance of that regime. The estimations for ignition case (2) and (3) took the point of origin and the middle between the data points of crossover on the duty cycle diagonal line. Those lines are similar compared to the red lines in Figure 7.7, which defined regions of the same average power in the T_{on}-T_{off} space. Obviously, the slope of the lines in those two figures is not identical. Nevertheless, it indicates that the average power supplied to the reactor will have an impact on which discharge pattern is observed. Thus, it remains open if the change in the time durations

(species activation and recombination) or the average power (i.e. reactor-wall heating) is the driving parameter for the different regimes observed.

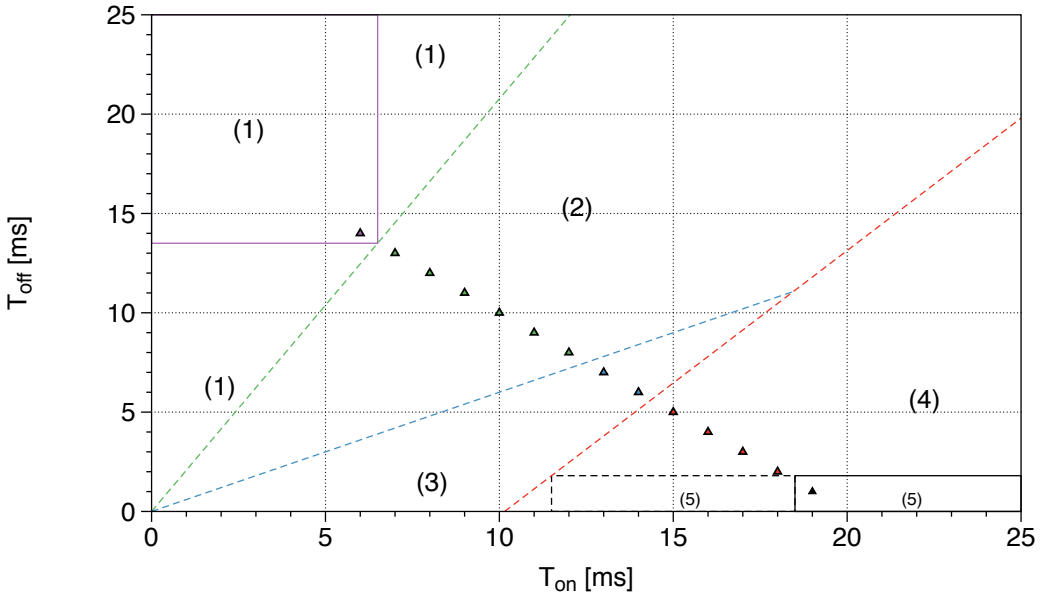

Figure 7.8 T_{on}-T_{off} space diagram showing the individual regimes found when varying the duty cycle based on the experimental settings given in Table 7.1. The triangles are marking the actual data points recorded. The dashed lines are separating the individual discharge pattern regions based on estimation and correspond to the lower boundary, i.e. the regime is to the right of it. The solid boxes surround regimes, which are guaranteed based on the data. Purple represents case (1), green represents case (2), blue represents case (3), red represents case (4) and black represents case (5). The T_{on} axis represents continuous wave excitation.

The purple solid box defines a region, where discharge instability is guaranteed, i.e. if T_{on} is reduced even more or T_{off} is increased even more than for 30 % duty cycle the discharge will remain instable. Similarly, the black box is an extension of the disturbed continuous discharge observed for 95 % duty cycle. When T_{on} is increased more the same behavior will be seen. Additionally, it is believed that the same behavior will be seen if T_{on} is reduced to a point that the discharge is fully developed (12 ms). The two adjunct triangles are assumed to be regions of discharge instability, but this will need to be verified. This is represented by the black dashed box. It is reasonable to assume intersection between cases (3) and (4) and (4) and (5) resulting in the dashed red line.

7.6 Influence of the on time for a constant 10 ms off time

The pulsing analysis performed in Section 7.5 resulted in a first approximation of the T_{on}-T_{off} space as shown in Figure 7.8. However, it is of importance to narrow the boundaries between the four discharge patterns in the T_{on}-T_{off} space more accurate. Hence, a series of recordings with a constant off time T_{off} of 10 ms is performed. The on times T_{on} are varied between 5 and 24 ms. The discharge is pulsed between 0 and 3000 W to compare the data points with those from Section 7.5. A summary of the experimental settings is shown in Table 7.2. The individual data points are represented as a horizontal line going through the T_{on}-T_{off} space at T_{off} of 10 ms (see Figure 7.7). This should allow to cover and further investigate discharge formation patterns (1), (2), (3) and (4). The off time of 10 ms is significantly higher than in previous modeling efforts. Off times around 2 ms [201, 140] or even in the µs range [148] were reported. The addition of more data points may result in the identification of even more different discharge formation patterns and will provide a deeper insight of the previously observed results.

Pulsing parameters		Dependent parameters			
T_{on} ms	T_{off} ms	duty cycle %	P_{avg} W	f Hz	Spatially different discharge parameters
5	10	33.3	1000	66.7	(6): formation of two seperated discharges
6	10	37.5	1125	62.5	(6): formation of two seperated discharges
8	10	44.4	1333	55.6	(2): formation of one inhomogenous arc
10	10	50	1500	50	(2): formation of one inhomogenous arc
15	10	60	1800	40	transition between (2) and (3)
20	10	67	2000	33	(3): formation of one homogenous arc
24	10	70.6	2118	29.4	(3): formation of one homogenous arc

Table 7.2 Different pulsing parameter settings used to study discharge formation for duty cycles between 30 % and 95 %.

It was found that all settings of pulsing durations investigated in this section resulted in a stable discharge formation. A surprising observation was made for T_{on} of 5 and 6 ms

as shown in Figure 7.9. Two arc-like discharges are present, a green arc ignites on the SCD substrate. Additionally, a purple arc can be seen in the vicinity of the steady state position. The reduction of T_{off} compared to the data point of a 30 % duty cycle (T_{on} = 6 ms, T_{off} = 14 ms) moved the conditions in the T_{on}-T_{off} space down enough to be in a stable and new discharge regime. As the discharge develops the two discharges are moving towards each other until the finally form into one spherical discharge 1.8 ms after ignition. The discharge detaches from the SCD substrate at the same time. The purple discharge changes its appearance and into a green discharge with a narrow and thin purple layer, much in analogy to the discharge seen in Figure 7.6. One could speculate, that the discharge observed in Figure 7.6 initially consisted out of two discharges as well, which merged together, but at a much higher rate, so that the camera cannot record this fast enough and it appears that only one inhomogeneous discharge occurred.

The formation of the discharge by increasing T_{on} further followed the trend as suspected. The discharge formation for T_{on} of 8 ms was exactly the same as the observation made for duty cycles between 35 and 55 % in Section 7.5 (discharge pattern (2), see Figure 7.6), i.e. an inhomogeneous arc-like discharge with the three different regions forms, develops into a dumbbell-shaped discharge and finally detaches from the SCD substrate as green spherical discharge. This observation follows the approximation of the different discharge regions within the T_{on}-T_{off} space, as shown in Figure 7.8. Note that T_{on} of 10 ms represents the data point of a 50 % duty cycle. Analogously, the discharge formation for T_{on} of 20 and 24 ms was found to be exactly that of duty cycles between 60 and 70 %, i.e. one green arc-like discharge forms on the SCD substrate, detaches and floats to its steady state position (discharge pattern (3), see Figure 7.4).

Figure 7.10 shows a comparison of the discharge 400 µs after the ignition for increasing

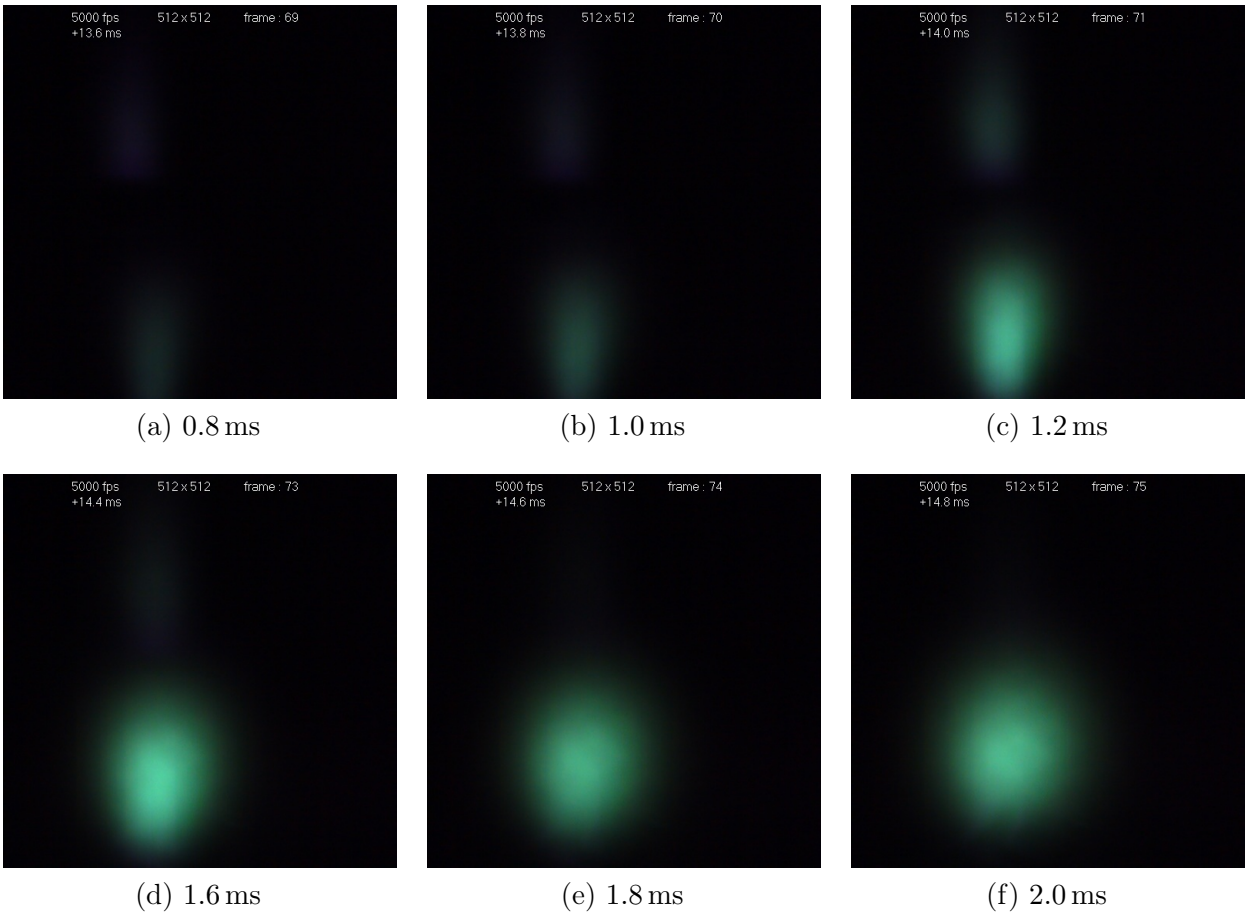

(a) 0.8 ms (b) 1.0 ms (c) 1.2 ms

(d) 1.6 ms (e) 1.8 ms (f) 2.0 ms

Figure 7.9 Temporal development of two discharges merging into once created with T_{on} of 5 ms and T_{off} of 10 ms corresponding to a 33.3 % duty cycle with a pulsing frequency of 66.7 Hz.

T_{on} of this data series. The images appear like a temporal development themselves, but are all taken at the same time within the individual discharge development cycle. Especially the development of the thin and narrow purple region seems to follow that trend and moves down with increasing T_{on}. One could speculate that there is only one fundamental temporal development for the formation of the pulsed discharge given by the case when T_{on} and T_{off} will result in a discharge, which is only marginally stable. Now, when changing T_{on} and T_{off}, the conditions inside the reactor are changing and are comparable to a time further into the development of that fundamental formation pattern. This would result in the periodic

discharge ignition with that exact pattern within the fundamental cycle and could explain, why several different ignition patterns were observed in this study. However, more research will be required in order to either verify this speculation or to provide a different explanation.

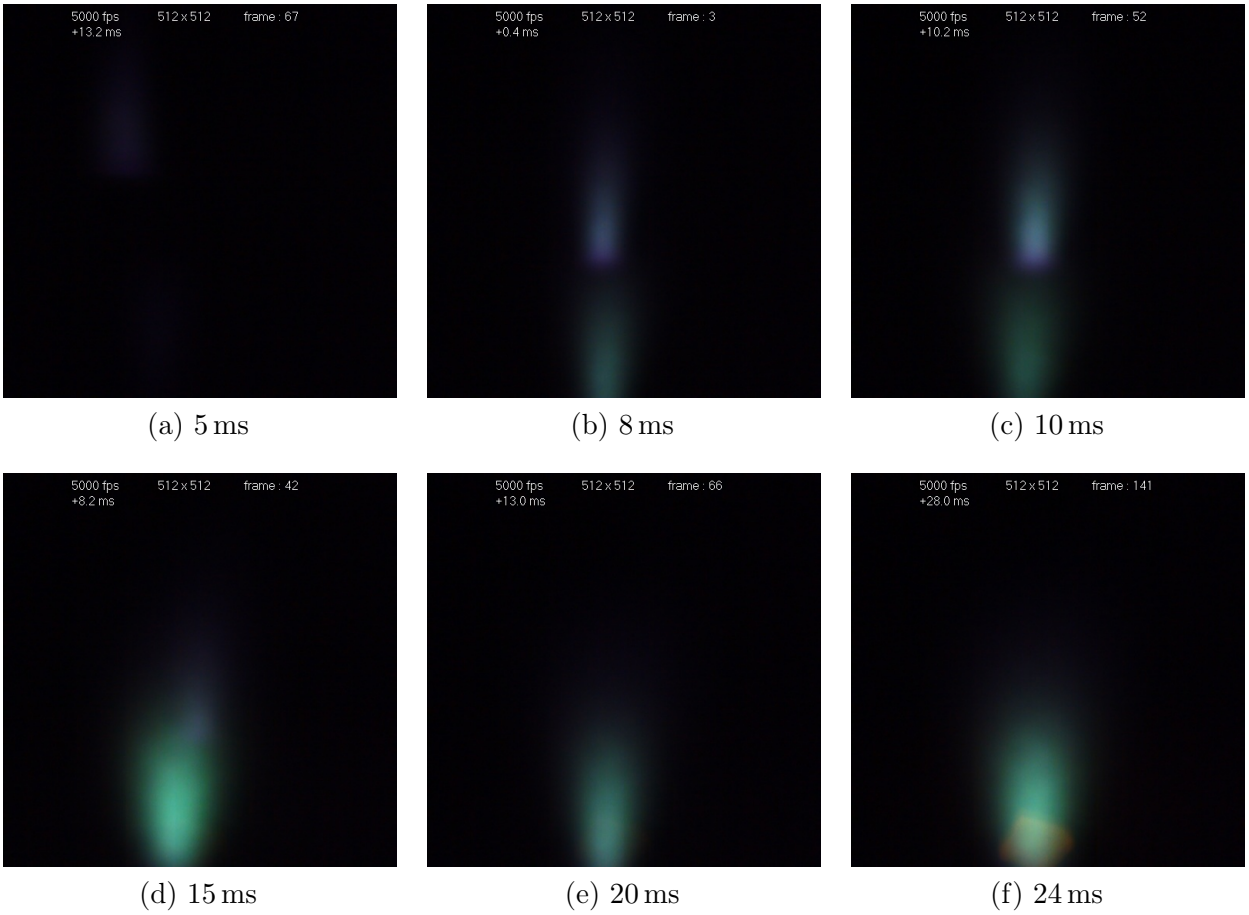

(a) 5 ms (b) 8 ms (c) 10 ms

(d) 15 ms (e) 20 ms (f) 24 ms

Figure 7.10 Discharge ignition for pulsing under a constant off time T_{off} of 10 ms and on times T_{on} increasing from 5 to 24 ms. The individual images are showing the second image of the formation of each individual discharge. The second image corresponds to a time duration of 400 µs after discharge ignition.

A really interesting observation was made for T_{on} of 15 ms. The green arc-like discharge on the SCD substrate becomes dominant, as seen in Figure 7.10, but a faint of purple is still noticeable on the top right of the discharge making the discharge merely inhomogeneous. This purple disappears for higher T_{on}. Thus, T_{on} of 15 ms defines the crossover between discharge pattern (2) and discharge pattern (3) in the T_{on}-T_{off} space. This data point can be adapted

for an extrapolation to the data points recorded for the duty cycle series in Section 7.5.

Figure 7.11 shows the T_{on}-T_{off} space diagram introduced in Figure 7.8 including the updated data points from the T_{on} series from this section. Thoey are represented by inverse triangles. The newly found discharge pattern, case (6), where two separated discharges are forming is illustrated by orange. The special case, which was characterized as the boundary between case (2) and (3) is plotted in cyan. The assumed regions of each of the discharge patterns illustrated by the dashed lines was updated. The presence of the newly found case (6) was acknowledged for low T_{on} times. Hence, the lower limit for case (2) was adjusted by using the intersects (T_{on} = 5.5 ms and T_{off} = 10 ms) and the intersect from Section 7.5 (T_{on} = 6.5 ms and T_{off} = 13.5 ms). Additionally, the boundary between (2) and (3) was adjusted using the newly found boundary point (T_{on} = 15 ms and T_{off} = 10 ms) and the intersect from Section 7.5. As a result, (3) does not intersect with the point of origin anymore. The data points with T_{on} of 20 and 24 ms revealed, that the discharge is still igniting on the SCD surface. Hence, the region (4) for ignition detached from the SCD is assumed to be limited to low T_{off} times.

Comparing the development of the individual discharges 4.0 ms after the ignition of the individual discharges for increasing T_{on} is shown in Figure 7.12. It can be seen that the development of the discharge lags more and more behind the smaller T_{on}. The comparison for increasing T_{on} in Figure 7.12 appears like a temporal development of one discharge again, analogous to the observation in Figure 7.10. This illustrates, that the experimentally observed expansion of pulsed microwave discharges is highly dynamic. The expansion phase of the discharge has a significant effect on the formation of ionized species, especially [CH_3] [140]. Specifically, Brinza et al. [140] show in their Figure 6 the exact same numerically obtained temporal development of [H] and [CH_3] for discharges with T_{on} of 8, 11 and 15 ms. T_{off} in

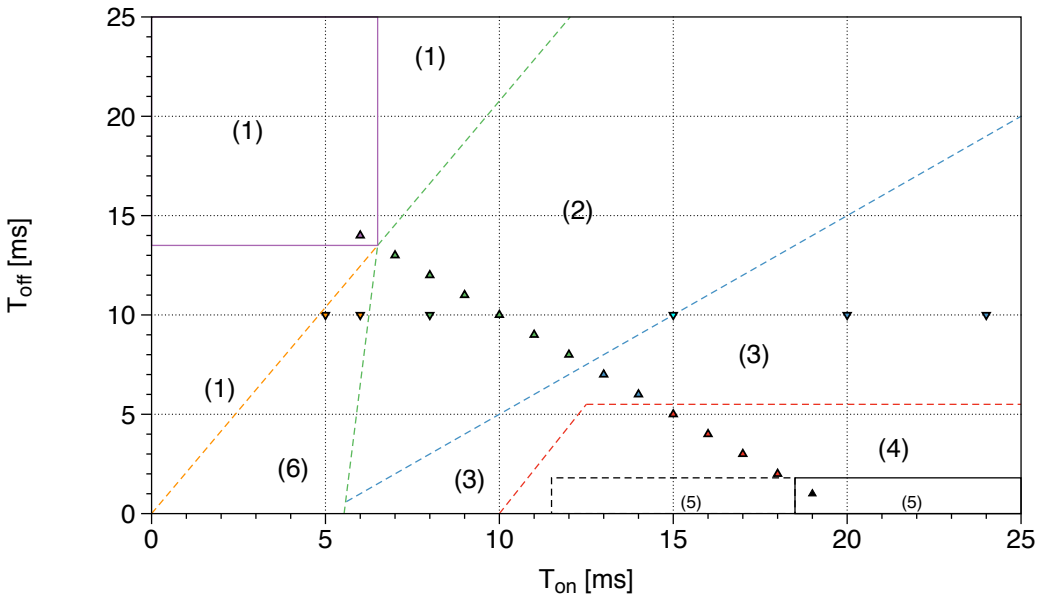

Figure 7.11 Updated T_{on}-T_{off} space diagram containing the data points from Figure 7.8 and the data points of the T_{on} series shown as inverse triangles. The newly found regime (6), where two discharges are forming is illustrated in orange. The data point representing the boundary between (2) and (3) is shown in cyan. The discharge regimes have been updated according to the new data.

their numerical model was lower with 2 ms. The closest data point this study contains is that of the 90 % duty cycle in Section 7.5 (T_{on} = 18 ms and T_{off} = 2 ms), a data point where the discharge actually ignited in a completely different location inside the reactor. Thus, it is plausible to assume, that the temporal development of the active species is dependent from T_{on} and T_{off} and will actually fluctuate by a decent amount. This means, that the current numerical description and understanding of the discharge ignition phase is too simplistic. Hence, it is of importance to gain a better understanding of the actual processes happening, but the adjustment of the numerical description by using more advanced dynamic models will be required to fully understand the pulsed discharge. Doing so is of significant importance in order to optimize the MPACVD SCD growth process utilizing pulsed microwave discharges.

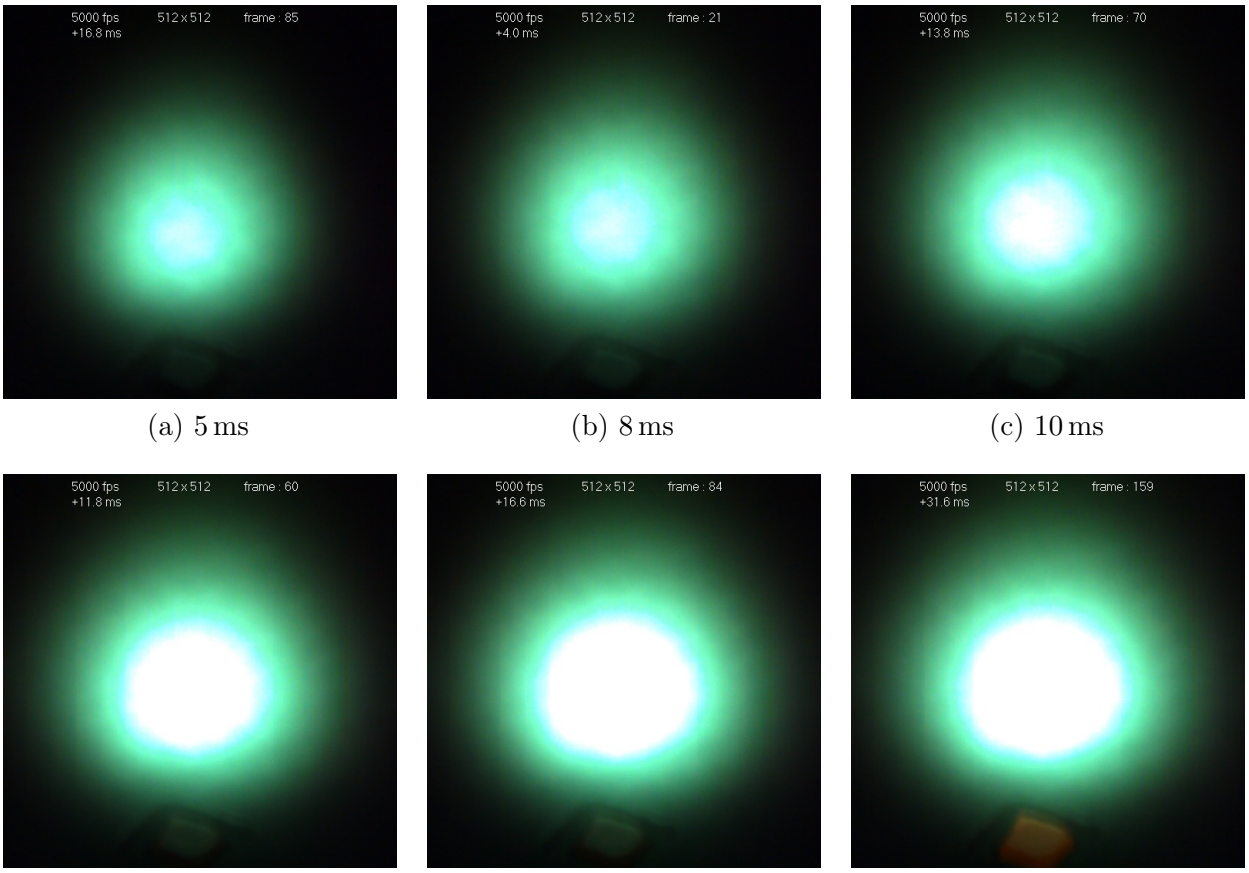

(a) 5 ms (b) 8 ms (c) 10 ms

(d) 15 ms (e) 20 ms (f) 24 ms

Figure 7.12 Discharge expansion for pulsing under a constant off time T_{off} of 10 ms and on times T_{on} increasing from 5 to 24 ms. The individual images are showing the twentieth image of the formation of each individual discharge. The second image corresponds to a time duration of 4 ms after discharge ignition.

7.7 Influence of the pulsing frequency

The influence of the pulsing frequency on the discharge formation was evaluated as well. Frequencies were between 50 and 500 Hz as T_{on} and T_{off} were restricted to 50 % duty cycles. The selection of frequencies is limited due to the microwave power supply. A summary of the recorded data points is shown in Table 7.3. Variation of the pulsing frequency is interesting as this set of data is studying pulsed discharges with significantly higher frequencies than those in Section 7.5 and Section 7.6, which corresponds to significantly lower T_{on} and T_{off}

times. The data points in this series are located on the dashed line in Figure 7.7 representing the duty cycle of 50 %.

Pulsing parameters		Dependent parameters		
T_{on} ms	T_{off} ms	duty cycle %	P_{avg} W	f Hz
1	1	50	1500	500
2	2	50	1500	250
3	3	50	1500	166.7
4	4	50	1500	125
5	5	50	1500	100
6	6	50	1500	83.3
7	7	50	1500	71.4
8	8	50	1500	62.5
9	9	50	1500	55.6
10	10	50	1500	00

Table 7.3 Different pulsing parameter settings used to study the effect of the discharge formation when changing the pulsing frequency between 50 and 500 Hz.

The frame of discharge ignition for the analyzed frequency spectra is shown in Figure 7.13. It needs to be mentioned, that the video recordings were from a previous session. It appears that the tripod setup had a slightly smaller angle and focused on the steady state position instead of onto the SCD substrate. That is the reason why the recorded videos and images appear different, i.e. only a single homogeneous discharge is visible at 50 Hz. When analyzing the same pulsing parameters with an adjusted camera setup it was possible to record the color variation inside the arc-like discharge, see Figure 7.6. Thus, it is not possible to differentiate the ignition behaviors of cases (2), (3) and (6). All of them would appear the same. It is still possible to separate if the discharge is igniting on the SCD substrate or separated from it. It was found, as shown in Figure 7.13, that the discharge is igniting on the SCD substrate for low pressures in an arc-like discharge and then expanding as in Figure 7.6. When increasing the frequency (moving from the 50 % duty cycle point in T_{on}-T_{off} space to the point of origin) the arc is still forming on the SCD substrate, but has a fan shape and the opening

angle increases with pulsing frequency. The ignition pattern changes for 166.7 Hz, where the discharge becomes elliptical and starts to detach from the SCD substrate. Hence the data point at 166.7 Hz may be seen as another boundary point. The discharge for pulsing frequencies of 250 and 500 Hz ignites away from the SCD surface, similar to ignition case (4) in Section 7.5.

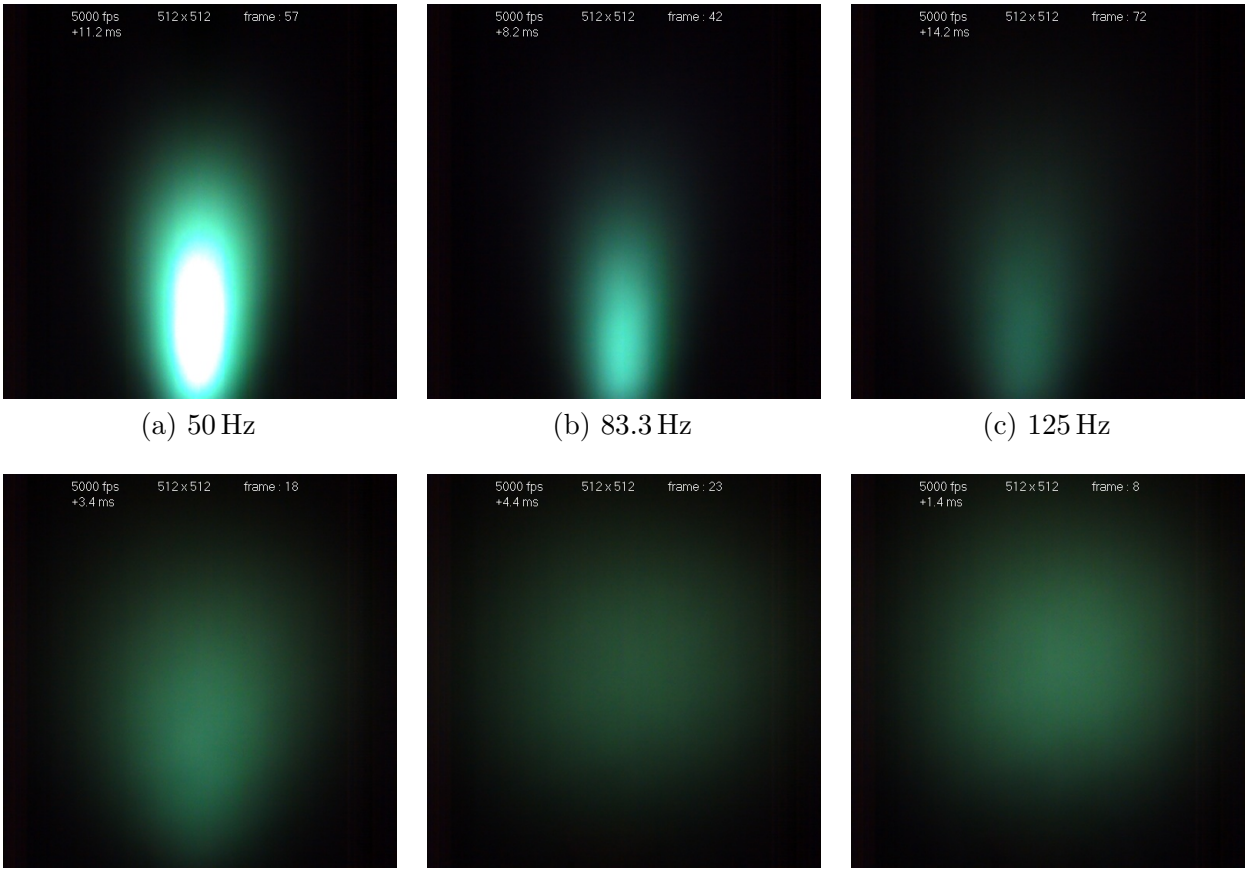

(a) 50 Hz (b) 83.3 Hz (c) 125 Hz

(d) 166.7 Hz (e) 250 Hz (f) 500 Hz

Figure 7.13 First frame (200 µs) of the igniting discharge for pulsed MW discharges between 50 and 500 Hz.

Figure 7.14 shows the updated T_{on}-T_{off} space diagram including the data points of the pulsing frequency series. The added data is represented by triangles pointing to the right. The high frequency discharges, which showed discharge ignition detached from the substrate are represented by red triangles. The observations for lower frequencies are plotted with sky

blue triangles as those were indistinguishable between cases (2), (3) and (6). Overall it can be seen, that the addition of this new set of data is complicating the definition of the regions of existence for the individual cases in T_{on}-T_{off} space. The data points up to 125 Hz are within prediction for cases (2) and (6) given by Figure 7.11. However, the high frequency ignition videos showed a clear detachment from the SCD substrate (case (4)). Thus, the previously observed region of (4) extends to significantly lower T_{on} times and potentially all the way to the point of origin in T_{on}-T_{off} space. It appears that 166.7 Hz (T_{on} = 3 ms and T_{off} = 3 ms) is approximately defining a boundary point between ignition on the SCD substrate and detached from it. The interesting observation here is, that the results presented in this section and for high duty cycles in Section 7.5 have significantly different T_{on}, but T_{off} is in the same range. As previously discussed, the occurrence for discharge ignition separated from the SCD substrate is appears to be largely independent from T_{on} and only related to T_{off} times, which are short enough to ensure that a sufficient amount of ionized species is still available upon reignition of the discharge.

Another observation was, that the maximum discharge intensity before the plasma decayed and turned off was significantly lower for the higher frequencies of 166.7 Hz and above. The individual pulsing durations were becoming so short, that the plasma barely expanded, i.e. T_{on} for 500 Hz is only 1.0 ms, while it was shown in Section 7.5, that 12 ms and more are needed to fully expand and utilize the plasma. This is consistent with the fact, that a periodic pulsing was observed for 500 Hz, while T_{off} is only 1.0 ms as well. Overall, the plasma discharge is much dimmer and corresponds to a continuous discharge with a much smaller overall power level compared to the case of 3000 W.

The effect of this phenomenon was verified when recording the SCD substrate temperature as a function of the pulsing frequency. The substrate temperature was using a IRCON

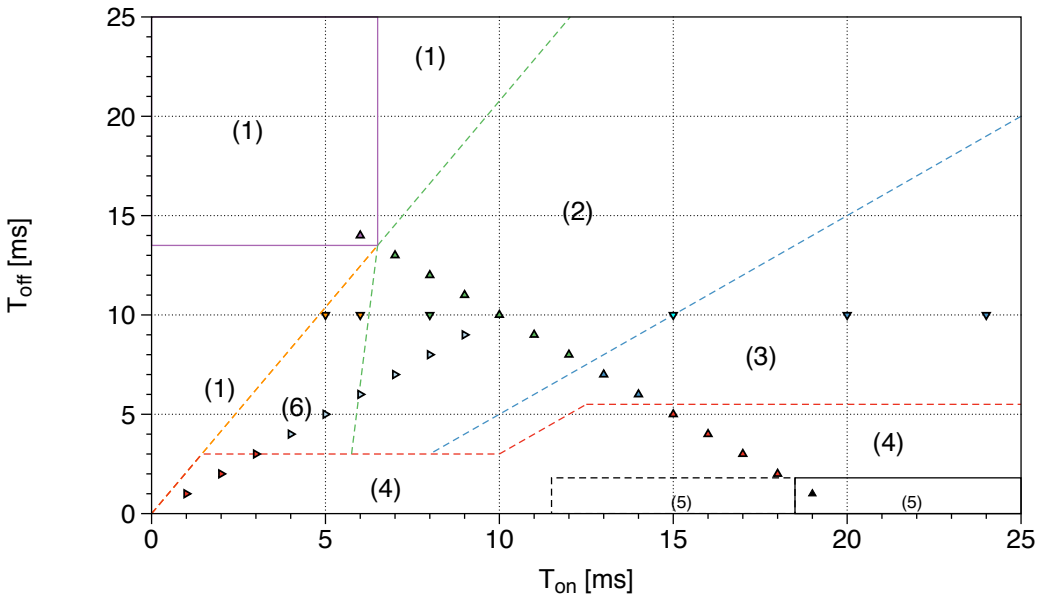

Figure 7.14 Updated T_{on}-T_{off} space diagram containing the data points from Figure 7.8 and Figure 7.11 as well as the data points of the pulsing frequency series shown as triangles pointing to the right. The discharge regimes have been updated according to the new data.

Ultimax one-color infrared pyrometer. The emissivity was set to 0.6. the average power was 1500 W for all pulsed settings. Additionally, the substrate temperature was measured and compared to a 1500 W continuous discharge. The results are shown in Figure 7.15. It can be seen that the substrate temperature increases between 30 and 60 °C for all pulsing frequencies compared to a continuous discharge. However, a significant frequency dependency was found. The SCD substrate temperatures are the highest and stable for frequencies between 50 and 125 Hz. However, a linear decrease of the substrate temperature can be seen when increasing the frequency up to 500 Hz.

One logical explanation is, that the reactor geometry used was optimized under c.w. excitation. Hence, when pulsing at low frequencies the coupling efficiency remains high and the power provided can be efficiently coupled to the plasma even with a pulsed discharge. It appears, that this is not the case for higher pulsing frequencies. Instead the power provided is not utilized by the discharge. As a result, the discharge appears dim and the SCD substrate

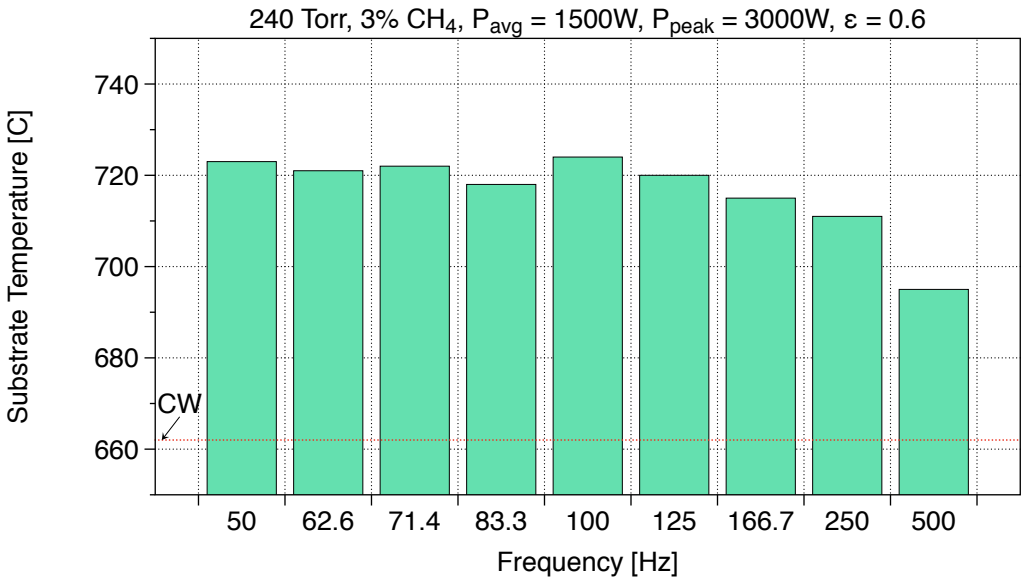

Figure 7.15 SCD substrate temperature as a function of the pulsing frequency.

temperature is lower. It seems likely, that a significant amount of power is absorbed by the reactor walls instead of the discharge region under those high excitation frequencies. Overall, it can be summarized that low pulsing frequencies, which allow a certain time period of c.w. operation seems more efficient and therefore more favorable over high frequency pulsing. This can be achieved especially for pulsing frequencies below 100 Hz. This is in accordance with the numerical data from Brinza et al. [140].

7.8 Summary

Video recording of the pulsed microwave discharges at a pressure of 300 Torr and 5 % methane conditions were recorded utilizing a MPCR (Reactor B). Those are typical operation conditions for MPACVD of SCD. The absorbed power P_{abs} in continuous wave excitation is replaced by a set of four variables when using a pulsed microwave discharge; the power levels and time durations of the high and low cycle of the square wave pulse. It was shown, that the periodic

cycle of pulsed microwave discharges consists of discharge ignition, discharge expansion, steady state discharge behavior during the on stage of the pulse T_{on}, discharge decay and a time duration, where the visible discharge vanished during the off stage of the pulse T_{off}. Thereby it was found, that the decay of the pulsed discharge, when the supplied power is cut off, decays within close to 2 ms, which is constituent with the numerical calculations by Brinza et al. [140].

Overall, six different patterns of discharge ignition behavior were found. Two special cases were found, which do not follow the pattern of periodic discharge reignition. Those two are found as: (1) instability, which results in the discharge to go off without possibility of reignition and (5) a pseudo-continuous discharge, which gets periodically disturbed by the off cycle, but never goes off. Additionally, four different patterns of periodic discharge development were found: (2) ignition of a single arc-like discharge between the SCD substrate and the steady state discharge position, which contains three different regions; (3) ignition of a single homogeneous arc-like discharge on the SCD substrate; (4) ignition of a spherical discharge detached from the substrate and (6) ignition of two separated arc discharges, one on SCD substrate and one in the steady state discharge region. Additionally, it was observed that the area of discharge ignition was different from where the discharge vanished.

The discharge expansion behavior was highly dynamic for ignition patterns (2) and (6), i.e. the inhomogeneous arc-like discharge turned into a dumbbell-shape with a localized area of a purple hydrogen discharge before detaching from the SCD and evolving into a uniform spherical discharge. The two discharges observed in (6) would merge into one discharge and detach from the SCD substrate at the same time. And even the discharge development for (3) showed some level of dynamic behavior as the initial arc-like discharge became spherical when detaching from the SCD substrate and floating towards its steady state position.

A diagram of the T_{on}-T_{off} space was used to plot and compare the individual discharge ignition and expansion behaviors recorded for the variation of the duty cycle, T_{on} with a constant T_{off} and the pulsing frequency. Unfortunately, the series recorded for the pulsing frequencies had a slightly different video setup, which did not allow to separate between discharge ignition cases (2), (3) and (6). The individual data points were added to the T_{on}-T_{off} space diagram and regions within the T_{on}-T_{off} space were approximated, where each of the individual discharge patterns will occur. Those regions were indicated by dashed lines and a color code. The initial approximation was updated twice using and the final diagram was shown in Figure 7.14. Additionally, two definitive areas have been defined, where the special cases (1) and (5) will occur. While this diagram will serve as a good start for approximating which pulsing behavior can be expected based on a given T_{on} and T_{off} it is crucial to expend the map and to probe the remaining combinations in order to have a full mapping based on data instead of having to approximate some of the regions. Unfortunately, there is a total of 576 combinations of given T_{on} and T_{off} and even when the number can be reduced below 450 due to several instable combinations it will take a lot of effort to analyze all the data available. The final step would be to expand the two-dimensional map by probing different power levels, but this would increase the number of combinations to analyze into the tens of thousands.

It was found that speed of the temporal development of the pulsed microwave discharge was dependent on T_{on} and T_{off}, i.e. discharges, which ignited as described by (4) expanded and reached its steady state position faster than discharges, which ignited under conditions as described by (2) or (6). One possible explanation was, that the different ignition patterns all represent selections out of one fundamental ignition behavior and the starting point within this sequence depends on the pulsing variables.

The use of pulsed microwave discharges increased the SCD substrate temperature compared to continuous wave excitation with the same absorbed power. Low pulsing frequencies (50 – 125 Hz) resulted in a higher increase of the SCD substrate temperatures for the higher frequency discharges (166.7 – 500 Hz).

It was shown, that the microwave discharge ignition detached from the SCD substrate happens, if a sufficient amount of activated species is still available in the discharge region. This is achieved by utilizing pulsing parameters with sufficiently low T_{off} so that not enough recombination occurs during the off stage.

Overall, it was demonstrated that the ignition and formation of pulsed microwave discharges is a highly dynamic and complicated process, which has not been properly described in the past. Gicquel et al. [139] suggested, that the ignition of the discharge contains some dynamical behavior, before being properly described by stationary 1D-axial and stationary numerical descriptions. However, the experimental data here shows great differences dependent on the external pulsing parameters, which have significant impact on ignition and the temporal development of the discharge, i.e. it was shown that the speed of which the discharge is developing different depending on pulsing parameters, such as T_{on}. This is in clear contradiction to previous numerical calculations performed by Brinza et al. [140], which predicted exactly the same temporal development for discharges pulsed with Ton between 8 and 15 ms.

The experimental results presented here shows the urgency of performing more systematic studies on the development of pulsed discharges in order to identify all possible dynamical patterns, but also raises the importance on the development of more sophisticated numerical models in order to describe the experimentally observed phenomena. The availability of accurate numerical models will be of great benefit to select the optimal pulsing parameters

when adapting pulsed microwave discharges for MPACVD of SCD in order to maximize the growth rate and crystalline quality.

Chapter 8

Methods to further increase the growth rate - exploratory data and preliminary results

8.1 Introduction

The effects on MPACVD growth of diamond by increasing the operating pressure (see Section 6.3.2) and the methane concentration (see Section 6.3.3.1) have been studied in detail in this dissertation. The results of the experiments, which were presented in Chapter 6 and Chapter 7, suggested that additional approaches can be utilized to further improve the growth rates for SCD deposition. These include the utilization of the pulsable power supply to grow SCD using a pulsed microwave discharge. The past research work, that has been reported by others (see Section 2.9) suggests, that SCD growth rates can be significantly enhanced under otherwise unchanged conditions without a reduction of crystalline quality of the grown material [144, 148].

Another approach is to retune the reactor configuration. Spefically, by varying the short

position L_s and the position of the substrate inside the reactor, i.e. by varying L_1 and L_2. This can move the discharge to a position optimized for diamond growth. If done properly, the discharge can pull down to the substrate, thereby reducing the boundary layer between the discharge and the substrate. This can significantly increase the growth rate without increasing the input power. Additionally, this would allow to increase the operational pressure even further. As suggested in Chapter 6, a slight change in the reactor geometry would move the plasma closer to the substrate. The potential use of this approach was identified in Section 6.2.3 and Section 6.3.2.1.

This chapter contains a few preliminary experimental runs that indiciate the potential of further enhancing the growth rate by using these two approaches. Thus, the data presented here is only of an exploratory nature and is presented here only to prove the potential viability of those two approaches. It is not an in-depth study of those approaches and does not attemp to optimize those approaches either. This is specifically illustrated in Section 8.3. Instead of retuning all variables of the reactor geometry only the short position L_s was changed. As a result, this forces the plasma discharge onto the substrate holder during high pressure operational condition, which was sufficient to suggest a proof of concept study. Unfortunately, this made it impossible to properly measure the substrate temperature throughout the deposition experiments. Hence, the realization was simplistic and had minor flaws. An actual implementation would require a more sophisticated approach, such as varying reactors' length L_s, L_p, L_1 and L_2, as indicated by Nad et al. [57] under lower pressure growth conditions. It was indicated at lower pressure, that one could reposition the discharge, while still achieving a well-matched reactor, if one had several degrees of freedom, such as L_s, L_p, L_1 and L_2. The growth rates presented here will most likely be improved even more future process optimization investigations. Additionally, it seems worth mentioning that both approaches

should be investigated simultaneously as both positive effects on the growth rate can be used in conjugation to maximize the potential positive effects on the SCD growth rate.

8.2 SCD growth under pulsed excitation

A comparison of pulsed versus continuous microwave excitation for SCD deposition was performed at 300 Torr and 5 % CH_4 without the addition of nitrogen for a total of 50 h. Pulsing was done utilizing the pulsing capability of the new microwave power supply and the power levels were pulsed between $P_{on} = 3000$ W and $P_{off} = 0$ W. The pulsing durations were $t_{on} = 14$ ms and $t_{off} = 6$ ms. Hence, the resulting pulsing frequency was 50 Hz, the duty cycle was 70 % and the resulting average power P_{avg} was 2100 W. The substrate temperature increased from 880 to 920 °C over the course of the deposition process. This temperature increased was caused because the average pulsed power input was held constant during deposition. At the same time, the diamond was growing vertically towards the plasma. This results in a variable and increasing substrate temperature with increasing growth time [67]. Nevertheless, the substrate temperature range was comparable to the experiment which used continuous microwave excitation. The substrate temperature was between 890 and 910 °C for this experiments. 2700 W of absorbed power were used to sustain the substrate temperature. All other process parameters were the same as for the pulsed experiment. Thus, it was possible to reduce the average power consumption by 23 % under otherwise similar growth conditions by utilizing a pulsed microwave discharge. This is in accordance with the observations in Section 7.7, where pulsing increased the substrate temperature for the same average power level.

The growth rate of the SCD grown under pulsed condition was 33.9 µm h^{-1} for a total

grown thickness of 1.7 mm compared to 19.6 µm h^{-1} for the SCD grown under c.w. excitation (see Section 6.3.2.1). This means, that a 73.4 % increase in growth rate was achieved by utilizing a pulsed discharge. This increase in growth rate is higher compared to other reports in literature, who were using pulsed discharges in the same frequency range [140, 144, 146].

Figure 8.1 shows a comparison of the film morphology of the SCDs grown under pulsed (a) and c.w. (b) conditions. The overall crystalline quality of the SCD grown under pulsed deposition looks visually okay, but it can be seen, that the morphology is not as smooth as for the SCD grown under c.w. conditions. Instead, the formation of several overlapping terraces is seen. Hence, the overall morphology is not as good for the SCD grown under pulsed conditions. However, the thickness difference of the CVD-grown diamond, due to the formation of terraces, is less than 20 µm.

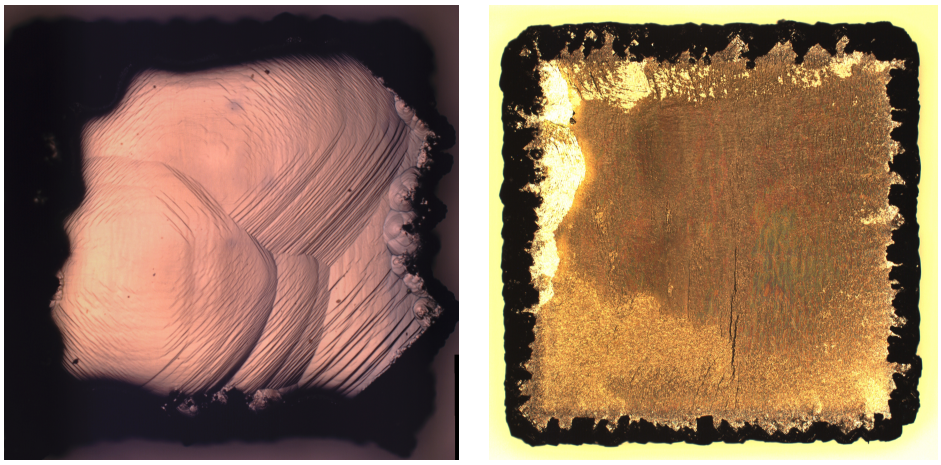

(a) pulsed (b) c.w.

Figure 8.1 Top surface of grown SCD films grown at 300 Torr, 5 % methane under continuous and pulsed microwave excitation.

Figure 8.2 compares the birefringence images of the freestanding SCD plates grown under pulsed (a) and c.w. (b) conditions. It can be seen, that the pulsed SCD plate has a significant amount of internal stress all across the plate, while the c.w. plate is virtually stress free. The

actual amount of stress in the pulsed plate is even higher than assumed based on Figure 8.2 as the exposure time had to be reduced to 500 ms due to oversaturation of the image recorded at 2000 ms.

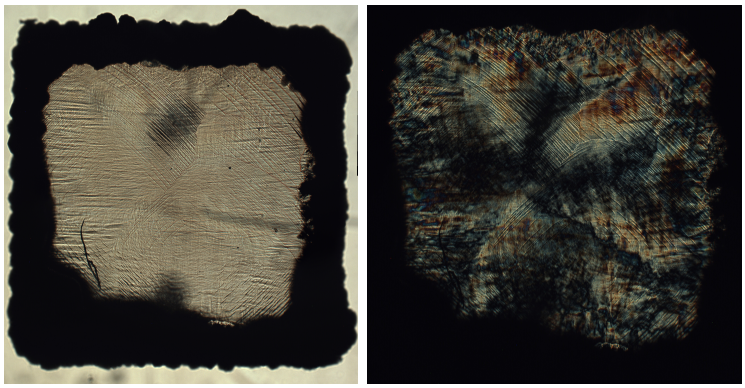

(a) pulsed, 50 Hz, 70 % duty cycle

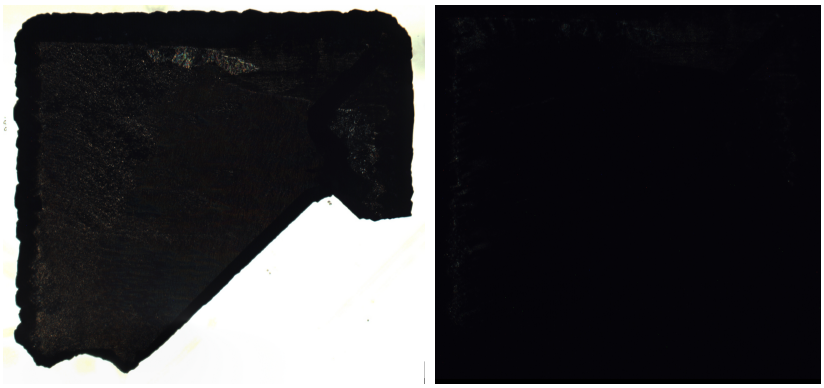

(b) c.w.

Figure 8.2 Through (left) and birefringence (right) images of the freestanding SCD plates from Figure 8.1 using continuous and pulsed microwave excitation.

The SCD plate grown under pulsed conditions incorporated significantly more nitrogen under otherwise identical conditions. This can be visualized in Figure 8.3, which shows optical photographs of the freestanding SCD plates grown under pulsed conditions and a high quality CVD plates containing less than 100 ppb nitrogen, which was grown under comparable conditions. While the SCD plate grown under continuous excitation appears almost colorless, the SCD plate obtained from the pulsed experiment has a clear brown coloration, which can be attributed to a significantly higher amount of nitrogen being incorporated into the

diamond.

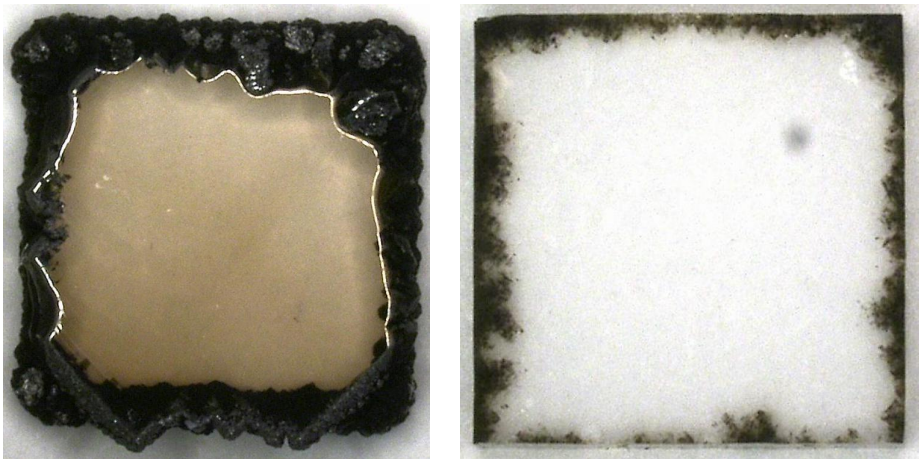

(a) pulsed (b) c.w.

Figure 8.3 Photograph of freestanding SCD plates grown under pulsed and c.w. microwave excitation. The thickness of the SCD plate grown under pulsed conditions is 1.5 mm and is 1.1 mm for c.w. excitation.

Overall, a significant increase of the growth rate of over 70 % was observed, while simultaneously reducing the power consumption by over 23 %. These observations are in accordance with previous observations by Tallaire et al. [144]. Unfortunately, the preliminary data shows that the crystalline quality of the grown SCD is low, i.e. it is reasonable to assume, that a significant amount of internal stress and nitrogen were incorporated into the grown SCD. A future in-depth study to optimize the growth conditions will be required in order to utilize the growth rate enhancement while retaining a high crystalline quality, that has been reported elsewhere [144].

8.3 Reactor detuning to force the plasma onto the substrate holder

A simplistic realization of retuning the reactor was applied, where only L_s was changed. Verification, that the position of the plasma discharge changed as desired was achieved by visual inspection of the discharge. Changing the short position from 21.4 cm to 21.55 cm was sufficient to force the plasma discharge onto the holder. The detuning resulted in the appearance of 41 to 54 W of reflected power. Unfortunately, by moving the plasma onto the holder it was impossible to focus the temperature readout on the substrate without probing through the discharge. Hence, it was either impossible to get a proper temperature readout at all or the measured values were not comparable to the previous temperature measurements. Hence, the growth rates reported here may be impacted by different substrate temperatures, which are not accounted for in this discussion, i.e. similar temperatures are assumed in the discussion. Lu et al. [31] showed a rather strong influence of the growth rate when changing the substrate temperature.

SCD deposition was carried out at 300 and 400 Torr for 20 hours each using the detuned plasma position. The methane concentration was 5 %. Hence the resulting growth rates can be compared to the data presented in Section 6.3.2.1 and Section 8.2. The comparison of the growth rate is shown in Figure 8.4. The green boxes represent the growth rates of the detuned position, while the black boxes represent the tuned position. All of these data points were obtained using a c.w. microwave excitation. Additionally, the data point for SCD growth using pulsed microwave excitation, discussed in Section 8.2, is represented by the red box. The growth rate for the detuned plasma position was approximately doubled as compared to the previously studied plasma position. For example, the growth rate increased

from 19.6 µm h^{-1} to 39 - 42 µm h^{-1} for 300 Torr and from 27 - 28 µm h^{-1} to 47 - 50 µm h^{-1} for 400 Torr. The increase in growth rate is even higher than when a pulsed discharge is used (33.9 µm h^{-1} at 300 Torr). These experiments indicate the potential to significantly increase the growth rates beyond those given in Chapter 6 while still growing high quality SCD.

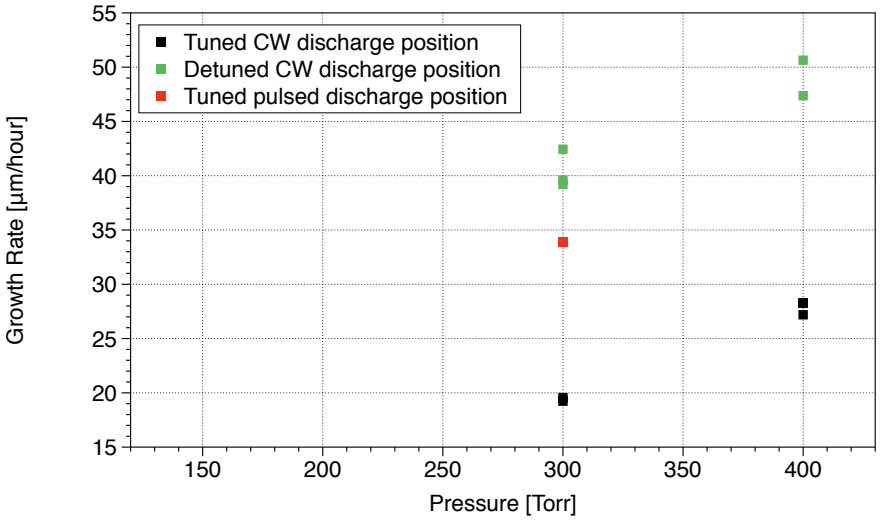

Figure 8.4 Comparison of the the growth rate as function of the pressure for tuned and detuned CW and pulsed reactor operation

Figure 8.5 and Figure 8.6 show optical photographs of two CVD-grown SCD films on (i) a small (3.5 mm × 3.5 mm) and (ii) a large (7.0 mm × 7.0 mm) HPHT seed crystal. Deposition times were 24 h each. The growth rate for the large HPHT seed crystal, grown at 300 Torr was 42 µm h^{-1} and the growth rate for the small HPHT seed crystal, grown at 400 Torr, was 47 µm h^{-1}. Hence, the overall thickness of the CVD-grown SCD films were 1.0 and 1.14 mm. The grown films, as shown in Figure 8.5 and Figure 8.6 were not removed from the seed crystals. Visual inspection however shows a very good, flat and uniform film morphology. Outgrowing of the SCD surface area was first observed for both substrates. This was achieved by using the optimized holder designs discussed in Section 3.1.4. Figure 8.5 (a) shows, that some of the jagged edge SCD material on the right started to turn into PCD. This may be

attributed to the fact, that the right side grew out of the pocket due to the high growth rate of over $50\,\mu m\,h^{-1}$ resulting in a total growth of over 1 mm. Both seeds with the grown SCD on top appear yellow, see Figure 8.5 and Figure 8.6, the initial color of the HPHT seeds. Based on visual inspection, it can be assumed, that the grown SCD will be of good quality, almost colorless, once being processed into freestanding SCD plates. Thus, the nitrogen incorporation is significantly lower than for the SCD grown under pulsed conditions, see Figure 8.3, and can be assumed to be in the sub-ppm level.

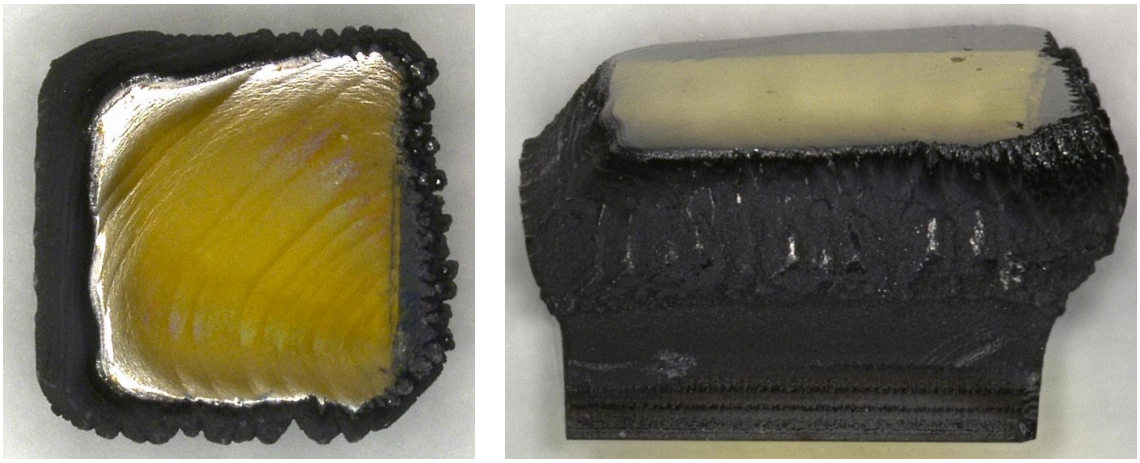

(a) Top view (b) Side view

Figure 8.5 Top and siew view of a SCD film grown on a 3.5 mm × 3.5 mm HPHT seed under detuned discharge conditions.

8.4 Summary

The use of a pulsed microwave discharge and purposeful detuning of the reactor cavity were preliminarily evaluated for its usefulness in increasing the SCD growth rate in support of increasing the process pressure.

The use of a discharge, which was pulsed between 0 and 3000 W at 50 Hz and a 70 % duty cycle led to an SCD growth rate of $34\,\mu m\,h^{-1}$. This corresponded to a 73.4 % increase in

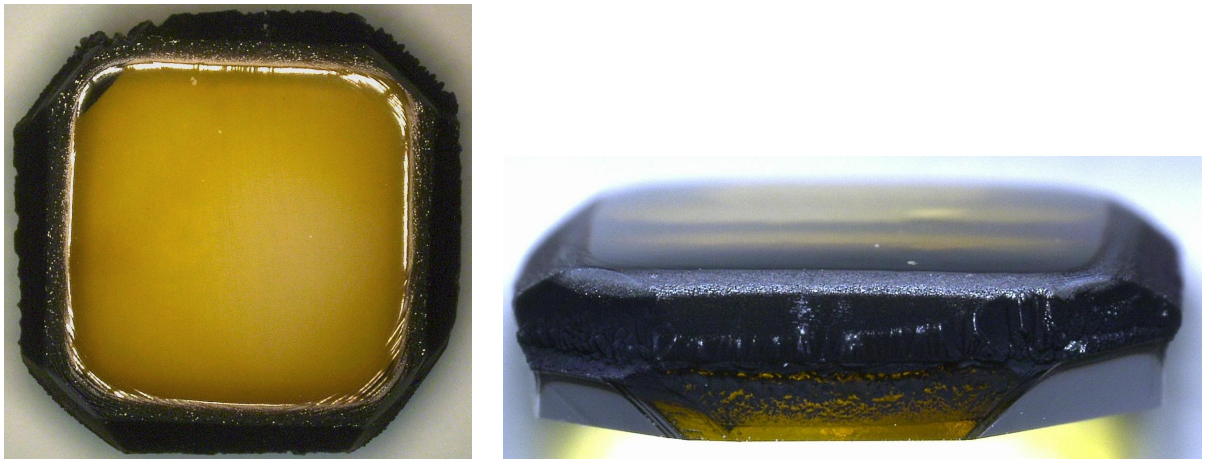

(a) Top view (b) Side view

Figure 8.6 Top and siew view of a SCD film grown on a 7.0 mm × 7.0 mm HPHT seed under detuned discharge conditions.

growth rate compared to SCD growth under c.w. excitation and otherwise similar process conditions. Additionally, the average power consumption was reduced by 23 %. However, the quality of the film morphology was not as good as for the optimized c.w. growth process. Additionally, it was found, that significant amounts of nitrogen were incorporated and that the CVD-grown SCD contained internal stress. It remains to be seen, if the degraded crystalline quality can be improved to a level of the c.w. growth process as it has been reported for lower process pressures [144].

A second approach was by purposefully retuning the reactor in order to move the discharge region closer to the SCD substrate. This would reduce the boundary layer between the discharge and the holder which then allows for an increased flux of ionized species to increase the growth rate. The cavity length was changed from 21.4 to 21.55 cm. The detuning resulted in a visible attachment of the discharge onto the holder. The appearance of 41 to 54 W of reflected power illustrate, that the reactor was not operated in electromagnetically well matched conditions. It was found, that the growth rate under otherwise unchanged conditions more than doubled to 39 - 42 µm h^{-1} at a process pressure of 300 Torr and increased over

80 % to 47 - 50 µm h^{-1} for 400 Torr. Optical inspection of the grown SCD material indicates high crystalline quality.

The experiments were not optimized for achieving a maximum effect. Further research on the optimization of the approaches will be needed. However, these two approaches offer the opportunity to increase the growth rate along increases when increasing the process pressure. Thus, in-depth studies to optimize the growth conditions and to understand certain phenomena, i.e. the reduction of crystalline quality when using the pulsed microwave discharge, will be required and are encouraged.

8.5 Experimental data of the SCD growth processes

This final section serves as a summary of all SCD growth runs, which were performed in this dissertation. Table 8.1 contains an overview of the experimental conditions as well as growth rates, wich were used for the discussions in the previous sections. The following variables were constant throughout all experiments and hence not included in the table: hydrogen flow at 400 sccm, cooling stage water flow at 2.05 gallons per minute, as well as the reactor variables $L_p = 3.6$ cm and $Z_s = -4$ mm.

The experimental data is separated into four different groups: (1) pressure series (see Section 6.3.2.1), (2) methane concentration series (see Section 6.3.3.1), (3) pulsed SCD growth (see Section 8.2) and (4) detuning (see Section 8.3).

The power reported inTable 8.1 for the pulsed experiment, marked as *, represents the average power. Pulsing of the discharge was done with $P_{on} = 3000$ W, $P_{off} = 0$ W, $T_{on} = 14$ ms and $T_{off} = 6$ ms.

Series	Pres. Torr	Time h	P_{abs} W	P_{ref} W	CH_4 %	L_s cm	T_s °C	dep. rate µm h^{-1}	growth µm
1	180	20	2795-2850	0	5	21.4	850 - 870	9.33	194.0
1	240	20	2700	0	5	21.4	880 - 895	16.22	300.7
1 - 4	300	20	2700	0	5	21.4	890 - 905	19.56	389.8
1	340	20	2400-2550	0	5	21.4	895 - 915	25.49	509.8
1	380	20	2700	0	5	21.4	885 - 905	28.09	550.6
1	400	20	2250-2400	0	5	21.4	900 - 910	27.19	526.3
2	300	20	2100-2400	0	6	21.4	885 - 910	20.83	413.9
2	300	20	2180	0	7	21.4	895 - 915	22.42	445.0
2	300	20	2100	0	8	21.4	895 - 905	26.57	531.3
2	300	20	2020-2100	0	9	21.4	890 - 910	27.14	533.5
1	300	50	2100*	0	5	21.4	880 - 920	33.91	1698.0
4	300	24	2850	41	5	21.55	880 - 905	42.44	1033.5
4	300	30	2100-2250	54	5	21.55	875 - 910	39.19	1187.3
4	300	30	2100	41	5	21.55	890 - 925	39.61	1198.8
4	400	22.5	2400-2550	41	5	21.55	905 - 920	50.64	1135.0
4	400	24	2400-2550	54	5	21.55	905 - 910	47.37	1144.4

Table 8.1 Overview of the experimental conditions of the SCD growth experiments presented in Chapter 6 and Chapter 8.

Chapter 9

Summary, accomplishments and outlook

9.1 Summary and accomplishments

This dissertation addresses several crucial tasks for the technological advancement to 2 inch SCD wafers and their economic manufacturing. The major accomplishments are summarized below in the following subsections. In-depth summaries of the individual tasks can be found in the summary of each corresponding chapter.

9.1.1 SCD processing

Overall, it was shown that a cutting laser is a good tool for SCD shaping and SCD plate engineering. In particular, when operated under proper conditions the laser can leave the bulk material unchanged. It was also shown however, that laser cutting is not sufficient for large area SCD wafer slicing. This is attributed to the amount of material loss cause by the triangularly wedged cutting profile. This loss increases with wafer dimensions. It was shown when using conventional SCD growth technologies that PCD formation on the outer SCD edges grows into the top SCD surface. This reduces the SCD top surface area throughout the vertical growth process cycle. Hence, it is necessary to remove any PCD material by

laser cutting in between individual deposition runs. A detailed summary of Chapter 4 can be found in Section 4.6. The major accomplishments are summarized below.

- A three stage process for separation of CVD-grown SCD from a seed crystal was introduced and analyzed. The procedure included (1) separation of the grown material from the seed using laser cutting, (2) mechanical polishing of the laser cut surface and (3) laser-based edge trimming to remove overgrown diamond.

- Laser cutting was an efficient tool for shaping of SCD, which does not alter the material properties, if proper settings of the cutting laser were used.

- PCD formation on the outer SCD edges will grow into the top SCD surface and reduce the SCD surface area available. Thus it is critical to to remove any existing PCD material in between the SCD deposition steps and further to optimize growth conditions in order to surpress the formation of PCD material altogether.

- Fabrication of SCD plates requires mechanical polishing in order to remove non-carbon species and subsurface damage introduced by the cutting procedure.

- Material losses for SCD wafer separation were found to scale linear with the wafer dimensions. Losses for a 10 mm × 10 mm SCD wafer were found to be 500 µm. For a 2 inch wafer this would scale to about 2.5 mm of material loss. Hence, laser cutting is not a sufficient method for the economic separation of large MPACVD grown SCD wafers.

9.1.2 Loss-free separation of grown SCD wafers

Ion implantation based Lift-Off has been proven to be a loss-free SCD slicing technique for dimensions up to several inches. The research performed in this dissertation demonstrates

the successful Lift-Off of SCD plates using protons, carbon, and oxygen ions. It was shown that electrochemical etching is the only viable approach for the removal of the graphite, which was created by ion implantation. Thermal oxidation separation was diffusion limited for SCD wafers larger than 2 mm × 2 mm, and had a chance of oxidizing the SCD material, especially in the areas surrounding any crystalline defects. A detailed summary of the results from Chapter 5 can be found in Section 5.8. The major accomplishments of this activity are summarized below.

- A process to bombard SCD wafers with ions in the MeV energy range was established to locally destroy the crystalline structure in a narrow subsurface region.
- The use of carbon and oxygen ions is favorable over protons because significantly reduced doses are required.
- The destroyed region forms into nano-crystalline graphite during MPACVD deposition if a sufficient amount of damage was introduced.
- Both, electrochemical etching and thermal oxidation are successful in removeing the graphite.
- Lift-Off of SCD wafers was successfully demonstrated.
- Thermal oxidation can etch the SCD wafer, preferentially nearby crystalline defects.
- Electrochemical etching is the only scalable approach for the graphite removal because the process is not diffusion limited.
- Lift-Off is a scalable SCD wafer separation technique with virtually no losses.

9.1.3 Extending the reactor operation up to 400 Torr

The existing MCPR deposition system was improved by adding a stable power supply, which also allowed pulsed operation. This allowed the increase of the operating pressure for MPACVD up to 400 Torr. The reactor behavior in this new regime was quantitatively and qualitatively explored and measured. In particular, the plasma volume and absorbed power density were recorded and the operational field map of the reactor performance in this high pressure regime was established. It was found that the newly investigated pressure regime (300 to 400 Torr) behaves different when compared to lower pressure regimes. It was found that the absorbed discharge power density increases more rapidly as pressure was increased than at the lower pressure operation. At high pressures, 380 Torr and above, higher absorbed input power levels were necessary in order to to maintain a discharge in close contact with the SCD seed in order to establish substrate temperatures suitable for SCD deposition. This was attributed to the fact, that the plasma dimensions shrink with increasing pressure. Hence, when the pressure is increased, the discharge pulls away and separates from the SCD substrate and holder. Thus, operation at higher absorbed power would be necessary in order to compensate for this phenomena. An alternative method of compensation is by retuning the reactor variables so that the plasma discharge is pulled down to be closer to the SCD substrate [57]. A detailed summary on the key results can be found in Section 6.4. The major accomplishments are summarized below.

- The growth window for SCD was increased into the 300 to 400 Torr regime.
- The discharge volume descreases and the absorbed microwave power densities increases with pressure. The absorbed power densities were found to be 535 to 670 $\mathrm{W\,cm^{-3}}$ in the 300 to 400 Torr regime.

- The plasma discharge descreased in size and pulled away from the SCD seed substrate and substrate holder for high pressures (above 380 Torr).

- Efficient operation at high pressures (above 380 Torr) requires higher input power levels and/or a retuning of the reactor configuration.

9.1.4 SCD growth up to 400 Torr

SCD growth up to 400 Torr was also demonstrated. The growth rate behavior and observations of the crystalline quality in this new pressure regime were in accordance with the established Harris-Goodwin theory [41, 49], i.e. the growth rate increases when increasing either the pressure or the methane concentration, but while the crystalline quality also increased when increasing the pressure, it decreased with increasing methane concentration. The formation of soot when operating at high methane concentrations (above 6 %) remains a limiting factor for efficient operation in this high pressure regime. It was found that the absorbed discharge power density increases with pressure. Contrary to that, the growth rate as a function of the pressure is not increasing any further for pressures of 380 Torr and above. This is further evidence, that the plasma discharge pulled away from the SCD substrate and a retuning of the reactor is needed to further increase the operating pressure in order to enable efficient operation. It was shown, that rimless SCD material without detectable internal stress can be grown in this new pressure regime. A detailed summary of the results can be found in Section 6.4. The major accomplishments are summarized below.

- SCD growth of high crystalline quality without internal stress and a PCD rim was demonstrated for pressures up to 400 Torr.

- The current understanding of diamond growth versus pressure was verified up to 400 Torr.
- SCD top surface areas expanded by up to 40 % through vertical growth.
- Increase of the methane concentration resulted in an increased formation of crystalline defects, introduced internal stress and changed the growth morphology.
- Formation of internal stress can be independent of the stress pattern of the underlying seed crystal.
- A PCD rim appeared for growth under high (more than 7 %) methane concentrations.
- SCD growth rates did not further increase for high pressures (above 380 Torr) illustrating the need for retuning the reactor configuration.

9.1.5 Temporal development of pulsed microwave discharges

Video filming was utilized to record the ignition, expansion, steady state operation, decay and vanishing of pulsed microwave discharges. It was demonstrated that the discharge ignition depends on the four pulsing input parameters P_{high}, P_{low}, T_{high} and T_{low}. A particular pulsing setup was investigated by fixing the power levels to 3000 W for P_{high} and 0 W for P_{low}. This resulted in a true on-off pulsing of the discharge. Six different pulsing discharge behaviors were identified and were plotted in the two-dimensional T_{on}-T_{off} space. Their occurance in T_{on}-T_{off} space was approximated. This included combinations of T_{on} and T_{off}, where a pulsed discharge cannot be sustained. Additionally, the T_{on}-T_{off} space includes c.w. excitation, represented as the horizontal line with T_{off} being zero. The T_{on}-T_{off} space also included the variation of the dependent pulsing parameters, i.e. average power and

duty cycle, which are affecting the pulsing behavior as well. It was demonstrated that the transient development of pulsed discharges is depending on the T_{on} and T_{off}. Investigation of the pulsing frequency showed, that individual pulsing frequencies below 100 Hz seem more favorable to enhance the SCD substrate temperature and the growth rate. It was shown, that conventional numerical models describing pulsed microwave discharges do not properly describe the ignition phase and do not account for variations of how fast the discharge is developing. Thus, a more sophisticated model needs to be developed to describe the phenomena accordingly. A detailed summary of Chapter 7 can be found in Section 7.8. The major accomplishments are summarized below.

- It was shown, that the pulsed discharge decays in approximately 2 ms, which is in accordance with numerical calculations [140].

- The formation of pulsed microwave discharges was recorded as a function of (i) the duty cycle, (ii) by varying T_{on} with a constant T_{off}, and (iii) as a function of the pulsing frequencies. Thereby, a total of six different discharge behavior patterns were found.

- Two of these cases are special cases as they do not represent a periodic repetition of the observed discharge development cycle. One marked a region, where the discharge became instable and unsustainable. The other was a continuous discharge with periodic disturbance, but the plasma would never go off visibly.

- A total of four different patterns of discharge ignition and development was observed, where the discharge reignited periodically. Those four discharges were in detail: (1) the formation of two separated thermal discharges, which then merge into a single one, (2) the formation of an inhomogeneous thermal discharge on the SCD surface, (3) the

formation of one homogeneous thermal discharge on the SCD and (4) the ignition as a spherical discharge detached from the SCD substrate.

- Expansion of the pulsed microwave discharges showed a highly dynamic behavior. The thermal discharges formed on the SCD substrate eventually detached from the SCD substrate, turned into a spherical discharge and floated towards the steady state position.

- The location of vanishing of the pulsed microwave discharge and the location of reignition were not the same inside the reactor.

- The T_{on}-T_{off} space was introduced in order to visualize and compare the different discharge patterns. The individual regions of occurrence of each of those six cases were refinded based on the individual video recordings.

- It was shown, that the timely development of a pulsed microwave discharge depends on the input parameters, i.e. the discharge develops slower when T_{on} is reduced under a constant T_{off}. This is in contradiction to numerical calculations, which suggested an idenditcal development [140].

- Pulsing of a microwave discharge enhances the SCD substrate temperature compared to continuous excitation.

- Lower pulsing frequencies (50 to 125 Hz) were found to be more efficient in increaing the SCD substrate temperature than higher frequencies (166.7 to 500 Hz).

9.1.6 Further enhancement of the growth rate

Based on the results presented in Chapter 6 and Chapter 7 a selection of exploratory experiments to further increase the growth rate was carried out by two different approaches: (1) using a pulsed microwave discharge and (2) detuning the reactor dimensions as a simplistic realization of retuning the reactor dimensions. The detuning was achieved by changing the cavity length from 21.4 to 21.55 cm and caused the appearance of 41 to 54 W of reflected power. Then the discharge was visibly pushed onto the substrate holder. It was demonstrated that both approaches increased the growth rate by 70 to 100 %. Using a pulsed discharge lowered the average power consumption by 23 %. These results were achieved under non-optimized growth conditions. Thus, an even higher improvement of the growth rate may be possible, when optimizing the process. Rimless growth was initially demonstrated, until the diamonds grew out of the pocket due to the significantly higher growth rates. Initial evaluation of the crystalline quality of the grown SCD films varied from being significantly worse to appearing to be comparable to the high quality shown in chapter 6. However, a detailed study of to optimize the processes will be needed. A detailed summary of Chapter 8 can be found in Section 8.4. The major accomplishments are summarized below.

- The SCD growth rate was increased by over 73 % when using a pulsed microwave discharge, while simultaenously reducing the power consumption by 23 %.
- The freestanding SCD plate grown under pulsed conditions showed a significant amount of internal stress and incorporation of nitrogen.
- The SCD growth rate was more than doubled by purposefully detuning the reactor at 300 Torr and this increased the growth rate by over 80 % for 400 Torr.

- Visual inspection of the CVD-grown SCD, which was still attached to the seed crystal, indicated a high crystalline quality thereof.

Finally it is noted that the research performed in this dissertation addresses several suggestions for future research made by Lu [60] in the outlook of her PhD dissertation, i.e. further enhancing the operating pressure above 280 Torr and increasing the methane concentration above 7 % in order to increase the growth rate. An additional suggestion was to controllably pulse the microwave discharge, which was achieved in this dissertation by using a new microwave power supply.

9.2 Outlook and future research

The studies performed within this dissertation are crucial for the realization of 2 inch SCD wafers and addressed several key technological challenges to be solved. Several research areas have been identified, which should be investigated in the future for further enhancing the SCD wafer technology, but also for a broader and more in-depth understanding of the MPACVD technology. Suggestions for future research are as follows:

Lift-Off was demonstrated as an alternative SCD separation technique without material loss. However, the process was not optimized economically. Hence, future research should be conducted to identify the lowest dose necessary to successfully perform Lift-Off. This will reduce the required irradiation time. Additionally, the current electrochemical etching process is a purely physical ablation process without the support of chemical reactions, as shown in Section 5.4.3. It can be assumed that utilization of chemical oxidation reactions without having diffusion limitations by applying the external electric field would result in vastly higher etch rates compared to a physical removal of the graphite. This may be achieved

by using hot acid solutions as aqueous medium, but this would require significant changes to the setup for safety reasons.

Further enhancement of the SCD growth rate is of importance for economic manufacturing of SCD wafers. Based on the preliminary results shown in Chapter 8 an in-depth study of retuning the reactor seems an easy way to double the growth rate under otherwise unchanged reactor conditions without suffering on the SCD quality. Additionally, retuning the reactor and possibly increasing the absorbed power levels may produce an increase of the SCD growth window into the 500 Torr pressure regime. Doing so would increase the reactor performance knowledge, i.e. by studying plasma discharges with even higher absorbed power densities, but should also increase the SCD growth rate and crystalline quality even further. Increasing the SCD growth rate further is of particular importance in order to reduce the total growth time required for the flipped side approach, For example, it would take a total of 208 days to perform all the growth steps proposed in Table 2.1 when assuming a growth rate of $50\,\mu m\,h^{-1}$, as obtained in Section 8.3.

The pocket holder used in this dissertation was shallower (d = 2.0 mm) compared to other work at MSU reporting on lateral SCD surface enlargement during vertical growth (d = 2.3 mm, d=2.6 mm) [67, 72]. Hence, a detailed study of different pocket holder geometries with varying pocket widths and depths should be carried out to identify the optimum values for lateral outgrowing. Additionally, the pocket optimization should be adopted for larger substrates in order to evaluate the scalability of lateral outgrowing for larger SCD wafer dimensions.

Controlled pulsing of a Reactor B was experimentally explored for the first time. While it was found, that a pulsed microwave discharge can be a useful tool for enhancing the growth rate, an in-depth study of the effects of pulsing on the growth rate and crystalline quality will

be needed. This study should take into account, that pulsing complicates the input parameter space, i.e. P_{abs}, which describes the absorbed power for a continuously excited discharge is replaced by a set of four parameters (P_{high}, P_{low}, T_{high} and T_{low}) which themselves define three new dependent variables (duty cycle, frequency and P_{abs}). Utilizing of pulsing for enhancing the growth rate is of particular interest as a combination of high P_{high} power levels and low duty cycles can significantly increase the available SCD growth area for otherwise comparable P_{abs} levels and growth conditions.

Video recording deemed a useful tool in the study of the temporal development of pulsed microwave discharges. Future research should study the temporal formation of microwave discharges depending on the four pulsing parameters (P_{high}, P_{low}, t_{high} and t_{low}) in order to identify all possible discharge ignition and expansion patterns. Once a suitable set of different discharge behaviors are identified, it is suggested to record the microwave discharge formation using different bandpass filters. By doing so it is possible to see the distribution and influence of each individual excited species. This information will be critical for defining more detailed numerical models for describing pulsed microwave discharges at pressures realistic for SCD growth.

While not being mentioned in this dissertation, the requirements to increase the SCD wafer technology to 2 inches and above will require the scaling of the 2.45 GHz MPACVD SCD technologies and processes to 915 MHz. A uniform discharge is desirable for high quality and uniform SCD growth. Unfortunately, discharge dimensions for the 2.45 GHz technology for high pressures can be less than 30 mm in diameter making uniform deposition over areas larger than 1 inch unlikely. The limitations of the 2.45 GHz technology for growing large area SCD wafers is laid out in Section 9.3.1, where a cost analysis for SCD wafer fabrication is presented. The analysis shows, that the use of 915 MHz technology will be neccessary for 2

inch SCD wafer fabrication. Additionally, it was demonstrated, that the 915 MHz technology utilizing multiple wafer growth is more economical compared to single wafer growth using 2.45 GHz technology.

9.3 Evaluation of commercial SCD wafer fabrication

9.3.1 Cost calculation for SCD wafer fabrication

The following discussion contains a rough cost estimate for inch size SCD wafer manufacturing comparing the 2.45 GHz and the 915 MHz technologies to illustrate how important upscaling of the reactor technology is. The assumption for the 2.45 GHz process in this cost breakdown is, that operation at 380 Torr using a retuned reactor allows uniform SCD growth at 50 µm h^{-1} over an area 30 mm in diameter; enough for fabrication of 1 inch diameter SCD wafers. The costs associated with power consumption and gas flow rates use the experimental results from Chapter 6 and Chapter 8 in this dissertation. An absorbed power of 2.5 kW is selected to describe the high end of the experimental runs. Hence, the overall wall plug power consumption in this cost calculation is 5.0 kW. The H_2 flow is 400 sccm and the CH_4 flow is 20 sccm. The ramp-up period ($\approx$ 20 min) is ignored in this cost estimate. Individual run times are 20 h based on the growth rate approximation in order to make 1 mm thick SCD wafers.

The different levels of efficiency for scaling to 915 MHz are reflected by analyzing different cases. A conservative scaling of the discharge dimensions was by approximating a 3.5 inch (89 mm) discharge diameter. This would allow simultaneous growth on eight 1 inch diameter SCD wafers as shown in Figure 9.1. Alternatively, a more optimistic case would result in a usable discharge area has a diameter of 5.5 inch (140 mm), similar to the work by Asmussen

et al. [166]. This would enable the simultaneous growth on nineteen 1 inch diameter SCD wafers as shown in Figure 9.1. H_2 flow is approximated to be 1000 sccm, CH_4 flow is 50 sccm. The absorbed power is assumed to be 10.0 kW for the smaller plasma diameter of 3.5 inches and increases to 12.5 kW for the case of a 5.5 inch plasma. Hence, the total wall plug power consumption is 20 and 25 kW, respectively.

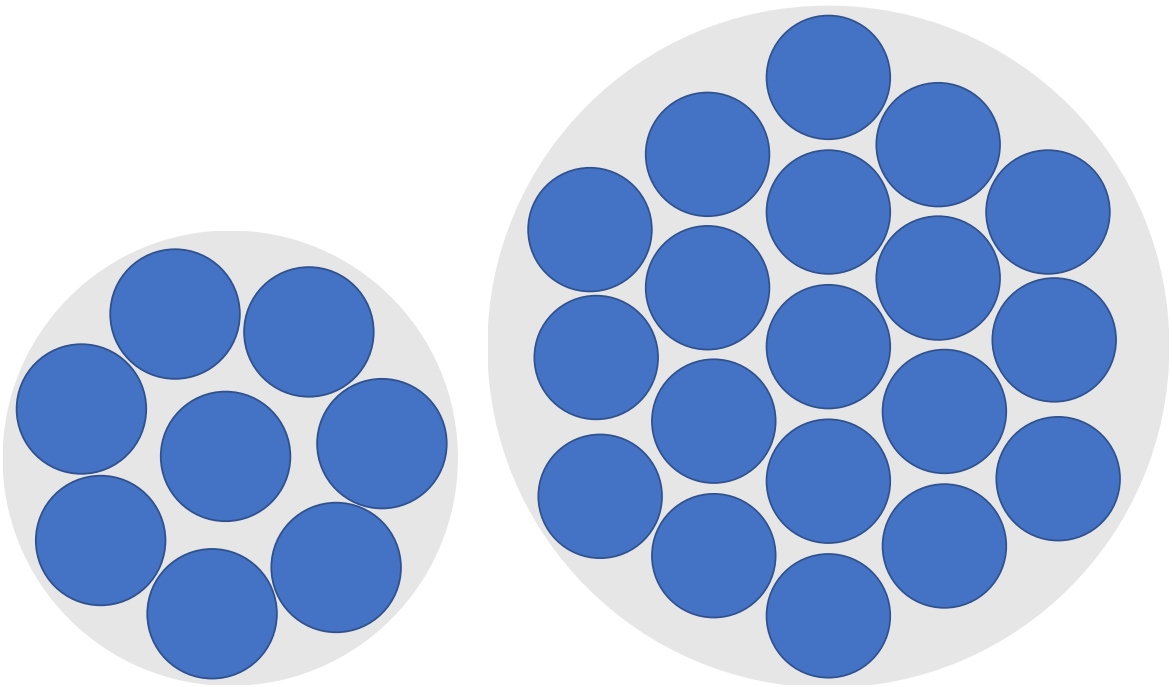

(a) 3.5 inch (b) 5.5 inch

Figure 9.1 Schematic illustration of the scaling of the discharge using 915 MHz technology. The grey circle represents the projected area onto the substrate holder of homogenous growth. The areas are 3.5 inch and 5.5 inch. The blue circles represent individual 1 inch wafers, which can be placed inside the discharge area for homogenous growth.

The growth rate for the 915 MHz process is evaluated under two cases as well. Optimistically, the same growth rate as in the 2.45 GHz process ($50\,\mu m\,h^{-1}$) can be achieved and individual growth processes will take 20 h. The conservative case only attributes for half the growth rate ($25\,\mu m\,h^{-1}$) and the growth time will increase to 40 h.

The discussion here illustrates, that 2.45 GHz system technology will not be sufficient for

growth of 2 inch wafers, and 915 MHz will be needed. Additionally, the growth of SCD wafers of smaller size, i.e. 1 inch, is more cost efficient. This can be seen based on the discussion below. However, the numbers for the estimate of the SCD wafer fabrication presented here are just estimates and simplified at times.

The costs associated with the gas consumption are estimated using the following assumptions: (i) full AL sized gas cylinders with an internal volume of 29.5 L have an average pressure of 2500 psi when delivered, (ii) gas cylinders are being used only to a pressure of 500 psi, (iii) cost of H_2 cylinders are \$200 and (iv) costs for CH_4 cylinders are \$500. Hence, the usable volume per gas cylinder at a process pressure of 380 Torr (0.5 atm) is:

$$V = \frac{p_{\text{cylinder}} \cdot V_{\text{cylinder}}}{p_{380\,\text{Torr}}} = \frac{2200psi \cdot 29.5\,\text{L}}{7.35psi} = 8026\,\text{L} \tag{9.1}$$

Then, the cost of 1 liter of gas is \$0.025 for H_2 and \$0.062 for CH_4.

The power consumption is estimated as twice the input power in order to account for the peripheral systems, especially the cooling system. Power consumption costs are estimated as \$0.1 per kW h.

In order to calculate the costs associated with maintenance and machine depreciation it is assumed that six twenty hour experiments and three forty hour experiments are carried out per week and the system is operated fifty weeks a year. Hence, 300 twenty hour experiments and 150 forty hour experiments will be performed per year. Annual maintenance costs are approximated at 3 % of the initial machine costs, which is assumed to be \$500,000 for a 2.45 GHz reactor and \$1,000,000 for a 915 MHz reactor. Hence, annual maintenance costs are \$15,000 and \$30,000 respectively and are accounted for across all runs. Additionally, it is assumed that the individual diamond reactors are depreciated over a time span of 10 years,

or $50,000 and $100,000 annually. The deprecation costs are distributed across all growth runs per year.

After defining the variable costs of the SCD growth process it is possible to calculate the costs per run and the costs per wafer by simply adding the associated costs of each run in Excel. The breakdown of the wafer growth costs is shown in Table 9.1.

Item	2.45 GHz	915 MHz			
Growth time	20	20	40	20	40
Runs per year	300	300	150	300	150
Discharge diameter [inch]	1.5	3.5	3.5	5.5	5.5
Wafers	1	8	8	19	19
Power costs [$]	10.00	40.00	80.00	50.00	100.00
H_2 costs [$]	12.00	30.00	60.00	30.00	60.00
CH_4 costs [$]	1.49	7.44	3.72	3.72	7.44
Maintenance costs [$]	50.00	100.00	200.00	100.00	200.00
Depreciation costs [$]	166.67	333.33	666.67	333.33	666.67
Run costs [$]	240.15	510.77	1010.39	517.05	1034.11
Costs per wafer [$]	240.15	63.85	126.30	27.21	54.43

Table 9.1 Estimated cost associated with the SCD growth attributed to each individual 1 inch SCD wafer calculated based on an optimized 2.45 GHz single wafer growth process and four different cases of multiple wafer growth using a scaled 915 MHz reactor.

It can be seen, that the growth costs per SCD wafer are smaller for the 915 MHz process. Even in the worst-case scenario (only 3.5 inch discharge diameter and half the growth rate) the deposition cost per SCD wafer is only slightly more than half of the costs for the 2.45 GHz process. The best-case scenario would result in nine-time cost reduction. Those promising numbers hold true in addition to the fact, that 2 inch SCD wafer can be easily achieved using 915 MHz technology.

In addition to the operational costs for the SCD growth, the wafer fabrication process has a set of additional fixed costs, i.e. labor and the external costs for ion implantation.

The associated labor costs with within the process chain, i.e. handling of the SCD seed, preparing the growth process, programming of the cutting profile for the framing prior to

wafer separation and many more are not discussed in detail or how scaling effects can be achieved. Instead, the associated labor costs for every wafer are assigned with fixed costs of $550 for labor. It needs to be mentioned, that some scaling effects are not attributed here. For example, overseeing a growth process in a 2.45 GHz system with only one 1 inch SCD wafer will take about the same amount of time than overseeing a 915 MHz process with 19 wafers.

The implantation costs for the Lift-Off consist of a $900 fixed cost associated per batch of irradiation carried out and nine 1 inch wafers can be irradiated per wafer. Assuming, that only full batches are irradiated, the fixed irradiation cost per SCD wafer is $100. Additional costs occur for the irradiation time. Costs of $150 are attributed per SCD wafer assuming an optimized irradiation process. Those numbers are obtained based on the time estimates, which were provided from Western Michigan University, and applying an industrial rate of $300 per hour. Cost reduction by developing a new holder configuration, which allows for the simultaneous irradiation of more than 9 SCD wafers at a time, would be a relatively easy approach in order to reduce the fixed cost per wafer associated with the ion implantation process. Reducing the cost associated with the implantation time is more complicated as it would require the upgrade of the implanter with an ion source, which is capable of higher ion fluxes, which would be a significant monetary investment.

The cost of the initial SCD wafer used for growth of new wafer generations has to be reflected in the equation as well as costs associated with the limited life time of a SCD wafer used for wafer cloning. In this scenario, a 10 % surcharge is added to the cost analysis in order to reflect costs of the initial SCD wafer and the wafer life time.

Finally, it needs to be acknowledged that not every single SCD wafer fabrication process will result in a usable wafer due to different reasons, i.e. the formation of defects during

growth or cracking during processing. Overall, a yield of 75 % is approximated within the early stages of SCD wafer fabrication on a commercialized level. A 25 % surcharge has been added to each SCD wafer in order to account for the losses created by a non-successful SCD wafer fabrication process.

The final costs accounting for all expenses introduced above are given in Table 9.2, which compares the costs for one 1 inch diameter SCD wafer produced to the specific growth cases introduced.

Item	2.45 GHz	915 MHz			
Growth time	20	20	40	20	40
Runs per year	300	300	150	300	150
Discharge diameter [inch]	1.5	3.5	3.5	5.5	5.5
Wafers	1	8	8	19	19
Power costs [$]	10.00	40.00	80.00	50.00	100.00
H_2 costs [$]	12.00	30.00	60.00	30.00	60.00
CH_4 costs [$]	1.49	7.44	3.72	3.72	7.44
Maintenance costs [$]	50.00	100.00	200.00	100.00	200.00
Depreciation costs [$]	166.67	333.33	666.67	333.33	666.67
Run costs [$]	240.15	510.77	1010.39	517.05	1034.11
Costs per wafer [$]	240.15	63.85	126.30	27.21	54.43
Labor costs [$]	550.00	550.00	550.00	550.00	550.00
Implantation costs [$]	250.00	250.00	250.00	250.00	250.00
Seed costs [$]	104.02	86.38	92.63	82.72	85.44
Yield costs [$]	286.04	215.96	231.57	206.80	213.61
Final cost per wafer [$]	1430.21	1166.19	1250.50	1116.74	1153.48

Table 9.2 Estimated total cost for the fabrication of 1 inch SCD wafers based on an optimized 2.45 GHz single wafer growth process and four different cases of multiple wafer growth using a scaled 915 MHz reactor and separation using Lift-Off.

It can be seen, that the overall predicted cost for 1 inch SCD wafers are cheaper utilizing multi wafer growth in a 915 MHz reactor compared to wafer growth using a 2.45 GHz reactor. Overall, the relative difference in cost is reduced as the majority of fabrication costs are associated to fixed costs, i.e. the best case in the 915 MHz has only $27.21 of costs associated to the actual wafer growth and $1190 in fixed cost.

It needs to be mentioned though, that the fixed cost assignment is only simplistic as it ignores certain synergies using a multi wafer growth, and a more detailed analysis will reduce the labor costs per wafer. For example, a machine operator has the same labor costs when monitoring a 2.45 GHz process with one wafer or a 915 MHz process with 19 wafers. Hence, the labor costs per wafer will be 19 times lower for the 915 MHz process. The simplistic approach of assigning a fixed cost per wafer was done, since an accurate reflection of the labor costs would require an in-depth breakdown of the individual tasks and costs associated while it seemed sufficient to have a rough estimate for the discussion presented here.

Overall it can be summarized, that the SCD wafer growth utilizing 915 MHz growth technology is much more economical, and can reduce the deposition costs by a factor of 2 to 9. At the same time, it needs to be mentioned, that the non-growth costs are the major sources of expenses. Hence, it will be necessary to streamline the growth and processing routine to reduce the labor cost and to scale the implantation process in order to irradiate as many wafers at a time as possible to minimize the experiment setup costs per wafer. Additionally, the fabrication process needs to be optimized in order to maximize the yield and how often a seed wafer can be reused.

9.3.2 SCD wafer fabrication using HPHT processes

High quality growth of SCD with dimensions in the centimeter range by the HPHT process was recently reported as well [204]. The Russian company New Diamond Technology (NDT) is specialized in the growth and fabrication of multi carat gem stones fabricated out of colorless HPHT diamonds. For example, in 2015, they reported on a 10.02 carat square emerald cut diamond, which was cut from a 32.26 carat rough diamond grown via HPHT [205]. The growth process took 300 h. The cut diamond had dimensions of approximately

14.4 mm × 10.7 mm × 6.9 mm.

Those numbers sound promising, but there are particular problems with the HPHT growth of large area SCD, which have to be mentioned. The first is, that the grown diamonds often feature inclusions of the metallic catalysts used within the HPHT process to enable diamond growth [204]. In order to obtain HPHT-grown SCD with lateral dimensions as large as reported by NDT, a significant amount of vertical growth is required. This can be seen in the schematic growth pattern of a HPHT diamond, shown in Figure 9.2 [206]. Additionally, the lateral growth causes the formation of several growth sectors, which will be incorporated, when a (100) SCD wafer is processed out of the HPHT grown diamond along the dotted line. It also needs to be pointed out, that a large amount of grown SCD is not used in the wafer fabrication process and the efficient yield is not high. Currently, the main use of these large HPHT-grown diamonds is for the gem stone market. Currently, the price range for a fully processed gem diamond is in the order of $125,000 to $150,000. The faceting and polishing of the rough diamond is adding value resulting in the final price tag. Nevertheless, it can be expected that the cost of the as grown HPHT diamond will be already several tens of thousands of dollars. This is far too high to justify processing the diamond into a SCD wafer, where dimensions will be between half and three quarters of an inch. At the moment, MPACVD growth of diamond seems the only viable option to develop and grow inch size SCD wafers and beyond.

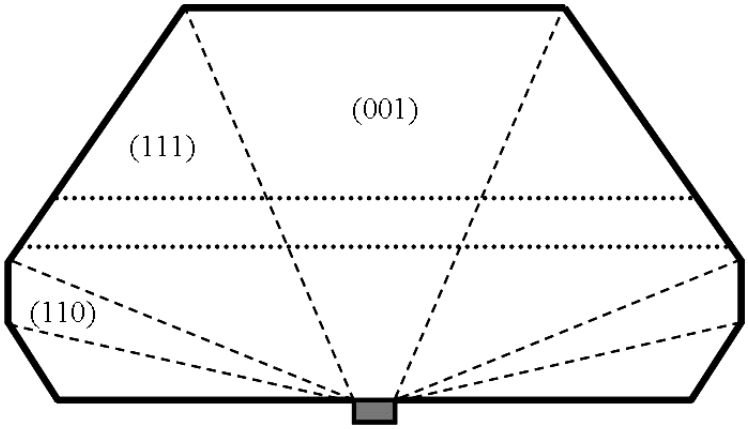

Figure 9.2 A schematic diagram showing a 110 cross-sectional view of growth sectors in a type IIa HPHT synthetic diamond sample produced from a (001) seed. Broken lines represent growth sector boundaries and dotted lines indicate how a (001) plate might be cut. [206]

REFERENCES

REFERENCES

[1] K. Miyoshi. Structures and mechanical properties of natural and synthetic diamonds. *NASA*, (19980210770), 1998.

[2] J. C. Dyment. Continuous operation of GaAs junction lasers on diamond heat sinks at 200°K. *Applied Physics Letters*, 11(9):292, 1967.

[3] M. Thumm. Progress on Gyrotrons for ITER and Future Thermonuclear Fusion Reactors. *IEEE Transactions on Plasma Science*, 39(4):971–979, 2011.

[4] M. Mathes, M. Cristinziani, H. Kagan, S. Smith, W. Trischuk, J. Velthuis, and N. Wermes. Characterization of a single crystal diamond pixel detector in a high energy particle beam. *Journal of Instrumentation*, 3(12):P12002, 2008.

[5] S. Stoupin. Novel diamond X-ray crystal optics for synchrotrons and X-ray free-electron lasers. *Diamond and Related Materials*, 49:39–47, 2014.

[6] L. E. Berman, J. B. Hastings, D. Peter Siddons, M. Koike, V. Stojanoff, and M. Hart. Diamond crystal x-ray optics for high-power-density synchrotron radiation beams. *Nuclear Instruments and Methods in Physics Research Section A: Accelerators, Spectrometers, Detectors and Associated Equipment*, 329(3):555–563, 1993.

[7] A. K. Freund, J. Hoszowska, J. P. F. Sellschop, R. C. Burns, and M. Rebak. Recent developments of high quality synthetic diamond single crystals for synchrotron x-ray monochromators. *Nuclear Instruments and Methods in Physics Research Section A: Accelerators, Spectrometers, Detectors and Associated Equipment*, 467:384–387, 2001.

[8] C. G. Schroer, M. Kuhlmann, U. T. Hunger, T. F. Günzler, O. Kurapova, S. Feste, F. Frehse, B. Lengeler, M. Drakopoulos, A. Somogyi, et al. Nanofocusing parabolic refractive x-ray lenses. *Applied Physics Letters*, 82(9):1485–1487, 2003.

[9] D. S. Knight and W. B. White. Characterization of diamond films by Raman spectroscopy. *Journal of Materials Research*, 4(2):385–393, 1989.

[10] R. P. Mildren, J. E. Butler, and J. R. Rabeau. Cvd-diamond external cavity raman laser at 573 nm. *Optics Express*, 16(23):18950–18955, 2008.

[11] C. D. Weis, A. Schuh, A. Batra, A. Persaud, I. W. Rangelow, J. Bokor, C. C. Lo, S. Cabrini, E. Sideras-Haddad, and G. D. Fuchs. Single atom doping for quantum device development in diamond and silicon. *Journal of Vacuum Science & Technology B: Microelectronics and Nanometer Structures*, 26(6):2596–2600, 2008.

[12] J. R. Weber, W. F. Koehl, J. B. Varley, A. Janotti, B. B. Buckley, C. G. Van de Walle, and D. D. Awschalom. Quantum computing with defects. *Proceedings of the National Academy of Sciences of the United States of America*, 107(19):8513–8, 2010.

[13] B. J. M. Hausmann, T. M. Babinec, J. T. Choy, Jonathan S. Hodges, S. Hong, I. Bulu, A. Yacoby, M. D. Lukin, and M. Lončar. Single-color centers implanted in diamond nanostructures. *New Journal of Physics*, 13(4):045004, 2011.

[14] G. Balasubramanian, P. Neumann, D. Twitchen, M. Markham, R. Kolesov, N. Mizuochi, J. Isoya, J. Achard, J. Beck, and J. Tissler. Ultralong spin coherence time in isotopically engineered diamond. *Nature Materials*, 8(5):383–387, 2009.

[15] M. Rohlfing, P. Krüger, and J. Pollmann. Quasiparticle band-structure calculations for c, si, ge, gaas, and sic using gaussian-orbital basis sets. *Physical Review B*, 48(24):17791, 1993.

[16] R. Ramamurti, M. F. Becker, T. Schuelke, T. A. Grotjohn, D. K. Reinhard, and J. Asmussen. Synthesis of boron-doped homoepitaxial single crystal diamond by microwave plasma chemical vapor deposition. *Diamond and Related Materials*, 17(7-10):1320–1323, 2008.

[17] R. Ramamurti, M. F. Becker, T. Schuelke, T. A. Grotjohn, D. K. Reinhard, and J. Asmussen. Deposition of thick boron-doped homoepitaxial single crystal diamond by microwave plasma chemical vapor deposition. *Diamond and Related Materials*, 18(5-8):704–706, 2009.

[18] Y. Kato, H. Umezawa, and S. Shikata. X-ray topographic study of defect in p- diamond layer of schottky barrier diode. *Diamond and Related Materials*, 57:22–27, 2015.

[19] T. A. Grotjohn, D. T. Tran, M. K. Yaran, and T. Schuelke. Heavy Phosphorus Doping by Epitaxial Growth on the (111) Diamond Surface. *Diamond and Related Materials*, 2014.

[20] S. Nicley, S. Zajac, R. B. Rechenberg, M. F. Becker, A. Hardy, T. Schuelke, and T. A. Grotjohn. Fabrication and characterization of a corner architecture schottky barrier diode structure. *physica status solidi (a)*, pages n/a–n/a, 2015.

[21] H. Kato, T. Makino, M. Ogura, D. Takeuchi, and S. Yamasaki. Fabrication of bipolar junction transistor on (001)-oriented diamond by utilizing phosphorus-doped n-type diamond base. *Diamond and Related Materials*, 34:41–44, 2013.

[22] H. Kawarada, T. Yamada, D. Xu, H. Tsuboi, T. Saito, and A. Hiraiwa. Wide temperature (10 K—700 K) and high voltage ($\approx$ 1000 V) operation of CH diamond MOSFETs for power electronics application. In *Electron Devices Meeting (IEDM), 2014 IEEE International*, page 11. IEEE, 2014.

[23] D. Takeuchi, T. Makino, H. Kato, M. Ogura, H. Okushi, H. Ohashi, and S. Yamasaki. High-Voltage Vacuum Switch with a Diamond pin Diode Using Negative Electron Affinity. *Japanese Journal of Applied Physics*, 51:090113, 2012.

[24] T. Makino, K. Yoshino, N. Sakai, K. Uchida, S. Koizumi, H. Kato, D. Takeuchi, M. Ogura, K. Oyama, T. Matsumoto, H. Okushi, and S. Yamasaki. Enhancement in emission efficiency of diamond deep-ultraviolet light emitting diode. *Applied Physics Letters*, 99(6):061110, 2011.

[25] E. Johnson. Physical limitations on frequency and power parameters of transistors. In *1958 IRE International Convention Record*, volume 13, pages 27–34. IEEE, 1966.

[26] P. O. Hahn. The 300 mm silicon wafer—a cost and technology challenge. *Microelectronic Engineering*, 56(1):3–13, 2001.

[27] GlobeNewswire. *https://globenewswire.com*, 2015.

[28] Element Six. *http://e6cvd.com/us/application/all/cvd-sc-plate-8-0x8-0x1-2mm.html*, 2017.

[29] University Wafer. *https://order.universitywafer.com/default.aspx?cat=Silicon*, 2017.

[30] K. W. Hemawan, T. A. Grotjohn, D. K. Reinhard, and J. Asmussen. Improved microwave plasma cavity reactor for diamond synthesis at high-pressure and high power density. *Diamond and Related Materials*, 19(12):1446–1452, 2010.

[31] J. Lu, Y. Gu, T. A. Grotjohn, T. Schuelke, and J. Asmussen. Experimentally defining the safe and efficient, high pressure microwave plasma assisted CVD operating regime for single crystal diamond synthesis. *Diamond and Related Materials*, 37:17–28, 2013.

[32] J. Asmussen, R. Mallavarpu, J. R. Hamann, and H. C. Park. The design of a microwave plasma cavity. *Proceedings of the IEEE*, 62(1):109–117, 1974.

[33] R. Mallavarpu, J. Asmussen, and M. C. Hawley. Behavior of a microwave cavity discharge over a wide range of pressures and flow rates. *IEEE Transactions on Plasma Science*, 6(4):341–354, 1978.

[34] R. M. Fredericks and J. Asmussen. High-Density Resonantly Sustained Plasma in a Variable-Length Cylindrical Cavity. *Applied Physics Letters*, 19(12):508–510, 1971.

[35] M. Brake, J. Hinkle, J. Asmussen, M. Hawley, and R. Kerber. Dissociation and recombination of oxygen atoms produced in a microwave discharge. Part I. Experiment. *Plasma Chemistry and Plasma Processing*, 3(1):63–78, 1983.

[36] S. F. Mertz, J. Asmussen, and M. C. Hawley. An Experimental Study of Reactions of Co and H2 in a Continuous Flow Microwave Discharge Reactor. *IEEE Transactions on Plasma Science*, 2(4):297–307, 1974.

[37] S. Whitehair, J. Asmussen, and S. Nakanishi. Microwave electrothermal thruster performance in helium gas. *Journal of Propulsion and Power*, 3(2):136–144, 1987.

[38] K. W. Hemawan, I. S. Wichman, T. Lee, T. A. Grotjohn, and J. Asmussen. Compact microwave re-entrant cavity applicator for plasma-assisted combustion. *Review of Scientific Instruments*, 80(5):053507, 2009.

[39] E. G. Lundblad. High pressure synthesis of diamond in Sweden in 1953. In *AIP Conference Proceedings*, volume 309, page 503, 1994.

[40] F. P. Bundy, H. T. Hall, H. M. Strong, and R. H. Wentorf. Man-made diamonds. *Nature*, 176(4471):51–55, 1955.

[41] D. G. Goodwin. Scaling laws for diamond chemical-vapor deposition. I. Diamond surface chemistry. *Journal of Applied Physics*, 74(11):6888, 1993.

[42] D. G. Goodwin. Scaling laws for diamond chemical-vapor deposition. II. Atomic hydrogen transport. *Journal of Applied Physics*, 74(11):6895, 1993.

[43] J. Asmussen. *Diamond films handbook*. Marcel Dekker, Inc., New York, 2002.

[44] M. Frenklach. The role of hydrogen in vapor deposition of diamond. *Journal of Applied Physics*, 65(12):5142, 1989.

[45] S. J. Harris and D. G. Goodwin. Growth on the reconstructed diamond (100) surface. *The Journal of Physical Chemistry*, 97(1):23–28, 1993.

[46] A. Tallaire, J. Achard, F. Silva, O. Brinza, and A. Gicquel. Growth of large size diamond single crystals by plasma assisted chemical vapour deposition: Recent achievements and remaining challenges. *Comptes Rendus Physique*, 14(2-3):169–184, 2013.

[47] P. W. May and Y. A. Mankelevich. Simulations of CVD Diamond Film Growth: 2D Models for the identities and concentrations of gas-phase species adsorbing on the surface. *MRS Proceedings*, 1282, 2011.

[48] J. C. Richley, Oliver J. L. Fox, M. N. R. Ashfold, and Y. A. Mankelevich. Combined experimental and modeling studies of microwave activated CH4/H2/Ar plasmas for microcrystalline, nanocrystalline, and ultrananocrystalline diamond deposition. *Journal of Applied Physics*, 109(6):063307, 2011.

[49] F. Silva, J. Achard, O. Brinza, X. Bonnin, K. Hassouni, A. Anthonis, K. De Corte, and J. Barjon. High quality, large surface area, homoepitaxial mpacvd diamond growth. *Diamond and Related Materials*, 18(5-8):683–697, 2009.

[50] C. C. Battaile, D. J. Srolovitz, and J. E. Butler. Morphologies of diamond films from atomic-scale simulations of chemical vapor deposition. *Diamond and Related Materials*, 6(9):1198–1206, 1997.

[51] K.-P. Kuo and J. Asmussen. An experimental study of high pressure synthesis of diamond films using a microwave cavity plasma reactor. *Diamond and Related Materials*, 6(9):1097–1105, 1997.

[52] J. Zhang, B. Huang, D. K. Reinhard, and J. Asmussen. An investigation of electromagnetic field patterns during microwave plasma diamond thin film deposition. *Journal of Vacuum Science & Technology A: Vacuum, Surfaces, and Films*, 8(3):2124–2128, 1990.

[53] J. Zhang. *Experimental development of microwave cavity plasma reactors for large area and high rate diamond film deposition.* Michigan State University, 1993.

[54] S. S. Zuo, M. K. Yaran, T. A. Grotjohn, D. K. Reinhard, and J. Asmussen. Investigation of diamond deposition uniformity and quality for freestanding film and substrate applications. *Diamond and Related Materials*, 17(3):300–305, 2008.

[55] S. Nicley. *The boron doping of single crystal diamond for high power diode applications.* Michigan State University, 2015.

[56] J. Achard, F. Silva, A. Tallaire, X. Bonnin, G. Lombardi, K. Hassouni, and A. Gicquel. High quality MPACVD diamond single crystal growth: high microwave power density regime. *Journal of Physics D: Applied Physics*, 40(20):6175–6188, 2007.

[57] S. Nad, Y. Gu, and J. Asmussen. Determining the microwave coupling and operational efficiencies of a microwave plasma assisted chemical vapor deposition reactor under high pressure diamond synthesis operating conditions. *Review of Scientific Instruments*, 86(7):074701, 2015.

[58] W. Tan and T. A. Grotjohn. Modelling the electromagnetic field and plasma discharge in a microwave plasma diamond deposition reactor. *Diamond and Related Materials*, 4(9):1145–1154, 1995.

[59] Y. Gu, J. Lu, T. A. Grotjohn, T. Schuelke, and J. Asmussen. Microwave plasma reactor design for high pressure and high power density diamond synthesis. *Diamond and Related Materials*, 24:210–214, 2012.

[60] J. Lu. *Single crystal microwave plasma assisted chemical vapor diamond synthesis at high pressures and high power densities*. Michigan State University, 2013.

[61] C. J. Widmann, W. Müller-Sebert, N. Lang, and C. E. Nebel. Homoepitaxial growth of single crystalline CVD-diamond. *Diamond and Related Materials*, 64:1–7, 2016.

[62] M. Füner, C. Wild, and P. Koidl. Simulation and development of optimized microwave plasma reactors for diamond deposition. *Surface and Coatings Technology*, 116:853–862, 1999.

[63] F. Silva, K. Hassouni, X. Bonnin, and A. Gicquel. Microwave engineering of plasma-assisted CVD reactors for diamond deposition. *Journal of Physics: Condensed Matter*, 21(36):364202, 2009.

[64] C.-S. Yan and Y. K. Vohra. Multiple twinning and nitrogen defect center in chemical vapor deposited homoepitaxial diamond. *Diamond and Related Materials*, 8(11):2022–2031, 1999.

[65] C.-S. Yan, Y. K. Vohra, H.-K. Mao, and R. J. Hemley. Very high growth rate chemical vapor deposition of single-crystal diamond. *Proceedings of the National Academy of Sciences*, 99(20):12523–12525, 2002.

[66] Y. Meng, C.-S. Yan, S. Krasnicki, Q. Liang, J. Lai, H. Shu, T. Yu, Andrew S., H.-K. Mao, and R. J. Hemley. High optical quality multicarat single crystal diamond produced by chemical vapor deposition. *physica status solidi (a)*, 209(1):101–104, 2012.

[67] S. Nad, Y. Gu, and J. Asmussen. Growth strategies for large and high quality single crystal diamond substrates. *Diamond and Related Materials*, 60:26–34, 2015.

[68] S. Nad and J. Asmussen. Analyses of single crystal diamond substrates grown in a pocket substrate holder via MPACVD. *Diamond and Related Materials*, 66:36–46, 2016.

[69] A. Chayahara, Y. Mokuno, Y. Horino, Y. Takasu, H. Kato, H. Yoshikawa, and N. Fujimori. The effect of nitrogen addition during high-rate homoepitaxial growth of diamond by microwave plasma CVD. *Diamond and Related Materials*, 13(11-12):1954–1958, 2004.

[70] A. Tallaire, J. Achard, F. Silva, R. S. Sussmann, and A. Gicquel. Homoepitaxial deposition of high-quality thick diamond films: effect of growth parameters. *Diamond and Related Materials*, 14(3-7):249–254, 2005.

[71] A. M. Zaitsev. *Optical Properties of Diamond: A Data Handbook*, volume 42. Springer, Bochum, 1st editio edition, August 2001.

[72] S. Nad, A. Charris, and J. Asmussen. MPACVD growth of single crystalline diamond substrates with PCD rimless and expanding surfaces. *Applied Physics Letters*, 109(16):162103, 2016.

[73] M. Naamoun, A. Tallaire, F. Silva, J. Achard, P. Doppelt, and A. Gicquel. Etch-pit formation mechanism induced on hpht and cvd diamond single crystals by h2/o2 plasma etching treatment. *physica status solidi (a)*, 209(9):1715–1720, 2012.

[74] M. Mayr, M. Fischer, O. Klein, S. Gsell, and M. Schreck. Interaction between surface structures and threading dislocations during epitaxial diamond growth. *physica status solidi (a)*, 212(11):2480–2486, 2015.

[75] O. Klein, M. Mayr, M. Fischer, S. Gsell, and M. Schreck. Propagation and annihilation of threading dislocations during off-axis growth of heteroepitaxial diamond films. *Diamond and Related Materials*, 65:53–58, 2016.

[76] A. Tallaire, J. Achard, O. Brinza, V. Mille, M. Naamoun, F. Silva, and A. Gicquel. Growth strategy for controlling dislocation densities and crystal morphologies of single crystal diamond by using pyramidal-shape substrates. *Diamond and Related Materials*, 33:71–77, 2013.

[77] T. Bauer, M. Schreck, and B. Stritzker. Homoepitaxial diamond layers on off-axis Ib HPHT substrates: Growth of thick films and characterisation by high-resolution X-ray diffraction. *Diamond and Related Materials*, 15(4-8):472–478, 2006.

[78] M. Naamoun, A. Tallaire, P. Doppelt, A. Gicquel, M. Legros, J. Barjon, and J. Achard. Reduction of dislocation densities in single crystal CVD diamond by using self-assembled metallic masks. *Diamond and Related Materials*, 58:62–68, 2015.

[79] M. P. Gaukroger, P. M. Martineau, M. J. Crowder, I. Friel, S. D. Williams, and D. J. Twitchen. X-ray topography studies of dislocations in single crystal CVD diamond. *Diamond and Related Materials*, 17(3):262–269, 2008.

[80] I. Friel, S. L. Clewes, H. K. Dhillon, N. Perkins, D. J. Twitchen, and G. A. Scarsbrook. Control of surface and bulk crystalline quality in single crystal diamond grown by chemical vapour deposition. *Diamond and Related Materials*, 18(5-8):808–815, 2009.

[81] A. Tallaire, O. Brinza, V. Mille, L. William, and J. Achard. Reduction of Dislocations in Single Crystal Diamond by Lateral Growth over a Macroscopic Hole. *Advanced Materials*, 2017.

[82] A. P. Bolshakov, V. G. Ralchenko, A. V. Polskiy, V. I. Konov, E. E. Ashkinazi, A. A. Khomich, G. V. Sharonov, R. A. Khmelnitsky, E. V. Zavedeev, A. V. Khomich, et al. Growth of single-crystal diamonds in microwave plasma. *Plasma physics reports*, 38(13):1113–1118, 2012.

[83] AP Bolshakov, VG Ralchenko, VY Yurov, AF Popovich, IA Antonova, AA Khomich, EE Ashkinazi, SG Ryzhkov, AV Vlasov, and AV Khomich. High-rate growth of single crystal diamond in microwave plasma in CH4/H2 and CH4/H2/Ar gas mixtures in presence of intensive soot formation. *Diamond and Related Materials*, 62:49–57, 2016.

[84] A. Tallaire, C. Rond, F. Bénédic, O. Brinza, J. Achard, F. Silva, and A. Gicquel. Effect of argon addition on the growth of thick single crystal diamond by high-power plasma CVD. *physica status solidi (a)*, 208(9):2028–2032, 2011.

[85] E. V. Bushuev, V. Y. Yurov, A. P. Bolshakov, V. G. Ralchenko, E. E. Ashkinazi, A. V. Ryabova, I. A. Antonova, P. V. Volkov, A. V. Goryunov, and A. Y. Luk'yanov. Synthesis of single crystal diamond by microwave plasma assisted chemical vapor deposition with in situ low-coherence interferometric control of growth rate. *Diamond and Related Materials*, 66:83–89, 2016.

[86] E. V. Bushuev, V. Y. Yurov, A. P. Bolshakov, V. G. Ralchenko, A. A. Khomich, I. A. Antonova, E. E. Ashkinazi, V. A. Shershulin, V. P. Pashinin, and V. I. Konov. Express in situ measurement of epitaxial CVD diamond film growth kinetics. *Diamond and Related Materials*, 2017.

[87] N. R. Parikh, J. D. Hunn, E. McGucken, M. L. Swanson, C. W. White, R. A. Rudder, D. P. Malta, J. B. Posthill, and R. J. Markunas. Single-crystal diamond plate liftoff achieved by ion implantation and subsequent annealing. *Applied Physics Letters*, 61(26):3124, 1992.

[88] M. Marchywka, P. E. Pehrsson, D. J. Vestyck, and D. Moses. Low energy ion implantation and electrochemical separation of diamond films. *Applied Physics Letters*, 63(25):3521, 1993.

[89] J. D. Hunn, S. P. Withrow, C. W. White, R. E. Clausing, L. Heatherly, C. Paul Christensen, and N. R. Parikh. The separation of thin single crystal films from bulk diamond by mev implantation. *Nuclear Instruments and Methods in Physics Research Section B: Beam Interactions with Materials and Atoms*, 99(1):602–605, 1995.

[90] J. B. Posthill, D. P. Malta, T. P. Humphreys, G. C. Hudson, R. E. Thomas, R. A. Rudder, and R. J. Markunas. Method of fabricating a free-standing diamond single crystal using growth from the vapor phase. *Journal of Applied Physics*, 79(5):2722–2727, 1996.

[91] J. Yang, C. F. Wang, E. L. Hu, and J. E. Butler. Lift-Off Process to get Free-Standing High Quality Single Crystal Diamond Films and Suspended Single Crystal Diamond Devices. In *MRS Proceedings*, volume 956, pages 0956–J17. Cambridge Univ Press, 2006.

[92] P. Olivero, S. Rubanov, P. Reichart, B. C. Gibson, S. T. Huntington, J. Rabeau, A. D. Greentree, J. Salzman, D. Moore, D. N. Jamieson, and S. Prawer. Ion-Beam-Assisted Lift-Off Technique for Three-Dimensional Micromachining of Freestanding Single-Crystal Diamond. *Advanced Materials*, 17(20):2427–2430, 2005.

[93] H. Yamada, A. Chayahara, Y. Mokuno, N. Tsubouchi, S. Shikata, and N. Fujimori. Developments of elemental technologies to produce inch-size single-crystal diamond wafers. *Diamond and Related Materials*, 20(4):616–619, 2011.

[94] Y. Mokuno, A. Chayahara, and H. Yamada. Synthesis of large single crystal diamond plates by high rate homoepitaxial growth using microwave plasma CVD and lift-off process. *Diamond and Related Materials*, 17(4-5):415–418, 2008.

[95] C.-F. Wang, R. Hanson, D. D. Awschalom, E. L. Hu, T. Feygelson, J. Yang, and J. E. Butler. Fabrication and characterization of two-dimensional photonic crystal microcavities in nanocrystalline diamond. *Applied Physics Letters*, 91(20):201112–201112, 2007.

[96] C. Uzan-Saguy, C. Cytermann, R. Brener, V. Richter, M. Shaanan, and R. Kalish. Damage threshold for ion-beam induced graphitization of diamond. *Applied Physics Letters*, 67(9):1194, 1995.

[97] P. John, N. Polwart, C. E. Troupe, and J. I. B. Wilson. The oxidation of (100) textured diamond. *Diamond and Related Materials*, 11(3):861–866, 2002.

[98] Y. Tzeng, J. Wei, J. T. Woo, and W. Lanford. Free-standing single-crystalline chemically vapor deposited diamond films. *Applied Physics Letters*, 63(16):2216, 1993.

[99] R. Locher, D. Behr, H. Güllich, N. Herres, P. Koidl, R. Samlenski, and R. Brenn. Lift-off technique of homoepitaxial CVD diamond films by deep implantation and selective etching. *Diamond and Related Materials*, 6(5-7):654–657, 1997.

[100] A. Chayahara, Y. Mokuno, N. Tsubouchi, and H. Yamada. Development of single-crystalline diamond wafers. *Synthesiology English edition*, 3(4):259–267, 2010.

[101] J. Czochralski. Ein neues verfahren zur messung der kristallisationsgeschwindigheit der metalle. *Zeitschrift für physikalische Chemie*, 92:219–212, 1918.

[102] J. Bardeen and W. H. Brattain. The transistor, a semi-conductor triode. *Physical Review*, 74(2):230, 1948.

[103] N. Ohtani, T. Fujimoto, T. Aigo, M. Katsuno, H. Tsuge, and H. Yashiro. Large high-quality silicon carbide single crystal substrates. *Nippon steel technical report. Overseas*, (84):36–41, 2001.

[104] H. Tang, H. Li, and J. Xu. *Growth and Development of Sapphire Crystal for LED Applications*. InTech, 2013.

[105] G. Janssen and L. J. Giling. Mosaic growth of diamond. *Diamond and Related Materials*, 4(7):1025–1031, 1995.

[106] C. Findeling-Dufour and A. Gicquel. Study for fabricating large area diamond single-crystal layers. *Thin solid films*, 308:178–185, 1997.

[107] H. Yamada, A. Chayahara, Y. Mokuno, H. Umezawa, S. Shikata, and N. Fujimori. Fabrication of 1 Inch Mosaic Crystal Diamond Wafers. *Applied Physics Express*, 3(5):051301, 2010.

[108] H. Yamada, A. Chayahara, H. Umezawa, N. Tsubouchi, Y. Mokuno, and S. Shikata. Fabrication and fundamental characterizations of tiled clones of single-crystal diamond with 1-inch size. *Diamond and Related Materials*, 24:29–33, 2012.

[109] H. Yamada, A. Chayahara, Y. Mokuno, N. Tsubouchi, and S. Shikata. Uniform growth and repeatable fabrication of inch-sized wafers of a single-crystal diamond. *Diamond and Related Materials*, 33:27–31, 2013.

[110] H. Yamada, A. Chayahara, Y. Mokuno, Y. Kato, and S. Shikata. A 2-in. mosaic wafer made of a single-crystal diamond. *Applied Physics Letters*, 104(10):102110, 2014.

[111] Y. Mokuno, A. Chayahara, H. Yamada, and N. Tsubouchi. Improving purity and size of single-crystal diamond plates produced by high-rate cvd growth and lift-off process using ion implantation. *Diamond and Related Materials*, 18(10):1258–1261, 2009.

[112] Y. Mokuno, A. Chayahara, Y. Soda, Y. Horino, and N. Fujimori. Synthesizing single-crystal diamond by repetition of high rate homoepitaxial growth by microwave plasma CVD. *Diamond and Related Materials*, 14(11-12):1743–1746, 2005.

[113] R. Polini and M. Tomellini. Analysis of size distribution functions of diamond crystallites formed in the early stages of chemical vapour deposition. *Diamond and Related Materials*, 4(12):1311–1316, 1995.

[114] X. Jiang, C.-P. Klages, R. Zachai, M. Hartweg, and H.-J. Füsser. Epitaxial diamond thin films on (001) silicon substrates. *Applied Physics Letters*, 62(26):3438–3440, 1993.

[115] H. Makita, K. Nishimura, N. Jiang, A. Hatta, T. Ito, and A. Hiraki. Ultrahigh particle density seeding with nanocrystal diamond particles. *Thin Solid Films*, 281:279–281, 1996.

[116] Y. Mitsuda, Y. Kojima, T. Yoshida, and K. Akashi. The growth of diamond in microwave plasma under low pressure. *Journal of Materials Science*, 22(5):1557–1562, 1987.

[117] T. Yara, H. Makita, A. Hatta, T. Ito, and A. Hiraki. Low temperature fabrication of diamond films with nanocrystal seeding. *Japanese Journal of Applied Physics*, 34(3A):L312, 1995.

[118] H. Liu and D. S. Dandy. Studies on nucleation process in diamond CVD: an overview of recent developments. *Diamond and Related Materials*, 4(10):1173–1188, 1995.

[119] Bristol University Diamond Group. *http://www.chm.bris.ac.uk/pt/diamond/semflat.htm*, 2017.

[120] R. Kohl, C. Wild, N. Herres, P. Koidl, B. R. Stoner, and J. T. Glass. Oriented nucleation and growth of diamond films on β-SiC and Si. *Applied Physics Letters*, 63(13):1792–1794, 1993.

[121] J. Robertson. Mechanism of bias-enhanced nucleation and heteroepitaxy of diamond on Si. *Diamond and Related Materials*, 4(5-6):549–552, 1995.

[122] M. Schreck, K.-H. Thürer, and B. Stritzker. Limitations of the process window for the bias enhanced nucleation of heteroepitaxial diamond films on silicon in the time domain. *Journal of Applied Physics*, 81(7):3092–3095, 1997.

[123] H. Kawarada, T. Suesada, and H. Nagasawa. Heteroepitaxial growth of smooth and continuous diamond thin films on silicon substrates via high quality silicon carbide buffer layers. *Applied Physics Letters*, 66(5):583–585, 1995.

[124] M. Schreck, F. Hörmann, H. Roll, J. K. N. Lindner, and B. Stritzker. Diamond nucleation on iridium buffer layers and subsequent textured growth: A route for the realization of single-crystal diamond films. *Applied Physics Letters*, 78(2):192–194, 2001.

[125] M. Schreck, S. Gsell, R. Brescia, and M. Fischer. on bombardment induced buried lateral growth: the key mechanism for the synthesis of single crystal diamond wafers. *Scientific Reports*, 7, 2017.

[126] S. Gsell, T. Bauer, J. Goldfuß, M. Schreck, and B. Stritzker. A route to diamond wafers by epitaxial deposition on silicon via iridium/yttria-stabilized zirconia buffer layers. *Applied Physics Letters*, 84(22):4541–4543, 2004.

[127] T. Bauer, S. Gsell, M. Schreck, J. Goldfuß, J. Lettieri, D. G. Schlom, and B. Stritzker. Growth of epitaxial diamond on silicon via iridium/SrTiO 3 buffer layers. *Diamond and Related Materials*, 14(3):314–317, 2005.

[128] M. Schreck, M. Mayr, O. Klein, M. Fischer, S. Gsell, A. F. Sartori, and B.-C. Gallheber. Multiple role of dislocations in the heteroepitaxial growth of diamond: A brief review. *physica status solidi (a)*, 213(8):2028–2035, 2016.

[129] M. Fischer, S. Gsell, M. Schreck, and A. Bergmaier. Growth sector dependence and mechanism of stress formation in epitaxial diamond growth. *Applied Physics Letters*, 100(4):041906, 2012.

[130] Y.-H. Tang and B. Golding. Stress engineering of high-quality single crystal diamond by heteroepitaxial lateral overgrowth. *Applied Physics Letters*, 108(5):052101, 2016.

[131] L. T. M. Hoa, T. Ouisse, D. Chaussende, M. Naamoun, A. Tallaire, and J. Achard. Birefringence microscopy of unit dislocations in diamond. *Crystal Growth & Design*, 14(11):5761–5766, 2014.

[132] S. Kono, T. Teraji, H. Kodama, and A. Sawabe. Imaging of diamond defect sites by electron-beam-induced current. *Diamond and Related Materials*, 59:54–61, 2015.

[133] Y. Kato, H. Umezawa, S. Shikata, and T. Teraji. Local stress distribution of dislocations in homoepitaxial chemical vapor deposite single-crystal diamond. *Diamond and Related Materials*, 23:109–111, 2012.

[134] C. Stehl, M. Fischer, S. Gsell, E. Berdermann, M. S. Rahman, M. Traeger, O. Klein, and M. Schreck. Efficiency of dislocation density reduction during heteroepitaxial growth of diamond for detector applications. *Applied Physics Letters*, 103(15):151905, 2013.

[135] G. Lombardi, X. Duten, K. Hassouni, A. Rousseau, and A. Gicquel. Effects of pulsed microwave plasmas on diamond deposition. *Journal of The Electrochemical Society*, 150(5):C311–C319, 2003.

[136] K. Hassouni, O. Leroy, S. Farhat, and A. Gicquel. Modeling of H_2 and H_2/CH_4 moderate-pressure microwave plasma used for diamond deposition. *Plasma chemistry and plasma processing*, 18(3):325–362, 1998.

[137] K. Hassouni, X. Duten, A. Rousseau, and A. Gicquel. Investigation of chemical kinetics and energy transfer in a pulsed microwave H 2 /CH 4 plasma. *Plasma Sources Science and Technology*, 10(1):61, 2001.

[138] S. I. Gritsinin, I. A. Kossyi, N. I. Malykh, V. G. Ral'Chenko, K. F. Sergeichev, V. P. Silakov, I. A. Sychev, N. M. Tarasova, and A. V. Chebotarev. Determination of the gas temperature in high-pressure microwave discharges in hydrogen. *Journal of Physics D: Applied Physics*, 31(20):2942, 1998.

[139] A. Gicquel, K. Hassouni, G. Lombardi, X. Duten, and A. Rousseau. New driving parameters for diamond deposition reactors: pulsed mode versus continuous mode. *Materials Research*, 6(1):25–37, 2003.

[140] O. Brinza, J. Achard, F. Silva, X. Duten, A. Michau, K. Hassouni, and A. Gicquel. Improvement of energetic efficiency for homoepitaxial diamond growth in a H2/CH4 pulsed discharge. *physica status solidi (a)*, 204(9):2847 – 2853, 2007.

[141] K. Hassouni, T. A. Grotjohn, and A. Gicquel. Self-consistent microwave field and plasma discharge simulations for a moderate pressure hydrogen discharge reactor. *Journal of Applied Physics*, 86(1):134–151, 1999.

[142] G. Lombardi, K. Hassouni, G.-D. Stancu, L. Mechold, J. Röpcke, and A. Gicquel. Modeling of microwave discharges of h 2 admixed with ch 4 for diamond deposition. *Journal of Applied Physics*, 98(5):053303, 2005.

[143] A. L. Vikharev, A. M. Gorbachev, V. A. Koldanov, R. A. Akhmedzhanov, D. B. Radishchev, T. A. Grotjohn, S. Zuo, and J. Asmussen. Comparison of pulsed and CW regimes of MPACVD reactor operation. *Diamond and related materials*, 12(3):272–276, 2003.

[144] A. Tallaire, J. Achard, F. Silva, and A. Gicquel. Effect of increasing the microwave density in both continuous and pulsed wave mode on the growth of monocrystalline diamond films. *physica status solidi (a)*, 202(11):2059–2065, 2005.

[145] A. Tallaire, J. Achard, A. Secroun, O. De Gryse, F. De Weerdt, J. Barjon, F. Silva, and A. Gicquel. Multiple growth and characterization of thick diamond single crystals using chemical vapour deposition working in pulsed mode. *Journal of crystal growth*, 291(2):533–539, 2006.

[146] A. B. Muchnikov, A. L. Vikharev, A. M. Gorbachev, and D. B. Radishev. Comparative study of homoepitaxial single crystal diamond growth at continuous and pulsed mode of MPACVD reactor operation. *Diamond and Related Materials*, 20(8):1225–1228, 2011.

[147] A. L. Vikharev, A. M. Gorbachev, A. B. Muchnikov, D. B. Radishev, E. A. Kopelovich, and M. M. Troitskiy. Investigation of the optimized parameters of microwave plasma-assisted chemical vapour deposition reactor operation in a pulsed mode. *Journal of Physics D: Applied Physics*, 45(39):395202, 2012.

[148] H. Yamada, A. Chayahara, and Y. Mokuno. Short-pulse excitation of microwave plasma for efficient diamond growth. *Applied Physics Letters*, 109(9):092102, 2016.

[149] Kadek Wardika Hemawan. *Investigation of microwave cavity applicators for plasma assisted CVD diamond synthesis and plasma assisted combustion*. Michigan State University, 2010.

[150] S. Nad. *Growth and characterization of large, high quality single crystal diamond substrates via microwave plasma assisted chemical vapor deposition*. Michigan State University, 2016.

[151] Western Michigan University Tandem Van de Graaff Accelerator. *http://www.wmich.edu/physics/accelerator*, 2016.

[152] A. Nussbaum and R. A. Phillips. *Contemporary Optics for Scientists and Engineers*. Prentice-Hall, 1976.

[153] J. C. Angus. Growth of Diamond Seed Crystals by Vapor Deposition. *Journal of Applied Physics*, 39(6):2915, 1968.

[154] C. J. H. Wort and Richard S. Balmer. Diamond as an electronic material. *Materials Today*, 11(1):22–28, 2008.

[155] R. P. Mildren and A. Sabella. Highly efficient diamond raman laser. *Optics Letters*, 34(18):2811–2813, 2009.

[156] Y. V. Shvyd'ko, S. Stoupin, A. Cunsolo, A. H. Said, and X. Huang. High-reflectivity high-resolution X-ray crystal optics with diamonds. *Nature Physics*, 6(3):196–199, 2010.

[157] B. Nohammer, J. Hoszowska, A. K. Freund, and C. David. Diamond planar refractive lenses for third-and fourth-generation x-ray sources. *Journal of Synchrotron Radiation*, 10(2):168–171, 2003.

[158] R. Barrett, J. Härtwig, C. Morawe, A. Rommeveaux, and A. Snigirev. X-ray optics at the esrf. *Synchrotron Radiation News*, 23(1):36–42, 2010.

[159] R. C. Burns, A. Chumakov, G. Carbone, S. H. Connell, D. Dube, H. P. Godfried, J. O. Hansen, J. Härtwig, F. Masiello, and M. Rebak. Diamonds for X-ray optical applications at 3rd and 4th generation X-ray sources. In *Proc. of SPIE Vol*, volume 6705, pages 67050K1–6, 2007.

[160] S. N. Polyakov, V. N. Denisov, N. V. Kuzmin, M. S. Kuznetsov, S. Y. Martyushov, S. A. Nosukhin, S. A. Terentiev, and V. D. Blank. Characterization of top-quality type IIa synthetic diamonds for new X-ray optics. *Diamond and Related Materials*, 20(5-6):726–728, 2011.

[161] S. Koizumi, K. Watanabe, M. Hasegawa, and H. Kanda. Ultraviolet emission from a diamond pn junction. *Science*, 292(5523):1899–1901, 2001.

[162] D. J. Twitchen, A. J. Whitehead, S. E. Coe, J. Isberg, J. Hammersberg, T. Wikstrom, and E. Johansson. High-voltage single-crystal diamond diodes. *IEEE Transactions on Electron Devices*, 51(5):826–828, 2004.

[163] J. Isberg, J. Hammersberg, DJ J. Twitchen, and A. J. Whitehead. Single crystal diamond for electronic applications. *Diamond and Related Materials*, 13(2):320–324, 2004.

[164] H. Schneider, J.-L. Sanchez, and J. Achard. The diamond for power electronic devices. In *Power Electronics and Applications, 2005 European Conference on*. IEEE, 2005.

[165] R. S. Balmer, J. R. Brandon, S. L. Clewes, H. K. Dhillon, J. M. Dodson, I. Friel, P. N. Inglis, T. D. Madgwick, M. L. Markham, and T. P. Mollart. Chemical vapour deposition synthetic diamond: materials, technology and applications. *Journal of Physics: Condensed Matter*, 21(36):364221, 2009.

[166] J. Asmussen, T. A. Grotjohn, T. Schuelke, M. F. Becker, M. K. Yaran, D. J. King, S. Wicklein, and D. K. Reinhard. Multiple substrate microwave plasma-assisted chemical vapor deposition single crystal diamond synthesis. *Applied Physics Letters*, 93(3):031502–031502, 2008.

[167] P. W. Butler-Smith, D. A. Axinte, M. Pacella, and M. W. Fay. Micro/nanometric investigations of the effects of laser ablation in the generation of micro-tools from solid CVD diamond structures. *Journal of Materials Processing Technology*, 213(2):194–200, 2 2013.

[168] T. Schuelke and T. A. Grotjohn. Diamond polishing. *Diamond and Related Materials*, 32:17–26, 2013.

[169] D. C. Harris. Properties of diamond for window and dome applications. *SPIE Proceedings*, 218:2286, 1994.

[170] I. Kiflawi, A. E. Mayer, P. M. Spear, J. A. Van Wyk, and G. S. Woods. Infrared absorption by the single nitrogen and a defect centres in diamond. *Philosophical Magazine Part B*, 69(6):1141–1147, 1994.

[171] N. V. Surovtsev, I. N. Kupriyanov, V. K. Malinovsky, V. A. Gusev, and Y. N. Pal'yanov. Effect of nitrogen impurities on the Raman line width in diamonds. *Journal of Physics: Condensed Matter*, 11(24):4767, 1999.

[172] B. P. Allen and T. Evans. Aggregation of nitrogen in diamond, including platelet formation. *Proceedings of the Royal Society A: Mathematical, Physical and Engineering Sciences*, 375(1760):93–104, 1981.

[173] F. Silva, X. Bonnin, J. Achard, O. Brinza, A. Michau, and A. Gicquel. Geometric modeling of homoepitaxial cvd diamond growth: I. the {100}{111}{110}{113} system. *Journal of Crystal Growth*, 310(1):187–203, 2008.

[174] J. W. Ager III and M. D. Drory. Quantitative measurement of residual biaxial stress by Raman spectroscopy in diamond grown on a Ti alloy by chemical vapor deposition. *Physical Review B*, 48(4):2601, 1993.

[175] Y. Meng, C.-S. Yan, J. Lai, S. Krasnicki, H. Shu, T. Yu, Q. Liang, H.-K. Mao, and R. J. Hemley. Enhanced optical properties of chemical vapor deposited single crystal diamond by low-pressure/high-temperature annealing. *Proceedings of the National Academy of Sciences*, 105(46):17620–17625, 2008.

[176] E. Woerner, C. Wild, W. Mueller-Sebert, and P. Koidl. CVD-diamond optical lenses. *Diamond and Related Materials*, 10(3):557–560, 2001.

[177] K. Evans-Lutterodt, J. Ablett, A. Stein, C.-C. Kao, D. Tennant, F. Klemens, A. Taylor, C. Jacobsen, P. Gammel, and H. Huggins. Single-element elliptical hard x-ray micro-optics. *Optics Express*, 11(8):919–926, 2003.

[178] Y. Mokuno, A. Chayahara, Y. Soda, H. Yamada, Y. Horino, and N. Fujimori. High rate homoepitaxial growth of diamond by microwave plasma CVD with nitrogen addition. *Diamond and Related Materials*, 15(4-8):455–459, 2006.

[179] M. Fischer, R. Brescia, S. Gsell, M. Schreck, T. Brugger, T. Greber, J. Osterwalder, and B. Stritzker. Growth of twin-free heteroepitaxial diamond on Ir/YSZ/Si(111). *Journal of Applied Physics*, 104(12):123531, 2008.

[180] M. Muehle, M. F. Becker, T. Schuelke, and J. Asmussen. Substrate crystal recovery for homoepitaxial diamond synthesis. *Diamond and Related Materials*, 42:8–14, 2014.

[181] H. A. Hoff, D. J. Vestyck, J. E. Butler, and J. F. Prins. Ion implanted, outdiffusion produced diamond thin films. *Applied Physics Letters*, 62(1):34, 1993.

[182] J. F. Ziegler, M. D. Ziegler, and J. P. Biersack. SRIM–The stopping and range of ions in matter. *Nuclear Instruments and Methods in Physics Research Section B: Beam Interactions with Materials and Atoms*, 268(11):1818–1823, 2010.

[183] M. S. Dresselhaus and R. Kalish. Implantation-induced modifications to diamond. In *Ion Implantation in Diamond, Graphite and Related Materials*, pages 129–158. Springer, 1992.

[184] E. Friedland, H. D. Carstanjen, G. Myburg, and M. A. Nasr. Dependence of damage efficiency of ions in diamond on electronic stopping. *Nuclear Instruments and Methods in Physics Research Section B: Beam Interactions with Materials and Atoms*, 230(1-4):129–135, 2005.

[185] D. P. Adams, M. J. Vasile, T. M. Mayer, and V. C. Hodges. Focused ion beam milling of diamond: effects of H_2O on yield, surface morphology and microstructure. *Journal of Vacuum Science & Technology B: Microelectronics and Nanometer Structures*, 21(6):2334–2343, 2003.

[186] J. Achard, A. Tallaire, R. Sussmann, F. Silva, and A. Gicquel. The control of growth parameters in the synthesis of high-quality single crystalline diamond by CVD. *Journal of Crystal Growth*, 284(3-4):396–405, 2005.

[187] Z. Liu, J. Z. Liu, Y. Cheng, Z. Li, L. Wang, and Q. Zheng. Interlayer binding energy of graphite: A mesoscopic determination from deformation. *Physical Review B*, 85(20):205418, 2012.

[188] J. Schindelin, I. Arganda-Carreras, E. Frise, V. Kaynig, M. Longair, T. Pietzsch, S. Preibisch, C. Rueden, S. Saalfeld, B. Schmid, et al. Fiji: an open-source platform for biological-image analysis. *Nature methods*, 9(7):676–682, 2012.

[189] J. Robertson. Diamond-like amorphous carbon. *Materials Science and Engineering: R: Reports*, 37(4):129–281, 2002.

[190] A. B. Muchnikov, A. L. Vikharev, A. M. Gorbachev, D. B. Radishev, V. D. Blank, and S. A. Terentiev. Homoepitaxial single crystal diamond growth at different gas pressures and MPACVD reactor configurations. *Diamond and Related Materials*, 19(5-6):432–436, 2010.

[191] Q. Liang, Y. F. Meng, C.-S. Yan, S. Krasnicki, J. Lai, K. W. Hemawan, H. Shu, D. Popov, T. Yu, W. Yang, H. K. . K. Mao, and R. J. Hemley. Developments in synthesis, characterization, and application of large, high-quality CVD single crystal diamond. *Journal of Superhard Materials*, 35(4):195–213, 2013.

[192] Q. Liang, C.-S. Yan, J. Lai, Y. Meng, S. Krasnicki, H. Shu, H.-K. Mao, and R. J. Hemley. Large Area Single-Crystal Diamond Synthesis by 915 MHz Microwave Plasma-Assisted Chemical Vapor Deposition. *Crystal Growth & Design*, 14(7):3234–3238, 2014.

[193] M. Schreck, J. Asmussen, S. Shikata, J.-C. Arnault, and N. Fujimori. Large-area high-quality single crystal diamond. *MRS Bulletin*, 39(06):504–510, 2014.

[194] A. K. Mallik. Microwave Plasma CVD Grown Single Crystal Diamonds–A Review. *Journal of Coating Science and Technology*, 3(2):000–000, 2016.

[195] M. A. Lobaev, S. A. Bogdanov, D. B. Radishev, A. L. Vikharev, and A. M. Gorbachev. Method of power density determination in microwave discharge, sustained in hydrogenmethane gas mixture. *Diamond and Related Materials*, 66:177–182, 2016.

[196] K. W. Hemawan, C. S. Yan, Q. Liang, J. Lai, Y. Meng, S. Krasnicki, H. K. Mao, and R. J. Hemley. Hot spot formation in microwave plasma CVD diamond synthesis. *IEEE Transactions on Plasma Science*, 39(11):2790, 2011.

[197] Y. Gu. *The New Generation Microwave Plasma Assisted CVD Reactor for Diamond Synthesis*. Michigan State University, 2011.

[198] J. A. Venables, G. D. T. Spiller, and M. Hanbucken. Nucleation and growth of thin films. *Reports on Progress in Physics*, 47(4):399, 1984.

[199] A. Rousseau, L. Tomasini, G. Gousset, C. Boisse-Laporte, and P. Leprince. Pulsed microwave discharge: a very efficient H atom source. *Journal of Physics D: Applied Physics*, 27(11):2439, 1994.

[200] J. Laimer and S. Matsumoto. Atomic hydrogen concentrations in pulsed microwave discharges used for diamond synthesis. *Plasma Chemistry and Plasma Processing*, 14(2):117–130, 1994.

[201] L. De Poucques, J. Bougdira, R. Hugon, G. Henrion, and P. Alnot. Time-resolved plasma diagnostics for a better understanding of the improvement of pulsed MWPACVD of diamond. *Journal of Physics D: Applied Physics*, 34(6):896, 2001.

[202] G. Lombardi, K. Hassouni, G.-D. Stancu, L. Mechold, J. Röpcke, and A. Gicquel. Modeling of microwave discharges of H2 admixed with CH4 for diamond deposition. *Journal of Applied Physics*, 98(5):053303, 2005.

[203] G. Lombardi, K. Hassouni, G. D. Stancu, L. Mechold, J. Röpcke, and A. Gicquel. Study of an H2/CH4 moderate pressure microwave plasma used for diamond deposition: modelling and IR tuneable diode laser diagnostic. *Plasma Sources Science and Technology*, 14(3):440, 2005.

[204] U. F. S. D'Haenens-Johansson, A. Katmsha, K. S. Moe, et al. Large colorless hpht synthetic diamonds from new diamond technology. *Gems & Gemology*, 51(3):260–279, 2015.

[205] New Diamond Technologies. *http://ndtcompany.com*, 2017.

[206] P. M. Martineau, M. P. Gaukroger, K. B. Guy, S. C. Lawson, D. J. Twitchen, I. Friel, J. O. Hansen, G. C. Summerton, T. P. G. Addison, and R. Burns. High crystalline quality single crystal chemical vapour deposition diamond. *Journal of Physics: Condensed Matter*, 21(36):364205, 2009.